



TÉCNICO
LISBOA

UNIVERSIDADE DE LISBOA
INSTITUTO SUPERIOR TÉCNICO

**Simulation of Transition from Laminar to Turbulent Regime in
Practical Applications of Incompressible Flow**

Rui Miguel Alves Lopes

Supervisor: Doctor Luís Rego da Cunha de Eça

Co-Supervisor: Doctor Guilherme Nuno Vasconcelos Beleza Vaz

Thesis approved in public session to obtain the PhD Degree in

Mechanical Engineering

Jury final classification: Pass with Distinction

2021

**Simulation of Transition from Laminar to Turbulent Regime in
Practical Applications of Incompressible Flow**

Rui Miguel Alves Lopes

Supervisor: Doctor Luís Rego da Cunha de Eça

Co-Supervisor: Doctor Guilherme Nuno Vasconcelos Beleza Vaz

**Thesis approved in public session to obtain the PhD Degree in
Mechanical Engineering**

Jury final classification: Pass with Distinction

Jury

Chairperson: Doctor Hélder Carriço Rodrigues, Instituto Superior Técnico, Universidade de Lisboa

Members of the Committee:

**Doctor Stephen Richard Turnock, Faculty of Engineering and Physical Sciences, School of Engineering,
University of Southampton, UK**

Doctor Serge Leon Toxopeus, Maritime Research Institute Netherlands - MARIN, the Netherlands

Doctor João Manuel Melo de Sousa, Instituto Superior Técnico, Universidade de Lisboa

Doctor Carlos Frederico Neves Bettencourt da Silva, Instituto Superior Técnico, Universidade de Lisboa

**Doctor Guilherme Nuno Vasconcelos Beleza Vaz, Faculty of Engineering,
University of Duisburg-Essen, Germany**

Doctor Meelan Muralidhar Choudhari, NASA Langley Research Center, USA

Funding Institution:

FCT - Fundação para a Ciência e a Tecnologia

Acknowledgments

This dissertation contains work that spanned over several years, a challenging journey whose completion was only possible thanks to the help and support of several people.

I would like to thank my two supervisors, Luís Eça and Guilherme Vaz, for their guidance, insight and imparted knowledge throughout these years, which will undoubtedly have a great impact during the rest of my professional life.

I would also like to thank João Baltazar, with whom I had the pleasure of sharing the workspace during the pre-pandemic times ever since I started my master's thesis. His fantastic hospitality and the discussions about CFD, sports, politics and life have been invaluable and something I will always cherish. On a similar note, I would also like to thank my former and current PhD colleagues, Filipe Pereira and João Muralha, for many fruitful discussions.

On the technical side, I would like to thank Maarten Kerkvliet, for his invaluable help with GridPro and assistance in generating the grids for the sickle wing, as well as support during my stay at MARIN.

I also acknowledge two of my friends, Hugo Torres and Gonçalo Saldanha, which have been a constant presence during these years.

Finally, I am thankful to my family, in particular, my parents, to whom I owe who I am today, and to my brother and his wife, who have encouraged me every step of the way.

Financial support was provided by Fundação para a Ciência e Tecnologia through a research grant under the Bolsas de Doutoramento and Pós-Doutoramento 2016 program and is gratefully acknowledged.

Resumo

A modelação de escoamentos a números de Reynolds moderados é actualmente uma das áreas principais no desenvolvimento da mecânica de fluidos computacional. A extensão considerável de escoamento laminar presente nestes escoamentos é incompatível com a solução numérica obtida pelos modelos de turbulência habitualmente usados, que prevêem uma extensão desprezável da região de escoamento laminar. As metodologias baseadas na teoria da estabilidade linear, das quais o método e^N é o exemplo mais popular, podem obter resultados exactos, especialmente em estudos paramétricos. No entanto, estas técnicas dependem de várias operações não locais, que são difíceis de implementar em códigos que resolvem as equações de Navier-Stokes em média de Reynolds (RANS), dado que estes dependem fortemente em paralelização. A alternativa mais promissora para a previsão de transição num cálculo com as equações RANS é o uso de modelos baseados em equações de transporte, os chamados modelos de transição, que tem sofrido um desenvolvimento significativo nos últimos anos. Este trabalho investiga o uso de três desses modelos, nomeadamente o modelo $\gamma - Re_\theta$ de Langtry e Menter, o modelo γ de Menter et al., e o modelo AFT de Coder e Maughmer. É considerado o seu acoplamento original com o modelo $k - \omega$ SST, bem como um acoplamento novo com o modelo $k - \sqrt{k}L$. Vários casos bidimensionais e tridimensionais são usados para avaliar quer os modelos de transição, quer o modelo de turbulência subjacente ao qual estão acoplados. Os resultados focam-se em aspectos que dizem respeito à precisão da solução numérica, e em aspectos de modelação que influenciam directamente a solução do modelo. São avaliados factores como as condições de fronteira da turbulência na entrada, o limitador de produção para as regiões de estagnação e a discretização do termo convectivo nas equações de transporte do modelo de turbulência. Estes factores mostram pouca influência para simulações sem modelo de transição nos casos testados, mas afectam severamente as soluções numéricas de cálculos com modelos de transição, com um impacto directo na localização da zona de transição. Torna-se claro que os comportamentos observados para o modelo de turbulência subjacente quando usado sozinho não são válidos quando um modelo de transição é incluído, que também leva a dificuldades numéricas acrescidas e um maior desafio em preparar as simulações devido a condições de fronteira que não são completamente conhecidas. No entanto, o uso de um modelo de transição melhora de forma considerável as previsões numéricas para escoamentos a números de Reynolds moderados, reduzindo as discrepâncias entre estas e medições experimentais de distribuições de pressão, do coeficiente de resistência de atrito e de forças aerodinâmicas, permitindo captar extensões significativas de escoamento laminar e efeitos como bolhas de separação laminar.

Palavras-chave: Modelação de Transição; Modelação de Turbulência; Equações de Navier-Stokes em Média de Reynolds; Verificação e Validação; Números de Reynolds Moderados.

Abstract

The modelling of flows at moderate Reynolds numbers is currently one of the key areas in the development of Computational Fluid Dynamics. The considerable extent of laminar flow present in these flows is incompatible with the numerical solution obtained by the standard turbulence modelling alternatives, which predict a negligible extent of laminar flow. Approaches based on linear stability theory, of which the e^N method is the most well-known example, can often provide accurate results, especially in regard to parametric trends. However, these techniques depend on numerous non-local operations, which are challenging to implement in solvers for the Reynolds-averaged Navier-Stokes (RANS) equations since these solvers rely strongly on parallelization. The most promising alternative for the prediction of transition in a RANS calculation is the use of models based on transport equations, the so called transition models, which have seen significant development in the recent years. This work investigates the use of three such models, namely the $\gamma - Re_\theta$ model by Langtry and Menter, the γ model by Menter et al., and the AFT model of Coder and Maughmer. Both the original coupling with the $k - \omega$ SST turbulence model, as well as a new coupling to the $k - \sqrt{k}L$ turbulence model are considered. Several two and three-dimensional test cases are used to assess both the transition models and the underlying turbulence model to which they are coupled. The results focus on aspects which concern the numerical accuracy of the solution, and on modelling aspects which directly influence the solution of the model. Factors such as the inlet turbulence quantities, the production limiter for stagnation regions and the discretization of the convection term of the turbulence transport equations are assessed. These have a small influence in simulations without a transition model for the tested cases, but can greatly affect numerical solutions of calculations using transition models with a direct impact on the predicted location of transition. This makes it clear that trends observed for the underlying turbulence models when used alone may not be valid when a transition model is included, which also leads to additional numerical difficulties and challenging modelling setup due to unknown precise inlet boundary conditions. Nonetheless, using a transition model greatly improves numerical predictions for flows at moderate Reynolds numbers, reducing the differences between these and experimental measurements of pressure coefficients, skin-friction coefficients and aerodynamic forces, and allowing for significant extents of laminar flow and phenomena such as laminar separation bubbles to be captured.

Keywords: Transition Modelling; Turbulence Modelling; Reynolds-averaged Navier-Stokes Equations; Verification and Validation; Moderate Reynolds Numbers.

Contents

Acknowledgments	iii
Resumo	v
Abstract	vii
List of Tables	xiii
List of Figures	xv
Nomenclature	xxv
1 Introduction	1
1.1 Motivation	1
1.2 Transition Modelling	2
1.3 Main Goals	3
1.4 Thesis Outline	6
2 Laminar-to-turbulent Transition - Theory and Modelling	9
2.1 The Physics of Transition	9
2.1.1 Natural transition	11
2.1.2 Bypass transition	13
2.1.3 Separation-induced transition	13
2.1.4 Crossflow transition	14
2.2 Modelling Transition	16
2.2.1 Direct Numerical Simulation and Large Eddy Simulation	16
2.2.2 The e^N method and stability theory based approaches	18
2.2.3 Empirical correlations for transition prediction	20
2.2.4 Low Reynolds number models	22
2.2.5 Transport equation based models	23
3 Mathematical Formulation	29
3.1 The Reynolds-averaged Navier-Stokes Equations	29
3.2 Turbulence Models	30
3.2.1 $k - \omega$ SST model	31
3.2.2 $k - \sqrt{k}L$ model	32
3.3 Transition Models	33

3.3.1	$\gamma - Re_\theta$ model	33
3.3.2	γ model	37
3.3.3	AFT model	40
4	Flow Solver and Numerical Setup	43
4.1	Flow Solver	43
4.2	Solution Procedure	44
4.3	Verification and Validation	46
4.4	Boundary Conditions	48
4.5	Decay of Turbulence Quantities	50
4.6	Two-dimensional Test Cases	51
4.6.1	Flat plate	51
4.6.2	NACA 0012	53
4.6.3	NACA 0015	57
4.6.4	NLF ₁ -0416	58
4.6.5	Eppler 387	58
4.6.6	S809	60
4.7	Three-dimensional Test Cases	60
4.7.1	6:1 prolate spheroid	60
4.7.2	SD7003 wing	63
4.7.3	Sickle wing	63
4.8	Features and Quantities of Interest	67
4.8.1	Numerical aspects	67
4.8.2	Modelling aspects and comparison with experimental data	67
4.8.3	Test case overview	68
4.8.4	Quantities of interest	68
5	Results Part I: Numerical Aspects	71
5.1	Introduction	71
5.2	Numerical Robustness	71
5.2.1	Introduction	71
5.2.2	Results	72
5.3	Discretization Scheme	77
5.3.1	Introduction	77
5.3.2	Results	78
5.4	Size of the First Near Wall Cell	88
5.4.1	Introduction	88
5.4.2	Results	91
5.5	Main Remarks	99

6	Results Part II: Modelling Aspects	101
6.1	Introduction	101
6.2	Turbulence Production Limiter	101
6.2.1	Introduction	101
6.2.2	Results	102
6.3	Influence of Inlet Boundary Conditions & Turbulence Decay	109
6.3.1	Introduction	109
6.3.2	Sensitivity studies	110
6.3.3	New approach for the control of turbulence decay	118
6.4	Main Remarks	125
7	Results Part III: Comparison with Experimental Data	129
7.1	Introduction	129
7.2	Two-dimensional Flows	130
7.2.1	NACA 0015	130
7.2.2	S809	131
7.2.3	NLF ₁ -0416	135
7.2.4	Eppler 387	138
7.3	Three-dimensional Flows	140
7.3.1	SD7003 wing	140
7.3.2	6:1 prolate spheroid	143
7.3.3	Sickle wing	152
7.4	Main Remarks	160
8	Conclusions	163
	References	169
A	Crossflow Extension	183
B	Preliminary Results for the SSG-LRR Reynolds Stress Model	185
B.1	Model Equations	185
B.2	Coupling with the $\gamma - Re_{\theta}$ Transition Model	187
B.3	Results	188
B.3.1	Iterative convergence	188
B.3.2	Effect of the size of the first near wall cell	189
B.3.3	Influence of the inlet boundary conditions	191
C	Equations for the Decay of Freestream Turbulence	195
C.1	$k - \omega$ SST Model	195
C.2	KSKL Model	197
C.3	SSG-LRR Model	198

List of Tables

3.1	Model constants of the 2003 formulation of the $k - \omega$ SST turbulence model [123].	32
3.2	Model constants of the $k - \sqrt{k}L$ turbulence model [124].	33
3.3	Constants for the $\gamma - Re_{\theta}$ model [23].	36
3.4	Constants for the γ model [29].	39
4.1	Details for the H grids for the flat plate test case.	52
4.2	Details for the OH grids for the flat plate test case.	53
4.3	Reference number of cells for each block for a base grid with 256 cells on the surface of the airfoil.	56
4.4	Details of the grid set for the NACA 0012 airfoil.	56
4.5	Details of the grid set for the NACA 0015 airfoil.	57
4.6	Details of the grid set used for the prolate spheroid test case.	63
4.7	Details of the grid set used for the SD7003 wing test case.	64
4.8	Details of the grid set generated with the Hexpress grid generation software for the Sickle Wing geometry.	66
4.9	Details of the grid set generated with the GridPro grid generation software for the Sickle Wing geometry.	66
4.10	Test case selection to study the numerical features.	68
4.11	Test case selection to study the modelling features.	69
5.1	Angle of attack and inlet turbulence quantities for each test case for the calculations performed for the study of the numerical robustness.	72
5.2	Angle of attack and inlet turbulence quantities for each test case for the calculations performed for the study of the effect of the convection discretization scheme.	78
5.3	Angle of attack and inlet turbulence quantities for each test case for the calculations performed for the study of the effect of the size of the first near wall cell and corresponding y^+ value.	90
6.1	Angle of attack and inlet turbulence quantities for each test case for the calculations performed for the study of the effect of turbulence production limiter.	102
6.2	Base inlet boundary conditions used with the H grids for the flat plate test case.	109
6.3	Inlet boundary conditions used for the NACA 0012 airfoil test case.	109

6.4	Inlet boundary conditions used for the prolate spheroid test case.	110
6.5	Inlet boundary conditions used for the OH grids for the flat plate test case to assess the performance of the approach to control the decay of turbulence.	120
6.6	Inlet boundary conditions used for the NACA 0012 test case to assess the performance of the approach to control the decay of turbulence.	122
6.7	Inlet boundary conditions used for the 6:1 prolate spheroid test case to assess the performance of the approach to control the decay of turbulence.	125
7.1	Angle of attack and inlet turbulence quantities for each test case for the comparison with experimental data study.	129
B.1	Model constants of the SSG-LRR Reynolds stress model [170].	186
D.1	Lift and drag coefficients for the NACA 0015 airfoil at different angles of attack.	203
D.2	Lift and drag coefficients for the S809 airfoil at different angles of attack. Experimental data from [152].	204
D.3	Start and end positions of transition on the upper and lower surfaces of the S809 airfoil for several angles of attack. Experimental data taken from [152].	204
D.4	Lift and drag coefficients for the NLF ₁ -0416 airfoil at different angles of attack. Experimental data from [147].	205
D.5	Start and end positions of transition on the upper and lower surfaces of the NLF ₁ -0416 airfoil for several angles of attack. Experimental data taken from [147].	205
D.6	Lift and drag coefficients for the Eppler 387 airfoil at different angles of attack. Experimental data from [151].	205
D.7	Start and end positions of transition on the upper surfaces of the Eppler 387 airfoil for several angles of attack. Experimental data from [149].	206
D.8	Lift and drag coefficients for the 6:1 prolate spheroid at different angles of attack. Simulations without crossflow extension.	206
D.9	Lift and drag coefficients for the 6:1 prolate spheroid at different angles of attack. Simulations with crossflow extension.	206
D.10	Lift and drag coefficients for the sickle wing. Simulations on the Hexpress grid set.	206
D.11	Lift and drag coefficients for the sickle wing. Simulations on the GridPro grid set.	207

List of Figures

2.1	The paths from Receptivity to Boundary Layer Turbulence, reproduced from Ref. [43].	11
2.2	An overview of the natural transition process. Reproduced from Ref. [46].	12
2.3	Example of a stability curve, taken from Ref. [42].	13
2.4	Overview of the time-averaged flow of a laminar separation bubble, taken from [51].	14
2.5	Pressure distribution on a laminar separation bubble, reproduced from Ref. [53].	15
2.6	Crossflow profile of the boundary layer on a swept wing, taken from Ref. [54].	15
2.7	Time and spanwise-averaged skin friction coefficient (left) and displacement thickness (right) for two different energy spectra. Reproduced from Ref. [57].	17
2.8	N factor for different disturbance frequencies and wavelengths. Reproduced from Ref. [67].	19
2.9	Comparison of experimental data with linear stability theory coupled with a RANS solver for the NLF1-0416 airfoil. Adapted from Ref. [68].	19
2.10	Mayle's correlation compared with experimental data. Reproduced from Ref. [14].	21
2.11	Comparison of the Jones-Launder Low Reynolds number turbulence model with experimental data. Reproduced from Ref. [20].	22
2.12	Comparison of the function modifying the eddy-viscosity calculation for several different low-Reynolds number models. Reproduced from Ref. [21].	23
2.13	Comparison of Suzen and Huang's model with experimental data and other two-equation turbulence models. Reproduced from Ref. [89].	24
2.14	Model of Menter et al. for the flow over flat plate. Reproduced from Ref. [93].	25
2.15	Comparison of different correlations developed for the $\gamma - Re_\theta$ model. Reproduced from Ref. [104].	25
4.1	H grid topology for the flat plate test case.	52
4.2	OH grid topology for the flat plate test case.	52
4.3	Close-up of the leading edge in the OH grid topology.	53
4.4	Depiction of the inner blocks and grid topology at the trailing edge of the NACA 0012 airfoil.	54
4.5	Depiction of the blocks and grid topology around the NACA 0012 airfoil.	54
4.6	Outer blocks and grid topology for the computational domain of the NACA 0012 airfoil test case.	55
4.7	Comparison of the grid at the trailing edge for the O topology (left) and the OH topology (right).	55

4.8	Illustration of the computational domain size (left) and grid topology around the NACA 0012 airfoil (right).	57
4.9	Illustration of the computational domain size (left) and grid topology around the NACA 0015 airfoil (right).	58
4.10	Illustration of the computational domain size (left) and grid topology around the NLF ₁ -0416 airfoil (right).	59
4.11	Illustration of the computational domain size (left) and grid topology around the Eppler 387 airfoil (right).	59
4.12	Illustration of the computational domain size (left) and grid topology around the S809 airfoil (right).	60
4.13	Grid on the symmetry plane for the coarsest grid of the prolate spheroid test case at $\alpha = 5^\circ$: full computational domain (left) and block encompassing the spheroid (right).	61
4.14	Grid on the symmetry plane for the coarsest grid of the prolate spheroid test case at $\alpha = 5^\circ$ around the spheroid.	62
4.15	Coarsest grid on the surface of the prolate spheroid at $\alpha = 5^\circ$: leading edge (left) half length of the spheroid (right).	62
4.16	3D grid used for the SD7003 wing with cell clustering at the root of the wing (top) and with equidistant spanwise spacing (bottom).	64
4.17	Geometry of the sickle wing. Taken from Ref. [9].	65
4.18	Grid topology at the root (left) and on the surface (right) of the sickle wing, generated with the Hexpress software.	66
4.19	Grid topology at the root (left) and on the surface (right) of the sickle wing, generated with the GridPro software.	66
5.1	Evolution of the residuals for the NACA 0012 airfoil on Grid 2048 using the $k - \omega$ SST model (top left) combined with the $\gamma - Re_\theta$ model (top right), the γ model (bottom left) and the AFT model (bottom right).	73
5.2	Number of iterations performed until the iterative convergence criteria was achieved for the NACA 0012 airfoil with each transition model coupled to the $k - \omega$ SST turbulence model for different grids.	73
5.3	Skin friction coefficient distribution on the finest grid (left) and number of iterations performed at each grid for each model (right) for the NLF ₁ -0416 airfoil.	74
5.4	Evolution of the residual of each transport equation for the flat plate test case when using the $\gamma - Re_\theta$ model on Grid 4.	74
5.5	Periodic behaviour of the residuals (left) and corresponding evolution of γ and F_{onset} on the cell with the highest residual (right) for the flat plate test case using the $\gamma - Re_\theta$ model on Grid 4.	75
5.6	Depiction of the F_{onset} function and the smooth formulation in the vicinity of $Re_T = 2.5$.	76

5.7	Evolution of the residual of each transport equation for the flat plate test case when using the $\gamma - Re_\theta$ model with the smooth formulation for F_{onset3} and F_{onset} on Grid 4.	76
5.8	Example of the residual evolution for a calculation on the prolate spheroid test case for Grid 5 using the $\gamma - Re_\theta$ model with the original (left) and smooth (right) formulations of the F_{onset} and F_{onset3} functions.	77
5.9	Convergence of the friction drag with grid refinement (left) and skin-friction coefficient distribution on the finest grid (right) for the NACA 0012 airfoil using the $\gamma - Re_\theta$ model with the original formulation and the smooth variant with $p = 300$ and $p = 600$	77
5.10	Effect of the discretization scheme used for the convection term of the $k - \omega$ SST turbulence model on $C_{d,f}$ for calculations without a transition model for the NACA 0012 (left) and the NLF ₁ -0416 (right) airfoils.	79
5.11	Effect of the discretization scheme used for the convection term of the $k - \omega$ SST turbulence model on $C_{d,p}$ for calculations without a transition model for the NACA 0012 (left) and the NLF ₁ -0416 (right) airfoils.	79
5.12	Skin friction coefficient distribution obtained with each transition model for the NACA 0012 (left) and the NLF ₁ -0416 (right) airfoils.	80
5.13	Effect of the discretization scheme used in the convection term of the transport equations of the turbulence and transition models using the $\gamma - Re_\theta$ model on the NACA 0012 airfoil: $C_{d,f}$ (left) and $C_{d,p}$ (right).	80
5.14	Effect of the discretization scheme used in the convection term of the transport equations of the turbulence and transition models using the γ model on the NACA 0012 airfoil: $C_{d,f}$ (left) and $C_{d,p}$ (right).	81
5.15	Effect of the discretization scheme used in the convection term of the transport equations of the turbulence and transition models using the AFT model on the NACA 0012 airfoil: $C_{d,f}$ (left) and $C_{d,p}$ (right).	81
5.16	Skin friction coefficient distribution for the NACA 0012 airfoil and different grids using the $\gamma - Re_\theta$ model for the LL set (left) and for the UL set (right).	82
5.17	Skin friction coefficient distribution for the NACA 0012 airfoil and different grids using the γ model for the LL set (left) and for the UL set (right).	83
5.18	Skin friction coefficient distribution for the NACA 0012 airfoil and different grids using the AFT model for the LL set (left) and for the UL set (right).	83
5.19	Evolution of the turbulence intensity in the region upstream of the NACA 0012 airfoil when using the $\gamma - Re_\theta$ model for the LL (left) and UL (right) sets.	84
5.20	Iterative convergence evolution for the QL set and Grid 2048 using the $\gamma - Re_\theta$ model (left) and the AFT model (right).	85
5.21	Number of iterations required to converge the numerical solution for the NACA 0012 using each transition model for different levels of grid refinement and different combinations of the discretization schemes.	85

5.22 Skin friction coefficient distribution for the NLF ₁ -0416 airfoil and different grids using the $\gamma - Re_{\theta}$ model for the LL set (left) and for the UL set (right).	86
5.23 Skin friction coefficient distribution for the NLF ₁ -0416 airfoil and different grids using the γ model for the LL set (left) and for the UL set (right).	86
5.24 Skin friction coefficient distribution for the NLF ₁ -0416 airfoil and different grids using the AFT model for the LL set (left) and for the UL set (right).	87
5.25 Number of iterations performed for the NLF ₁ -0416 airfoil with different combinations of discretization scheme and for each grid using the γ (left) and AFT (right) models.	88
5.26 Effect of the discretization scheme used in the convection term of the transport equations of the turbulence and transition models using the $\gamma - Re_{\theta}$ model on the 6:1 prolate spheroid: $C_{d,f}$ (left) and $C_{l,p}$ (right).	89
5.27 Effect of the discretization scheme used in the convection term of the transport equations of the turbulence and transition models using the γ model on the 6:1 prolate spheroid: $C_{d,f}$ (left) and $C_{l,p}$ (right).	89
5.28 Effect of the discretization scheme used in the convection term of the transport equations of the turbulence and transition models using the AFT model on the 6:1 prolate spheroid: $C_{d,f}$ (left) and $C_{l,p}$ (right).	90
5.29 Average (left) and maximum (right) y^+ values obtained for the flat plate test case for each grid using the $k - \omega$ SST turbulence model combined with the $\gamma - Re_{\theta}$ transition model.	91
5.30 Convergence of the friction coefficient of the plate obtained with the $k - \omega$ SST model coupled with the $\gamma - Re_{\theta}$ (top), γ (middle) and AFT (bottom) models, with grid refinement (left) and with the maximum y^+ value (right).	92
5.31 Convergence of the friction coefficient of the plate obtained with the KSKL model coupled with the $\gamma - Re_{\theta}$ (top) and γ (bottom) models, with grid refinement (left) and with the maximum y^+ value (right).	93
5.32 Convergence of the skin-friction coefficient with grid refinement at $Re_x = 5 \times 10^5$ (top) and at $Re_x = 6 \times 10^6$ (bottom) for the $k - \omega$ SST (left) and KSKL models combined with the $\gamma - Re_{\theta}$ transition model.	94
5.33 Skin friction coefficient distribution in the vicinity of the transition region for the coarsest and finest grids of set 9 and set 1 for the $k - \omega$ SST (left) and KSKL models combined with the $\gamma - Re_{\theta}$ transition model.	95
5.34 Average (left) and maximum (right) y^+ values obtained for the NLF ₁ -0416 airfoil test case for each grid using the $k - \omega$ SST turbulence model combined with the $\gamma - Re_{\theta}$ transition model.	96
5.35 Convergence of the friction (left) and pressure (right) components of the drag coefficient obtained with the $k - \omega$ SST + $\gamma - Re_{\theta}$ formulation with grid refinement.	96
5.36 Convergence of the friction (left) and pressure (right) components of the drag coefficient obtained with the $k - \omega$ SST + γ formulation with grid refinement.	97

5.37	Convergence of the friction (left) and pressure (right) components of the drag coefficient obtained with the $k - \omega$ SST + AFT formulation with grid refinement.	97
5.38	Convergence of the friction (left) and pressure (right) components of the drag coefficient obtained with the KSKL + $\gamma - Re_\theta$ formulation with grid refinement.	98
5.39	Convergence of the friction (left) and pressure (right) components of the drag coefficient obtained with the KSKL + γ formulation with grid refinement.	98
6.1	Skin-friction coefficient distribution for the flat plate test case using the $k - \omega$ SST model (top left) combined with the AFT model (top right), the $\gamma - Re_\theta$ model (bottom left) and the γ model (bottom right) for different formulations of the turbulence production limiter.	103
6.2	Skin-friction coefficient distribution for the NACA 0012 test case in the vicinity of the leading edge, using the $k - \omega$ SST model without a transition model, with different alternatives for the turbulence production limiter with inlet eddy-viscosity ratio of 100 (left) and 0.1 (right).	103
6.3	Skin-friction coefficient distribution for the NACA 0012 test case, using the $k - \omega$ SST + $\gamma - Re_\theta$ model with different alternatives for the turbulence production limiter with inlet eddy-viscosity ratios of 100 and 10 (left) and 1 and 0.1 (right).	104
6.4	Skin-friction coefficient distribution for the NACA 0012 test case, using the $k - \omega$ SST + γ model with different alternatives for the turbulence production limiter with inlet eddy-viscosity ratios of 100 and 10 (left) and 1 and 0.1 (right).	105
6.5	Skin-friction coefficient distribution for the NACA 0012 test case, using the $k - \omega$ SST + AFT model with different alternatives for the turbulence production limiter with inlet eddy-viscosity ratios of 100 and 10 (left) and 1 and 0.1 (right).	105
6.6	Evolution of $\tilde{Re}_{\theta t}$ obtained in the vicinity of the leading edge of the NACA 0012 airfoil when using the $k - \omega$ SST + $\gamma - Re_\theta$ model for different approaches of the turbulence production limiter: $c = 20$ (top left), $c = 15$ (top right), $c = 10$ (bottom left) and the Kato-Launder formulation (bottom right).	106
6.7	Evolution of the turbulence kinetic energy obtained in the vicinity of the leading edge of the NACA 0012 airfoil when using the $k - \omega$ SST + $\gamma - Re_\theta$ model for different approaches of the turbulence production limiter: $c = 20$ (top left), $c = 15$ (top right), $c = 10$ (bottom left) and the Kato-Launder formulation (bottom right).	107
6.8	Boundary-layer profiles at $x/c = 0.2$ of $\tilde{Re}_{\theta t}$ (left) and k (right) in the upper surface of the NACA 0012 airfoil for different approaches of the turbulence production limiter.	108
6.9	Skin-friction coefficient distribution on the surface of the prolate spheroid using the $k - \omega$ SST model combined with the $\gamma - Re_\theta$ model for different approaches of the turbulence production limiter: $c = 20$ (top left), $c = 15$ (top right), $c = 10$ (bottom left) and the Kato-Launder formulation (bottom right).	108
6.10	Skin-friction coefficient distribution for the flat plate test case using the $k - \omega$ SST model (top left) combined with the AFT model (top right), the $\gamma - Re_\theta$ model (bottom left) and the γ model (bottom right).	111

6.11 Skin-friction coefficient distribution for the flat plate test case using the KSKL model combined with the $\gamma - Re_\theta$ model (left) and the γ model (right).	112
6.12 Velocity (left) and eddy-viscosity (right) profiles for the flat plate test case obtained with the $k - \omega$ SST + $\gamma - Re_\theta$ model at $Re_x = 10^4$ for varying inlet boundary conditions.	112
6.13 Evolution of the turbulence intensity (left) and eddy-viscosity ratio (right) in the freestream for the flat plate test case obtained when using the $k - \omega + \gamma - Re_\theta$ model for varying inlet boundary conditions.	113
6.14 Skin-friction coefficient distribution for the NACA 0012 test case using the $k - \omega$ SST model (top left) combined with the AFT model (top right), the $\gamma - Re_\theta$ model (bottom left) and the γ model (bottom right) for varying inlet boundary conditions.	114
6.15 Boundary-layer profiles of the streamwise velocity (left) and $\tilde{Re}_{\theta t}$ (right) obtained with the $k - \omega$ SST + $\gamma - Re_\theta$ model at $x/c = 0.31$ for varying inlet boundary conditions.	114
6.16 Evolution of $\tilde{Re}_{\theta t}$ obtained with the $k - \omega$ SST + $\gamma - Re_\theta$ model at the vicinity of the leading edge of the NACA 0012 airfoil for an inlet eddy-viscosity ratio of 10 (left) and 1 (right).	115
6.17 Boundary-layer profiles of the streamwise velocity (left) and $Re_{\theta c}$ (right) obtained with the $k - \omega$ SST + γ model at $x/c = 0.31$ for varying inlet boundary conditions.	116
6.18 Evolution of \tilde{n} for the $k - \omega$ SST + AFT model in the upper surface of the NACA 0012 airfoil for an inlet eddy-viscosity ratio of 100 (left) and 0.1 (right).	116
6.19 Drag polar for the NACA 0012 test case using the $k - \omega$ SST model (top left) combined with the AFT model (top right), the $\gamma - Re_\theta$ model (bottom left) and the γ model (bottom right) for varying inlet boundary conditions.	117
6.20 Skin friction coefficient on the surface of the prolate spheroid with the $\gamma - Re_\theta$ transition model using set of boundary conditions A (left) and B (right).	118
6.21 Skin friction coefficient distribution (left) and turbulence intensity evolution on the freestream (right) on the flat plate test case for the T3AM conditions using the $k - \omega$ SST + $\gamma - Re_\theta$ model.	121
6.22 Skin friction coefficient distribution (left) and turbulence intensity evolution on the freestream (right) on the flat plate test case for the T3A conditions using the $k - \omega$ SST + $\gamma - Re_\theta$ model.	121
6.23 Skin friction coefficient distribution (left) and turbulence kinetic energy profile in the boundary layer (right) on the NACA 0012 test case using the $k - \omega$ SST + $\gamma - Re_\theta$ model for the dissipation based turbulence production limiter with $c = 15$	122
6.24 Evolution of the turbulence kinetic energy in the vicinity of the leading edge of the NACA 0012 airfoil for the $k - \omega$ SST + $\gamma - Re_\theta$ model with an inlet eddy-viscosity ratio of 100 and $\lambda = 1$ (left) and inlet eddy-viscosity ratio of 10 and $\lambda = 0.1$ (right) for the dissipation based turbulence production limiter with $c = 15$	123

6.25	Evolution of the turbulence kinetic energy in the vicinity of the leading edge of the NACA 0012 airfoil for the $k - \omega$ SST + $\gamma - Re_{\theta}$ model with an inlet eddy-viscosity ratio of 100 and $\lambda = 1$ (left) and inlet eddy-viscosity ratio of 10 and $\lambda = 0.1$ (right) for the Kato-Launder limiter.	124
6.26	Skin friction coefficient distribution (left) and turbulence kinetic energy profile in the boundary layer (right) on the NACA 0012 test case using the $k - \omega$ SST + $\gamma - Re_{\theta}$ model for the Kato-Launder limiter.	124
6.27	Skin-friction coefficient distribution on the surface of the prolate spheroid using the $k - \omega$ SST model combined with the $\gamma - Re_{\theta}$ model with an inlet eddy viscosity ratio of 250 and $\lambda = 1$ (top left), an inlet eddy-viscosity ratio of 25 and $\lambda = 1$ (top right), an inlet eddy-viscosity ratio of 25 and $\lambda = 0.1$ (bottom left) and an inlet eddy-viscosity ratio of 2.5 and $\lambda = 0.01$ (bottom right).	126
7.1	Skin friction coefficient distribution on the upper surface of the NACA 0015 airfoil at $\alpha = 5^{\circ}$ with the $\gamma - Re_{\theta}$ and γ models combined with the $k - \omega$ SST turbulence model without uncertainty (left) and with uncertainty (right).	130
7.2	Skin friction coefficient distribution on the upper surface of the NACA 0015 airfoil at $\alpha = 10^{\circ}$ with the $\gamma - Re_{\theta}$ and γ models combined with the $k - \omega$ SST turbulence model without uncertainty (left) and with uncertainty (right).	131
7.3	Skin friction coefficient distribution on the upper (left) and lower (right) surfaces of the S809 airfoil at $\alpha = 0^{\circ}$ with different turbulence and transition model combinations.	131
7.4	Pressure coefficient distribution on the surface of the S809 airfoil at $\alpha = 0^{\circ}$ with different turbulence and transition model combinations. Entire view (left), close-up of the transition region (right). Experimental data from [152].	132
7.5	Skin friction coefficient (left) and pressure coefficient (right) distributions on the surface of the S809 airfoil at $\alpha = 5^{\circ}$ with different turbulence and transition model combinations. Experimental data from [152].	133
7.6	Skin friction coefficient distribution on the upper surface of the S809 airfoil at $\alpha = 6^{\circ}$ (left) and $\alpha = 7^{\circ}$ (right) with different turbulence and transition model combinations.	133
7.7	Pressure coefficient distribution on the surface of the S809 airfoil at $\alpha = 7^{\circ}$ with different turbulence and transition model combinations. Entire view (left), close-up of the transition region (right). Experimental data from [152].	134
7.8	Lift coefficient as a function of the angle of attack (left) and drag polar (right) for the S809 airfoil at varying angle of attack with each transition model and experimental data from [152].	134
7.9	Start and end locations of transition on the upper and lower surface of the S809 airfoil for varying angle of attack obtained with the $k - \omega$ SST + $\gamma - Re_{\theta}$ model (top left), $k - \omega$ SST + γ model (top right), KSKL + $\gamma - Re_{\theta}$ model (bottom left) and KSKL + γ model (bottom right).	135

7.10 Skin friction coefficient distribution on the upper (left) and lower (right) surfaces of the NLF ₁ -0416 airfoil at $\alpha = -2^\circ$ with different turbulence and transition model combinations.	136
7.11 Pressure coefficient distribution on the surface of the NLF ₁ -0416 airfoil at $\alpha = -2^\circ$ (left) and $\alpha = 6^\circ$ (right) with different turbulence and transition model combinations. Experimental data from [147].	137
7.12 Lift coefficient as a function of the angle of attack (left) and drag polar (right) for the NLF ₁ -0416 airfoil at varying angle of attack with each transition model and experimental data from [147].	137
7.13 Start and end locations of transition on the upper and lower surface of the NLF ₁ -0416 for varying angle of attack obtained with the $k - \omega$ SST + $\gamma - Re_\theta$ model (top left), $k - \omega$ SST + γ model (top right), KSKL + $\gamma - Re_\theta$ model (bottom left) and KSKL + γ model (bottom right).	138
7.14 Skin-friction (left) and pressure (right) coefficient distributions on the surface of the Eppler 387 airfoil at $\alpha = 1^\circ$ for different transition models and experimental data from [149] and [148].	139
7.15 Skin-friction (left) and pressure (right) coefficient distributions on the surface of the Eppler 387 airfoil at $\alpha = 7^\circ$ for different transition models and experimental data from [149] and [148].	139
7.16 Lift coefficient as a function of the angle of attack (left) and drag polar (right) for the Eppler 387 airfoil at varying angle of attack with each transition model and experimental data [35, 148–151].	140
7.17 Location for flow separation and reattachment (left) and transition (right) for the Eppler 387 airfoil at varying angle of attack for different transition models and experimental data from [149].	141
7.18 Skin-friction (left) and pressure (right) coefficient distributions on the surface of the SD7003 wing at the symmetry plane for the $k - \omega$ SST + $\gamma - Re_\theta$ and $k - \omega$ SST + γ models for the slipwall boundary condition case.	141
7.19 Skin-friction coefficient on the upper surface of the wing (left) and on the symmetry plane (right) at the surface of the SD7003 wing for the $k - \omega$ SST model for the no-slip wall boundary condition case.	142
7.20 Time evolution of the friction (left) and pressure (right) components of the drag coefficient for the unsteady calculations of the SD7003 wing using the $k - \omega$ SST + $\gamma - Re_\theta$ and $k - \omega$ SST + γ models for the no-slip wall boundary condition case.	143
7.21 Skin-friction coefficient distribution on the upper surface of the SD7003 wing. Slipwall boundary condition using the $\gamma - Re_\theta$ (top left) and the γ (top right) model. Steady solution of the no-slip wall boundary condition using the $\gamma - Re_\theta$ (middle left) and the γ (middle right) model. Time-averaged unsteady solution of the no-lip wall boundary condition using the $\gamma - Re_\theta$ (bottom left) and the γ (bottom right) model.	144

7.22	Velocity field around the SD7003 wing at the symmetry plane. First row: experimental data (left) and wall boundary condition using only the $k - \omega$ SST model (right). Second row: slipwall boundary condition using the $\gamma - Re_{\theta}$ (left) and the γ (right) model. Third row: steady solution of the no-slip wall boundary condition using the $\gamma - Re_{\theta}$ (left) and the γ (right) model. Fourth row: time-averaged unsteady solution of the no-slip wall boundary condition using the $\gamma - Re_{\theta}$ (left) and the γ (right) model.	145
7.23	Skin friction coefficient on the surface of the prolate spheroid at $\alpha = 5^{\circ}$. Experimental data [154](top left), $k - \omega$ SST + AFT model (top right), $k - \omega$ SST + $\gamma - Re_{\theta}$ model (middle left), $k - \omega$ SST + γ model (middle right), KSKL + $\gamma - Re_{\theta}$ model (bottom left) and KSKL + γ model (bottom right).	147
7.24	Skin friction coefficient on the surface of the prolate spheroid at $\alpha = 5^{\circ}$ with the usage of the crossflow extension. $k - \omega$ SST + $\gamma - Re_{\theta}$ model (top left), $k - \omega$ SST + γ model (top right right), KSKL + $\gamma - Re_{\theta}$ model (bottom left) and KSKL + γ model (bottom right). . . .	148
7.25	Skin friction coefficient on the surface of the prolate spheroid at $\alpha = 10^{\circ}$. Experimental data [154](top), $k - \omega$ SST + $\gamma - Re_{\theta}$ model (top left), $k - \omega$ SST + γ model (top right), $k - \omega$ SST + $\gamma - Re_{\theta}$ model with crossflow extension (bottom left) and $k - \omega$ SST + γ model with crossflow extension (bottom right).	150
7.26	Skin friction coefficient on the surface of the prolate spheroid at $\alpha = 15^{\circ}$. Experimental data [154](top), $k - \omega$ SST + $\gamma - Re_{\theta}$ model with crossflow extension (bottom left) and $k - \omega$ SST + γ model with crossflow extension (bottom right).	151
7.27	Skin friction coefficient on the upper (left) and lower (right) surface of the sickle wing for the $k - \omega$ SST model on the Hexpress grid set and experimental transition line [163, 164].	152
7.28	Skin friction coefficient on the surface of the sickle wing for the $k - \omega$ SST + γ model on the Hexpress grid set and experimental transition line [163, 164]. Upper surface of the coarsest grid (top left), lower surface of the coarsest grid (top right), upper surface of an intermediate grid (middle left), lower surface of an intermediate grid (middle right), upper surface of the finest grid (bottom left), lower surface of the finest grid (bottom right).	154
7.29	Skin friction coefficient on the upper (left) and lower (right) surfaces of the sickle wing for the $k - \omega$ SST + $\gamma - Re_{\theta}$ model on the Hexpress grid set and experimental transition line [163, 164].	155
7.30	Skin friction coefficient on the upper (left) and lower (right) surfaces of the sickle wing for the $k - \omega$ SST + $\gamma - Re_{\theta}$ model using the crossflow extension on the Hexpress grid set and experimental transition line [163, 164].	155
7.31	Pressure coefficient distribution on the surface of the prolate spheroid obtained with the different modelling approaches on the Hexpress grid set and experimental data [163, 164] at the middle of the first section (top), middle of the second section (bottom left) and middle of the third section (bottom right).	156

7.32	Skin-friction coefficient distribution on the upper (left) and lower (right) surface of the sickle wing for the $k - \omega$ SST model on the GridPro grid set and experimental transition line [163, 164].	157
7.33	Skin-friction coefficient distribution on the upper (left) and lower (right) surface of the sickle wing for the $k - \omega$ SST + γ model on the GridPro grid set and experimental transition line [163, 164]. Coarsest grid (top) and finest grid (bottom).	158
7.34	Skin-friction coefficient distribution on the upper (left) and lower (right) surface of the sickle wing for the $k - \omega$ SST + γ model using the crossflow extension on the GridPro grid set and experimental transition line [163, 164].	159
7.35	Skin-friction coefficient distribution on the upper (left) and lower (right) surface of the sickle wing for the $k - \omega$ SST + $\gamma - Re_\theta$ model on the GridPro grid set and experimental transition line [163, 164].	159
7.36	Skin-friction coefficient distribution on the upper (left) and lower (right) surface of the sickle wing for the $k - \omega$ SST + $\gamma - Re_\theta$ model using the crossflow extension on the GridPro grid set and experimental transition line [163, 164].	160
B.1	Number of iterations performed for each grid of grid set 5 (left) and residual evolution on the finest grid (right) for the flat plate case using the SSG-LRR Reynolds stress model combined with the $\gamma - Re_\theta$ transition model.	189
B.2	Average (left) and maximum (right) y^+ values obtained for the flat plate test case for each grid using the SSG-LRR turbulence model combined with the $\gamma - Re_\theta$ transition model.	190
B.3	Convergence of the friction coefficient of the plate obtained with the SSG-LRR + $\gamma - Re_\theta$ formulation with grid refinement (left) and with the maximum y^+ value (right).	190
B.4	Convergence of the skin-friction coefficient with grid refinement at $Re_x = 5 \times 10^5$ (left) and $Re_x = 7 \times 10^6$ (right) for the SSG-LRR model combined with the $\gamma - Re_\theta$ transition model.	191
B.5	Skin friction coefficient distribution in the vicinity of the transition region for the coarsest and finest grids of set 9 and set 1 for the SSG-LRR model combined with the $\gamma - Re_\theta$ transition model.	191
B.6	Skin-friction coefficient distribution for the flat plate test case using the SSG-LRR model combined with the $\gamma - Re_\theta$ model for varying inlet boundary conditions.	192
B.7	Boundary-layer profiles at $x/L = 0.1$ of $\hat{Re}_{\theta t}$ (left) and $Re_{\theta, c}$ (right) for the flat-plate test case when using the $\gamma - Re_\theta$ model combined with the $k - \omega$ SST and SSG-LRR turbulence models.	193

Nomenclature

Greek Symbols

α	Angle of attack.	[°]
α	Error constant.	
δ_{ij}	Kronecker delta.	
γ	Intermittency.	
λ_θ	Pressure gradient parameter.	
μ	Dynamic viscosity of the fluid.	[kg/(m · s)]
μ_t	Dynamic eddy-viscosity.	[kg/(m · s)]
ν	Kinematic viscosity of the fluid.	[m ² /s]
ν_t	Kinematic eddy-viscosity.	[m ² /s]
Ω	Magnitude of the mean vorticity tensor, $\sqrt{2\Omega_{ij}\Omega_{ij}}$.	[1/s]
ω	Specific turbulence dissipation rate.	[1/s]
Ω_{ij}	Mean vorticity tensor, $0.5(\partial U_i/\partial x_j - \partial U_j/\partial x_i)$.	[1/s]
ρ	Density of the fluid.	[kg/m ³]
τ_w	Shear stress at the wall, $\mu(\partial U/\partial y)_w$.	[kg/(m · s ²)]
θ	Momentum thickness.	[m]
ε	Turbulence dissipation rate.	[m ² /s ³]

Latin Characters

\tilde{n}	Global amplification factor of the AFT model.	
c	Chord.	[m]
C_D	3-D drag coefficient, $D/(0.5\rho S_{ref}U_\infty^2)$.	
C_d	2-D drag coefficient, $D/(0.5\rho cU_\infty^2)$.	

C_f	Skin-friction coefficient, $\tau_w/(0.5\rho U_\infty^2)$.	
C_L	3-D lift coefficient, $L/(0.5\rho S_{ref}U_\infty^2)$.	
C_l	2-D lift coefficient, $L/(0.5\rho cU_\infty^2)$.	
C_p	Pressure coefficient, $(p - p_\infty)/(0.5\rho U_\infty^2)$.	
$C_{D,f}$	Friction component of the 3-D drag coefficient.	
$C_{d,f}$	Friction component of the 2-D drag coefficient.	
$C_{D,p}$	Pressure component of the 3-D drag coefficient.	
$C_{d,p}$	Pressure component of the 2-D drag coefficient.	
D	Drag.	[N]
d	Nearest wall distance.	
E	Simulation error.	
E_m	Modelling error.	
E_{disc}	Discretization error.	
E_{input}	Input error.	
E_{it}	Iterative error.	
E_{num}	Numerical error.	
$E_{round-off}$	Round-off error.	
E_{stat}	Statistical error.	
h_i	Typical cell size of grid i .	
k	Turbulence kinetic energy.	$[m^2/s^2]$
L	Lift.	[N]
P	Mean pressure relative to the hydrostatic pressure.	[Pa]
p	Instantaneous pressure relative to the hydrostatic pressure.	[Pa]
p	Order of convergence.	
Re	Reynolds number.	
Re_θ	Momentum thickness based Reynolds number.	
Re_c	Chord based Reynolds number.	
Re_L	Reference length based Reynolds number.	

$Re_{\theta,t}$	Transition onset momentum thickness Reynolds number.	
S	Magnitude of the mean strain-rate tensor, $\sqrt{2\overline{S_{ij}S_{ij}}}$.	[1/s]
S_{ij}	Mean strain-rate tensor, $0.5(\partial U_i/\partial x_j + \partial U_j/\partial x_i)$.	[1/s]
Tu	Turbulence intensity.	
U_e	Mean velocity at the edge of the boundary-layer.	[m/s]
U_i	Cartesian components of the mean velocity.	[m/s]
u_i	Cartesian components of the instantaneous velocity.	[m/s]
V_∞	Incoming flow velocity.	[m/s]
x_F	Plane normal to the x -axis upstream of which the transport equations of the turbulence model are solved without dissipation terms.	
y^+	Dimensionless wall distance.	

Superscripts

∞	Free-stream condition.
in	Conditions at the inlet of the computational domain.
LE	Conditions at the leading edge plane.
n	Normal component.
x, y, z	Cartesian components.
ref	Reference condition.
w	Wall direction.

Chapter 1

Introduction

1.1 Motivation

The simulation of transitional flows stands as one of the present challenges in the development of Computational Fluid Dynamics (CFD) [1]. Many aerospace and maritime applications deal with flows at high Reynolds numbers, in which the laminar region has a negligible extent. At model scale, where the Reynolds number is low, tripping is often employed in order to cause the flow to become turbulent. This situation is well reproduced by standard turbulence models used with the Reynolds-averaged Navier-Stokes (RANS) equations, which are still the most common framework used for industrial applications. These models predict transition to occur close to the stagnation point, as they were not designed for the prediction of flow transition.

However, there are many practical applications that do not deal with high Reynolds number flows. Examples of such cases are aerial and marine unmanned vehicles [2], small submarines [3], gliders [4] and wind turbines [5]. For these flows, the laminar region has a considerable extent, which has a significant impact on the forces and moments acting on the body. The same can hold true for model scale testing of high Reynolds number applications such as marine propellers [6] if tripping is not employed, or in methodologies that aim at taking advantage of laminar flow such as laminar wing design [7]. The turbulence models that have been developed for the high Reynolds number flows still lead to a very small extent of laminar flow under these conditions, an unphysical solution which fails to reproduce relevant flow features.

These shortcomings of the standard turbulence models, along with the increasing focus on unmanned vehicles and on drag reduction for fuel savings, have led to the recent development of transition models. It is the aim of these models to accurately predict the location where the flow undergoes transition from laminar to turbulent, enabling the RANS equations to be used for low and moderate Reynolds number flows. Nonetheless, these models are still fairly new and have yet to reach the degree of maturity that the turbulence models used for high Reynolds number flows have attained. For this reason, during the past decade, numerous groups from both aerospace and naval background have devoted their attention to this topic. This is evidenced by the NASA Transition Modeling Workshop held in 2017

[8], the AVT-313 panel group, the AIAA special session in the 2018 SciTech Forum [9] and the 1st AIAA Transition Modeling and Prediction Workshop held in 2021 [10]. The work developed during the course of this thesis has been a part of the workshops organized by the AVT-313 group, as well as of the 1st AIAA Transition Modeling and Prediction Workshop.

1.2 Transition Modelling

The extensively studied and used $k - \epsilon$ and $k - \omega$ models are unsuitable for modelling transition at moderate Reynolds numbers. These models were built for fully developed turbulent flows, and are calibrated following results such as the log-law or the decay of homogeneous isotropic turbulence [11]. It is then unsurprising that they fail outside the high Reynolds number regime: according to Wilcox [11], the $k - \omega$ model predicts transition to start at a Reynolds number of 8100, which leads to a negligible extent of laminar flow for Reynolds numbers above 10^5 . The Spalart-Allmaras model, commonly used in external aerodynamics also predicts transition too far upstream. Although its formulation includes a tripping term which can delay transition, it does not model it directly. Furthermore, the use of the tripping term has been shown to lead to non-unique solutions [12]. In simulations using these models, the lack of a formulation capable of accurate accounting for transition is often highlighted as one of the causes for discrepancies between numerical and experimental results [13].

One factor that poses challenges in the modelling of transition lies in the diversity of triggering mechanisms. During the transition process, laminar flow becomes unstable and turbulent. The instability is caused by flow perturbations, which can originate from the freestream and wall roughness, among other causes. These perturbations give rise to natural transition or bypass transition depending on their amplitude [14]. Other flow phenomena, such as flow separation, may also trigger laminar-to-turbulent transition. In the case of turbomachinery flows, transition can be caused by the impinging wake of preceding blade rows, a process termed wake-induced transition [15]. In three-dimensional flows, transition due to the crossflow occurring in the boundary layer, aptly named crossflow transition, may also trigger transition either by itself or through interaction with other mechanisms.

High fidelity approaches such as Direct Numerical Simulation (DNS) or Large Eddy Simulation (LES) can be suitable for the prediction of transition, but come with their own setbacks. The first corresponds to the unavoidable computational cost of these approaches which makes them unaffordable for industrial applications [16], even for the Reynolds number range of transitional flows. Another issue is caused by the physical nature of the transition process: an accurate simulation requires a correct specification of flow disturbances, which is far from trivial. In the case of LES, there is also some sensitivity to the subgrid-scale model used [17], introducing further difficulties.

One of the most successful approaches to predict transition is the e^N method, developed in 1956 [18, 19]. Its formulation based on linear stability theory along with accurate predictions in natural transition scenarios have granted it considerable popularity. However, the linear stability framework is not suitable for other transition mechanisms, and some empiricism is present in the method. In addition, the e^N method requires numerous non-local operations to be performed. This arises as a significant

obstacle in its use as a transition prediction method coupled with solvers based on the RANS equations. These solvers are built for High Performance Computing infrastructure making use of parallel domain decomposition, which makes non-local operations inconvenient and expensive.

Some attempts at using low-Reynolds number turbulence models to predict transition have been performed [20]. These modifications are usually done through the use of damping functions in some of the model terms, without the use of any empirical correlation for transition. While they maintain the local formulation of the underlying model, studies have found these models to be inaccurate [21]. The reason for the origin of low-Reynolds number models was to improve the modelling of turbulent flow at lower Reynolds numbers, not to model transition. In addition, their ability to predict transition is solely due to the similarities between the viscous sub-layer and the laminar boundary layer. Moreover, some formulations of $k - \epsilon$ models suffer from numerical issues which lead to converged solutions that are dependent on initial conditions or the solution procedure [22]. For these reasons, low Reynolds formulations are now seldom used.

Several models based on empirical correlations have also been developed. In principle, this approach can lead to accurate predictions, if proper correlations for a given application are selected. However, most transition criterion are formulated based on integral parameters such as the momentum-thickness Reynolds number. Thus, akin to the e^N method, non-local operations must be performed, which preclude these models from being easily used in a RANS environment.

Keeping in mind the requirement for a local formulation, the correlation-based $\gamma - Re_\theta$ model [23] became highly successful, as it was also capable of dealing with multiple transition mechanisms. The phenomenological $k_T - k_L - \omega$ model of Walters and Cokljat [24], based on the concept of the laminar fluctuation kinetic energy, has also gained some popularity in particular for turbomachinery applications, as it is suitable for bypass transition. Another model worthy of mention is the Amplification Factor Transport model of Coder and Maughmer [25]. This model attempts to mimic the procedure of the e^N in a local fashion, fully compatible with RANS formulations. Numerous other models have been proposed, whether based on similar concepts as the aforementioned ones, or simply by combining the different formulations in an attempt to keep their strengths. Additional extensions to these models to account for roughness [26] or crossflow transition [27] or simply different sets of correlations [28] have also been studied.

1.3 Main Goals

One particular aspect that the transition models addressed herein have in common is that they rely on well established turbulence models such as the $k - \omega$ SST or Spalart-Allmaras model to handle the turbulent regime. The purpose of the transition model is not to model the physics of the transition process, but to identify the region of the flow which should be laminar and equivalently, where transition should start. The laminar region is ensured by the deactivation of the underlying turbulence model, through changes in the source terms of the turbulence transport equations. The modelling of the transition region is left to the underlying turbulence model, once the transition model no longer prevents

the growth of turbulence kinetic energy and eddy-viscosity. As simulations with these models become common, they reveal that some aspects that had little importance in calculations using only turbulence models, such as the decay of turbulence in the freestream, can have a profound effect if a transition model is used. The experience and trends observed in turbulence models at high Reynolds numbers flows may not be the same at moderate Reynolds numbers, when additional transport equations are used for the prediction of transition.

The scope of this dissertation is to study both the numerical properties of transition models and the underlying turbulence models when coupled to the transition model, as well as the improved modelling accuracy provided by the coupling of the two models. The main goal is to identify the strengths and weaknesses of each model and to assess which may be the most adequate approaches for practical applications. Three different transition models are considered: the $\gamma - Re_\theta$ model of Langtry and Menter [23], the γ model of Menter et al. [29] and the AFT model of Coder and Maughmer [30]. These models were selected due to their widespread usage and ongoing development through the publication of extensions to the models, as well as due to the fact they cover different transition mechanisms and different modelling approaches. Although all of them have been coupled to the $k-\omega$ SST turbulence model, which is the main turbulence model used in this thesis, an additional coupling alternative to the two-equation $k - \sqrt{k}L$ (KSKL) model that was developed during this work is also addressed. The selection of the KSKL model for coupling with the transition models is based on its lower dependence on the near-wall cell size [31].

Alternative formulations were also tested, most notably the $k_T - k_L - \omega$ transition model [24] and the coupling of the SSG-LRR Reynolds stress model with the $\gamma - Re_\theta$ transition model [32]. However, none of these two approaches went through studies as detailed as the previously mentioned model combinations. Regarding the $k_T - k_L - \omega$ model, the lack of a capability to handle flow separation, along with difficulties in the iterative convergence of the solutions using this model [33] led to the decision of not giving it the same thorough treatment. In the case of the coupling between the $\gamma - Re_\theta$ and the SSG-LRR models, the recent publication of the formulation when compared to the remaining models prevented its application on all test cases. For this reason, the formulation of this model combination and the results obtained with it are given in the appendix.

Nine test cases are considered to assess the different transition modelling approaches which are studied. The simplest case consists of the flow over a flat plate, generally used to calibrate transition models due to available data [34]. While this makes any comparison with experimental data meaningless, it does not influence trends on numerical aspects that may be observed, and the simplicity of the case makes it a good stepping stone to the other test cases. The remaining two-dimensional flows consist of five airfoils: NACA 0012, NACA 0015, Eppler 387, NLF₁-0416 and S809. Most of these are selected due to significant extent of laminar flow and available experimental data for a wide range of angles of attack, which has led to these geometries being commonly used to evaluate transition models. Out of the five airfoils, the NACA 0015 is the only one for which measurements of the skin-friction coefficient are available. On the other hand, the NACA 0012 airfoil is the only geometry for which laminar flow separation is never involved as a triggering mechanism for transition, and it is also the only airfoil for

which comparisons with experimental data are not performed. The three-dimensional flows are those around the SD 7003 wing, a 6:1 prolate spheroid and a sickle wing. The SD 7003 wing is representative of that used in sailplanes [35]. The 6:1 prolate spheroid corresponds to an idealized shape of an aircraft fuselage or a submarine hull. Along with the sickle wing, these are prime test cases to investigate crossflow transition.

From the numerical standpoint, one of the features explored throughout this work relates to numerical robustness. The inclusion of additional transport equations in the non-linear system and the strong coupling between the turbulence and transition transport equations makes iterative convergence more difficult. This is further complicated by the fact that numerous switches and limiters are present in the models. Another aspect concerns the numerical schemes employed, namely the discretization scheme for the convection terms of the turbulence and transition transport equations. Due to the strong interaction between these equations in the studied models, along with the dependence on the turbulence decay on the freestream where grids are typically not refined, the standard choice of a first order scheme typically used for high Reynolds number flows may not be the most adequate. The final numerical detail studied in this thesis concerns the influence of the near-wall cell size. Evidently the use of wall functions is unsuitable for the laminar region of the flow, hence the full extent of the boundary-layer must be resolved and the shear-stress at the wall is determined from its definition. Grid generation procedures usually aim at a value of y_{max}^+ around 1 for simulations using only a turbulence model. However, the same criteria is also used when transition models are employed, and so the impact of this choice is studied herein. This aspect has been very recently been addressed for both simulations with and without transition models [31, 36, 37].

Throughout this dissertation, there is a significant focus on the numerical uncertainty of the simulations. Proper Verification and Validation [38] is essential to establish the credibility of numerical results. While an adequate Validation exercise would require detailed experimental data to evaluate the modelling error along with a thorough numerical study, Verification only necessitates the latter in order to estimate the numerical error. In CFD calculations of steady flows, the dominant component of the numerical error usually comes from the spatial discretization. Thus the numerical error can be assessed through grid refinement studies. Such studies are performed for all the cases discussed in this thesis.

From a physical perspective, the first topic addressed concerns the influence of the limiter of turbulence production in stagnation regions. Although for simulations without a transition model this influence is generally small, the excess production at the stagnation point can affect the turbulence level at the edge of the boundary-layer. In turn, considering how some of the transition models used in this study operate, this can have a direct impact on the predicted location of transition. The second aspect which is considered is the influence of the turbulence decay in the freestream. Dependency on freestream values has been pointed out as a disadvantage of turbulence models as for example in the $k - \omega$ model. However, due to the physical nature of the transition process, the influence of these values on the predicted location of transition is necessary and desirable. Lastly, the results from the simulations are compared against experimental data for several two- and three-dimensional flows. This does not constitute a rigorous Validation exercise, due to the limitations provided in the definition of the test case, in particular

the information for the inlet turbulence quantities. Without matching conditions between simulations and experiments, formal validation of the models is not possible. Given the lack of data regarding the turbulence boundary conditions, an evaluation of the modelling error is not definitive, for different conclusions could be reached if different boundary conditions were used. Nonetheless, simulations with and without transition models can be compared, for the solutions differ significantly so that the effect of the transition model can be assessed regardless of the boundary conditions employed.

1.4 Thesis Outline

The remainder of this thesis is outlined as follows: Chapter 2 presents a description of the physics of the transition process, considering some of the most prominent transition mechanisms. Approaches to include the effects of transition in numerical simulations are also presented, ranging from the e^N method, low-Reynolds number variants of turbulence models and a literature review on the local models that are used in this thesis.

The mathematical formulation of the problem at hand, based on the RANS-equations, is described in Chapter 3. A full description of the turbulence and transition models used is also presented in that chapter.

Chapter 4 describes the two- and three-dimensional test cases which are addressed in this dissertation. This includes defining features such as Reynolds number, geometry and angle of attack, domain size, boundary conditions as well as grid topology and characteristics. It also details which features are analysed in each test case and the quantities of interest which are looked at. Moreover, the flow solver used is described in this chapter, as well as the technique used to estimate the discretization error.

The results are presented in three chapters: Chapter 5 is focused on the numerical aspects and their impact on simulations with transition models, namely the iterative convergence behaviour, the discretisation scheme used for the turbulence and transition transport equations and the influence of the near-wall cell size. The second part of the results is discussed in Chapter 6 and is concerned with modelling aspects. The influence of the production limiter used for the turbulence model is discussed here, as well as the turbulence variables specified at the inlet and their decay along the freestream, all of which can have a significant impact on the location of transition. Comparisons with experimental results are shown in Chapter 7, allowing a qualitative assessment of the predictive capability of the models.

The conclusions of this work are summarized in Chapter 8, including an overview of the most important aspects observed. Current limitations on the use of transition models as a predictive tool are discussed. Suggestions for future work on transition models are also given.

There are several complementary aspects to the work developed in this thesis that are not detailed within the text. Appendix A describes the crossflow extension used together with the transition models. Appendix B presents the formulation of the SSG-LRR Reynolds stress model, its coupling with the $\gamma - Re_\theta$ model and preliminary results obtained with this model combination. The equations for the decay of turbulence for the underlying turbulence models used in this work are derived in Appendix C. Finally, Appendix D contains tables with the predicted values for the force coefficients as well as

the corresponding numerical uncertainty estimated from the grid refinement study for each of the flows addressed in the comparison with experimental data. Tables for the location of the transition region are also included, and available experimental data for each quantity of interest is given as well.

Chapter 2

Laminar-to-turbulent Transition - Theory and Modelling

This chapter is focused on the physics of the transition process and the methodologies to model or predict transition. The first aspect is addressed in Section 2.1, which presents an overview of different transition mechanisms such as natural transition, bypass transition, separation-induced transition and crossflow transition. Linear stability theory is also briefly addressed in the context of natural transition. Section 2.2 presents several alternatives for the inclusion of transitional effects in numerical simulations. These are DNS and LES, the e^N method, empirical correlations for the prediction of transition, low Reynolds number models and transport equation based models. Considerable focus is given on the latter, since it corresponds to the category of all models addressed in this work.

2.1 The Physics of Transition

The transition process corresponds to the instability of laminar flow due to flow perturbations, resulting in turbulent flow. Hence, a proper description of the transition process is inseparable from the definitions of laminar and turbulent flow.

In laminar flow, fluid particles follow smooth and well defined trajectories. For example, in the case of the laminar flow inside a pipe or channel, fluid particles move along straight lines in the direction of the axis of the pipe. The flow can be considered as adjacent layers which slide over one another without significant mixing, due to the different velocity of each layer according to the velocity profile [39]. Laminar flow typically occurs at small Reynolds numbers, such as in insect flight [40] and in microfluidics [41].

In the case of turbulent flow, there is no orderly movement of fluid particles: there are random velocity fluctuations with a wide range of amplitudes and frequencies and in all dimensions, as turbulence is inherently three-dimensional. Due to its random nature, the treatment of turbulent flows has to be done statistically. Turbulent flow has greater diffusion than laminar flow, leading to increased mixing and it occurs mainly at high Reynolds numbers [42]. Thus, there are considerable differences in the velocity profiles of laminar and turbulent flow. In addition, the growth of boundary layer thickness and other

integral parameters such as the momentum thickness and shape factor are also significantly different. Turbulent flow leads to a higher skin-friction at the wall when compared to laminar flow, and is more resistant to flow separation. Heat transfer coefficients are also larger in turbulent flow due to the increased mixing [39].

The transition region corresponds to the region where a given laminar flow becomes turbulent. In the case of a boundary-layer, the location and size of the transition region will depend on the wall roughness, the pressure gradient, and on disturbances coming in from the freestream. At small Reynolds numbers, the diffusion of the flow dampens out the disturbances and so the flow remains laminar. However, for higher Reynolds numbers, the action of viscosity is not able to dampen the disturbances which grow and eventually trigger the onset of turbulent flow. Typical values for the flow over a flat plate have transition starting at a Reynolds number of 3.5×10^5 to 10^6 [39]. The Reynolds number at which transition starts is termed the critical Reynolds number. Depending on how free of disturbances the flow is, the higher the critical Reynolds number can be. The transition process is significantly different between wall-bounded and free shear flows. Since the test cases addressed in this dissertation only correspond to the former, transition mechanisms in free shear flows are not addressed.

An overall view of the transition process is given in Figure 2.1 for different disturbance amplitudes, growing from left to right. Path A corresponds to natural transition, which occurs for very low disturbance amplitudes. Path E corresponds to bypass transition, typical of turbomachinery applications where the turbulence content in the freestream causes the transition process to be very fast and skip some of the stages observed in natural transition. The level of turbulence in the freestream is given by the turbulence intensity Tu , defined as the ratio between the root mean square of the velocity fluctuations and the mean velocity. For practical purposes, natural transition is often considered to occur when the freestream turbulence intensity is lower than 1%, while bypass transition corresponds to freestream turbulence intensity higher than 1%. These two paths correspond to a general description of the transition process. However, different paths for transition to turbulence may occur, related to transient growth. This consists on the interaction of stable modes, which may under some circumstances achieve large amplitudes and eventually cause the breakdown to turbulence.

The importance of the initial conditions on the transition process has led to considerable work on receptivity [43]. This concerns how effects such as the freestream turbulence level, acoustic waves or wall roughness cause disturbances in the boundary layer relating to their wavelength and amplitude. The understanding of receptivity is essential to establish the correct initial conditions and thus to provide an accurate description of the transition process.

While the schematic shown in Figure 2.1 is a broad description of transition, further details depend on the instability mechanism itself. Only some of these mechanisms are discussed in detail namely natural transition, bypass transition, separation-induced transition and crossflow transition. This choice is motivated due to the fact that these are the most prominent mechanisms both in the test cases addressed in this work as well as in the transition models which are subject of study. Although also relevant, other mechanisms such as Görtler vortices [44] or attachment line contamination [45] are not considered.

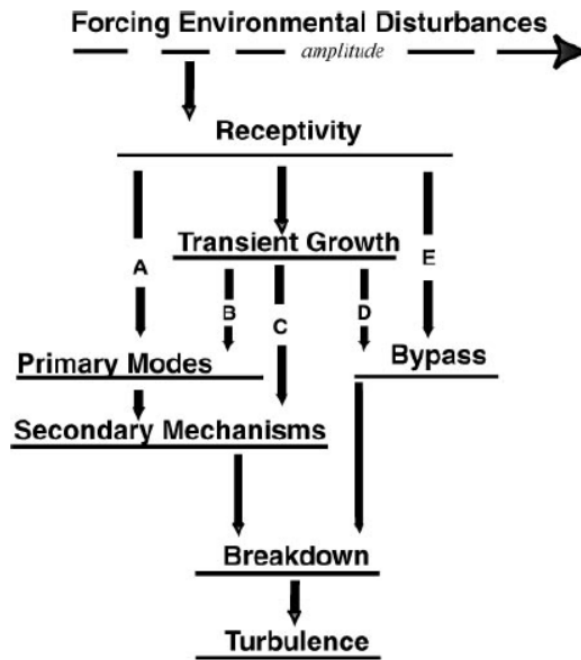


Figure 2.1: The paths from Receptivity to Boundary Layer Turbulence, reproduced from Ref. [43].

2.1.1 Natural transition

The process of natural transition takes place when the amplitude level of the disturbances is small. Natural transition has been extensively studied and can be characterised in different stages. The first stage corresponds to the appearance of two-dimensional perturbations termed Tollmien-Schlichting (TS) waves. These waves are destabilized by the viscosity of the fluid, and grow slowly. This slow growth extends over considerable streamwise distances and eventually leads to three-dimensional instabilities which give rise to hairpin vortices. These vortices decay and cause the formation of turbulent spots. As the turbulent spots erupt on the flow, they merge into a fully developed turbulent boundary layer. A depiction of the natural transition process is given in Figure 2.2. Tollmien-Schlichting waves were only first detected in 1947 by Schubauer and Skramstad [47] although their existence had already been theoretically established. However, it remained as a point of controversy since they were not observed in previous experiments. This was due to a too high level of freestream disturbance, which prevented the formation of the TS waves.

The early stages of natural transition can be properly described by linear stability theory. The basis for linear stability theory consists on decomposing the instantaneous flow (u_i) into a base steady state (U_i) and an unsteady fluctuation (\tilde{u}_i) of small amplitude. The application of this process to the incompressible Navier-Stokes equations, along with the assumption of two-dimensional, parallel or quasi-parallel flow leads to a set of linearized equations which can be further transformed into the extensively studied Orr-Sommerfeld equation. Regardless of the form, the stability equations form an eigenvalue problem for the solution of the natural modes of oscillation of the boundary-layer which correspond to the TS waves. The stream function Ψ is used to characterize a single perturbation with wave number α and amplitude

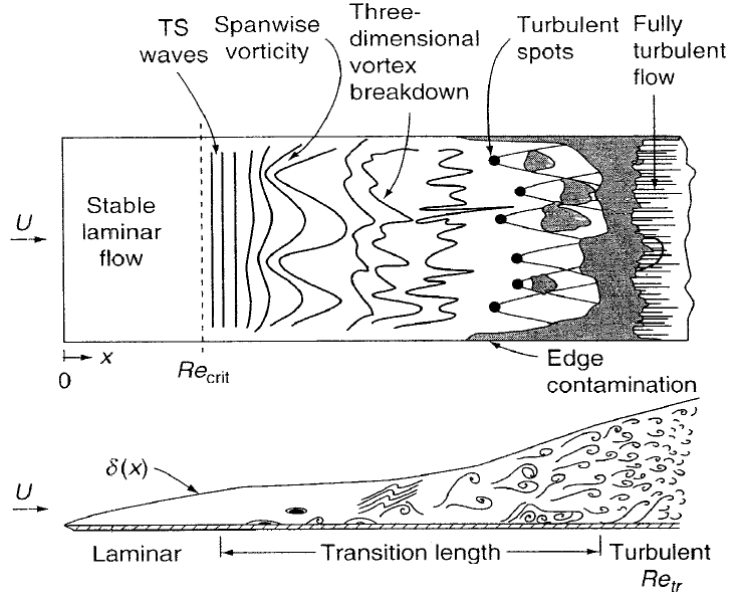


Figure 2.2: An overview of the natural transition process. Reproduced from Ref. [46].

function φ through

$$\Psi(x, y, t) = \varphi(y) e^{i(\alpha x - \omega t)}. \quad (2.1)$$

Thus, from the definition of the stream function it follows that the components of the velocity fluctuation \tilde{u} and \tilde{v} can be written as

$$\tilde{u} = \frac{\partial \Psi}{\partial y} = \varphi'(y) e^{i(\alpha x - \omega t)} \quad (2.2)$$

and

$$\tilde{v} = -\frac{\partial \Psi}{\partial x} = -i\alpha\varphi(y) e^{i(\alpha x - \omega t)} \quad (2.3)$$

The Orr-Sommerfeld equation is [39]:

$$(\bar{U} - \bar{c})(\varphi'' - \bar{\alpha}^2\varphi) - \bar{U}''\varphi = -\frac{i}{\bar{\alpha}Re}(\varphi'''' - 2\bar{\alpha}^2\varphi'' + \bar{\alpha}^4\varphi) \quad (2.4)$$

where $\bar{U} = U/U_\infty$, $\bar{c} = c/U_\infty$, $\bar{\alpha} = \alpha L$, $Re = U_\infty L/\nu$, and U_∞ is the reference velocity. The prime in Eq. 2.4 indicates differentiation with respect to y/L . The quantity c is defined as $c = \omega/\alpha$. The boundary layer thickness δ can be selected as the reference length L .

The solution of the Orr-Sommerfeld equation results in stability curves such as those shown in Figure 2.3. These curves show, for a given Reynolds number, the range of wave numbers for which the amplitude of the perturbation is amplified. If the Reynolds number is low enough, all disturbances are damped and no instability occurs. As the Reynolds number increases and reaches Re_{crit} , some perturbations may be amplified. For velocity profiles with an inflection point, there are always some perturbations that can be amplified regardless of how high the Reynolds number is. This is called inviscid instability, because it also happens in the limit of $Re \rightarrow \infty$. If the velocity profile has no inflection point, then the range of Reynolds numbers in which the amplitude of perturbations are amplified is much lower.

Linear stability theory cannot provide all the information regarding the transition process. The iden-

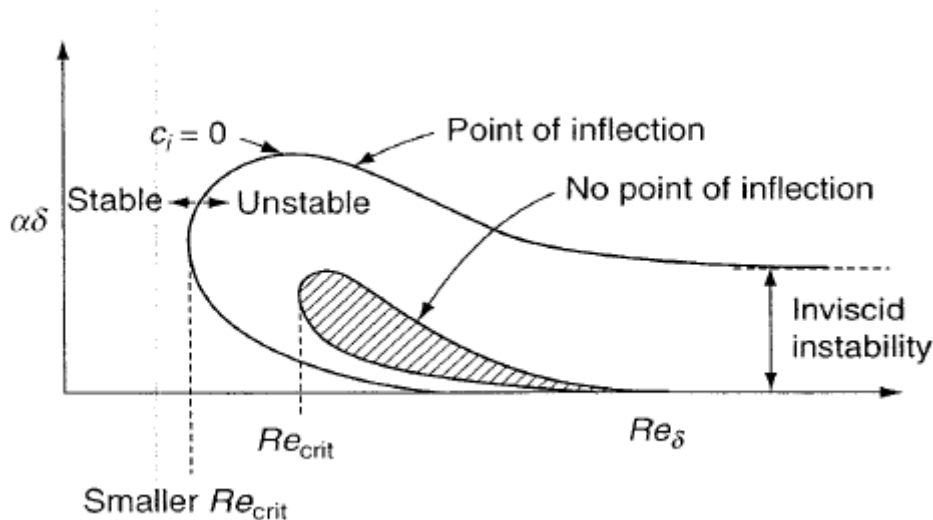


Figure 2.3: Example of a stability curve, taken from Ref. [42].

tification of the Reynolds number at which the disturbances start being amplified marks the start of transition and their growth corresponds to the primary mechanisms in Figure 2.1. However, the secondary mechanisms and the next stages consist of non-linear processes, which are not captured by linear stability theory. Another drawback is the assumption of parallel flow, which prevents the application of linear stability theory to flows with appreciable curvature. One possible approach to deal with these weaknesses is the use of more sophisticated approaches such as the parabolized stability equations [48, 49].

2.1.2 Bypass transition

Bypass transition is the dominant mechanism in turbomachinery, due to the high freestream turbulence intensity in these applications. Wall roughness can also cause bypass transition to take place. The main characteristic of this mechanism is the absence of Tollmien-Schlichting waves and corresponding growth, as turbulent spots are directly produced via the influence of the high amplitude disturbances. Consequently, this mechanism is impossible to handle using linear stability theory. In addition, bypass transition is much faster than natural transition since the growth of the TS waves is not present.

Under conditions favorable to bypass transition, there is a distortion of the velocity profile in the pre-transitional boundary layer as well as high-amplitude streamwise fluctuations named Klebanoff modes [50]. These fluctuations precede the formation of turbulent spots, and it is their growth that is presumed to be the cause for the turbulent spots.

2.1.3 Separation-induced transition

Separation-induced transition is a transition mechanism typically associated with low Reynolds number flows. This process occurs when a laminar boundary layer under an adverse pressure gradient separates before becoming turbulent. The resulting shear layer is unstable since an inflection point is

present in the velocity profile, causing transition to occur and the flow to become turbulent. Transition in the free-shear layer may be caused by natural or bypass transition as discussed previously, or by the Kelvin-Helmholtz instability. If the adverse pressure gradient is not too strong, the turbulent flow can reattach to the wall, encapsulating the region of separated flow on a time-averaged sense, and forming a laminar-separation bubble. A depiction of this process is shown in Figure 2.4.

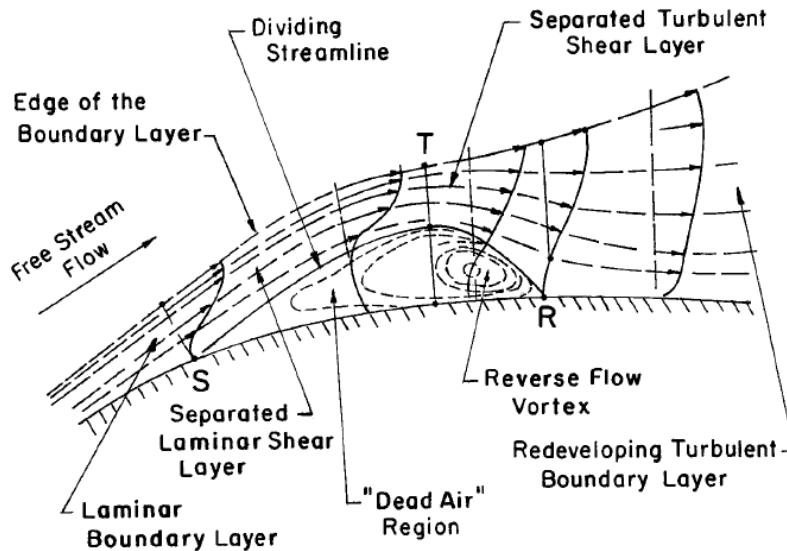


Figure 2.4: Overview of the time-averaged flow of a laminar separation bubble, taken from [51].

Depending on the Reynolds number, roughness, pressure gradient and freestream turbulence, the separated region may be larger or smaller. In the case of short bubbles, there is a small modification of the pressure distribution. In the case of a long bubble, which may take up to 20% or 30% of the chord, there is a region of constant pressure, aptly named pressure plateau, which corresponds to the laminar portion of the separated flow region. The effect of a laminar separation bubble on the pressure coefficient distribution is depicted in Figure 2.5. Laminar separation bubbles have a strong impact on the performance of airfoils employed in UAVs or wind turbines, flows in which laminar separation bubbles are common, through an increase in the drag coefficient [52], and also influencing lift and moment.

2.1.4 Crossflow transition

While all previously discussed mechanisms can be present in two-dimensional flows, crossflow transition can only take place in three-dimensional boundary layers. Swept wings, propellers, and wind turbines are examples of applications where crossflow effects are significant. The crossflow instability occurs due to a misalignment between the flow direction at the edge of the boundary layer and the flow direction at the wall [54]. A representation of the velocity profile in a swept wing is shown in Figure 2.6.

Whereas in the freestream the pressure gradient and the centripetal force are in balance, inside the boundary layer the streamwise velocity decreases, while the pressure gradient does not change along the wall normal direction. Thus, the balance that was verified at the edge of the boundary layer is not present inside it, giving rise to a secondary flow called crossflow. The crossflow velocity is the

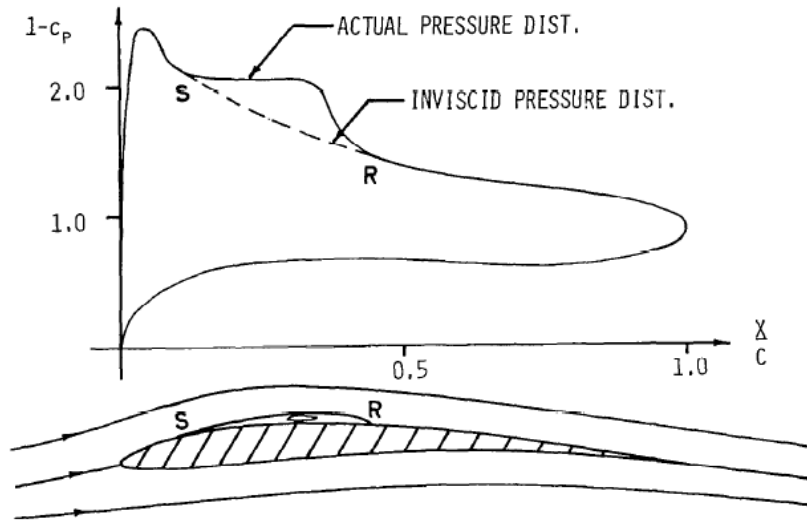


Figure 2.5: Pressure distribution on a laminar separation bubble, reproduced from Ref. [53].

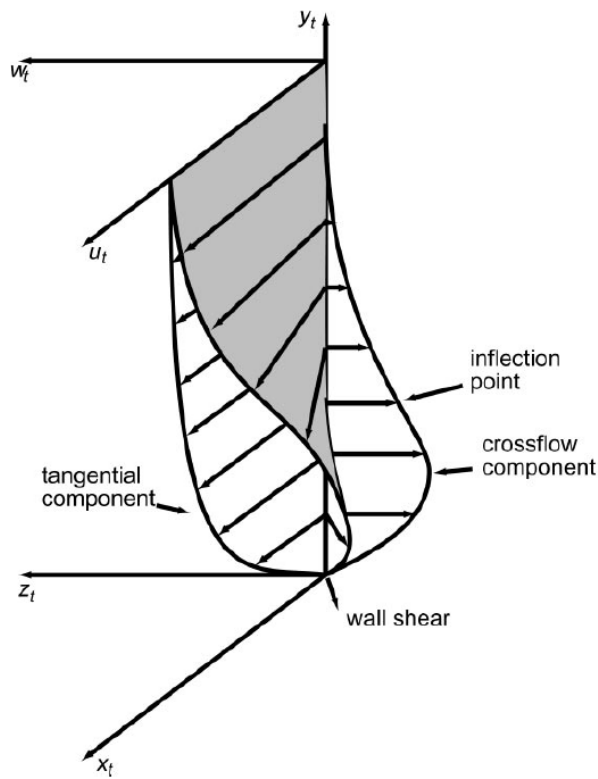


Figure 2.6: Crossflow profile of the boundary layer on a swept wing, taken from Ref. [54].

component of the velocity vector in the direction perpendicular to the direction of the streamline in the freestream. Since the crossflow velocity vanishes both at the edge of the boundary layer and at the wall, it follows that an inflection point exists in the crossflow velocity profile [54]. Similar to what was discussed for natural transition, this inflection point provides an inviscid instability of the boundary-layer.

The crossflow instability amplifies disturbances in both stationary and travelling waves. While the latter are more relevant in high-turbulence scenarios, the former are dominant in cases with low freestream turbulence. In the case of stationary crossflow waves, secondary instabilities are created which lead to a "saw-tooth" pattern of the transition line.

2.2 Modelling Transition

While the previous section dealt with distinct transition processes and their physical mechanisms, this section is concerned with the prediction of transition in CFD. Possible approaches to predict the onset of the transition region are discussed, ranging from the theory-based e^N method to the high-fidelity approaches such as DNS and LES, empirical correlations and criteria based on integral boundary-layer quantities and models with local formulations that are compatible with solvers for the RANS equations.

2.2.1 Direct Numerical Simulation and Large Eddy Simulation

All stages of the transition process can be accurately simulated using Direct Numerical Simulation (DNS) [55]. In DNS, the unsteady Navier-Stokes equations are solved without any averaging, as all flow scales are resolved. Extremely fine grids and time steps are required, which scale strongly with the Reynolds number of the flow. This makes this approach costly and currently unaffordable for complex geometries or high Reynolds number flows [1, 16]. The main virtues of DNS lie in the amount of data it can provide, which may be difficult or impossible to obtain experimentally, and the ability to prescribe exact inflow conditions. Thus, the main use of DNS is not for industrial applications and predicting transition, but rather to get a better description of the physical mechanisms and structures that come into play, which can be of help in the development of new models.

In Ref. [56], DNS is used to study the effect of freestream fluctuations on separation-induced transition. It is found that if no disturbances are specified, the Kelvin-Helmholtz instability of the boundary-layer was caused by numerical error, causing a rapid transition to turbulence. The addition of freestream turbulence reduces the size of the laminar separation bubble. The influence of freestream turbulence on laminar separation bubbles is also addressed in Ref. [57], which further details that the presence of freestream turbulence causes the growth of Klebanoff modes in the laminar boundary-layer upstream of the separation point. These modes undergo exponential growth in the free-shear layer, causing the earlier transition and shorter bubble in the presence of freestream turbulence. Furthermore, it is shown that different energy spectra lead to different sizes of the separation bubble, despite having the same level of freestream turbulence. This is depicted in Figure 2.7.

Studies on the late stages of transition using DNS have also been performed [58]. They show that the

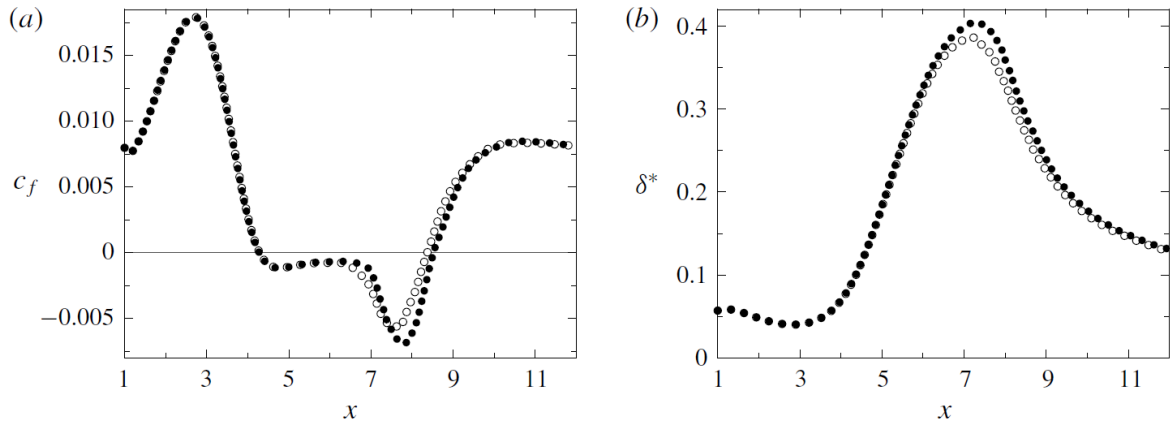


Figure 2.7: Time and spanwise-averaged skin friction coefficient (left) and displacement thickness (right) for two different energy spectra. Reproduced from Ref. [57].

late stages of transition have the same nature, regardless of being caused by Tollmien-Schlichting waves or by Klebanoff modes. The results presented exhibit the vortical structures typical of the transition process such as horseshoe and hairpin vortices.

In Ref. [59] the influence of distributed roughness on bypass transition caused by freestream turbulence is addressed. It is shown that for large roughness elements there is no formation of turbulent spots, unlike what happens when transition is triggered by the freestream turbulence. The combination of roughness and freestream turbulence leads to earlier instability, causing the location of transition to shift upstream. However, the breakdown patterns of the unstable streaks are different and depend on whether they are caused by roughness or by freestream turbulence.

A further study on the effect of roughness is given in Ref. [60] for a swept-wing boundary layer. Both sub-critical and critical roughness elements are studied, highlighting the different instability mechanisms between both cases. It is shown that large elements are able to immediately cause turbulent flow.

An alternative approach to DNS is Large Eddy Simulation (LES), which consists in using a coarser grid so that only the largest scales are resolved. In order to account for the smaller scales, a subgrid-scale model is used. One of the earliest models, the Smagorinsky model, has been shown [61] to be excessively dissipative, causing relaminarization of transitional flows. However other models have proven to be reliable alternatives. One example is given in Ref. [62], which compares LES and DNS calculations for transitional channel flow. The LES approach provides good results for the proposed model, both in the transitional and turbulent phase.

Monokrousos et al. [63] have presented a study of bypass transition on a flat plate using both LES and DNS. The main goal was to study the control and delay of the onset of transition based on blowing and suction at the wall. Their results show that with a careful selection of the subgrid-scale model, the LES results can capture details of the transition process, greatly reducing the computational cost when compared to DNS.

A study on a turbine rotor blade [64] has shown that a flow pattern similar of DNS results is obtained with LES. However, in the suction side of the blade, the predicted location of transition is considerably delayed when compared to the DNS calculations. In the pressure side, the agreement between the two

approaches is much closer. Differences are attributed to lack of grid resolution in the suction side, as well as to the subgrid-scale model.

LES has also been applied to the simulation of separation-induced transition over a flat-plate with imposed pressure distribution [65]. The results shown LES to be able to correctly capture the transition mechanism in the free-shear layer as well as flow reattachment. Further work with different levels of freestream turbulence on both a flat plate and a compressor blade [17] has shown that for low levels of freestream turbulence, the LES results have a strong dependence on the subgrid-scale model used and significant differences to DNS solutions are found.

Despite their potential in predicting transition, neither LES or DNS are routinely used for industrial applications, even in the case of moderate Reynolds flows. While both alternatives can provide an accurate description of different stages observed during transition as well as correctly predict the location of transition, the computational resources that are required are too demanding, preventing their common use. Furthermore, both approaches require full knowledge of unsteady flow conditions regarding to boundary conditions as the flow disturbances must be correctly specified. This specification is far from trivial and can greatly affect the simulation of the transition process.

2.2.2 The e^N method and stability theory based approaches

The most mature approach to the prediction of transition is the so-called e^N method. It was developed independently and simultaneously by Van Ingen [18] and Smith and Gamberoni [19]. Dating back to 1956, it is still viewed in industry as a "high-fidelity" transition prediction method. Its popularity comes from the accurate results it has exhibited and its basis on linear stability theory.

The underlying principle of the e^N method is to superimpose a disturbance in the laminar flow and to track its growth or decay. The local linear stability equations with the parallel flow assumption are used to compute the local amplification rate of a disturbance. The local rate is then integrated along a streamline, in order to compute a global amplification factor, defined as the ratio between the amplitude at a given streamwise position and the initial amplitude of the disturbance. Transition is considered to start when the global amplification factor reaches a critical value, which is often calibrated for a specific test model and experimental facility. It should be noted that the e^N method is simply a transition prediction method, as some other approach is needed to compute both the laminar and turbulent flow solution.

The calculation of the local amplification rates can be computationally expensive, since they have to be done for different disturbance frequencies. One option to reduce the cost is to make use of pre-computed solutions for velocity profiles of self-similar boundary layers, such as Falkner-Skan profiles [66]. The crucial step is then to estimate the local amplification rate of the actual velocity profile from the available database. Implementations of the e^N method using this technique are often called the database approach. An example of the application of the e^N method [67] is given in Figure 2.8, and a comparison of its results with experimental data [68] is presented in Figure 2.9.

Although it acquires a more complex form, the e^N method can be extended to 3D geometries. In one approach, two critical amplification factors are used, one for the Tollmien-Schlichting waves, and another

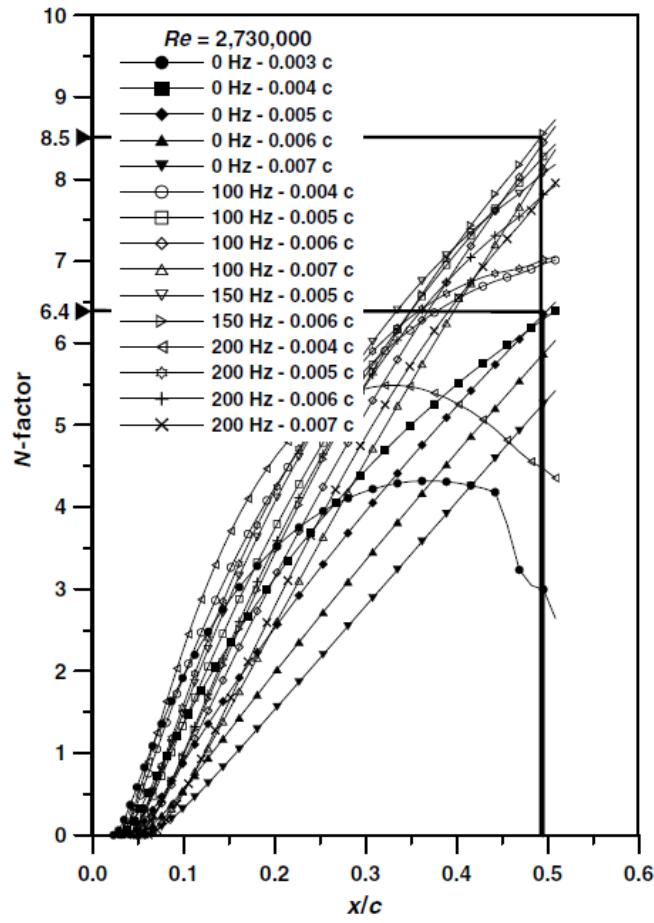


Figure 2.8: N factor for different disturbance frequencies and wavelengths. Reproduced from Ref. [67].

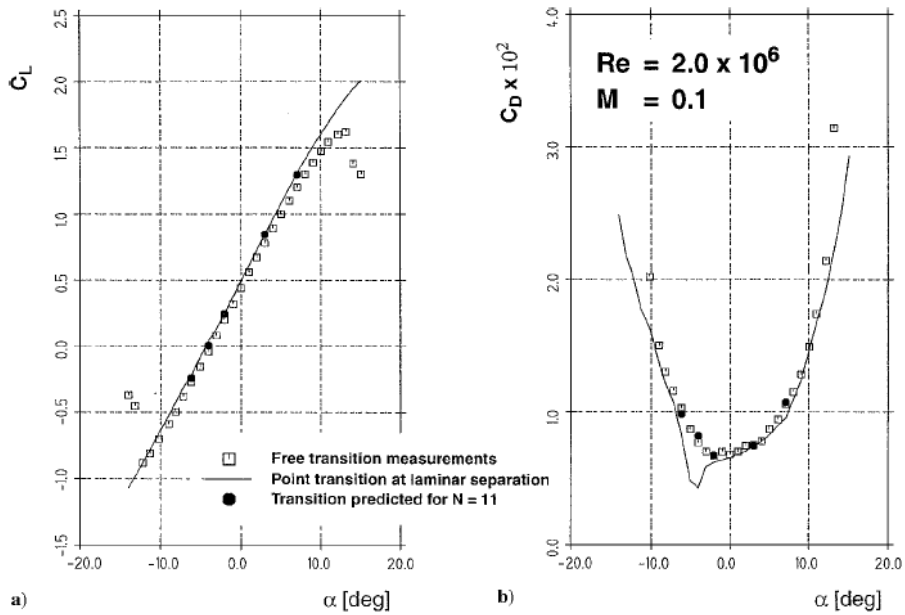


Figure 2.9: Comparison of experimental data with linear stability theory coupled with a RANS solver for the NLF1-0416 airfoil. Adapted from Ref. [68].

for the crossflow mode. Another option, the so-called envelope approach, simply uses the largest amplification rate, without a decomposition in the two components. Details on these two approaches can be found in Refs. [69, 70]. Effects such as compressibility can also play a significant role. A detailed study on the linear stability equations for 2D and 3D compressible and incompressible flows is given in Ref. [71].

Despite its success, the e^N method has some disadvantages. Since it is based on linear stability theory, the method can only account for the primary, linear mechanisms. This means that it cannot describe the entire transition process, but only the start. Due to the same reason, the e^N method is only suitable for natural transition, and in principle cannot be applied in cases where bypass transition or roughness play a role. In practice, it is still used, and the critical value for the amplification factor is related to the freestream turbulence level to promote earlier transition. Nevertheless, the selection of the critical value is still an empirical choice, which often relies on calibration of the method. One possibility to improve upon the e^N method is to make use of the parabolized stability equations for the computation of the local amplification rates. This approach is able to include non-linear effects, and is not restricted by the parallel flow assumption [72, 73].

The natural coupling of the e^N method is with boundary-layer codes, since these are able to provide the well-resolved velocity profiles that the method requires. The integration of the e^N method with RANS approaches is possible [67, 68, 74, 75] but more difficult, due to the reliance on unstructured grids and domain decomposition. The current trends towards highly parallelized codes do not facilitate the inclusion of non-local operations such as integration or search algorithms. Finally, since the e^N method only provides the start of transition, some other approach is needed to handle the entire transition region in the RANS solver, since point transition can be harmful to the convergence properties of the coupled system.

2.2.3 Empirical correlations for transition prediction

Several correlations based on experimental observations have been developed. Perhaps the most popular one for natural transition is the correlation of Abu-Ghannam and Shaw [76]. This correlation accounts for the effect of the pressure gradient ($\lambda_\theta = \frac{\theta^2}{\nu} \frac{dU_e}{dx}$) and freestream turbulence intensity (Tu) in order to determine the momentum-thickness Reynolds number ($Re_{\theta,t}$) at which transition starts.

$$Re_{\theta,t} = 163 + \exp \left[F(\lambda_\theta) \left(1 - \frac{Tu}{6.91} \right) \right], \quad (2.5)$$

$$F(\lambda_\theta) = \begin{cases} 6.91 + 12.75\lambda_\theta + 63.34\lambda_\theta^2, & \lambda_\theta \leq 0; \\ 6.91 + 2.48\lambda_\theta - 12.27\lambda_\theta^2, & \lambda_\theta > 0. \end{cases} \quad (2.6)$$

The Arnal-Habiballah-Delcourt (AHD) transition criteria [77] is adequate for natural transition. It is given by:

$$Re_{\theta,t} = \exp \left[\frac{52}{H} - 14.8 \right] - 206 \exp \left(25.7 \overline{\Lambda_{2T}} \right) \left[\ln(16.8Tu) - 2.77, \overline{\Lambda_{2T}} \right] \quad (2.7)$$

$$\overline{\Lambda_{2T}} = \frac{1}{x - x_{tr}} \int_{x_{tr}}^x \lambda_{\theta} dx. \quad (2.8)$$

It has been extended for compressible flows up to a Mach number of 1.3 [78].

Mayle [14] provides a correlation for the transition onset in the case of bypass transition:

$$Re_{\theta,t} = 400Tu^{-5/8}. \quad (2.9)$$

The fit between the correlation and experimental data is presented in Figure 2.10.

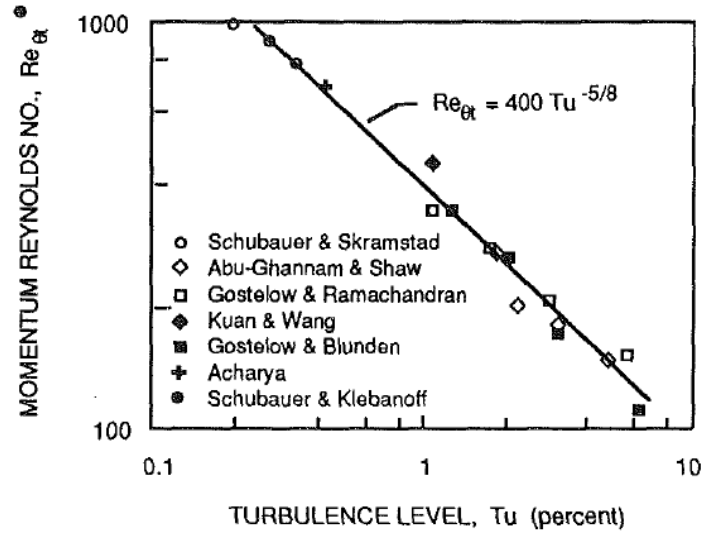


Figure 2.10: Mayle's correlation compared with experimental data. Reproduced from Ref. [14].

A common correlation for crossflow transition is the C1 criterion [77]. Crossflow transition takes place when $R_{\delta_2} > R_{\delta_2 T}$ with:

$$R_{\delta_2 T} = \begin{cases} 150, & H \leq 2.31; \\ \frac{300}{\pi} \arctan\left(\frac{0.106}{(H-2.3)^{2.092}}\right) (1 + \frac{\gamma-1}{2} M^2), & H > 2.31, \end{cases} \quad (2.10)$$

where $R_{\delta_2} = \frac{U_e \delta_2}{\nu}$ and $\delta_2 = -\int_0^{\delta} \frac{w}{U_e} dy$.

Although the previously mentioned correlations allow the estimation of the onset of transition, they provide no details on the extent of the transition region. One way to do so was proposed by Dhawan and Narasimha [79], by defining an intermittency function for the transitional and turbulent zones as:

$$\gamma = 1.0 - \exp(-0.41\xi^2), \quad (2.11)$$

where

$$\xi = \frac{x - x_t}{x_{\gamma=0.75} - x_{\gamma=0.25}}. \quad (2.12)$$

2.2.4 Low Reynolds number models

Low Reynolds number turbulence models consist on modifications of functions or constants of existing turbulence models. The initial aim of these modifications were to improve the predictions of these models for turbulent flow at low Reynolds numbers. One of the earliest examples of this type of model comes from Jones and Launder [20], with a low Reynolds number $k - \epsilon$ model. The comparison of the model prediction with experimental data is presented in Figure 2.11. In general, good agreement with experimental data is observed although the authors do note that there is room for improvement in the formulation.

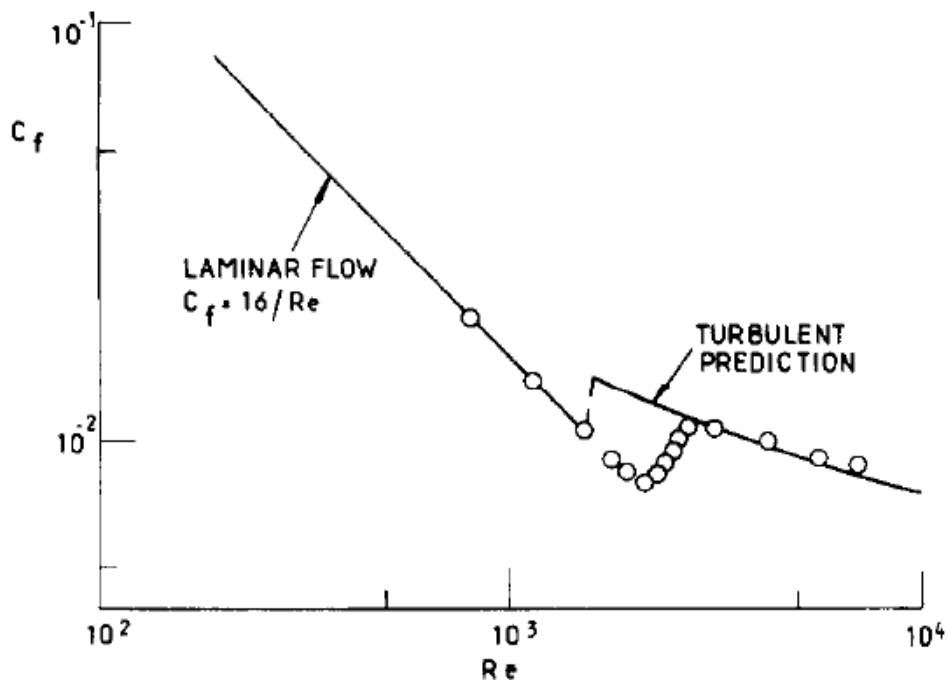


Figure 2.11: Comparison of the Jones-Launder Low Reynolds number turbulence model with experimental data. Reproduced from Ref. [20].

In a review by Patel and et al. [21], eight different low-Reynolds number models are compared. These comprise seven $k - \epsilon$ models and one $k - \omega$ model. All models included a function modifying the calculation of the eddy-viscosity, considered essential for model performance. This function was defined differently for each single model, as shown in Figure 2.12. In the study, several models are deemed unsuitable as they fail to reproduce the skin friction coefficient and velocity profiles for the simple test case of a flat plate. Additional improvements are pointed out for the remaining models.

As low Reynolds number models showed some capability in the prediction of transition, their potential for these applications started to be investigated [80]. Due to not requiring an additional model for transition and already describing turbulent flows, the computational cost incurred by these alternatives was the same as for high Reynolds number flows. In the work by Schmidt and Patankar [81, 82], the model of Jones and Launder [20] and that of Lam and Bremhorst [83] are compared with a focus on the prediction of flow transition. They conclude that the reproduction of transition by these models is caused by the similarities between the near-wall region in a fully turbulent boundary layer and the development

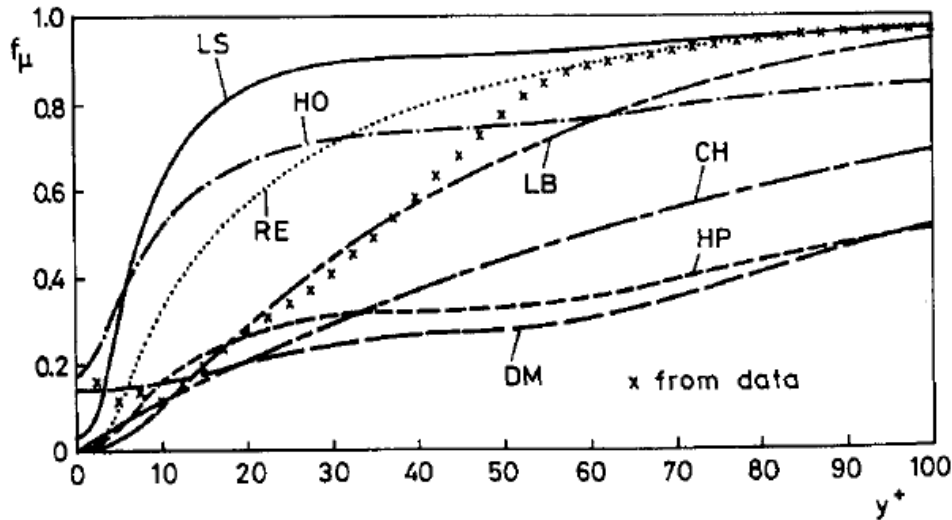


Figure 2.12: Comparison of the function modifying the eddy-viscosity calculation for several different low-Reynolds number models. Reproduced from Ref. [21].

of laminar boundary layers. Further work on low Reynolds number models is given in Refs. [84–86].

In the recent years, this approach has been mostly abandoned for the prediction of transition. The coupling between the prediction of the transition region and the modelling of the viscous sub-layer prevents a proper calibration of the former without sacrificing the latter. Furthermore, this approach is not amenable to the inclusion of additional transition mechanisms such as separation-induced transition or crossflow transition. An additional issue for low Reynolds number $k - \epsilon$ models lies in the fact that these can exhibit solutions that are dependent on numerical parameters that should not affect the final solution, such as the initial conditions or the solution procedure, which comprises their use [22]. As a final point, the development of more sophisticated and accurate approaches outperform low Reynolds number models in the prediction of flow transition [87].

2.2.5 Transport equation based models

A further step in the implementation of transition prediction methods in CFD calculations consists in the use of models that incorporate transport equations, usually for the intermittency. An example of this type of models is the model of Steelant and Dick [88], which resorts to the conditionally-averaged Navier-Stokes equations for the modelling of bypass transition, and an intermittency equation with a source term that aims at reproducing the intermittency distribution of Dhawan and Narasimha [79]. Such approach leads to the solution of two sets of continuity and momentum equations, one for laminar and transitional flow, and another for turbulent flow. For the latter, a $k - \epsilon$ model is used.

In their work, Suzen and Huang [89] propose a transport equation for the intermittency, which is considered as a blending between that of Refs. [90] and [88]. This transition model is coupled to the $k - \omega$ SST model, and it affected the turbulence model by directly multiplying the eddy-viscosity by the intermittency. The main purpose of this approach was to combine the realistic behaviour of γ in the crossstream direction of the Cho and Chung model [90] with the correct streamwise behaviour given by

Steelant and Dick's model [88]. The new model was tested for the flow over a flat plate under different freestream turbulence values as well as different pressure gradients where it exhibited good results, illustrated in Figure 2.13.

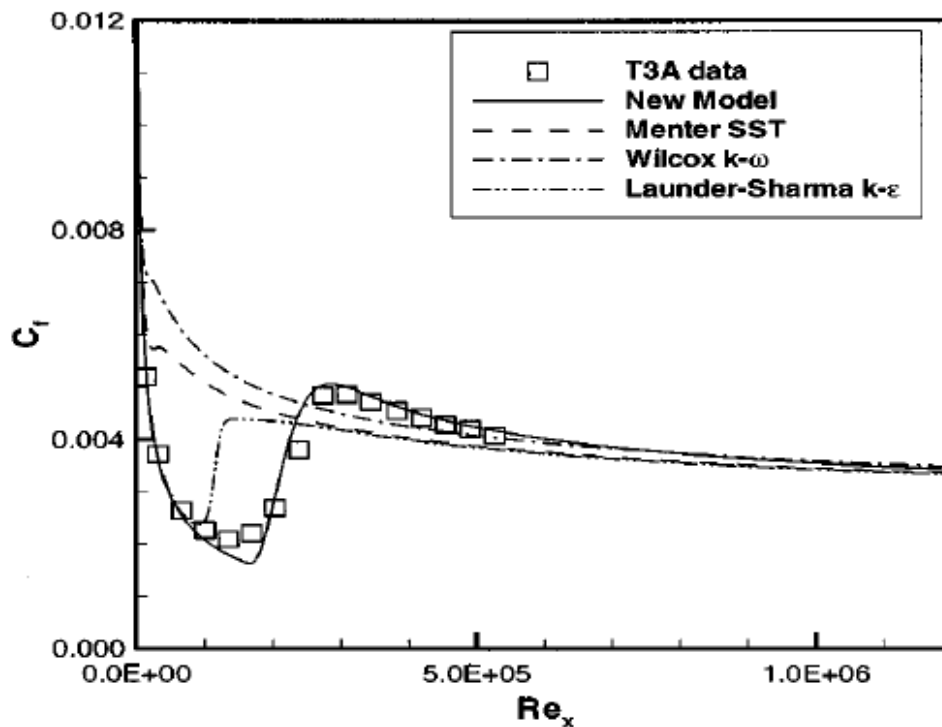


Figure 2.13: Comparison of Suzen and Huang's model with experimental data and other two-equation turbulence models. Reproduced from Ref. [89].

Pecnik et al. [91] compare the model of Suzen and Huang and a further development of the model of Steelant and Dick [92], which solves a transport equation for a turbulence weighting factor τ . This factor combines both the effects of the intermittency factor as well as a freestream factor meant to account for the diffusion of turbulent eddies present in the freestream into the boundary layer. In their findings, Pecnik et al. conclude that Steelant and Dick's model performs better than Suzen and Huang's model.

While the previous models are usable in a RANS environment, their formulation includes non-local quantities such as the momentum thickness. The trend of CFD in relying on unstructured grids and parallelization through domain decomposition introduces significant disadvantages in the algorithms required for the calculation of integral quantities. Inevitably, this stands as a significant obstacle in the widespread usage of these models. These difficulties were identified by Menter et al. [93] in what is the precursor work to the now widespread $\gamma - Re_\theta$ model. Menter et al. proposed a new intermittency based model that was used to control the production term of the $k - \omega$ SST model and avoided the need for non-local operations. Testing of the model revealed that it did not respond properly in flows with pressure gradients and further work was necessary, as shown in Figure 2.14.

Building upon the work done in 2002, Menter et al. publish in 2006 the $\gamma - Re_\theta$ model [94, 95]. It is also based on a local formulation and empirical correlations to determine the onset of transition, and is capable of handling natural, bypass and separation-induced transition. The model makes use of

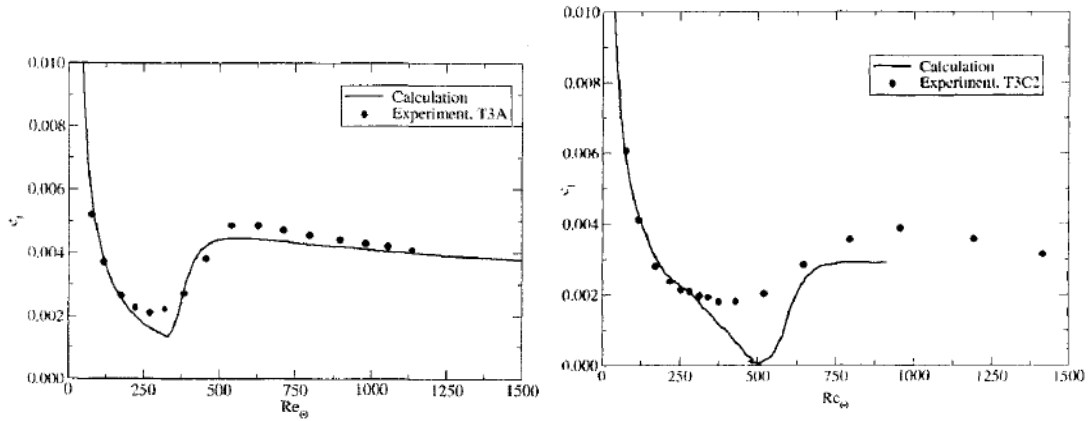


Figure 2.14: Model of Menter et al. for the flow over flat plate. Reproduced from Ref. [93].

the vorticity based Reynolds number, a concept introduced by Van Driest and Blumer [96], in order to estimate the momentum thickness Reynolds number. Besides a transport equation for the intermittency, the model includes a transport equation for the transition onset momentum thickness Reynolds number, which is computed at the edge of the boundary layer through an empirical correlation that introduces the influence of freestream turbulence and pressure gradient. The transition onset momentum thickness Reynolds number is then diffused into the boundary layer, avoiding the need for non-local operations.

In its initial publication, the model lacked some correlations which were deemed proprietary. This prevented direct use of the model, as alternative correlations had to be used or developed, usually using the same cases for calibration which had been used in the original model. Examples of such approaches are given in Refs. [28, 97–103]. The full formulation of the model including the missing correlations was published in 2009 [23], thus ending these efforts. A comparison of the behaviour of the model when using some of the developed correlations and the original ones [104] is illustrated in Figure 2.15.

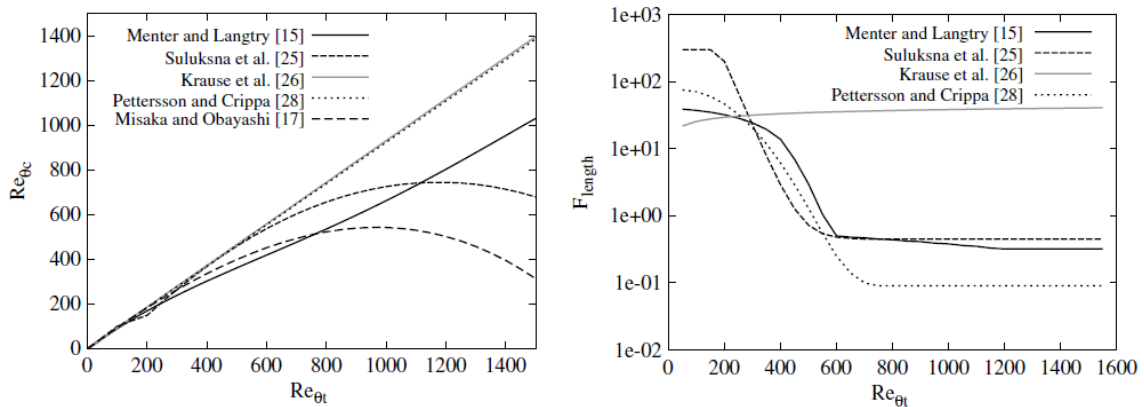


Figure 2.15: Comparison of different correlations developed for the $\gamma - Re_\theta$ model. Reproduced from Ref. [104].

With the complete formulation of the model published, focus turned to its application and comparison with available data. The study of Seyfert and Krumbein [104] compares the $\gamma - Re_\theta$ model predictions for several airfoils with those of the e^N method. They find very good results when the freestream turbulence intensity is lower than 0.1% and when separation-induced transition takes place. In Ref. [105] the

accuracy of the $\gamma - Re_\theta$ model is tested for a NACA 66-312 airfoil. The results of the model show good agreement with experimental data regarding pressure coefficient and velocity profile in the vicinity of the separation bubble. Lanzafame et al. [5] also shows the model to provide good results for wind turbines, although some of the correlations are modified. The $\gamma - Re_\theta$ model has also been used for diverse applications such as marine propellers [6], helicopter and turbine rotor blades [106, 107], and even for the simulation of transition on dolphins [108].

Despite its success, the $\gamma - Re_\theta$ model is not free of flaws. Although it can handle multiple transition mechanisms, the original formulation of the model does not account for roughness. Some groups have developed extensions or alternative correlations capable of incorporating the effects of roughness [26, 109]. In the same sense, the model is unable to capture crossflow transition, which can be of major importance in three dimensional flows. Several approaches to remedy this have also been proposed [27, 110, 111]. The introduction of two transport equations for transition, along with the two equations of the $k - \omega$ SST model, not only makes numerical robustness more difficult [112] as it inevitably increases the computational cost due to the higher number of iterations required to iteratively converge the solution. Furthermore, the formulation of the model is not Galilean invariant, so its application can be troublesome on problems where walls move in respect to the coordinate system.

To address this last point, some work has been done on simplifying the model [29, 113] through the replacement of the transport equation for Re_θ for an algebraic relation which can be evaluated inside the boundary-layer. In particular, the work of Menter et al. [29], from here on out referred to as the γ model, has gained significant traction as a successor of the $\gamma - Re_\theta$ model. It also eliminates the latter's disadvantage of not employing a Galilean invariant formulation. Due to the close resemblance between the two models, it is expected that some of the crossflow correlations developed for the $\gamma - Re_\theta$ model may also be applicable for the γ model. While initially coupled to the $k - \omega$ SST turbulence model, a formulation that enables both the $\gamma - Re_\theta$ and γ models to be coupled to the Spalart-Allmaras model has been proposed [114–116]. The use of the $\gamma - Re_\theta$ model along with a Reynolds stress model has also been presented [32].

An alternative to intermittency based models is given by Walters and Leylek [117], which resorts to the concept of laminar kinetic energy, k_L , introduced by Mayle and Schulz [118]. This relates to the high amplitude fluctuations that are observed in the pre-transitional boundary layer for freestream turbulence intensity above 1%, conditions that correspond to bypass transition. Despite this, the model is also built to account for natural transition. It includes a transport equation for k_L and a $k - \epsilon$ formulation for the turbulent regime. Instead of relying on empirical correlations for transition, it is built based on physical arguments. The three equations are tightly coupled through source terms which represent the transfer of laminar kinetic energy to turbulent kinetic energy. Further developments on the $k - k_L - \epsilon$ model have seen it being adapted into a $k - k_L - \omega$ formulation in the work by Walters and Cokljat [24]. Both approaches avoid the computation of integral quantities, and rely only on local quantities, making them fully compatible with commonly used RANS solvers and the $k - k_L - \omega$ model in particular has become considerably popular.

Based on the long standing success of linear stability theory, a novel approach in the prediction of

transition has been proposed by Coder [25], termed the Amplification Factor Transport (AFT) model. This model attempts to replicate the methodology of the e^N method in a local formulation, by estimating integral quantities through a nondimensional pressure gradient parameter. Similarly to the e^N method, it is necessary to specify a value from the critical amplification rate from which transition is considered to start. Since its publication in 2014 [25] the model has undergone several changes. Initially coupled with the Spalart-Allmaras model, a coupling strategy with the $k - \omega$ SST model has been developed in Ref. [30]. Further modifications on the formulation have also seen a change in the way the pressure gradient parameter is computed [119], as well as the addition of a transport equation for the intermittency, changing the way the coupling with the turbulence model is done [120].

New approaches relying on the use of algebraic models [121] or models attempting to employ transition criteria in a local formulation [122] are still under development. RANS compatible transition models comprise the current state of the art in transition modelling and prediction, as approaches with a lower degree of modelling are too expensive for practical applications. The most widespread models are the $\gamma - Re_\theta$ and its one equation variant, the $k_T - k_L - \omega$ and the AFT models, each model with its own range of applications. Due to its formulation, the applicability and accuracy of the $\gamma - Re_\theta$ is inherently connected to the correlations employed. The AFT model, as it attempts to follow linear stability theory, should be suitable for natural transition but not for bypass transition. Accordingly, the $k_T - k_L - \omega$ is mainly aimed at bypass transition since that stands at the origin of the laminar kinetic energy concept. This situation is unsurprising as the development of a universal model capable of accounting for all possible transition mechanisms seems unattainable.

This thesis is devoted to this class of models, which employ local formulations, as these stand as the most promising option to incorporate the effects on transition on calculations based on the RANS equations. Different models are selected, in order to cover different modelling methodologies. The AFT model represents a stability based approach, whereas the $\gamma - Re_\theta$ model is the prime candidate for the correlation-based approach. The γ model, which stands as a simpler and more general formulation than the $\gamma - Re_\theta$ model, therefore eliminating some of the latter's deficiencies, is also employed. In the early stages of this work, the $k_T - k_L - \omega$ model was used as well, as an example of the approach based on laminar kinetic energy. However, it was not as thoroughly tested as the remaining models, due to robustness issues and poor performance when flow separation takes place [33], and as such it is not further considered herein.

Chapter 3

Mathematical Formulation

This chapter presents the mathematical formulation that stands as the framework of the calculations done throughout this work. Section 3.1 presents the basis for the Reynolds-averaged Navier-Stokes equations, which are used in all models addressed herein. The Boussinesq hypothesis is presented in Section 3.2, along with the turbulence models used: the $k - \omega$ SST [123] and the $k - \sqrt{k}L$ [124] two-equation eddy-viscosity turbulence models. The formulation of each transition model studied in this work is given in Section 3.3. These are the $\gamma - Re_\theta$ model [23], the γ model by Menter et al. [29] and the Amplification Factor Transport model [30, 119]. The coupling between each transition model and turbulence model is also given in Section 3.3.

3.1 The Reynolds-averaged Navier-Stokes Equations

This work deals with the Reynolds-averaged Navier-Stokes (RANS) equations, which are the most commonly used approach to handle turbulent flows for industrial applications. In all cases addressed in this work, a single-phase, incompressible, Newtonian fluid is considered and as such, all relevant equations presented include these assumptions. Under these conditions, the continuity and the Navier-Stokes equations can be written as:

$$\frac{\partial u_i}{\partial x_i} = 0, \quad (3.1)$$

$$\rho \frac{\partial u_i}{\partial t} + \rho u_j \frac{\partial u_i}{\partial x_j} = -\frac{\partial p}{\partial x_i} + \frac{\partial}{\partial x_j} \left[\mu \left(\frac{\partial u_i}{\partial x_j} + \frac{\partial u_j}{\partial x_i} \right) \right]. \quad (3.2)$$

u_i are the components of the instantaneous velocity, p is the instantaneous pressure relative to the hydrostatic, ρ is the fluid's density and μ is the dynamic viscosity of the fluid. x_i are the coordinates of the Cartesian coordinate system.

The first step in the derivation of the RANS equations is to decompose all flow variables into a mean and fluctuating component

$$u_i = U_i + u'_i, \quad (3.3)$$

$$p = P + p'. \quad (3.4)$$

Lowercase letters are used to represent instantaneous quantities, while uppercase letters correspond to the mean quantities and the prime denotes the component pertaining to flow fluctuations. For statistically steady flows, U_i is defined as

$$U_i = \overline{u_i} = \lim_{T \rightarrow \infty} \frac{1}{T} \int_{t_0}^{t_0+T} u_i dt, \quad (3.5)$$

where the overline represents the averaging operator.

Applying the mean operator of Eq. 3.5 to the continuity and momentum transport equations and replacing instantaneous variables by the Reynolds decomposition leads to the RANS equations

$$\frac{\partial U_i}{\partial x_i} = 0, \quad (3.6)$$

$$\rho \frac{\partial U_i}{\partial t} + \rho U_j \frac{\partial U_i}{\partial x_j} = -\frac{\partial P}{\partial x_i} + \frac{\partial}{\partial x_j} \left[\mu \left(\frac{\partial U_i}{\partial x_j} + \frac{\partial U_j}{\partial x_i} \right) \right] + \frac{\partial}{\partial x_j} \left(-\rho \overline{u'_i u'_j} \right). \quad (3.7)$$

The last term of the right-hand side of Eq. 3.7 is the Reynolds stress tensor and it represents the influence of velocity fluctuations on the mean flow. As they stand, the RANS equations comprise a set of four equations for ten different variables: the mean velocity components U_i , the mean pressure P and the six independent components of the symmetric Reynolds stress tensor $-\rho \overline{u'_i u'_j}$. Important quantities that are required in the turbulence and transition models used in this work are the mean strain rate tensor S_{ij} and the mean vorticity tensor W_{ij} . These are defined as

$$S_{ij} = \frac{1}{2} \left(\frac{\partial U_i}{\partial x_j} + \frac{\partial U_j}{\partial x_i} \right), \quad (3.8)$$

$$W_{ij} = \frac{1}{2} \left(\frac{\partial U_i}{\partial x_j} - \frac{\partial U_j}{\partial x_i} \right). \quad (3.9)$$

Also used is the magnitude of these two tensors, referred to as the mean strain rate magnitude S and the mean vorticity magnitude Ω , calculated through

$$S = \sqrt{2S_{ij}S_{ij}}, \quad (3.10)$$

$$\Omega = \sqrt{2W_{ij}W_{ij}}. \quad (3.11)$$

3.2 Turbulence Models

Since there are more unknowns than equations in the RANS equations, additional relations are needed in order to close the system. One possibility is to solve a transport equation for each component of the Reynolds stress tensor, which is the approach undertaken by Reynolds stress models. The other alternative is to employ Boussinesq's hypothesis, which relates the Reynolds stress tensor to the eddy-viscosity μ_t through

$$-\rho \overline{u'_i u'_j} = \mu_t \left(\frac{\partial U_i}{\partial x_j} + \frac{\partial U_j}{\partial x_i} \right) - \frac{2}{3} \rho k \delta_{ij}. \quad (3.12)$$

Introducing Eq. 3.12 in Eq. 3.7 leads to

$$\rho \frac{\partial U_i}{\partial t} + \rho U_j \frac{\partial U_i}{\partial x_j} = -\frac{\partial \tilde{P}}{\partial x_i} + \frac{\partial}{\partial x_j} \left[(\mu + \mu_t) \left(\frac{\partial U_i}{\partial x_j} + \frac{\partial U_j}{\partial x_i} \right) \right], \quad (3.13)$$

with

$$\tilde{P} = P + \frac{2}{3} \rho k. \quad (3.14)$$

Although this reduces the number of unknowns, these still outnumber the number of available equations. In order to determine μ_t and k , an eddy-viscosity turbulence model is required.

3.2.1 $k - \omega$ SST model

The $k - \omega$ Shear Stress Transport turbulence model is based on a blend between a $k - \omega$ formulation and a $k - \epsilon$ formulation. Aiming to combine the advantages of the two models, the SST model switches from a $k - \epsilon$ in the freestream and in free shear layers to the $k - \omega$ model inside the boundary-layer. By doing so, it avoids the freestream dependency of the $k - \omega$ formulation, while retaining its superior behaviour in the viscous layer. Initially published in 1994 [125], the version presented here corresponds to that given in Ref. [123]. The SST model solves two transport equations, one for the turbulence kinetic energy k and another for the turbulence specific dissipation ω :

$$\frac{\partial (\rho k)}{\partial t} + \frac{\partial (\rho U_j k)}{\partial x_j} = P_k - D_k + \frac{\partial}{\partial x_j} \left[(\mu + \sigma_k \mu_t) \frac{\partial k}{\partial x_j} \right], \quad (3.15)$$

$$\frac{\partial (\rho \omega)}{\partial t} + \frac{\partial (\rho U_j \omega)}{\partial x_j} = \frac{\alpha}{\mu_t} P_k - \rho \beta \omega^2 + \frac{\partial}{\partial x_j} \left[(\mu + \sigma_\omega \mu_t) \frac{\partial \omega}{\partial x_j} \right] + 2(1 - F_1) \frac{\rho \sigma_{\omega 2}}{\omega} \frac{\partial k}{\partial x_j} \frac{\partial \omega}{\partial x_j}. \quad (3.16)$$

The production term of the k transport equation is given by

$$P_k = \min (\mu_t S^2, 15 D_k), \quad (3.17)$$

which includes a limiter to prevent excess turbulence production in stagnation regions, based on the destruction term. It should be noted that the constant of 15 is a departure from the value of 20 given in the 1994 version of the model and the value of 10 from the 2003 version. This change is motivated by the need to ensure the limiter is only active in stagnation regions and to avoid its activation in turbulent regions [126]. The destruction term is

$$D_k = \rho \beta^* k \omega. \quad (3.18)$$

F_1 is the blending function designed to switch between the $k - \epsilon$ and $k - \omega$ formulations. This is done by a blend in the model constants, and the introduction of the cross-diffusion term in the ω equation. The cross-diffusion term appears when the ω equation is derived from the ϵ equation using the relation $\omega = \epsilon / (k \beta^*)$. The activation of the cross-diffusion term is controlled by F_1 , defined as

$$F_1 = \tanh (\arg_1^4), \quad (3.19)$$

where

$$\arg_1 = \min \left[\max \left(\frac{\sqrt{k}}{\beta^* \omega d}, \frac{500\nu}{d^2 \omega} \right), \frac{4\rho\sigma_{\omega 2} k}{CD_{k\omega} d^2} \right], \quad (3.20)$$

$$CD_{k\omega} = \max \left(2\rho\sigma_{\omega 2} \frac{1}{\omega} \frac{\partial k}{\partial x_j} \frac{\partial \omega}{\partial x_j}, 10^{-10} \right). \quad (3.21)$$

Model constants are identified by a subscript 1 or 2 depending on what part of the formulation is active. The blend is done through

$$\phi = F_1 \phi_1 + (1 - F_1) \phi_2, \quad (3.22)$$

where ϕ represents an arbitrary constant.

The eddy-viscosity is calculated according to

$$\mu_t = \frac{\rho a_1 k}{\max(a_1 \omega, S F_2)}, \quad (3.23)$$

with

$$F_2 = \tanh(\arg_2^2), \quad (3.24)$$

$$\arg_2 = \max \left(2 \frac{\sqrt{k}}{\beta^* \omega d}, \frac{500\nu}{d^2 \omega} \right). \quad (3.25)$$

The model constants for the $k - \omega$ SST model [123] are given in Table 3.1.

Table 3.1: Model constants of the 2003 formulation of the $k - \omega$ SST turbulence model [123].

α_1	α_2	σ_{k1}	σ_{k2}	$\sigma_{\omega 1}$	$\sigma_{\omega 2}$	β_1	β_2	β^*	κ	a_1
5/9	0.44	0.85	1.0	0.5	0.856	0.075	0.0828	0.09	0.41	0.31

3.2.2 $k - \sqrt{k}L$ model

The $k - \sqrt{k}L$ (KSKL) [124] turbulence model has two transport equations, one for the turbulence kinetic energy and another for $\Phi = \sqrt{k}L$, where L represents a length scale. The two transport equations are

$$\frac{\partial(\rho k)}{\partial t} + \frac{\partial(\rho U_j k)}{\partial x_j} = P_k - D_k + \frac{\partial}{\partial x_j} \left[\left(\mu + \frac{\mu_t}{\sigma_k} \right) \frac{\partial k}{\partial x_j} \right], \quad (3.26)$$

$$\frac{\partial(\rho \Phi)}{\partial t} + \frac{\partial(\rho U_j \Phi)}{\partial x_j} = \frac{\Phi}{k} \mu_t S^2 \left[\zeta_1 - \zeta_2 \left(\frac{L}{L_{v\kappa}} \right)^2 \right] - \zeta_3 \rho k - 6\mu \frac{\Phi}{d^2} f_\Phi + \frac{\partial}{\partial x_j} \left[\left(\mu + \frac{\mu_t}{\sigma_\Phi} \right) \frac{\partial \Phi}{\partial x_j} \right]. \quad (3.27)$$

The production and dissipation terms of the k transport equation are given by

$$P_k = \mu_t S^2, \quad (3.28)$$

$$D_k = \rho c_\mu^{3/4} \frac{k^{3/2}}{L} + 2\mu \frac{k}{d^2}. \quad (3.29)$$

While the production term is similar to that of the $k - \omega$ SST turbulence model, it does not include any limiter. The dissipation term is made of two contributions. The first corresponds to the standard form of

the dissipation term, while the second is an added term for improved modelling of the viscous sub-layer [124]. The quantity $L_{v\kappa}$ is calculated as

$$L_{v\kappa} = \kappa \frac{S}{\sqrt{\nabla S \cdot \nabla S}}, \quad (3.30)$$

and the eddy-viscosity is

$$\mu_t = \min \left(\rho c_\mu^{1/4} \Phi, \frac{\rho a_1 k}{S} \right), \quad (3.31)$$

$$a_1 = a_1^{SST} f_b + (1 - f_b) a_1^{REAL}. \quad (3.32)$$

a_1^{SST} and a_1^{REAL} are constants and f_b is a function which takes the value of one inside the boundary-layer and zero outside. It is defined as

$$f_b = \tanh \left[\left(\frac{20 \left(\rho c_\mu^{1/4} \Phi + \mu \right)}{\kappa^2 \rho S d^2 + 0.01 \mu} \right)^2 \right]. \quad (3.33)$$

All constants of the KSKL model are given in Table 3.2.

Table 3.2: Model constants of the $k - \sqrt{k}L$ turbulence model [124].

σ_k	σ_Φ	ζ_1	ζ_2	ζ_3	c_μ	κ	a_1^{SST}	a_1^{REAL}
2/3	2/3	0.8	1.47	0.0288	0.09	0.41	0.32	0.577

3.3 Transition Models

3.3.1 $\gamma - Re_\theta$ model

The $\gamma - Re_\theta$ model [23] solves two transport equations, one for the intermittency γ , and another for the transition onset momentum-thickness Reynolds number $\tilde{Re}_{\theta t}$:

$$\frac{\partial(\rho\gamma)}{\partial t} + \frac{\partial(\rho U_j \gamma)}{\partial x_j} = P_\gamma - E_\gamma + \frac{\partial}{\partial x_j} \left[\left(\mu + \frac{\mu_t}{\sigma_f} \right) \frac{\partial \gamma}{\partial x_j} \right], \quad (3.34)$$

$$\frac{\partial(\rho \tilde{Re}_{\theta t})}{\partial t} + \frac{\partial(\rho U_j \tilde{Re}_{\theta t})}{\partial x_j} = P_{\theta t} + \frac{\partial}{\partial x_j} \left[\sigma_{\theta t} (\mu + \mu_t) \frac{\partial \tilde{Re}_{\theta t}}{\partial x_j} \right]. \quad (3.35)$$

The destruction or relaminarization term of the γ transport equation, E_γ , is responsible for decreasing the value of γ in the laminar boundary-layer and can be written as

$$E_\gamma = c_{a2} \rho \Omega \gamma F_{turb} (c_{e2} \gamma - 1), \quad (3.36)$$

where c_{a2} and c_{e2} are constants. The first controls the magnitude of the destruction term, while the second enforces a minimum bound on γ . Thus, $\gamma \geq \frac{1}{c_{e2}}$. The F_{turb} function switches off E_γ in the

turbulent boundary layer, ensuring that the flow remains turbulent and is given by

$$F_{turb} = \exp \left[- \left(\frac{R_T}{4} \right)^4 \right], \quad (3.37)$$

with

$$R_T = \frac{\rho k}{\mu \omega}. \quad (3.38)$$

The production term of the γ equation is

$$P_\gamma = F_{length} c_{a1} \rho S [\gamma F_{onset}]^{0.5} (1 - c_{e1} \gamma). \quad (3.39)$$

The constant c_{e1} guarantees an upper bound on γ of 1. The F_{length} correlation depends on $\tilde{Re}_{\theta t}$ and controls how fast the transition process takes place. The $F_{sublayer}$ function ensures that F_{length} takes its maximum value of 40 in the viscous sublayer to prevent an unphysical sharp increase of the skin friction which could occur at higher Reynolds numbers.

$$F_{length} = F_{length,1} (1 - F_{sublayer}) + 40.0 F_{sublayer}, \quad (3.40)$$

$$F_{length,1} = \begin{cases} 39.8189 + (-119.270 \cdot 10^{-4}) \tilde{Re}_{\theta t} + (-132.567 \cdot 10^{-6}) \tilde{Re}_{\theta t}^2, & \tilde{Re}_{\theta t} < 400; \\ 263.404 + (-123.939 \cdot 10^{-2}) \tilde{Re}_{\theta t} + (194.548 \cdot 10^{-5}) \tilde{Re}_{\theta t}^2 \\ \quad + (-101.695 \cdot 10^{-8}) \tilde{Re}_{\theta t}^3, & 400 \leq \tilde{Re}_{\theta t} < 596; \\ 0.5 - (3.0 \cdot 10^{-4}) (\tilde{Re}_{\theta t} - 596.0), & 596 \leq \tilde{Re}_{\theta t} < 1200; \\ 0.3188, & 1200 \leq \tilde{Re}_{\theta t}. \end{cases} \quad (3.41)$$

$$F_{sublayer} = \exp \left[- \left(\frac{Re_\omega}{200} \right)^2 \right], \quad (3.42)$$

$$Re_\omega = \frac{\rho \omega d^2}{\mu}. \quad (3.43)$$

The onset of transition is triggered via the F_{onset} function. It depends mainly on F_{onset1} , through the comparison between the local vorticity-based Reynolds number, Re_V , and the critical momentum thickness Reynolds number $Re_{\theta c}$. F_{onset2} ensures a rapid change from 0 to 1, so that the production of γ starts once F_{onset1} has exceeded one. The build-up of γ during transition triggers the production term of the k equation in the $k - \omega$ SST model, effectively increasing the eddy-viscosity and the diffusion of the flow. In turn, this leads to a local decrease of the strain-rate magnitude S , which could cause the transition process to stall since F_{onset1} would decrease as well. In order to prevent this from happening, the F_{onset3} function is introduced [46], responsible for increasing F_{onset} as the turbulence Reynolds number R_T increases.

$$F_{onset} = \max(F_{onset2} - F_{onset3}, 0), \quad (3.44)$$

$$F_{onset3} = \max \left[1 - \left(\frac{R_T}{2.5} \right)^3, 0 \right], \quad (3.45)$$

$$F_{onset2} = \min(\max(F_{onset1}, F_{onset1}^4), 2.0), \quad (3.46)$$

$$F_{onset1} = \frac{Re_V}{2.193 Re_{\theta c}}, \quad (3.47)$$

$$Re_V = \frac{\rho S d^2}{\mu}. \quad (3.48)$$

The critical momentum thickness Reynolds number $Re_{\theta c}$ is obtained from an empirical correlation which depends only on $\tilde{Re}_{\theta t}$.

$$Re_{\theta c} = \begin{cases} (-396.035 \cdot 10^{-2}) + (10120.656 \cdot 10^{-4}) \tilde{Re}_{\theta t} + (-868.230 \cdot 10^{-6}) \tilde{Re}_{\theta t}^2 \\ \quad + (696.506 \cdot 10^{-9}) \tilde{Re}_{\theta t}^3 + (-174.105 \cdot 10^{-12}) \tilde{Re}_{\theta t}^4, & \tilde{Re}_{\theta t} \leq 1870; \\ \tilde{Re}_{\theta t} - (593.11 + 0.482 (\tilde{Re}_{\theta t} - 1870.0)), & 1870 < \tilde{Re}_{\theta t}. \end{cases} \quad (3.49)$$

The production term for the $\tilde{Re}_{\theta t}$ equation is

$$P_{\theta t} = c_{\theta t} \frac{\rho}{T} (Re_{\theta t}^{eq} - \tilde{Re}_{\theta t}) (1.0 - F_{\theta t}), \quad (3.50)$$

where $c_{\theta t}$ is a constant and T is a timescale introduced for dimensional purposes. The production term is built so that in the freestream, identified by $F_{\theta t} = 0$, the value of $\tilde{Re}_{\theta t}$ matches that given by $Re_{\theta t}^{eq}$. The definitions of T and $F_{\theta t}$ are given by:

$$T = \frac{500\mu}{\rho U^2}, \quad (3.51)$$

$$U = \sqrt{U_k U_k}, \quad (3.52)$$

$$F_{\theta t} = \min \left[\max \left(F_{wake} \exp \left(- \left(\frac{d}{\delta} \right)^4 \right), 1.0 - \left(\frac{c_{e2}\gamma - 1}{c_{e2} - 1} \right)^2 \right), 1.0 \right], \quad (3.53)$$

$$\delta = \frac{375\Omega\mu\tilde{Re}_{\theta t}d}{\rho U^2}, \quad (3.54)$$

$$F_{wake} = \exp \left[- \left(\frac{Re_{\omega}}{1 \cdot 10^5} \right)^2 \right]. \quad (3.55)$$

The correlation $Re_{\theta t}^{eq}$ depends on the turbulence intensity and pressure gradient:

$$Re_{\theta t}^{eq} = \begin{cases} (1173.51 - 589.428Tu + 0.2196Tu^{-2}) F(\lambda_{\theta}), & Tu \leq 1.3; \\ 331.50 (Tu - 0.5658)^{-0.671} F(\lambda_{\theta}), & Tu > 1.3. \end{cases} \quad (3.56)$$

$$F(\lambda_{\theta}) = \begin{cases} 1 + [12.986\lambda_{\theta} + 123.66\lambda_{\theta}^2 + 405.689\lambda_{\theta}^3] \exp \left(- \left(\frac{Tu}{1.5} \right)^{1.5} \right), & \lambda_{\theta} \leq 0; \\ 1 + 0.275 [1 - \exp(-35.0\lambda_{\theta})] \exp \left(- \frac{Tu}{0.5} \right), & \lambda_{\theta} > 0. \end{cases} \quad (3.57)$$

$$\lambda_{\theta} = \frac{\rho\theta_t^2}{\mu} \frac{dU}{ds}, \quad (3.58)$$

$$\frac{dU}{ds} = \frac{U_m U_n}{U^2} \frac{\partial U_m}{\partial x_n}, \quad (3.59)$$

$$Re_{\theta t}^{eq} = \frac{\rho U \theta_t}{\mu}. \quad (3.60)$$

The calculation of $Re_{\theta t}^{eq}$ is done iteratively, since the same variable is required to compute θ_t and consequently, λ_θ and $F(\lambda_\theta)$. The turbulence intensity is calculated from

$$Tu = 100 \frac{\sqrt{2k/3}}{U}, \quad (3.61)$$

where U is the velocity magnitude.

The model computes an effective intermittency γ_{eff} by

$$\gamma_{eff} = \max(\gamma, \gamma_{sep}), \quad (3.62)$$

where

$$\gamma_{sep} = \min \left(s_1 \max \left[0, \left(\frac{Re_V}{3.235 Re_{\theta c}} \right) - 1 \right] F_{reattach}, 2 \right) F_{\theta t}, \quad (3.63)$$

$$F_{reattach} = \exp \left[- \left(\frac{R_T}{20} \right)^4 \right]. \quad (3.64)$$

γ_{sep} is intended to trigger transition in separated flows, with the $F_{reattach}$ function deactivating this term when the flow reattaches. It should be pointed out that due to the introduction of γ_{sep} , the effective intermittency can exceed a value of 1, unlike the transported variable γ . This boosts the production of k whenever separation-induced transition takes place.

Table 3.3 shows the values for all the constants in the model.

Table 3.3: Constants for the $\gamma - Re_\theta$ model [23].

c_{a1}	c_{a2}	c_{e1}	c_{e2}	$c_{\theta t}$	s_1	σ_γ	$\sigma_{\theta t}$
2.0	0.06	1.0	50	0.03	2	1.0	2.0

Coupling with the $k - \omega$ SST model

The coupling of the $\gamma - Re_\theta$ transition model with the $k - \omega$ SST turbulence model is given in Refs. [23, 46]. It is done by adapting the production and dissipation terms of the k transport equation as follows:

$$P_k = \gamma_{eff} P_{k,SST}, \quad (3.65)$$

$$D_k = \min(\max(\gamma_{eff}, 0.1), 1.0) D_{k,SST}. \quad (3.66)$$

$P_{k,SST}$ and $D_{k,SST}$ are the original production and destruction terms of the SST model given in Eqs. 3.17 and 3.18 respectively. The equation for ω is not changed.

The final modification to the $k - \omega$ SST model is done by changing the F_1 blending function in order to ensure that $F_1 = 1$ in the laminar boundary layer. Hence, F_1 is now defined as:

$$F_1 = \max(F_{1,SST}, F_3) \quad (3.67)$$

where $F_{1,SST}$ is the definition of F_1 used in the SST model and F_3 is given by

$$F_3 = \exp \left[- \left(\frac{R_y}{120} \right)^8 \right], \quad (3.68)$$

$$R_y = \frac{\rho d \sqrt{k}}{\mu}. \quad (3.69)$$

Coupling with the $k - \sqrt{k}L$ model

The coupling between the $\gamma - Re_\theta$ model and the KSKL model [127] follows closely that performed for the $k - \omega$ SST model. The production and dissipation terms of the k transport equation are changed to

$$P_k = \gamma_{eff} P_{k,KSKL}, \quad (3.70)$$

$$D_k = \min(\max(\gamma_{eff}, 0.1), 1.0) D_{k,KSKL}, \quad (3.71)$$

where $P_{k,KSKL}$ and $D_{k,KSKL}$ are the original production and dissipation terms of the KSKL model respectively. Once again, the equation for the second variable of the model, Φ , is not modified.

In order to sensitize the f_b function to the laminar boundary layer, its definition is changed to

$$f_b = \max(f_{b,KSKL}, F_3), \quad (3.72)$$

where $f_{b,KSKL}$ corresponds to the definition of the f_b function given in the KSKL model and F_3 is

$$F_3 = \exp \left[- \left(\frac{R_y}{120} \right)^8 \right], \quad (3.73)$$

with

$$R_y = \frac{\rho d \sqrt{k}}{\mu}. \quad (3.74)$$

The KSKL model does not solve directly for ω , which is required in several of the transition model's functions. In order to overcome this [127], an estimate of ω based on the definition of the eddy-viscosity is used:

$$\omega = \frac{\rho k}{\mu_t}. \quad (3.75)$$

3.3.2 γ model

The γ model [29] solves one transport equation for the intermittency γ

$$\frac{\partial(\rho\gamma)}{\partial t} + \frac{\partial(\rho U_j \gamma)}{\partial x_j} = P_\gamma - E_\gamma + \frac{\partial}{\partial x_j} \left[\left(\mu + \frac{\mu_t}{\sigma_f} \right) \frac{\partial \gamma}{\partial x_j} \right]. \quad (3.76)$$

Although the form of the transport equation given in Eq. 3.76 matches that of the $\gamma - Re_\theta$ model in Eq. 3.34, the definitions of E_γ and P_γ undergo some changes. In the case of E_γ , the form is the same as in

Eq. 3.36, but the definition of F_{turb} is changed:

$$E_\gamma = c_{a2}\rho\Omega\gamma F_{turb} (c_{e2}\gamma - 1), \quad (3.77)$$

$$F_{turb} = \exp \left[- \left(\frac{R_T}{2} \right)^4 \right]. \quad (3.78)$$

In the case of P_γ , the definition is simplified to

$$P_\gamma = F_{length}\rho S\gamma F_{onset} (1 - \gamma). \quad (3.79)$$

F_{length} , which took on the form of a correlation in the $\gamma - Re_\theta$ model, is now a constant. On the other hand, the structure of F_{onset} and subsequent functions is mostly unchanged:

$$F_{onset} = \max(F_{onset2} - F_{onset3}, 0), \quad (3.80)$$

$$F_{onset3} = \max \left[1 - \left(\frac{R_T}{3.5} \right)^3, 0 \right], \quad (3.81)$$

$$F_{onset2} = \min(F_{onset1}, 2.0), \quad (3.82)$$

$$F_{onset1} = \frac{Re_V}{2.2Re_{\theta c}}. \quad (3.83)$$

The main difference between the $\gamma - Re_\theta$ and the γ model lies in the calculation of $Re_{\theta c}$. In the $\gamma - Re_\theta$ model, the value of $Re_{\theta t}$ in the boundary-layer was diffused in from the freestream where it matched an empirical correlation based on the turbulence intensity and pressure gradient. In the γ model the correlation is evaluated inside the boundary layer, which removes the need for the diffusion mechanism and the transport equation for $\tilde{Re}_{\theta t}$. Hence, $Re_{\theta c}$ is obtained from

$$Re_{\theta c} = 100.0 + 1000.0 \exp(-Tu_L F_{PG}), \quad (3.84)$$

where Tu_L is the local turbulence intensity computed from

$$Tu_L = \min \left(100 \frac{\sqrt{2k/3}}{\omega d_w}, 100 \right). \quad (3.85)$$

The function F_{PG} introduces the effect of the pressure gradient in the calculation of $Re_{\theta c}$ and is defined as:

$$F_{PG} = \begin{cases} \min(1 + 14.68\lambda_{\theta L}, 1.5), & \lambda_{\theta L} \geq 0; \\ \min(1 - 7.34\lambda_{\theta L}, 3.0) & \lambda_{\theta L} < 0, \end{cases} \quad (3.86)$$

$$\lambda_{\theta L} = -7.57 \times 10^{-3} \frac{dV}{dy} \frac{\rho d_w^2}{\mu} + 0.0128. \quad (3.87)$$

The following limiters are used to enforce positive values:

$$F_{PG} = \max(F_{PG}, 0), \quad (3.88)$$

$$\lambda_{\theta L} = \min (\max (\lambda_{\theta L}, -1.0), 1.0). \quad (3.89)$$

The calculation of the wall-normal derivative of the wall-normal velocity $\frac{dV}{dy}$ is done, following the work of Coder [119], through the gradient of the wall distance:

$$\frac{dV}{dy} = \nabla (\vec{n} \cdot \vec{U}) \cdot \vec{n}, \quad (3.90)$$

$$\vec{n} = \nabla d. \quad (3.91)$$

The constants used in the γ model are given in Table 3.4.

Table 3.4: Constants for the γ model [29].

c_{a2}	c_{e2}	F_{length}	σ_γ
0.06	50	100	1.0

Coupling with the $k - \omega$ SST turbulence model

The coupling of the γ model with the $k - \omega$ SST model is done by modifying P_k and D_k as

$$P_k = \gamma P_{k,SST} + P_k^{lim}, \quad (3.92)$$

$$D_k = \max(\gamma, 0.1) D_{k,SST}, \quad (3.93)$$

where $P_{k,SST}$ and $D_{k,SST}$ correspond to the production and dissipation terms of k transport equation of the original SST model, given in Eqs. 3.17 and 3.18 respectively. P_k^{lim} is an additional production term given by:

$$P_k^{lim} = 5 \max(\gamma - 0.2, 0) (1 - \gamma) F_{on}^{lim} \max(3\mu - \mu_t, 0) S\Omega, \quad (3.94)$$

$$F_{on}^{lim} = \min \left(\max \left(\frac{Re_V}{2420} - 1, 0 \right), 3 \right). \quad (3.95)$$

The blending function F_1 is modified in the same way as in the $\gamma - Re_\theta$ model using Eqs. 3.67, 3.68 and 3.69.

Coupling with the $k - \sqrt{k}L$ turbulence model

When using the γ model combined with the KSKL turbulence model, the production and dissipation terms of the k transport equation are changed to

$$P_k = \gamma P_{k,KSKL} + P_k^{lim}, \quad (3.96)$$

$$D_k = \max(\gamma, 0.1) D_{k,KSKL}. \quad (3.97)$$

The P_k^{lim} term is the same as that written in Eq. 3.94. Similarly to the coupling between the $\gamma - Re_\theta$ and KSKL models, the f_b function is modified according to Eqs. 3.72, 3.73 and 3.74. The final modification

is the value of the constant c_{e2} of the γ model which is changed from 50 to 250. This decreases the minimum value of γ from 0.02 to 0.004, preventing an unphysical peak of k in the laminar boundary layer [127]. Since ω is required in some of the γ model's functions, the estimate of ω presented in Eq. 3.75 is used.

3.3.3 AFT model

The Amplification Factor Transport model [119] solves one transport equation for the local amplification rate \tilde{n} :

$$\frac{\partial(\rho\tilde{n})}{\partial t} + \frac{\partial(\rho U_j \tilde{n})}{\partial x_j} = \rho \Omega F_{crit} F_{growth} \frac{d\tilde{n}}{dRe_{\delta 2}} + \frac{\partial}{\partial x_j} \left[(\mu + \mu_t) \frac{\partial \tilde{n}}{\partial x_j} \right]. \quad (3.98)$$

The various functions which are part of the source term depend on the estimate of the integral shape factor H_{12} obtained by

$$H_{12} = 0.1818 + \left[\frac{H_L + 2.3609}{0.5178} \right]^{\frac{1}{2}}, \quad (3.99)$$

where H_L is a local pressure-gradient parameter

$$H_L = \frac{d^2}{\mu} \left[\nabla \left(\rho \vec{U} \cdot \nabla d \right) \cdot \nabla d \right], \quad (3.100)$$

which is limited as

$$-0.24 < H_L < 200. \quad (3.101)$$

The F_{growth} function is defined as

$$F_{growth} = D(H_{12}) \frac{[1 + m(H_{12})] l(H_{12})}{2}. \quad (3.102)$$

The correlations $l(H_{12})$ and $m(H_{12})$ are part of Drela and Giles' work [128] and are based on the boundary-layer growth of Falkner-Skan profiles, while $D(H_{12})$ was developed for use in the AFT model.

$$l(H_{12}) = \frac{6.54H_{12} - 14.07}{H_{12}^2}, \quad (3.103)$$

$$m(H_{12}) = \left(0.058 \frac{(H_{12} - 4)^2}{H_{12} - 1} - 0.068 \right) \frac{1}{l(H_{12})}, \quad (3.104)$$

$$D(H_{12}) = \frac{H_{12}}{0.6202H_{12} - 0.6387}. \quad (3.105)$$

F_{crit} controls the production of \tilde{n} and is dependent on the vorticity-based Reynolds number Re_V . It should be noted that in the AFT model, the eddy-viscosity is used in Re_V , unlike the definition given in the $\gamma - Re_\theta$ and γ models.

$$F_{crit} = \begin{cases} 0, & Re_V < Re_{V,0}, \\ 1, & Re_V \geq Re_{V,0}, \end{cases} \quad (3.106)$$

$$Re_V = \frac{\rho S d^2}{\mu + \mu_t}, \quad (3.107)$$

$$Re_{V,0} = k_V Re_{\delta 2,0}, \quad (3.108)$$

$$k_V = 0.2231H_{12}^2 - 0.1617H_{12} + 0.1121, \quad (3.109)$$

$$\log_{10}(Re_{\delta 2,0}) = 0.7 \tanh\left(\frac{14}{H_{12}-1} - 9.24\right) + \frac{2.492}{(H_{12}-1)^{0.43}} + 0.62. \quad (3.110)$$

Finally, $\frac{d\tilde{n}}{dRe_{\delta 2}}$ is given by

$$\frac{d\tilde{n}}{dRe_{\delta 2}} = 0.028(H_{12}-1) - 0.0345 \exp\left[-\left(\frac{3.87}{H_{12}-1} - 2.52\right)^2\right]. \quad (3.111)$$

Coupling with the $k - \omega$ SST turbulence model

The coupling of the AFT model to the $k - \omega$ SST model is described in Ref. [30]. It is done by adding a term to the k transport equation, P_{trans} , responsible for suppressing the production of turbulence in the laminar region. Thus, the k transport equation becomes

$$\frac{\partial(\rho k)}{\partial t} + \frac{\partial(\rho U_j k)}{\partial x_j} = P_k - D_k - P_{trans} + \frac{\partial}{\partial x_j} \left[(\mu + \sigma_k \mu_t) \frac{\partial k}{\partial x_j} \right], \quad (3.112)$$

with

$$P_{trans} = 0.5F_1\mu_t S \left(S - \frac{(\mu\chi)^2}{\rho k^2 d^2 (\mu + \mu_t)} \right) f_{t2}, \quad (3.113)$$

$$f_{damp} = \frac{\chi^{4.23}}{\chi^{4.23} + 7\chi^{3.23} + 255}, \quad (3.114)$$

$$\frac{\mu_t}{\mu} = \chi f_{damp}. \quad (3.115)$$

The calculation of χ is done iteratively using Eq. 3.114 and Eq. 3.115. The f_{t2} function controls when the turbulence suppression term is active, based on the local value of \tilde{n} and the critical value N_{crit} .

$$f_{t2} = [1 - \exp(2(\tilde{n} - N_{crit}))] \exp(-0.05\chi^2) \quad (3.116)$$

N_{crit} can be set to a given value, or it can be related to the inlet turbulence intensity Tu_{in} according to Ref. [129]:

$$N_{crit} = -8.43 - 2.4 \ln\left(\frac{Tu_{in}(\%)}{100}\right). \quad (3.117)$$

Similarly to the $\gamma - Re_\theta$ and γ models, the F_1 blending is modified according to Eqs. 3.67, 3.68 and 3.69.

Chapter 4

Flow Solver and Numerical Setup

This chapter describes the entire computational and numerical setup for the test cases that are addressed throughout this dissertation. Section 4.1 describes the flow solver used in this work. The discretization options for the differential equations being solved are presented in Section 4.2 and details on the procedure to estimate the discretization error and associated uncertainty are given in Section 4.3. Section 4.4 presents a description of the boundary conditions which are used in the numerical simulations. The issue of turbulence decay is briefly addressed in Section 4.5. The description of the test cases is divided in two sections. Section 4.6 presents the two-dimensional test cases, comprised of a flat plate and five different airfoils: NACA 0012, NACA 0015, Eppler 387, S809 and NLF₁-0416. The grid topology is the same for the five airfoils. Therefore, it is only described in detail once for the NACA 0012 airfoil. The three-dimensional test cases consisting of the 6:1 prolate spheroid, the SD7003 wing, and the sickle wing are addressed in Section 4.7. Geometrical considerations such as angle of attack and domain size, as well as grid size and topology are all described in those two sections. Finally, an overview of the aspects relevant to transition flow simulations that will be studied as well as the selected quantities of interest is given in Section 4.8.

4.1 Flow Solver

The flow solver used for the calculations performed throughout this work is ReFRESH [130]. It is an incompressible flow solver aimed at the maritime community, developed and verified by the Maritime Research Institute Netherlands in cooperation with several universities. The equations are discretised using a finite-volume approach with cell-centered collocated variables in strong-conservation form. A pressure-correction equation based on the SIMPLE algorithm is used to ensure mass conservation, with a pressure-weighted interpolation method to prevent pressure oscillations [131]. Time integration is performed implicitly with first or second-order backward schemes. At each implicit time step, the non-linear system for velocity and pressure is linearised with Picard's method. The implementation is face-based, which permits grids with elements consisting of an arbitrary number of faces (hexahedrals, tetrahedrals, prisms, pyramids, etc.) and if needed h-refinement (hanging nodes). Several other features

such as moving and deforming grids, cavitation and acoustics models, among others, are also available in ReFRESKO, but are not used in this work.

4.2 Solution Procedure

The general form of a transport equation for a scalar quantity ϕ is

$$\frac{\partial(\rho\phi)}{\partial t} + \nabla \cdot (\rho\phi U) = \nabla \cdot (\Gamma \nabla \phi) + \rho Q_\phi, \quad (4.1)$$

where Γ represents the diffusivity of ϕ and Q_ϕ is a source or sink of ϕ . Integrating in control volume V with surface S and outward normal vector n and using Gauss's divergence theorem in Eq. 4.1, which is the application of the finite volume method [132], leads to

$$\frac{\partial}{\partial t} \int_V (\rho\phi) dV + \int_S \rho\phi U \cdot n dS = \int_S \Gamma \nabla \phi \cdot n dS + \int_V \rho Q_\phi dV. \quad (4.2)$$

The discretization of the volume integrals is done using the midpoint rule, leading to

$$\int_V f dV = f_c \Delta V, \quad (4.3)$$

where f_c represents the cell center value of f and ΔV is the cell's volume. The midpoint rule is also used for the discretization of the surface integrals

$$\int_S f dS = \sum_{i=1}^{N_f} f_{f_i} S_{f_i}, \quad (4.4)$$

where f_{f_i} represents the value of f at the centre of face i and N_f is the total number of faces.

ReFRESKO has a first-order and a second-order implicit backward schemes available for the discretization of the time derivative term shown in the left hand side of Eq. 4.2. Although most of the calculations done in this work are steady, the first-order scheme is used for the few unsteady simulations performed. This choice is mainly motivated by robustness issues. The application of the first order scheme leads to

$$\frac{\partial}{\partial t} \int_V (\rho\phi) dV = \frac{(\rho_c \phi_c)^j - (\rho_c \phi_c)^{j-1}}{\Delta t} \Delta V. \quad (4.5)$$

The diffusion term takes the form

$$\int_S \Gamma (\nabla \phi \cdot n) dS = \sum_{i=1}^{N_f} \Gamma_{f_i} (\nabla \phi_{f_i} \cdot \mathbf{S}_{f_i}), \quad (4.6)$$

where \mathbf{S}_{f_i} is the surface area vector. The value of $\nabla \phi_{f_i}$ at the face is calculated using a second order central scheme. Non-orthogonality corrections are also applied [133].

The convection term becomes

$$\int_S \rho \phi (U \cdot n) dS = \sum_{i=1}^{N_f} \rho_{f_i} \phi_{f_i} (U_{f_i} \cdot \mathbf{S}_{f_i}), \quad (4.7)$$

where $U_{f_i} \cdot \mathbf{S}_{f_i}$ is taken from the values of the previous iteration, which corresponds to the process of Picard linearization. The calculation of the value of ϕ at the face for the convection term can be done using a first order upwind scheme, in which the value at the face is assumed to be equal to the value at the upwind cell center, or using a quadratic upwind scheme (QUICK)

$$\phi_f = \phi_U + \frac{1}{4} \left(\frac{3}{2} (\phi_D - \phi_U) + \frac{1}{2} (\phi_U - \phi_{UU}) \right) \quad (4.8)$$

where ϕ_D is the value of ϕ at the cell centre downwind of the face, ϕ_U is the value of ϕ at the cell centre upwind of the face and ϕ_{UU} is the value of ϕ at the neighbouring upwind cell. Despite the superior accuracy when compared to the first order upwind scheme, the QUICK scheme can produce numerical oscillations. This is avoided through the introduction of flux limiters, which prevent overshoots and undershoots. There are several flux limiters available in ReFRESKO, with the one used in this work being described in detail in Ref. [134]. In general, the QUICK scheme with flux limiters is employed in all transport equations for the vast majority of the calculations presented in this thesis. The few exceptions correspond to cases where laminar flow separation occurs and to the three-dimensional geometries. These are detailed further in this chapter, in the description of each test case.

Finally, to compute the gradients at the cell centers, required for the calculation of the diffusive fluxes or the second order convection scheme, Gauss's theorem is used:

$$\nabla \phi_c = \frac{1}{\Delta V} \sum_{i=1}^{N_f} \phi_{f_i} \mathbf{S}_{f_i}. \quad (4.9)$$

Two different types of relaxation methods are employed in the solution of the resulting system of equations. The first is that of explicit relaxation in which the solution to the linear system of equations $Ax = b$ obtained at the end of iteration $k + 1$ is written as

$$x^{k+1} = x^k + \omega_{exp} (x^* - x^k), \quad (4.10)$$

where x^k is the solution obtained at the end of iteration k , x^* is the result of the procedure used to solve the linear system of equations and ω_{exp} is the explicit relaxation factor, selected such that $0 < \omega_{exp} \leq 1$. Choosing small values of ω tends to lead to slower, but more stable convergence. The second type of relaxation is that of implicit relaxation. Again, considering the linear system of equations $Ax = b$, the main idea of implicit relaxation is to write the equivalent expression

$$\left(A + \frac{1 - \omega_{imp}}{\omega_{imp}} dA \right) x^{k+1} = b + \left(\frac{1 - \omega_{imp}}{\omega_{imp}} dA \right) x^k, \quad (4.11)$$

where dA is the diagonal part of A and ω_{imp} is the implicit relaxation factor. The use of implicit relaxation

ensures the diagonal dominance of the matrix of the linear system. Thus, similarly to explicit relaxation, this leads to slower, albeit more stable convergence.

There are many more aspects in the details of ReFRESKO, both in terms of the discretization, such as non-orthogonality and eccentricity corrections, as well as the pressure-weighted interpolation method that allows the use of collocated grids, while avoiding pressure oscillations. From the numerical point of view, several choices for pre-conditioners are available, in addition to different choices for the solver for the linear system of equations. While all of these features are used for the calculations, a thorough description of each falls out of the scope of this dissertation, as they have a minimal impact on the final solution of the iterative procedure.

4.3 Verification and Validation

The final output of a CFD calculation is a numerical solution for the equations that are being solved. To properly evaluate the quality of the solution one needs to perform a rigorous Verification and Validation exercise. These two concepts possess different meanings [135]. Verification concerns only the numerical solution and aims at showing that it corresponds to the solution of the mathematical model that is solved, being often described as "solving the equations right". As such, the final outcome of a Verification procedure is a numerical error or uncertainty of a given numerical simulation. Validation on the other hand, which can be interpreted as "solving the right equations", is intended to show that the selected model produces an accurate representation of reality. It involves a careful comparison with experimental data, which also has some uncertainty associated with it, and the output of such an exercise is a modelling error or uncertainty [38].

Verification can be divided into two separate components [136]. The first corresponds to Code Verification and is mainly concerned with programming bugs in codes and algorithms, which compromise the results of a calculation. The second component consists of Solution Verification, and it assesses the difference between the numerical solution and the exact solution of the mathematical model, which is generally unknown. In this thesis focus is given to Solution Verification, as Code Verification exercises for ReFRESKO can be found in Ref. [137].

The error E of a quantity of interest ϕ is given by the difference between the result obtained from a simulation ϕ_S and the true value ϕ_T .

$$E = \phi_S - \phi_T. \quad (4.12)$$

This error has three distinct components

$$E = E_m + E_{input} + E_{num}. \quad (4.13)$$

The first component is the modelling error E_m , which corresponds to how well the mathematical model represents reality. It is given by the difference between the true value and the exact solution of the mathematical model, using the exact input quantities in the simulations. The second component is the input error E_{input} , which relates to differences in the settings of the numerical simulation and the physical

experiment. This concerns effects such as the size of the computational domain and the accuracy of boundary conditions in terms of flow properties or even in the geometry itself. The third component is the numerical error, E_{num} which is generally divided in four contributions:

1. Round-off error, $E_{round-off}$, which arises from the finite precision in which computers and algorithms operate [138]. This error can be reduced by using double instead of single precision, or quadruple instead of double precision. As spatial or time refinements are performed using finer grids or smaller time-steps, the importance of this error increases.
2. Iterative error, E_{it} , a consequence of the iterative algorithms used to solve the non-linear system of equations obtained from the discretization of all transport equations [38]. This error can be assessed using metrics such as the L_2 or L_∞ norm of the residuals, which also provide a way to control and reduce it, at the cost of more computing time.
3. Discretization error, E_{disc} , due to the spatial and temporal discretization [139]. It can be reduced through grid refinement or decreasing time step. The temporal contribution only exists in the case of unsteady flows.
4. Statistical error, E_{stat} , present in the simulation of unsteady flows or in stochastic simulations that use input parameters defined by distributions. In the case of unsteady flows, it is caused by the influence of the initial condition on the final solution and can be assessed using techniques such as those described in Ref. [140]. For stochastic simulations it is related to the sampling techniques required to propagate the probabilistic distributions.

$$E_{num} = E_{round-off} + E_{it} + E_{disc} + E_{stat} \quad (4.14)$$

In this work, all calculations are performed in double precision. This justifies that for the cases at hand, the round-off error can be considered negligible. In the same way, all simulations are ran until the residuals of the transport equations have been significantly decreased. For the two dimensional test cases the criteria adopted is to run all simulations until the L_∞ norm of the normalized residuals of all transport equations are under 10^{-8} . For the three dimensional cases, this is changed to 10^{-6} . The normalized residuals correspond to dimensionless variable changes in a single Jacobi iteration. This criterion is strict enough to make the iterative error negligible when compared to the discretization error. The vast majority of the calculations also correspond to steady flows, which means that statistical error does not exist, and that the discretization error stems only from grid refinement and not from temporal refinement. Thus, the discretization error is the dominant component of the numerical error.

To perform an estimate of E_{disc} , grid refinement studies are performed in most cases. The assessment of the discretization error is performed considering a power series expansion of the error

$$E_{disc} = \phi_i - \phi_0 \approx \alpha h_i^p, \quad (4.15)$$

where ϕ_i is the value of ϕ in grid i , ϕ_0 is the exact solution of the mathematical problem, α is the error constant, p is the order of grid convergence and h_i is the typical cell size of grid i .

In principle, the results of three geometrically similar grids would be enough to obtain the unknowns p , α and ϕ_0 . However such is only true if the topology of the grids allows for their density to be characterized by a single parameter, which is generally not the case for the unstructured grids used in CFD calculations for complex geometries. Furthermore it is also required that the grids are fine enough to be in the asymptotic range, where Eq. 4.15 is valid. Another difficulty lies in the scatter of data caused by noise in the solution, a consequence of the limiters employed in discretization schemes and numerous switches in the formulation of turbulence and transition models.

In order to overcome these issues, Eq. 4.15 is solved using a least-squares fit with data from more than three grids. In addition, the procedure used aims at estimating the discretization uncertainty on grid i , U_i , such that it defines an interval that contains the exact solution ϕ_0 with 95% coverage

$$\phi_i - U_i \leq \phi_0 \leq \phi_i + U_i. \quad (4.16)$$

The calculation of U_i depends on the estimated discretization error, on the quality of the least-squares fit measured through the standard deviation and on the difference between the fit and the solution obtained for grid i . The procedure is fully described in Ref. [139] and it is equivalent to the Grid Convergence Index in the case of smooth monotonically convergent data.

Whereas Solution Verification is only concerned with how well the numerical solution obtained represents the solution of the mathematical model and thus does not require experimental information, Validation cannot be performed without resorting to experimental data. A proper Validation exercise needs not only experimental measurements, but also the experimental uncertainty associated with that measurement [38]. Rigorous Verification on the numerical solution is also required, so that the numerical uncertainty that may suitably estimated. Furthermore, the conditions of the experiment need to be carefully controlled, so that the influence of the input uncertainty, present in Eq. 4.13, is not overwhelming.

The strict requirements needed on the experimental data in order to perform Validation are far from attained by the experimental data-sets available for the test cases used in this thesis. Experimental uncertainty is rarely provided, and there is insufficient information to guide the selection of the two turbulence variables at the inlet, which is a significant problem in the modelling of transition given its dependence on flow perturbations. Due to the latter, input uncertainty would also have to be thoroughly investigated. While these obstacles prevent formal Validation, comparisons between experimental data and the numerical solutions obtained with and without transition models are performed nonetheless, allowing a qualitative assessment of the advantages of including a transition model.

4.4 Boundary Conditions

Boundary conditions are an essential step in the setup of any CFD calculation, determining the conditions of the flow. Given that all calculations were performed with the same flow solver, it is enough to characterize the boundary conditions types that were employed across all cases. These correspond to inflow, outflow, pressure, symmetry, slip wall and no-slip wall boundary conditions. Each type of

boundary condition is treated as follows:

- Inflow boundary condition. At a boundary assigned an inflow boundary condition, constant values for the velocity components, turbulence variables and transition variables are specified at this boundary. While the velocity and turbulence variables must be user-specified, the transition variables are automatically applied depending on the transition model being used. The remaining variable, pressure, is obtained from the interior of the domain, considering a zero normal derivative. This boundary condition is always used at the inlet of the computational domain.
- Outflow boundary condition. At an outflow boundary, zero normal derivatives are imposed for all variables. Despite the name, this boundary condition is only used at the outlet of the domain for a single test case.
- Pressure boundary condition. At a pressure boundary condition, the normal derivatives of all flow variables are set to zero, with the sole exception of the pressure, which is set to a user specified value. This boundary condition is used for most test cases at the outlet of the domain.
- Symmetry boundary condition. This boundary condition is intended to force symmetry upon the solution, by enforcing zero normal derivatives for all variables with the exception of the normal velocity at the boundary, which is set to zero.
- Slip wall boundary condition. At a slip wall boundary condition, zero normal derivatives are set for all flow variables, except for the normal velocity, which is set to zero.
- No-slip wall boundary condition. This boundary condition corresponds to solid walls. At boundaries to which this boundary condition was assigned, all velocity components are set to zero, as well as k and $\sqrt{k}L$, while ω is set at the nearest wall cell centre according to its near-wall analytic solution [141]. Zero normal derivatives are enforced for all other flow variables.

All of the transition models used in this thesis have well-defined boundary conditions that do not require user input. In the case of the $\gamma - Re_\theta$ and γ models, the intermittency is set to one at the inflow boundary, while Re_θ is obtained from the turbulence intensity value using Eq. 3.56, assuming a zero pressure gradient. For the AFT model, \tilde{n} has the value of zero at the inflow boundary. At no-slip walls, all variables corresponding to transition models have a zero normal derivative boundary condition.

Each of the turbulence models used in this study requires the specification of values for the dependent variables at the inlet. In the case of the $k - \omega$ SST model, inlet values for k and ω must be provided. The first is generally obtained from the turbulence intensity level Tu through the assumption of isotropic turbulence, leading to

$$k = \frac{3}{2} (TuV_\infty)^2. \quad (4.17)$$

On the other hand ω is generally not specified directly, but its value is instead computed from the eddy-viscosity ratio $\frac{\mu_t}{\mu}$ through

$$\omega = k \left(\frac{\mu_t}{\mu} \right)^{-1} \frac{1}{\mu}. \quad (4.18)$$

In the case of the KSKL model, the situation is the same: k is obtained from the intended turbulence intensity and $\sqrt{k}L$ is calculated from the desired value for $\frac{\mu_t}{\mu}$.

4.5 Decay of Turbulence Quantities

The phenomena of flow transition can be regarded as a boundary value problem in the sense that the location of transition will depend on the frequency and amplitude of the disturbances present in the flow. In the RANS context, this information is contained in the freestream turbulence level, and as such, most transition models are sensitive to these values. The freestream turbulence level depends on the values set for the variables of the turbulence model set at the inlet of the computational domain.

The consequences of the choice for the values at the inlet for the turbulence quantities are small for calculations where the turbulence models are not combined with a transition model. This is thoroughly addressed in Ref. [142], in which this choice and its corresponding effect are considered from a consistency point of view, where slight changes would be enough to affect the outcome of code verification exercises for example. However, this choice is much more meaningful in calculations with transition models, directly impacting the predicted location of transition. Also addressed in Ref. [142] and equally relevant is the effect of turbulence decay. On the freestream, where the flow can be considered as flowing uniformly along one direction, the variables of the turbulence model will decay at a rate which depends on the values themselves, a consequence solely of the turbulence model. In transition models such as the $\gamma - Re_\theta$ model, which rely on the freestream level of the turbulence intensity for the prediction of transition, the effect of turbulence decay becomes a critical factor.

The equations for the freestream decay of k and ω can be obtained from the transport equations of each turbulence model, and a equation for $\frac{\mu_t}{\mu}$ can be built from those for k and ω . The detailed process for each of the models is given in Appendix C. For the $k - \omega$ SST model, the decay equations are

$$k^* = \frac{k_{in}^*}{\left(1 + \beta(x^* - x_{in}^*) k_{in}^* \left(\frac{\mu}{\mu_t}\right)_{in} Re\right)^{\frac{\beta^*}{\beta}}}, \quad (4.19)$$

$$\omega^* = \frac{\omega_{in}^*}{1 + \beta(x^* - x_{in}^*) k_{in}^* \left(\frac{\mu}{\mu_t}\right)_{in} Re} \quad (4.20)$$

where $k^* = \frac{k}{U_\infty^2}$, $\omega^* = \frac{\omega L}{U_\infty}$ and $x^* = \frac{x}{L}$, with L being a length scale. The equation for the decay of the eddy-viscosity ratio is

$$\frac{\mu_t}{\mu} = \frac{\left(\frac{\mu_t}{\mu}\right)_{in}}{\left(1 + \beta(x^* - x_{in}^*) k_{in}^* \left(\frac{\mu}{\mu_t}\right)_{in} Re\right)^{\frac{\beta^*}{\beta} - 1}}. \quad (4.21)$$

These equations show that both k and ω undergo a steep decay while the eddy-viscosity decays at a much slower rate, due to the exponent $\frac{\beta^*}{\beta} - 1$. In addition, it is also concluded that the decay becomes more pronounced as the Reynolds number is increased, and that it can be reduced through the increase of the eddy-viscosity at the inlet. The issue is further amplified due to the large distances at which inflow boundaries are placed, whether to simulate infinite atmospheres or to prevent interactions

between the boundary and the interior flow field. These results stem directly from the calibration of the turbulence model, which relies on the decay of homogeneous isotropic turbulence to determine the ratio $\frac{\beta^*}{\beta}$ [141]. Therefore, these equations do not correspond to an accurate depiction of the decay of freestream turbulence for practical applications [142].

The decay of turbulence is the main reason why high values of the eddy-viscosity at the inlet are specified in flow calculations using transition models. It is not uncommon to see values for $\left(\frac{\mu}{\mu_t}\right)_{in}$ ranging from 100 to 1000, as a means to maintain a moderate turbulence level throughout the region between the inlet and the body being studied. Other alternatives consist in setting minimum values for k and ω in this region, or to solve the transport equations without dissipation terms up to a certain plane of the domain, which effectively transports the inlet values up until a desired location. The latter approach is used here, as for all test cases the incoming flow is aligned with the x axis. In this sense, the variable x_F is introduced. For cells located at $x < x_F$ the transport equations of the turbulence model are solved without dissipation terms.

Since the influence of the inlet turbulence quantities is directly evaluated in this work, and considering their crucial role in the prediction of transition, these boundary conditions are not given in this chapter. Furthermore, the same geometry may be used with different boundary conditions. For these reasons, instead of being presented in the description of the test cases, turbulence boundary conditions for each particular case are given in Chapters 5, 6 and 7.

4.6 Two-dimensional Test Cases

4.6.1 Flat plate

The flow over a flat plate is the most simple case considered herein. It is generally used for calibration of transition models, based on experimental data available from the ERCOFTAC database [34]. The domain is a rectangle with a length of $1.5L$ where L is the length of the plate which extends from $x = 0$ to $x = L$. The inlet and outlet boundaries are placed $0.25L$ away from the plate's leading and trailing edges, respectively. The height of the domain is $0.25L$. The plate is modelled as a zero-thickness surface and no effects of the leading edge curvature are considered, as these are not expected to have a significant impact on the location of transition. The Reynolds number based on the plate's length is $Re_L = 10^7$. An inflow boundary condition is used at the inlet, while an outflow boundary condition is set at the outlet. Symmetry boundary conditions are set on the bottom regions upstream and downstream of the plate. At the surface of the plate a no-slip wall boundary condition is imposed. Finally, a pressure boundary condition is used at the top boundary of the domain.

Two sets of five grids with different topologies are used. Both sets are generated using in-house grid generation tools [143, 144]. The first set consists of a Cartesian grid (H block) made of a single block, with cell clustering in the streamwise direction at the leading edge and the trailing edge. The grid topology is shown in Figure 4.1 and details on each grid are given in Table 4.1. The second set of grids has an O topology around the leading and trailing edge of the plate, while retaining the H type

grid on the plate. This approach avoids the highly stretched and high aspect ratio cells that propagate downstream of the plate in the H topology. As a consequence, this set of grids leads to much faster iterative convergence, in particular for the finest grids. An illustration of the grid for the entire domain is shown in Figure 4.2, with a close up of the leading edge displayed in Figure 4.3. Details on each grid of the set are given in Table 4.2. The y_{max}^+ values presented throughout the description of each test case correspond to those obtained for calculations with the $k - \omega$ SST + $\gamma - Re_\theta$ formulation. Although some differences occur when changing the transition model or the underlying turbulence model, these do not significantly impact the values presented.

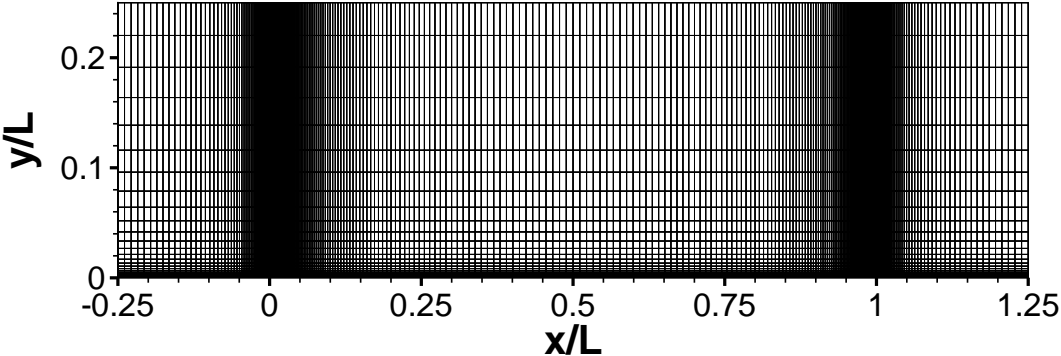


Figure 4.1: H grid topology for the flat plate test case.

Table 4.1: Details for the H grids for the flat plate test case.

Grid Designation	Grid 5	Grid 4	Grid 3	Grid 2	Grid 1
# of Surface faces	512	640	768	896	1024
# of Cells	73,728	115,200	165,888	225,792	294,912
y_{max}^+	0.54	0.44	0.38	0.34	0.30
h_i/h_1	2.0	1.6	1.33	1.14	1.0

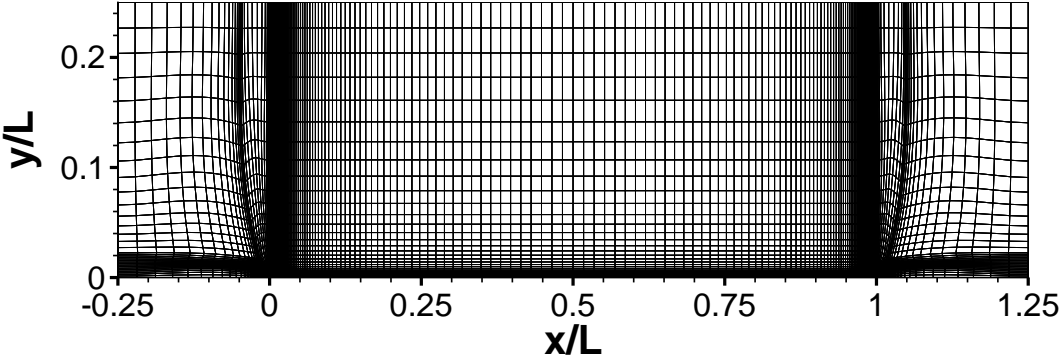


Figure 4.2: OH grid topology for the flat plate test case.

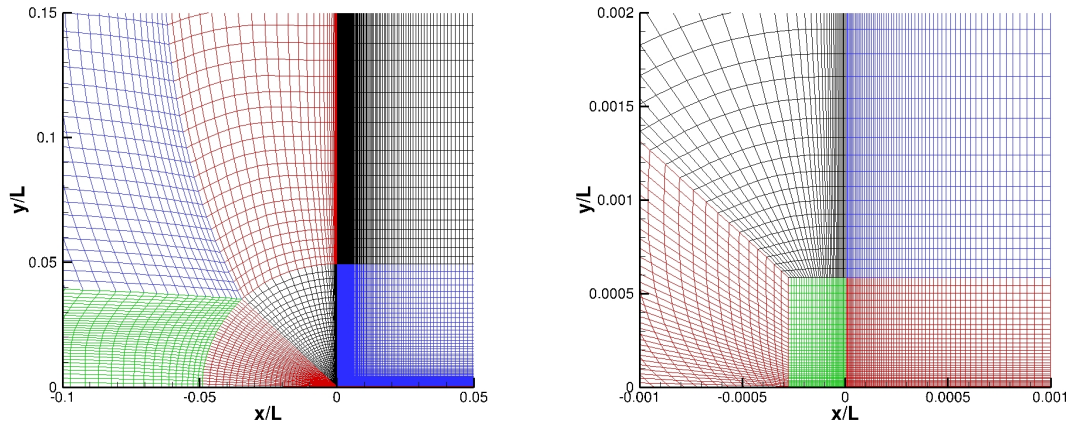


Figure 4.3: Close-up of the leading edge in the OH grid topology.

Table 4.2: Details for the OH grids for the flat plate test case.

Grid Designation	Grid 5	Grid 4	Grid 3	Grid 2	Grid 1
# of Surface faces	512	640	768	896	1024
# of Cells	81,920	128,000	184,320	250,880	327,680
y_{max}^+	0.52	0.44	0.38	0.33	0.30
h_i/h_1	2.0	1.6	1.33	1.14	1.0

4.6.2 NACA 0012

Although it is not widely considered as a transition test case, the NACA 0012 airfoil is used in this study at a Reynolds number of 2.88×10^6 . The grid topology used for all airfoil test cases is the same, hence it is only described once for the NACA 0012 airfoil. It consists of a multiblock structured grid with 23 blocks. The first five blocks are adjacent to the airfoil and form a C-topology that extends slightly downstream of the trailing edge as depicted in Figure 4.4. Blocks 6 through 12 wrap around the C-shape effectively giving rise to an O-block topology. This is shown in Figure 4.5. The remaining blocks conform the internal topology to the domain boundaries as shown in Figure 4.6. The angle of attack α is imposed by rotating the inner blocks (1 to 5) of the grid. This keeps the incoming flow aligned with the x -axis. The shape of the airfoil is obtained from the NACA 4-digit family definition [145].

The combination of the C and O topologies has significant benefits. When compared to a simple C-type grid, it prevents the propagation to the wake of the thin cells required to properly capture the boundary-layer. This results in cells with a very large aspect ratio, since some expansion in the stream-wise direction is often employed, which strongly penalizes iterative convergence. On the other hand, the use of a O-topology can cause misalignment (cell skewness) between the cell center vector and the cell face shared by cells that are on opposite sides of the grid line that starts from the trailing edge. One possible alternative to deal with this problem in grids with an O topology would to use a rounded trailing edge instead of a sharp one. As shown in Figure 4.7, this is avoided in the present approach that combines the two topologies, resulting in a grid with higher quality.

The grid refinement level present in the figures used to illustrate the grid topology is much lower than

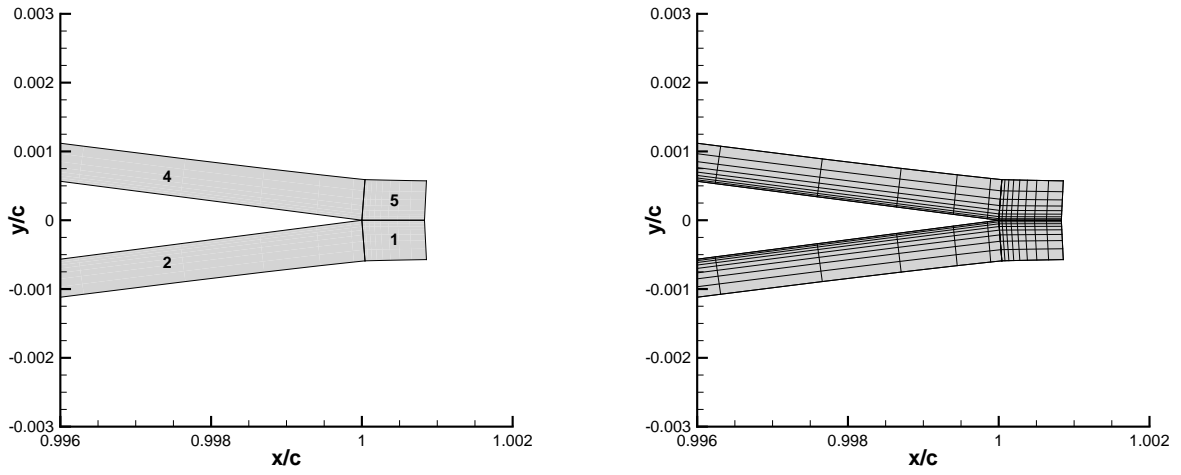


Figure 4.4: Depiction of the inner blocks and grid topology at the trailing edge of the NACA 0012 airfoil.

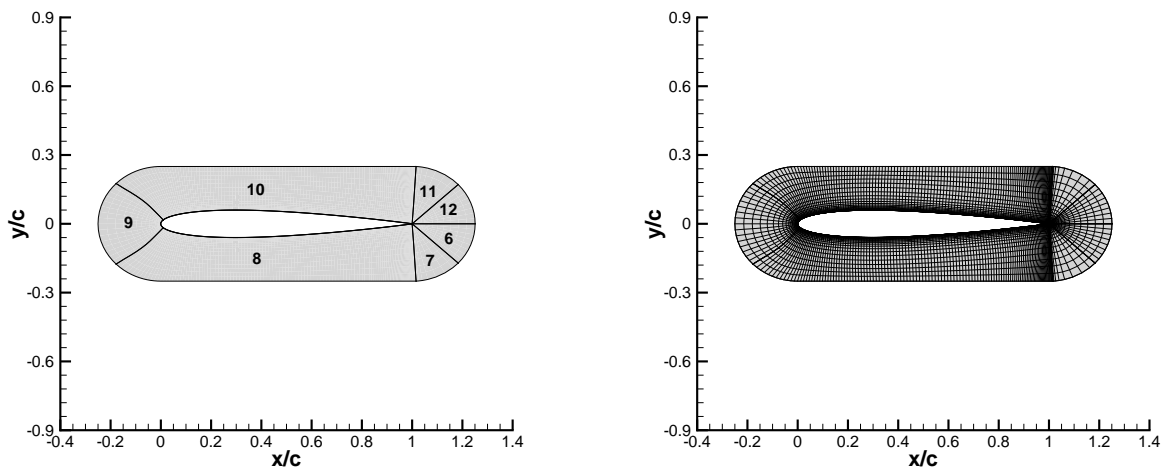


Figure 4.5: Depiction of the blocks and grid topology around the NACA 0012 airfoil.

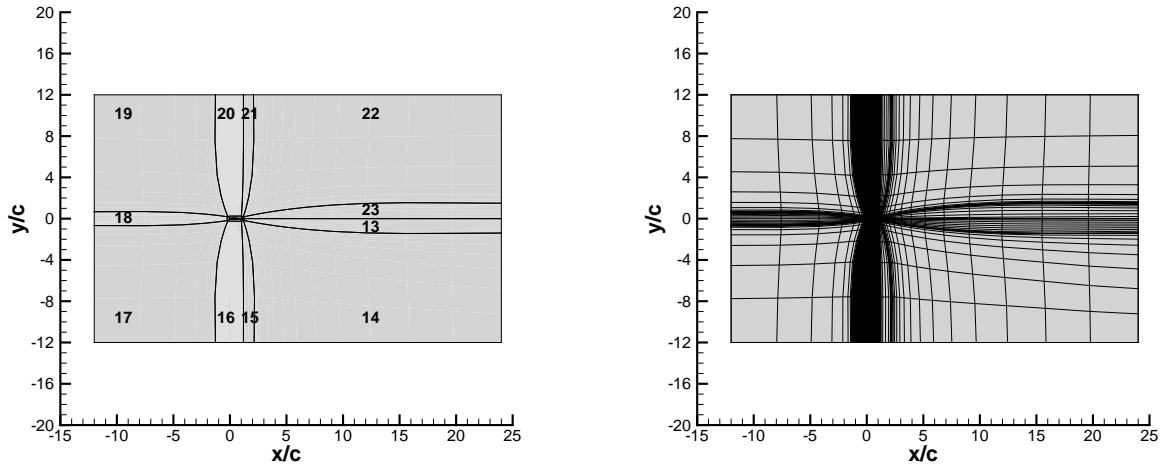


Figure 4.6: Outer blocks and grid topology for the computational domain of the NACA 0012 airfoil test case.

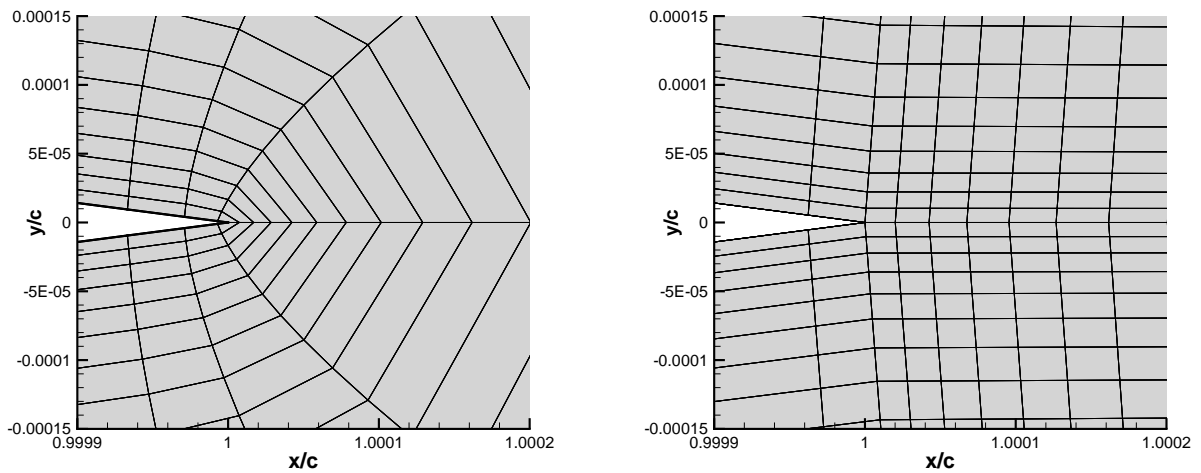


Figure 4.7: Comparison of the grid at the trailing edge for the O topology (left) and the OH topology (right).

that used for the calculations, but it allows for a better display of the grid structure. To further describe the grid, Table 4.3 presents the number of cells in the normal n_n and tangential n_t directions for each block, for a base grid with 256 cells on the airfoil surface. For the outer blocks (13 to 23), n_n represents the number of cells in the y direction, and n_t represents the number of cells in the x direction. As for the flat-plate, the grid of the NACA 0012 and all other airfoils was generated using an in-house grid generation tool [144].

Table 4.3: Reference number of cells for each block for a base grid with 256 cells on the surface of the airfoil.

Blocks	n_t	n_n
1, 5, 15, 17, 19, 21	8	8
2, 4, 16, 20	120	8
3, 13, 14, 18, 22, 23	16	8
6, 7, 11, 12	8	24
8, 10	120	24
9	16	24

For $\alpha = 0^\circ$, the airfoil's leading edge is placed at $x/c = 0$ and the trailing edge is located at $x/c = 1$. The computational domain extends $12c$ upstream of the leading edge, where an inflow boundary condition is used, and $23c$ downstream of the trailing edge where the pressure boundary condition is imposed. A slip wall boundary condition is used at the top and bottom boundaries which are placed at $y = \pm 12c$. The surface of the airfoil is modelled using a no-slip wall boundary condition. As with the previous case, no wall functions are used. Several angles of attack ranging from $\alpha = 0^\circ$ to $\alpha = 6^\circ$ are tested.

A set of 9 nearly geometrically similar grids has been generated for this airfoil. Table 4.4 details the designation of each grid, which are identified by the number of faces on the surface of the airfoil. Also shown is the total number of cells in the computational domain for each grid, as well as the grid refinement ratio between each grid and the finest grid of the set, h_i/h_1 .

Table 4.4: Details of the grid set for the NACA 0012 airfoil.

Grid Designation	Grid 512	Grid 640	Grid 768	Grid 896	Grid 1024
# of Surface faces	512	640	768	896	1024
# of Cells	47,616	74,400	107,136	145,824	190,464
y_{max}^+	0.75	0.59	0.49	0.42	0.36
h_i/h_1	4.0	3.2	2.67	2.29	2.0
Grid Designation	Grid 1280	Grid 1536	Grid 1792	Grid 2048	
# of Surface faces	1280	1536	1792	2048	
# of Cells	297,600	428,544	583,296	761,856	
y_{max}^+	0.29	0.24	0.21	0.18	
h_i/h_1	1.6	1.33	1.14	1.0	

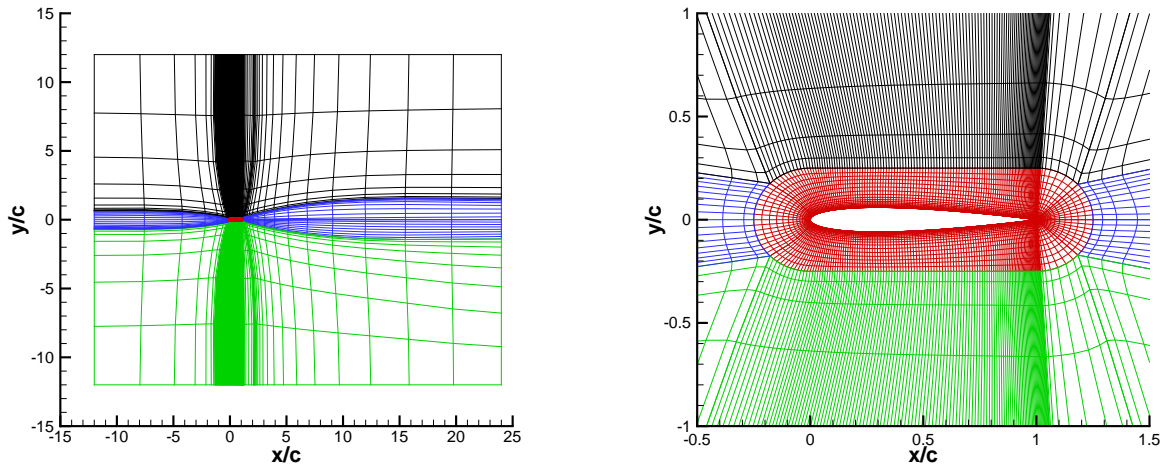


Figure 4.8: Illustration of the computational domain size (left) and grid topology around the NACA 0012 airfoil (right).

4.6.3 NACA 0015

Although it also belongs to the 4-digit NACA family, the NACA 0015 airfoil test case is considerably different from that of the NACA 0012 due to the lower Reynolds number of this test case $Re_L = 1.5 \times 10^5$. This, along with the increased thickness of the airfoil and the higher angles of attack tested of $\alpha = 5^\circ$ and $\alpha = 10^\circ$, causes the dominant transition mechanism in the upper surface to be separation-induced transition. Experimental data in the form of the skin-friction distribution is available for this airfoil [146]. As with the NACA 0012, the shape is defined according to the equation for the NACA 4-digit family.

The computational domain is also different, as it is selected to match the tunnel size for which data was measured [146]. As such, the inlet is placed $7.2c$ away from the leading edge and the outlet is located $14.5c$ away from the leading edge of the airfoil. The top and bottom boundaries, treated with a slipwall boundary condition, are placed at $y = \pm 2.5c$. A depiction of the domain size and grid are given in Figure 4.9. While the grid topology follows that described for the NACA 0012 airfoil, the level of grid refinement is different. Details of the grid set for this case are given in Table 4.5. Furthermore, due to the significant extent of flow separation that occurs for this flow, calculations for geometry were performed using a first order upwind scheme for the convection term of the transport equations corresponding to the turbulence model.

Table 4.5: Details of the grid set for the NACA 0015 airfoil.

Grid Designation	Grid 1024	Grid 1280	Grid 1536	Grid 1792	Grid 2048
# of Surface faces	1024	1280	1536	1792	2048
# of Cells	391,168	611,200	880,128	1,194,592	1,564,672
y_{max}^+	0.14	0.11	0.09	0.08	0.07
h_i/h_1	2.0	1.6	1.33	1.14	1.0

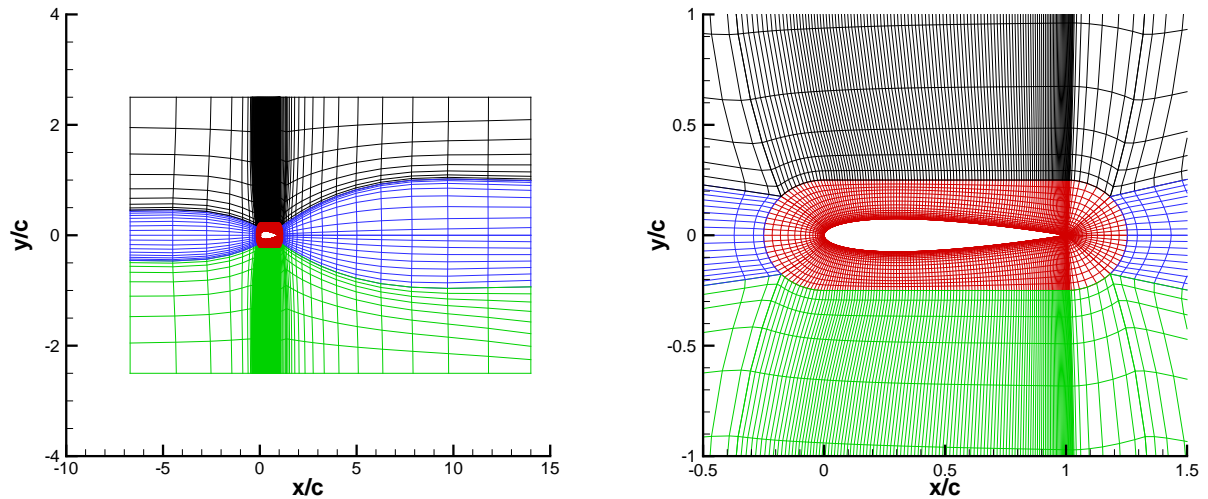


Figure 4.9: Illustration of the computational domain size (left) and grid topology around the NACA 0015 airfoil (right).

4.6.4 NLF₁-0416

The NLF(1)-0416 is a natural-laminar-flow airfoil, designed to keep the flow laminar for a large extent of the airfoil without resorting to flow control techniques such as boundary-layer suction. The ultimate goal in the design of this airfoil was to obtain lower drag coefficients for general aviation applications. Experimental data from the Langley Low-Turbulence Pressure Tunnel at Reynolds numbers in the range of 10^6 and several angles of attack is available in Ref. [147], although here the only Reynolds number considered is 4×10^6 . Under these conditions, the flow in the upper surface undergoes natural transition for most angles of attack, whereas the mechanism responsible for transition in the lower surface is a small separation bubble. The shape of the airfoil is obtained from fitting cubic splines to the airfoil coordinates given in [147]. Domain size and boundary conditions follow those described for the NACA 0012 airfoil. The same is valid for the grid topology, which is displayed in Figure 4.10. Grid properties match those presented previously in Table 4.4.

This geometry has been used as a common test case for transitional flow simulations, due to the significant extent of laminar flow on both surfaces. It was used as one of the two-dimensional test cases in the CFD Transition Modeling and Predictive Capabilities session at the AIAA SciTech 2018 conference [9] and in the development of coupling between the $\gamma - Re_\theta$ model and the SSG/LRR Reynolds Stress model [32].

4.6.5 Eppler 387

The Eppler 387 airfoil operates mainly at Reynolds numbers of the order of 10^5 , as its main field of applications is sailplanes. Thus, it also serves as a good test case for transition, as experimental data concerning pressure coefficient distributions from different facilities [148, 149] is available. Additional data in the form of force coefficients is also available from [35, 150, 151]. The airfoil coordinates available in [149] are used for the definition of the airfoil's shape.

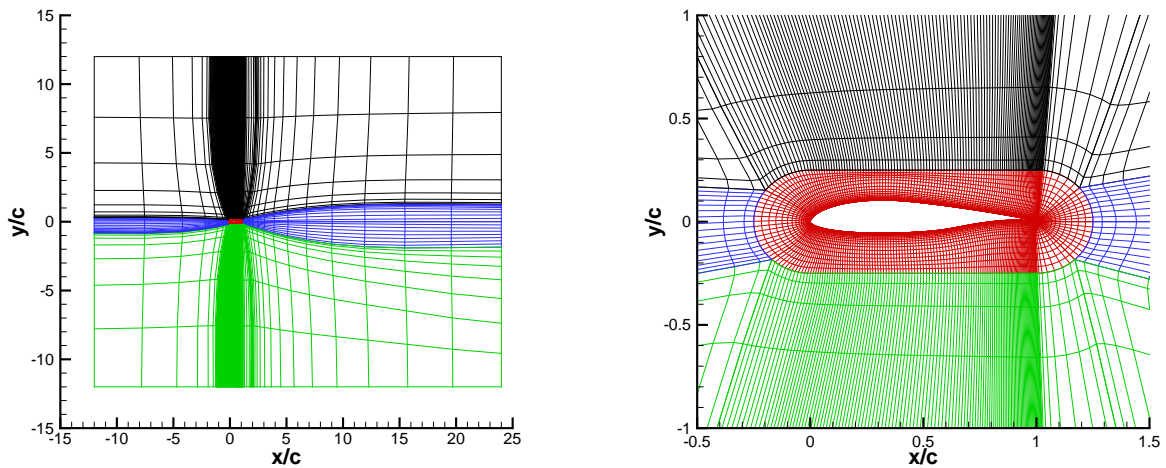


Figure 4.10: Illustration of the computational domain size (left) and grid topology around the NLF₁-0416 airfoil (right).

The Reynolds number considered is 3×10^5 . Under these conditions conditions, the flow in the lower surface is laminar for most angles of attack, while a laminar separation bubble encompassing around 20% of the chord is present in the upper surface. Transition takes place in the shear layer and the flow reattaches back to the surface of the airfoil. Experimental data shows that the separated region is no longer present at the highest angle of attack.

The domain size is the same as that used for the NACA 0012 airfoil, while the grid refinement level matches that of the grid set described for the NACA 0015. An example of the grid and airfoil geometry is given in Figure 4.11.

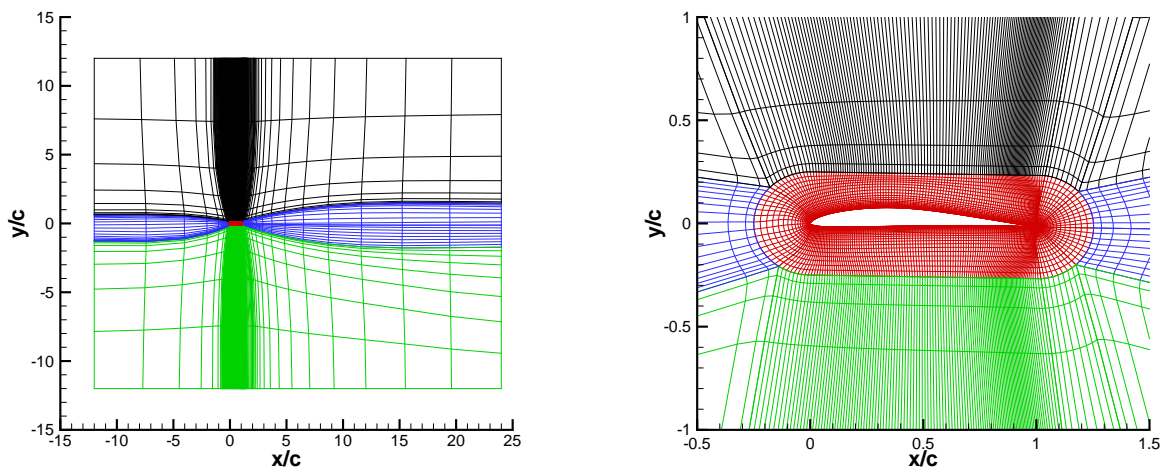


Figure 4.11: Illustration of the computational domain size (left) and grid topology around the Eppler 387 airfoil (right).

4.6.6 S809

The S809 airfoil is a laminar flow airfoil, designed for application in horizontal-axis wind turbines. It was tested in the low-turbulence wind tunnel at Delft University of Technology [152] in the Netherlands. As with the Eppler 387 and NLF₁-0416 airfoils, the shape of the airfoil is determined by fitting cubic splines to the airfoil coordinates available in [152]. Experimental data in the form of pressure coefficient distributions, transition location in the upper and lower surfaces and force coefficients is available for a wide range of angles of attack at a Reynolds number of 2×10^6 . For most angles of attack, transition is triggered by flow separation on both surfaces of the airfoil. As the angle of attack increases past 6° , the mechanism for transition in the upper surface becomes natural transition. A depiction of the grid topology is given in Figure 4.12, and the details of the grid set match those of the NACA 0012 airfoil. Similarly to the NACA 0015 airfoil, the convection term of the transport equations of the turbulence model was discretized using a first-order upwind scheme.

The S809 airfoil has been consistently used as a benchmark case for flow transition in CFD. It has been used by Langtry and Menter [23] in the validation of the $\gamma - Re_\theta$ model and by Walters and Cokljat [24] in the validation of the $k_T - k_L - \omega$ model. It is one of the cases used by Medida and Baeder [115] to validate the coupling of the Spalart-Allmaras model to the $\gamma - Re_\theta$ model, and was also used in the CFD Transition Modeling and Predictive Capabilities session at the AIAA SciTech 2018 conference [9].

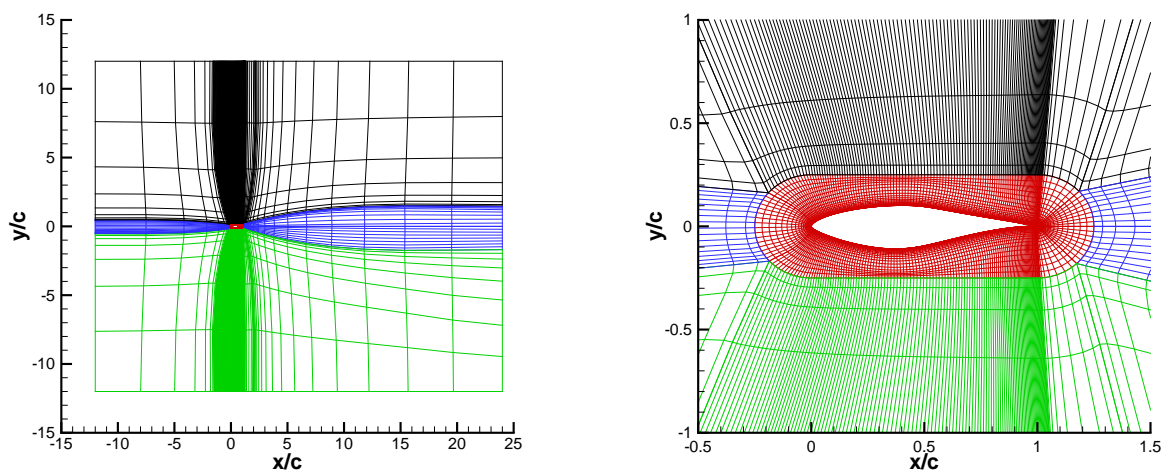


Figure 4.12: Illustration of the computational domain size (left) and grid topology around the S809 airfoil (right).

4.7 Three-dimensional Test Cases

4.7.1 6:1 prolate spheroid

The 6:1 prolate spheroid is considered as an idealised submarine shape, making it representative of such cases and explaining the interest in this particular geometry. For this reason, prolate spheroids

have been the subject of considerable experimental work [153–156]. In particular, the data available from [154] regarding the skin-friction coefficient in the surface of the spheroid is used in this work. The surface of the spheroid is described by

$$x^2 + 36y^2 + 36z^2 = \frac{1}{4}. \quad (4.22)$$

The Reynolds number based on the spheroid's length L is $Re_L = 6.5 \times 10^6$, and three different incidence angles are tested: 5° , 10° , 15° . While natural transition is the dominant mechanism at the lower incidence angle, at $\alpha = 15^\circ$ there is a significant crossflow component that is responsible for transition. The computational domain is a box with length and height $200L$ and $100L$ width, where all boundaries are approximately $100L$ away from the spheroid except the boundary at the symmetry plane of the spheroid. A slip wall boundary condition is employed at the bottom, top and side boundaries, and a pressure boundary condition is imposed at the outlet. Similarly to the airfoil cases, the incidence angle is imposed by rotating the spheroid. Therefore, the incoming flow is always aligned with the x -axis. Flow conditions and domain size settings follow those described in Ref. [9]. The grid on the symmetry plane is depicted in Figures 4.13 and 4.14, while the grid on the surface of the spheroid is shown in Figure 4.15. For this case, the convection term of the momentum transport equations was discretized using a second order upwind scheme (QUICK) without flux limiters.

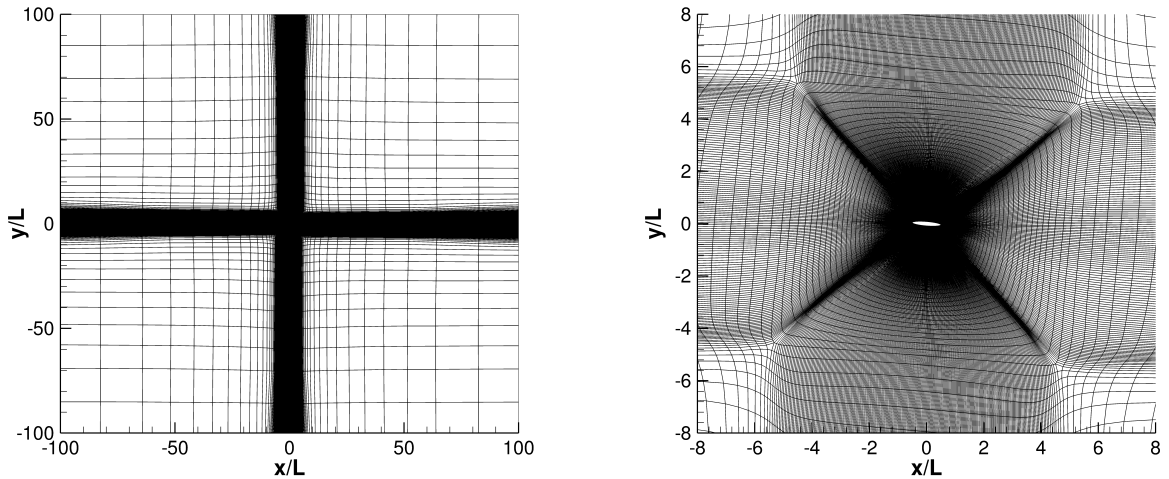


Figure 4.13: Grid on the symmetry plane for the coarsest grid of the prolate spheroid test case at $\alpha = 5^\circ$: full computational domain (left) and block encompassing the spheroid (right).

The grids for this test case have been generated with the GridPro package [157]. The grid is a multi-block structured grid, with an O-topology encircling the spheroid, and then conforming to the rectangular domain. Table 4.6 presents details on the five grids generated in terms of the total number of cells (# Cells) and the number of surface faces on the spheroid (# Surface faces). The value of y_{max}^+ obtained for calculations with the $\gamma - Re_\theta$ model is presented as well, showing all five grids to be well below 1.0. The grid refinement ratio between each grid and the finest grid (h_i/h_1) is also shown. It is estimated

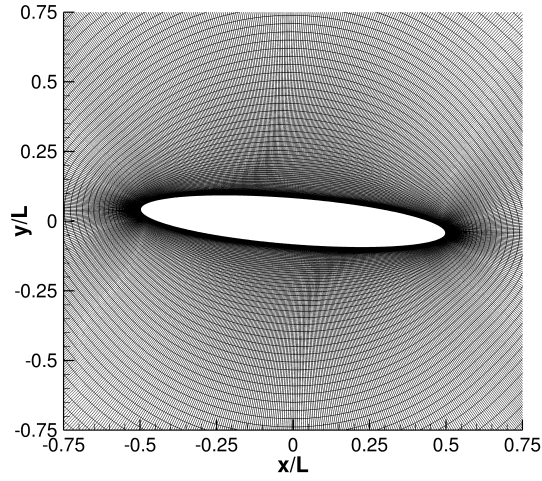


Figure 4.14: Grid on the symmetry plane for the coarsest grid of the prolate spheroid test case at $\alpha = 5^\circ$ around the spheroid.

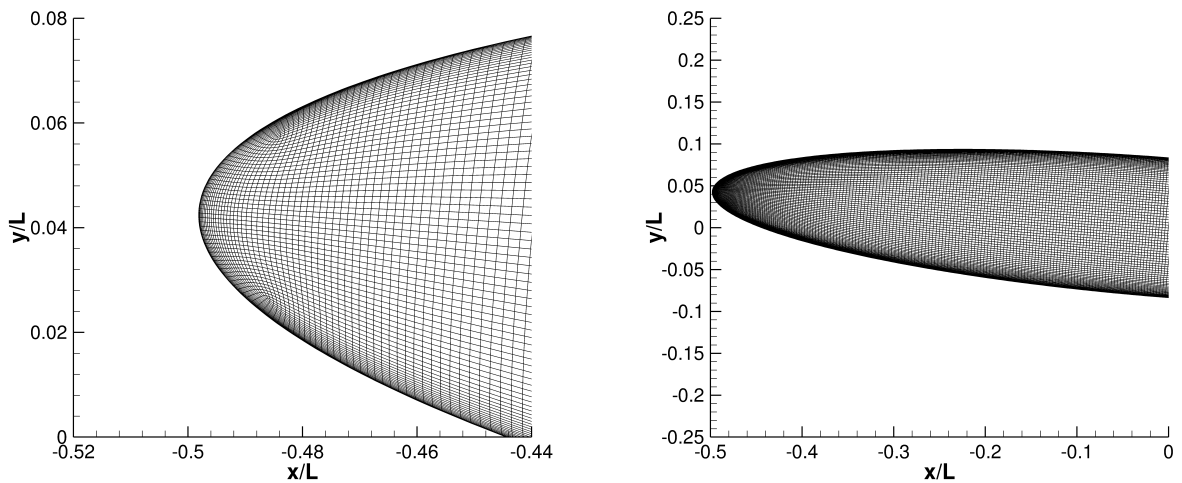


Figure 4.15: Coarsest grid on the surface of the prolate spheroid at $\alpha = 5^\circ$: leading edge (left) half length of the spheroid (right).

from

$$\frac{h_i}{h_1} = \left(\frac{N_1}{N_i} \right)^{1/3}, \quad (4.23)$$

where N_i is the total number of cells of grid i .

Table 4.6: Details of the grid set used for the prolate spheroid test case.

Grid Designation	Grid 5	Grid 4	Grid 3	Grid 2	Grid 1
# Cells	5.3M	10.3M	17.9M	28.3M	42.6M
# Surface faces	31,504	48,750	70,884	95,816	126,016
y_{max}^+	0.71	0.57	0.47	0.40	0.35
h_i/h_1	2.0	1.61	1.33	1.14	1.0

4.7.2 SD7003 wing

The SD7003 wing has been extensively studied both numerically [158–160] and experimentally [161] due to the long laminar separation bubble that develops over the upper surface of the wing. The Reynolds number for this test case is $Re_L = 6 \times 10^4$. This makes this case a prime candidate to assess the performance of each transition models at the lower end of the Reynolds number range of their applications. However, this low Reynolds number creates challenges due to excessive flow separation that is incompatible with the statistically steady flow assumption that is used for all the previous cases.

The domain size for this test case is selected to match the wind tunnel experiment detailed in [161]. As such, the inlet is located at $x/c = -2.5$ and the outlet at $x/c = 5$. The top and bottom boundaries are located at $y/c = \pm 1$. The two side boundaries are placed at $z/c = 0$ and $z/c = 2.8$. As for the airfoils used in the 2D test cases, the leading edge of the wing is placed at $x/c = 0$. For this flow, a first order upwind scheme was used in the discretization of the transport equations of the turbulence model.

For this test case two different three-dimensional grids are considered. The first grid has equidistant spacing in the spanwise direction, while the second has cell clustering in one direction. For the latter grid, the corresponding boundary at which the clustering is located is treated as a no-slip wall boundary condition, in order to mimic the influence of the tunnel wall. For the grid with equidistant spacing, a slip wall boundary condition is used at the side wall instead. A grid set of two-dimensional grids is also used, in order to assess the difference between the two-dimensional computation and the three-dimensional simulation using a slip wall boundary condition on the side walls. The two-dimensional grid has an O-topology around the trailing edge of the airfoil, and it corresponds to a section of constant span of the three-dimensional grid. A depiction of the 3D grid with cell clustering at the side wall is shown in Figure 4.16 and details on each grid are given in Table 4.7.

4.7.3 Sickle wing

This geometry was designed by Petzold and Radespiel [162] specifically as a test case for assessing and validating transition prediction methods. The wing has a section with no sweep angle at the root,

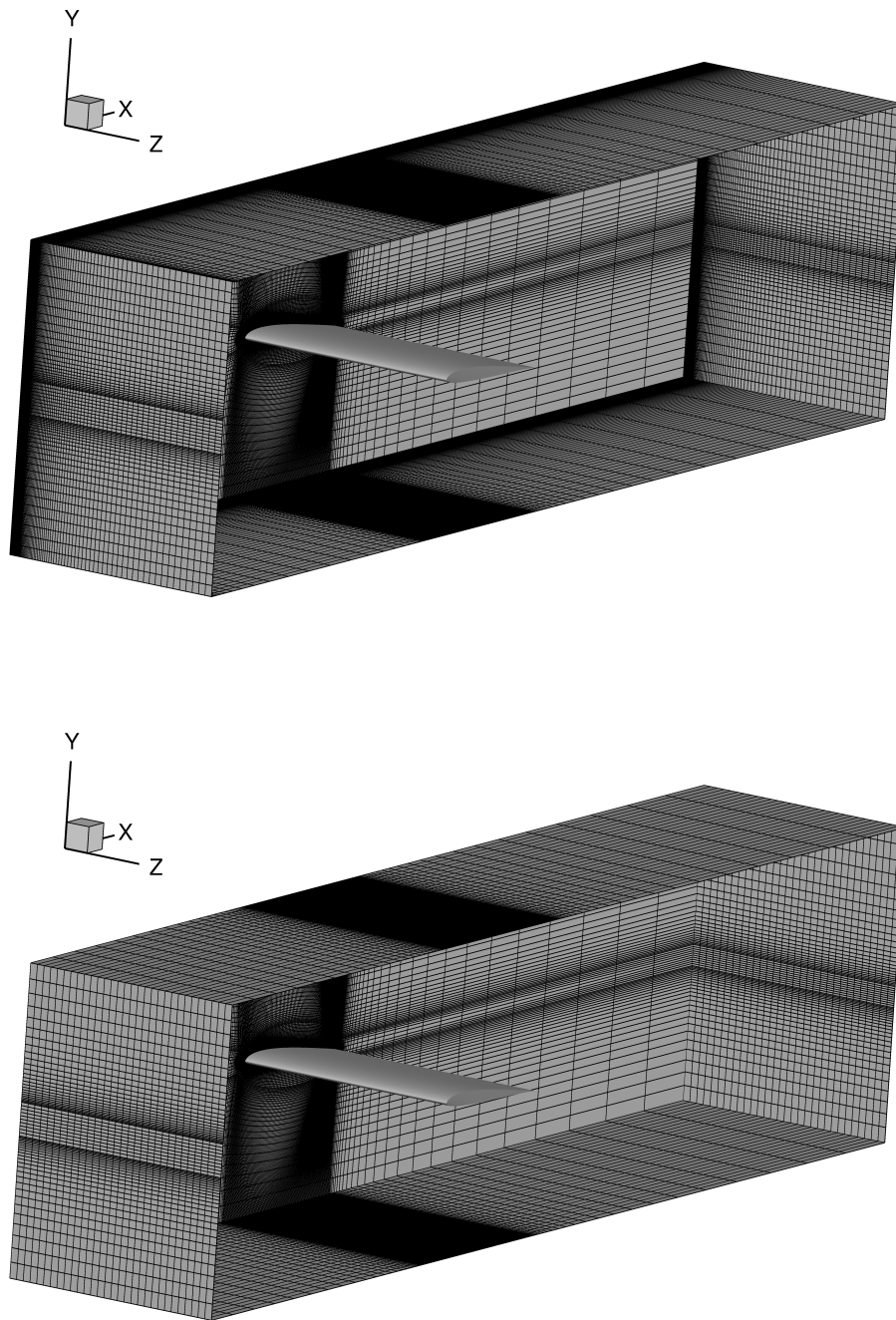


Figure 4.16: 3D grid used for the SD7003 wing with cell clustering at the root of the wing (top) and with equidistant spanwise spacing (bottom).

Table 4.7: Details of the grid set used for the SD7003 wing test case.

Grid Designation	Grid 301 (3D - no slip sidewall)	Grid 301 (3D - slip sidewall)	Grid 601 (2D)
# Cells	3.0M	0.75M	100,000
# Surface faces	36,000	9000	601
y_{max}^+	0.61	0.36	0.16

in order to reduce the influence of the boundary-layer developing on the tunnel wall, and then sections with sweep angles of 30° , 45° and 55° . This geometry causes stronger crossflow as the wing's tip is approached, providing an excellent case to assess the modelling of crossflow transition. Experimental data [163, 164] in the form of the transition line and pressure coefficient are used for this case. An illustration of the wing shape is given in Figure 4.17.

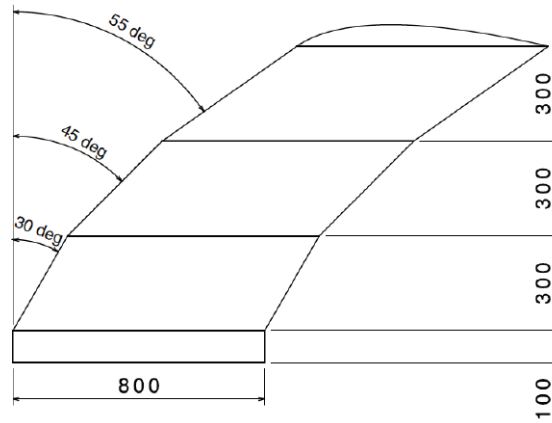


Figure 4.17: Geometry of the sickle wing. Taken from Ref. [9].

There are several different conditions [9] that explore the effect of Reynolds number, Mach number and angle of attack. Only one of them is considered herein, at an angle of attack of $\alpha = -2.6^\circ$ and a Reynolds number of $Re_c = 4.45 \times 10^6$. In this case, a QUICK scheme without flux limiters was used for the convection term of the momentum transport equations, while the discretization of the same term but for the variables of the turbulence model was done with a first order upwind scheme. At the root of the wing, the leading edge is located at $x/c = 0$. As with previous cases, the incoming flow is aligned with the x -axis. In an attempt to reproduce the dimensions of the wind tunnel, the inlet is located at $x/c = -4.6$, the outlet is placed at $x/c = 8.455$, treated using a pressure boundary condition. The top and bottom boundaries are located at $z/c = \pm 1.633$, and the tunnel side wall is located at $y/c = 2.8$. All tunnel wall boundaries are treated with a slip wall boundary condition.

Two different sets of grids are used for this case. The first set was built using the Hexpress grid generation package [165], resulting in an hexahedral unstructured grid. A depiction of the coarsest grid is shown in Figure 4.18 and details of the grid set are given in Table 4.8. The second grid set was generated using the GridPro package [157]. The coarsest grid is illustrated in Figure 4.19 and the grid set is detailed in Table 4.9. For both grid sets, the calculation of h_i/h_1 is done by considering the number of volume cells, according to Eq. 4.23. The unstructured grid set is easier to generate, but has a lower grid quality than the multi-block structured grid due to the presence of hanging nodes and cell misalignment.

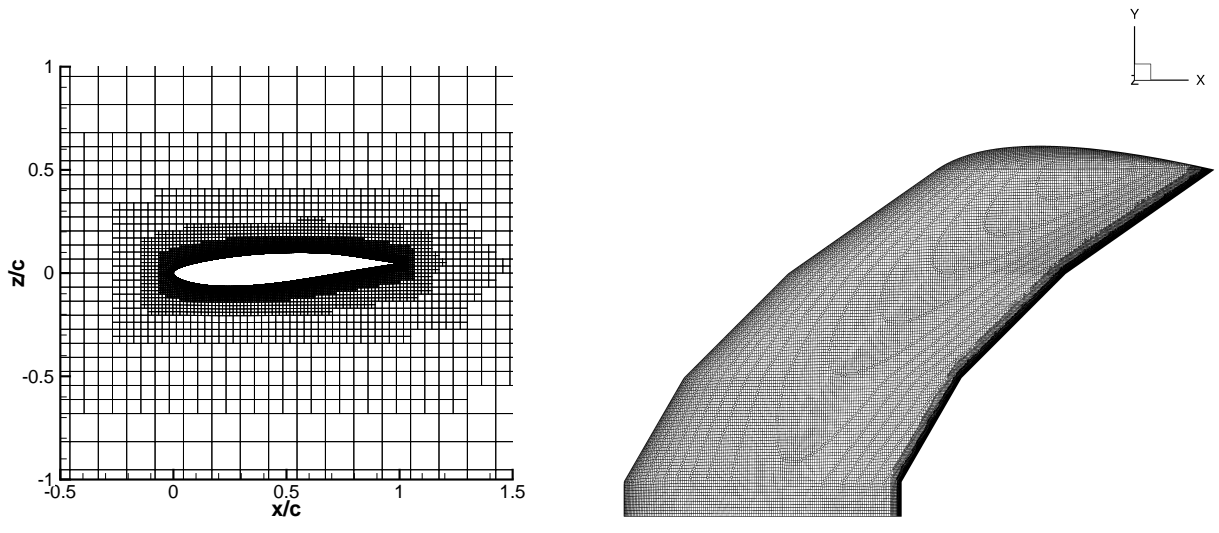


Figure 4.18: Grid topology at the root (left) and on the surface (right) of the sickle wing, generated with the Hexpress software.

Table 4.8: Details of the grid set generated with the Hexpress grid generation software for the Sickle Wing geometry.

Grid Designation	Grid 5	Grid 4	Grid 3	Grid 2	Grid 1
# Cells	9,920,004	18,083,265	29,247,107	44,663,536	64,031,708
# Surface faces	217,984	324,547	452,070	599,703	767,544
y_{max}^+	0.96	0.77	0.55	0.45	0.39
h_i/h_1	1.86	1.52	1.30	1.13	1.0

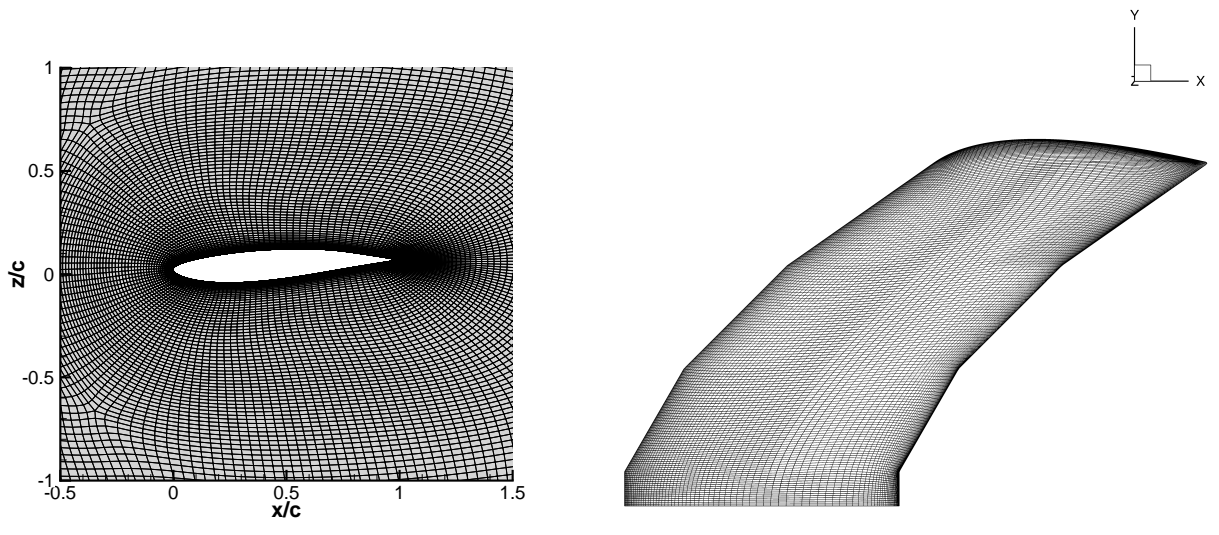


Figure 4.19: Grid topology at the root (left) and on the surface (right) of the sickle wing, generated with the GridPro software.

Table 4.9: Details of the grid set generated with the GridPro grid generation software for the Sickle Wing geometry.

Grid Designation	Grid 5	Grid 4	Grid 3	Grid 2	Grid 1
# Cells	2,870,784	5,601,600	9,657,468	13,219,600	22,742,784
# Surface faces	27,936	43,650	62,856	77,600	111,744
h_i/h_1	1.99	1.59	1.33	1.20	1.0

4.8 Features and Quantities of Interest

Several distinct aspects of the calculations are addressed in this thesis, which can be mainly divided in three groups. The first concerns numerical aspects, which are relevant in order to reduce the numerical error of the simulations but do not affect the exact solution of the model. The second category is that of modelling aspects, in which features that directly impact the final solution of the model and a final comparison with experimental data are performed. The final group is the comparison with experimental data. In many cases, calculations using only the underlying turbulence model without any transition model are performed as well for comparison of trends observed with and without transition modelling.

4.8.1 Numerical aspects

The numerical robustness of the models is the first numerical aspect to be addressed. The formulation of transition models is heavily coupled with the turbulence quantities or the momentum quantities themselves. Thus it is natural to expect that the complete turbulence and transition model formulation is not as robust as the formulation which only consists of the turbulence model. Additional difficulties may arise when laminar flow separation takes place, which would be very unlikely to occur in a calculation without any sort of transition modelling. Strategies to improve the formulation of the transition models are also presented and assessed.

The second numerical aspect concerns the discretization of the convection terms of the turbulence and transition transport equations. This is mainly irrelevant for flows at high Reynolds numbers i.e., when transition models are not used. The typical choice under these conditions is a first order upwind scheme for the turbulence model, motivated by the higher numerical stability. In the context of transition modelling, there are two factors that highlight why the discretization of the convection scheme is much more relevant. The first consists on the decay of turbulence, which directly affects the predicted location of transition, and leads to high gradients of the turbulence variables at the inlet, where grids are typically coarse. The second factor is the strong coupling between the turbulence and transition models.

The third numerical feature considered is the effect of y_{max}^+ . The general criteria observed for numerical calculations without transition models is $y_{max}^+ < 1$. This choice has been shown to depend on the turbulence model used [31, 36]. A similar trends has been observed when transition models are included in the simulations as well [37]. Calculations are performed considering different underlying turbulence models and also for grid sets with different near-wall cell sizes. This serves to establish the effect of y_{max}^+ for each underlying turbulence model, and also provides some insight on the importance of this effect when compared to general grid refinement.

4.8.2 Modelling aspects and comparison with experimental data

One of the features investigated from the modelling point of view is the influence of the turbulence production limiter. This limiter, which aims at avoiding excess turbulence production in stagnation regions, influences the turbulence level at the edge of the boundary layer, which plays a central role in the

prediction of transition. While it is not given much importance when a transition model is not used, this choice can lead to discrepancies in the results due to the limiter used. In turn, this impacts not only code verification exercises using reference solutions, but also validation and comparison with experimental data as well.

The second modelling issue addressed concerns the influence of the turbulence boundary conditions and turbulence decay in the freestream. As previously stated, the level of turbulence in the freestream is crucial in the prediction of transition. The effect of slight variations of the inlet boundary conditions are studied for both natural and separation-induced transition. Also performed are comparison studies in which a reference turbulence level at a given location are matched, but the decay is different. A technique to control the decay without resorting to the eddy-viscosity is also considered.

The final part of the results consists of an overall comparison with experimental data. Despite the more difficult setup of transition flow calculations, a consequence of its higher sensitivity to aspects that have a low impact at high Reynolds numbers, the careful use of transition models can lead to better predictions when compared to calculations without any sort of transition modelling capability.

4.8.3 Test case overview

Not every single test case is used to address all intended numerical and modelling aspects mentioned previously. So as to provide a clear map on what test cases are used to evaluate specific effects, this is shown in Tables 4.10 and 4.11 for the numerical and modelling features respectively. In regards to the comparison with experimental data, all geometries with the exception of the flat plate and the NACA 0012 are addressed.

Table 4.10: Test case selection to study the numerical features.

	Iterative convergence	Convective discretization scheme	Effect of y^+
Flat Plate	✓		✓
NACA 0012	✓	✓	
NACA 0015			
Eppler 387			
NLF1-0416	✓	✓	✓
S809			
SD 7003			
6:1 Prolate Spheroid	✓	✓	
Sickle Wing			

4.8.4 Quantities of interest

Several distinct quantities of interest are used to evaluate the previously discussed features on transitional flow simulations. These are selected based on their adequacy for transitional flows, as well as on the availability of experimental data for each test case.

Table 4.11: Test case selection to study the modelling features.

	Turbulence production limiter	Inlet turbulence quantities
Flat Plate	✓	✓
NACA 0012	✓	✓
NACA 0015		
Eppler 387		
NLF1-0416		
S809		
SD 7003		
6:1 Prolate Spheroid		✓
Sickle Wing		

The first quantity is the pressure coefficient distribution C_p , defined as

$$C_p = \frac{p - p_\infty}{\frac{1}{2}\rho V_\infty^2}. \quad (4.24)$$

The C_p distribution can be indicative of the transition region, particularly when separation-induced transition takes place. Experimental data for it is also available for the majority of the test cases.

More difficult to obtain experimentally, but much more helpful in the analysis of flow transition is the skin-friction coefficient C_f

$$C_f = \frac{\tau_w}{\frac{1}{2}\rho V_\infty^2}, \quad (4.25)$$

where τ_w is the shear stress at the wall, directly obtained through the no-slip condition

$$\tau_w = \mu \left(\frac{\partial U_t}{\partial x_n} \right)_w, \quad (4.26)$$

where U_t is the tangential velocity, x_n is the wall normal direction, and the subscript w indicates that the derivative is evaluated at the wall. From the C_f distribution, the start and end of both the transition region and separated flow region, if flow separation occurs, can be easily found for two-dimensional flows. The separated flow region is marked by the region where C_f has a negative value, with the separation and reattachment points being identified by the locations at which $C_f = 0$. In the case of the transition region, identified by the sharp increase of the skin-friction coefficient, the start of transition is considered as the minimum of C_f and the end of transition by the maximum of C_f .

Also used are the lift and drag coefficients, expressed as C_l and C_d for the two-dimensional cases, and as C_L and C_D for the three-dimensional flows. They are obtained from

$$C_l = \frac{l}{\frac{1}{2}\rho V_\infty^2 c}, \quad C_L = \frac{L}{\frac{1}{2}\rho V_\infty^2 S_{ref}}, \quad (4.27)$$

$$C_d = \frac{d}{\frac{1}{2}\rho V_\infty^2 c}, \quad C_D = \frac{D}{\frac{1}{2}\rho V_\infty^2 S_{ref}}. \quad (4.28)$$

where S_{ref} is the reference area, l and d are the lift and drag forces per unit span obtained in the two-dimensional calculations, and L and D are the lift and drag forces. The drag coefficient is also considered in the individual pressure and friction contributions, identified as $C_{d,p}$ and $C_{d,f}$ respectively.

For the lift coefficient, the friction component is generally negligible when compared to the friction one. For this reason, only the total lift coefficient is considered.

Chapter 5

Results Part I: Numerical Aspects

5.1 Introduction

This chapter is focused on the analysis of three numerical aspects pertaining to transitional flow calculations. These affect the numerical accuracy of the calculations, but have no impact on the exact solution of the mathematical model. The first aspect is addressed in Section 5.2 and concerns the numerical robustness of the models. The iterative convergence of different transition models is compared both between themselves and with calculations without a transition model. Difficulties in the convergence are traced back to the terms in the models which cause them, and an approach to remedy the situation is given and extended to all transition models. Section 5.3 consists of a study on the effect of the discretization scheme used in the convection term of the transport equations of the transition and turbulence models. Calculations using first order and second order schemes on the convection term are performed, in order to identify the importance of the discretization in each model. Finally, the effect of the size of the near-wall cell is discussed in Section 5.4. This is assessed by using several sets of grids with different sizes for the first near-wall cell. The main conclusions of the three studies are summarized in Section 5.5.

5.2 Numerical Robustness

5.2.1 Introduction

Four test cases are considered for the study of the numerical robustness. These are the flat plate, the NACA 0012 and Eppler 387 airfoils and the 6:1 prolate spheroid. Details on the values set for the turbulence variables at the inlet for each case are given in Table 5.1. The value of the turbulence intensity obtained in the freestream at the leading edge plane Tu_{LE} is given as well. The grid sets used correspond to those described in Chapter 4.

It is also worth mentioning that an evaluation of numerical robustness through the number of iterations is influenced by the relaxation parameters used in the simulations. Furthermore, the remaining two

Table 5.1: Angle of attack and inlet turbulence quantities for each test case for the calculations performed for the study of the numerical robustness.

Case	Angle of Attack	Tu_{in}	$(\mu_t/\mu)_{in}$	x_F	N_{crit}	Tu_{LE}
Flat Plate (OH Grid)	-	1%	25	Not used	-	0.64%
NACA 0012	0°	1%	0.1	Not used	2.6	0.01%
NLF ₁ -0416	0°	1%	0.1	Not used	-	0.01%
6:1 Prolate Spheroid	5°	0.5%	250.0	Not used	-	0.14%

aspects that are addressed in this Chapter can also have an important contribution, as using second (or higher) order schemes will lead to a decrease in the numerical robustness, with the same being true for the use of grids with smaller sizes of the near-wall cell. In order to minimize differences owing to these factors, all settings are kept constant across each case, with regards to relaxation parameters for each equation, as well as the discretization scheme employed. Naturally, the same set of grids is always used for each different model.

5.2.2 Results

The first test case addressed is the flow around the NACA 0012 airfoil. Figure 5.1 shows the evolution of the residuals of each transport equation for the $k - \omega$ SST model without any transition model and with each of them. Although it is only the evolution for a single calculation, it is representative of nearly every single calculation done with a transition model. The use of any transition model leads to a higher oscillation in the residuals when compared to the situation where only the underlying turbulence model is employed. It can also be observed that the residuals of the transport equations associated with the transition model are generally at least one order of magnitude higher than the remaining ones, particularly when the iterative convergence criteria is reached. In the vast majority of cases, the use of a transition model also leads to a higher number of iterations required to lower the residuals. This is displayed in Figure 5.2, where the number of iterations performed for the entire grid set is shown for each model. With the exception of the finest grid, the $k - \omega$ SST model without any transition model is consistently the formulation that requires the fewest iterations.

The numerical robustness of the models is also deeply connected to the flow itself. Flow separation, be it laminar or turbulent, generally introduces difficulties. However, laminar separation is not a flow phenomena that is easily predicted without the use of a transition model. An example of this is given by the NLF₁-0416 airfoil. As displayed in Figure 5.3, the $\gamma - Re_\theta$ model is the only one that leads to laminar flow separation on the upper surface. Consequently, it is also the model that exhibits the worst robustness for this case, as none of the simulations reached the set iterative convergence criteria.

The inclusion of a transition model does not necessarily entail additional difficulties due to the change in flow regime. The later transition promoted by the use of transition models when compared to that predicted by the $k - \omega$ SST model results in a higher skin friction coefficient level on the turbulent regime. In the cases where separation of the turbulent flow can occur, the extent of the separated region may be larger for the case without a transition model, thus penalizing the iterative convergence of such simulations.

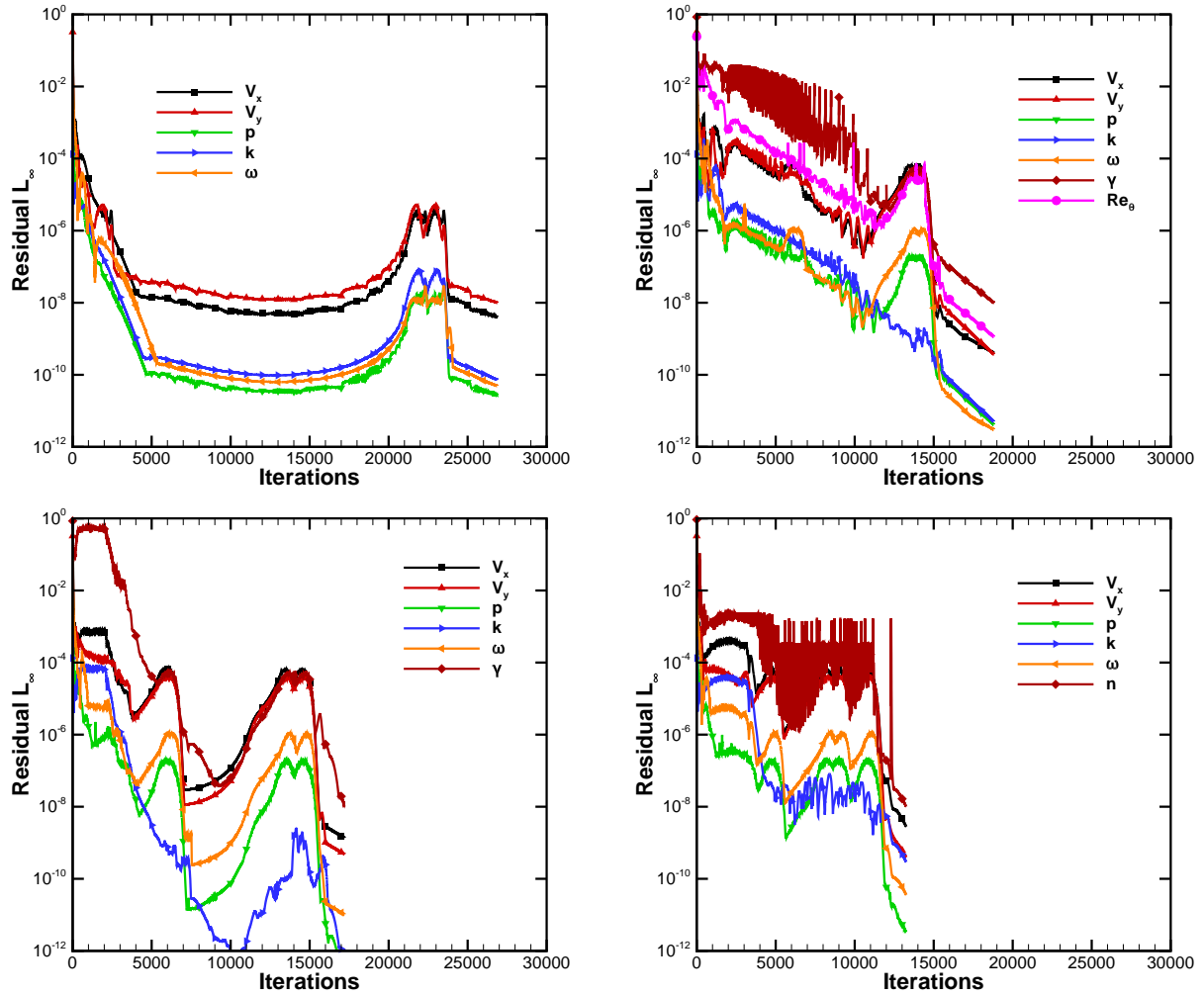


Figure 5.1: Evolution of the residuals for the NACA 0012 airfoil on Grid 2048 using the $k - \omega$ SST model (top left) combined with the $\gamma - Re_{\theta}$ model (top right), the γ model (bottom left) and the AFT model (bottom right).

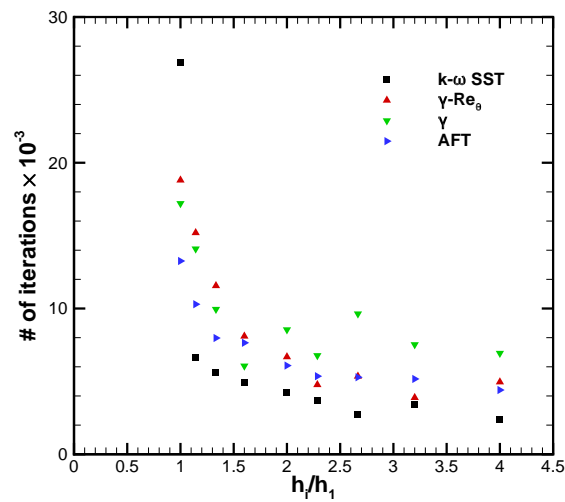


Figure 5.2: Number of iterations performed until the iterative convergence criteria was achieved for the NACA 0012 airfoil with each transition model coupled to the $k - \omega$ SST turbulence model for different grids.

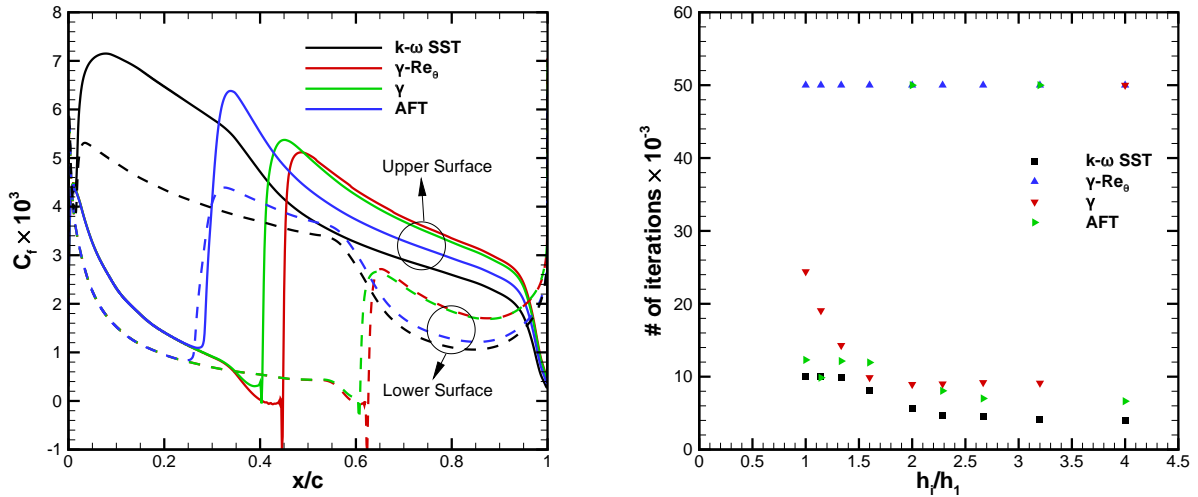


Figure 5.3: Skin friction coefficient distribution on the finest grid (left) and number of iterations performed at each grid for each model (right) for the NLF₁-0416 airfoil.

While all these effects are directly related to the iterative convergence of the simulations, they are not inherent to the formulation of the model. The difficulties in converging a solution with separated regions are a consequence of the steady flow approximation becoming inadequate. On the other hand, it is also natural that the complete formulation with transition model requires more iterations: the turbulence model still needs to be converged, and the coupling between each model also introduces further difficulties. However, this does not mean that the formulation of transition models are entirely robust. Figure 5.4 depicts a calculation for the flat plate test case in which residual stagnation occurs and is only solved through modification of relaxation parameters, in particular by lowering the explicit relaxation of the equations associated with the turbulence model. This is not exclusive to the $\gamma - Re_{\theta}$ model, and occurs for other models and in other test cases as well. Even though in this case residual stagnation happens at a level that is not excessively concerning, as the highest residual is that of γ at around 10^{-4} , in some other cases this may hover around 10^{-2} or even 10^{-1} .

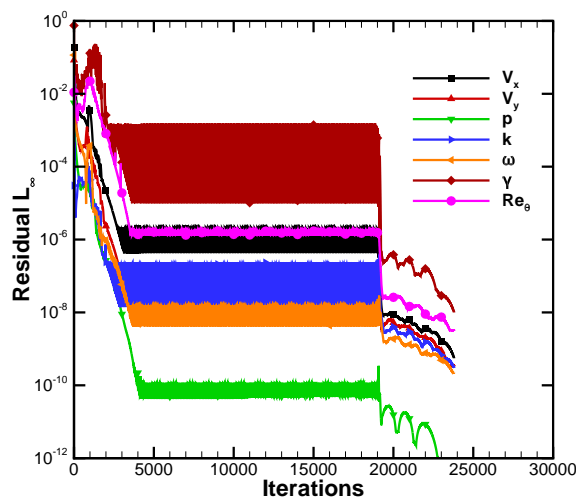


Figure 5.4: Evolution of the residual of each transport equation for the flat plate test case when using the $\gamma - Re_{\theta}$ model on Grid 4.

A closer inspection of the evolution of the residuals shows a periodic behaviour, typical of flow oscillation between two solutions. This is shown in Figure 5.5. An analysis of the region where the maximum residuals occur shows that the residual oscillation comes from a variation in γ in just a few cells, as this is a localized behaviour at the transition region. The variation of γ is caused by changes in the production and dissipation term of γ . However, since these are proportional to γ , they are also affected by it. The root cause of this oscillating behaviour comes from the limiters in the formulation of the transition models. In the present example, F_{onset} is the function responsible for the changes in γ .

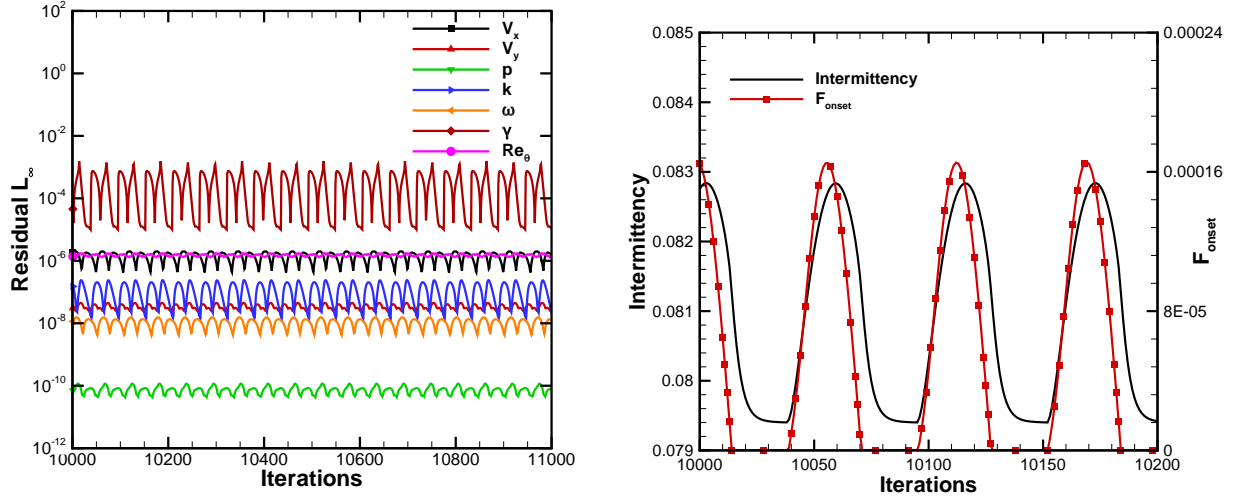


Figure 5.5: Periodic behaviour of the residuals (left) and corresponding evolution of γ and F_{onset} on the cell with the highest residual (right) for the flat plate test case using the $\gamma - Re_{\theta}$ model on Grid 4.

The definition of F_{onset} (Eq. 3.44) includes a \max function, which is continuous, but its derivative is not. An example of the issues that \max or \min functions can introduce is illustrated in Figure 5.6 for the F_{onset3} function, which has a similar formulation. Although the function is continuous, the sharp discontinuity in the derivative at $R_T = 2.5$ does not promote stability. Furthermore, these functions are limited to zero. As seen in Figure 5.5, there is a strong difference between F_{onset} taking low values, which still enable the production term of γ to be active, and taking the value of zero, which forcefully cuts off production, causing γ to decrease. In the case of the AFT model, residual stagnation may also occur due to the discontinuous F_{crit} function (Eq. 3.106) that controls the production of \tilde{n} .

The solution to this issue is also presented in Figure 5.6 and consists of adopting an alternative formulation for F_{onset3} and F_{onset} , which has a smooth evolution in the vicinity of $R_T = 2.5$. Following the work of Ref. [166], this is done by approximating the \max functions as follows:

$$\max(g_1, g_2) \approx \begin{cases} \max(g_1, g_2), & |g_1 - g_2| > -\frac{\log(|p| \cdot |p_{mach}|)}{|p|} \\ \frac{\log(\exp(pg_1) + \exp(pg_2))}{p}, & |g_1 - g_2| \leq -\frac{\log(|p| \cdot |p_{mach}|)}{|p|} \end{cases} \quad (5.1)$$

In this formulation, p_{mach} is a small value close to machine precision, while p is a value that controls how much the approximation resembles the \max function. This approach is employed simultaneously in the F_{onset} and F_{onset3} functions, but it is only used in cases which display difficulties in the iterative convergence. Using this formulation on the case displayed previously leads to convergence of the

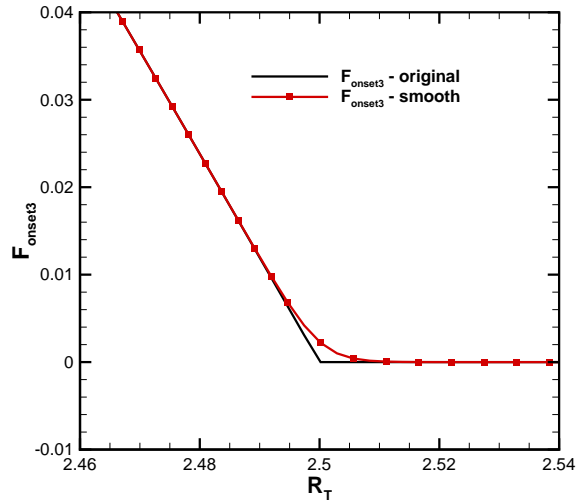


Figure 5.6: Depiction of the F_{onset} function and the smooth formulation in the vicinity of $R_T = 2.5$.

solution in under 5000 iterations, as illustrated in Figure 5.7. Another example of its application is given in Figure 5.8 for the prolate spheroid, showing that it leads to a good behaviour, without requiring user input midway through the computation. This example also illustrates that the level at which the residuals stagnate can be quite high. For the AFT model this approach is not suitable, since the issue there is caused by a discontinuity in the function itself, and not due to the application of a \max function.

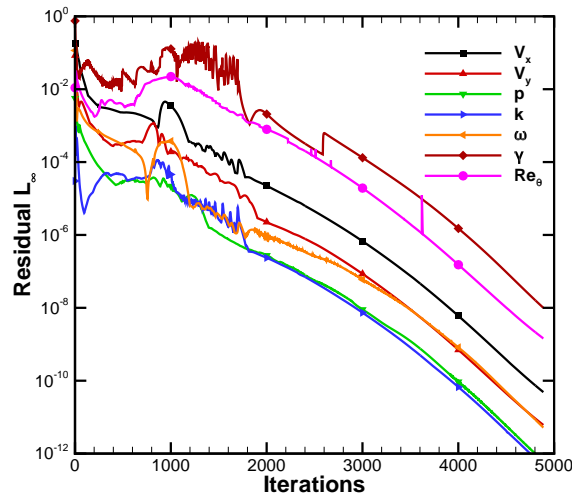


Figure 5.7: Evolution of the residual of each transport equation for the flat plate test case when using the $\gamma - Re_\theta$ model with the smooth formulation for F_{onset3} and F_{onset} on Grid 4.

Even though the use of Eq. 5.1 promotes numerical robustness, it is nonetheless a modification to the original formulation of each transition model. In order to assess the potential impacts of this change, Figure 5.9 presents a comparison of the skin friction coefficient and friction resistance for the NACA 0012 airfoil using the $\gamma - Re_\theta$ model. Three sets of calculations are done, two with the use of Eq. 5.1 for $p = 300$ and $p = 600$, and another with the original formulation of the models. This case does not exhibit any problem in the iterative convergence, and so the use of the smooth variant of F_{onset} and F_{onset3} is not needed. This allows to check the influence of the change of the formulation on the solution itself. At each grid level there is a decrease in $C_{d,f}$ when Eq. 5.1 is used, as the solutions for $p = 300$ and $p = 600$

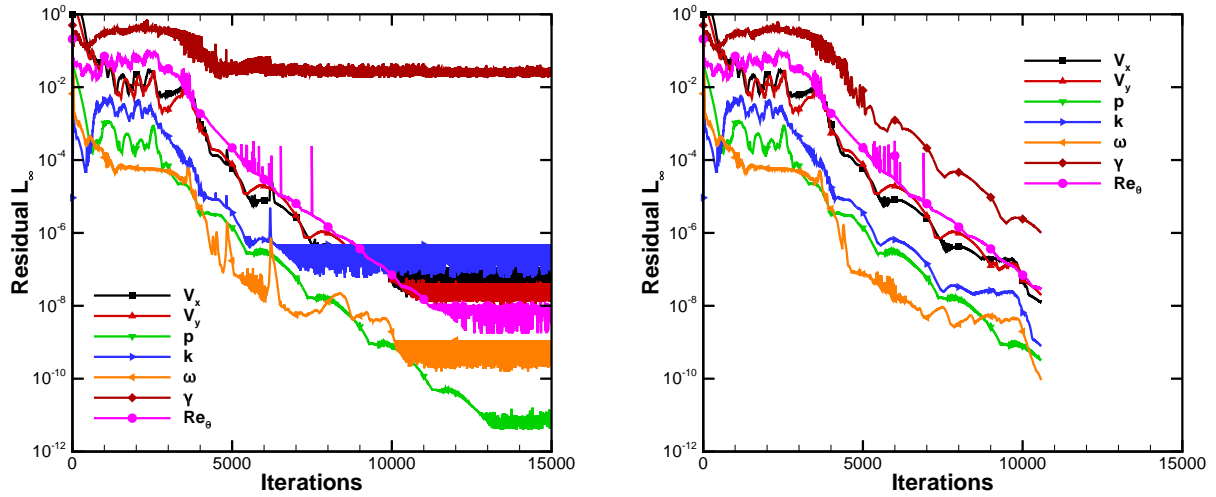


Figure 5.8: Example of the residual evolution for a calculation on the prolate spheroid test case for Grid 5 using the $\gamma - Re_\theta$ model with the original (left) and smooth (right) formulations of the F_{onset} and F_{onset3} functions.

are nearly coincident. The decrease in $C_{d,f}$ is caused by the transition location moving downstream, although for the finest grid this corresponds to a change of only two cells.

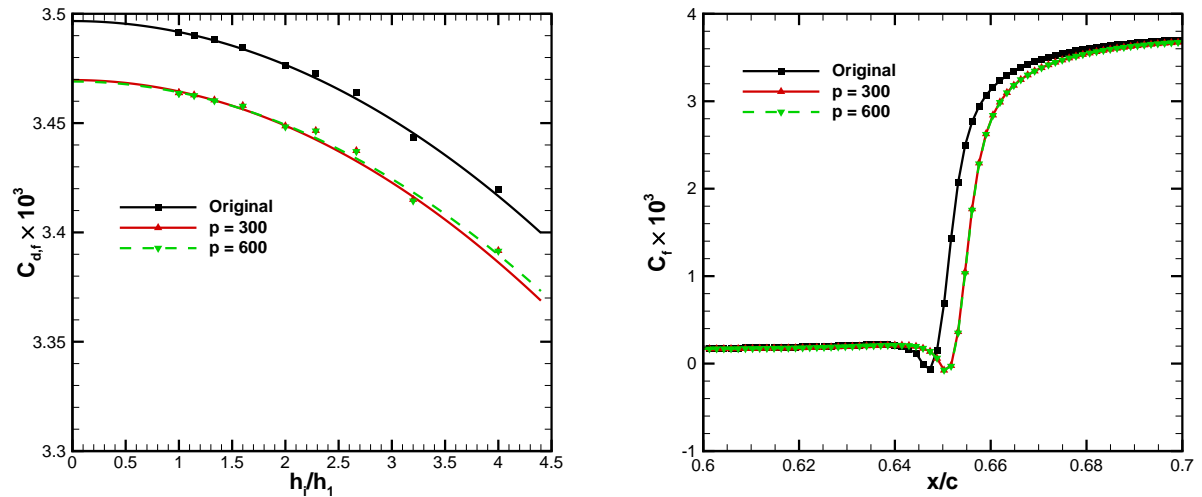


Figure 5.9: Convergence of the friction drag with grid refinement (left) and skin-friction coefficient distribution on the finest grid (right) for the NACA 0012 airfoil using the $\gamma - Re_\theta$ model with the original formulation and the smooth variant with $p = 300$ and $p = 600$.

5.3 Discretization Scheme

5.3.1 Introduction

All calculations performed for this section are identified by a pair of two letters. The first letter corresponds to the discretization scheme used in convection term of the transport equations of the turbulence model. The second letter is analogous but refers instead to the transport equations of the transition model. Calculations without a transition model are performed as well. In this case, the second letter is

not used. Three different approaches are employed:

- a first order upwind scheme, denoted by U;
- a QUICK scheme without flux limiters, identified by Q;
- a QUICK scheme with flux limiters, referenced as L.

As an example, if a set of calculations is labeled with UL, that means that set was computed using a first order upwind scheme in the convection term of the transport equations for the turbulence variables, and using the limited QUICK scheme for the convection term of the transport equations pertaining to the transition model.

The three test cases considered for this study are the NACA 0012 and NLF₁-0416 airfoils and the 6:1 prolate spheroid. Specific conditions are given in Table 5.2. For the NACA 0012 airfoil, all possible combinations of schemes are tested. For the NLF₁-0416 airfoil, variations are performed independently for the turbulence and transition model, meaning that only the LL, LQ, LU, QL and UL sets are considered. Finally, for the prolate spheroid, only the influence of the scheme used on the turbulence model is assessed, using the LL and UL sets. Furthermore, only the $k - \omega$ SST turbulence model is employed, as the combinations of the transition models with the KSKL model are not used.

Table 5.2: Angle of attack and inlet turbulence quantities for each test case for the calculations performed for the study of the effect of the convection discretization scheme.

Case	Angle of Attack	Tu_{in}	$(\mu_t/\mu)_{in}$	x_F	N_{crit}	Tu_{LE}
NACA 0012	0°	1%	0.1	Not used	2.6	0.1%
NLF ₁ -0416	0°	1%	0.1	Not used	2.6	0.1%
6:1 Prolate Spheroid	5°	0.1917%	5.2	-1.5L	6.6	0.15%

For several of the cases presented in this section, the convergence of the quantities of interest with grid refinement is considered. In those cases, the least squares fit of the data to Eq. 4.15 is shown and the estimated numerical uncertainty is also provided. However, these are obtained by considering only the data from the five finest grids. This means that for the two-dimensional geometries, the coarsest grids are not used in the uncertainty estimation procedure. Nonetheless, they are useful to assess the trend of the results, and are more representative of the level of grid refinement of the three-dimensional test cases.

5.3.2 Results

Starting with the baseline calculations without a transition model, Figure 5.10 presents the friction component of the drag coefficient for the two airfoils with different schemes employed in the turbulence transport equations. It is evident that the effect of the flux limiters in the case of the QUICK scheme is negligible, and the difference between the first order upwind and QUICK schemes is also very small. The same holds true for the pressure component of the drag coefficient, shown in Figure 5.11. This shows that in for this particular case, there is little benefit in using high order schemes in the turbulence

model to calculate mean flow quantities, if a transition model is not used. However, this trend may not hold for unstructured grids [167].

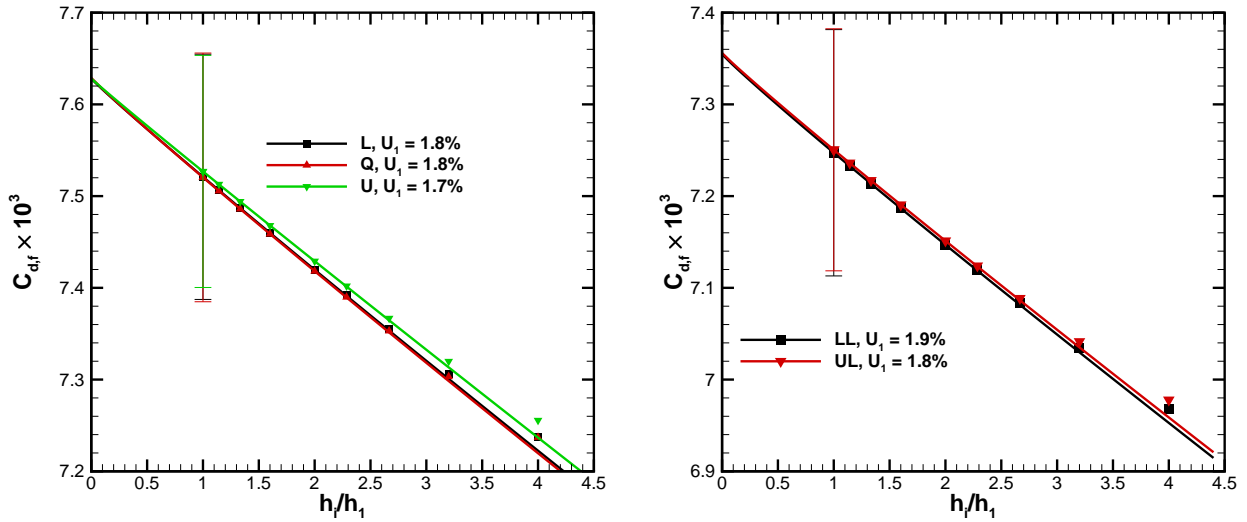


Figure 5.10: Effect of the discretization scheme used for the convection term of the $k-\omega$ SST turbulence model on $C_{d,f}$ for calculations without a transition model for the NACA 0012 (left) and the NLF₁-0416 (right) airfoils.

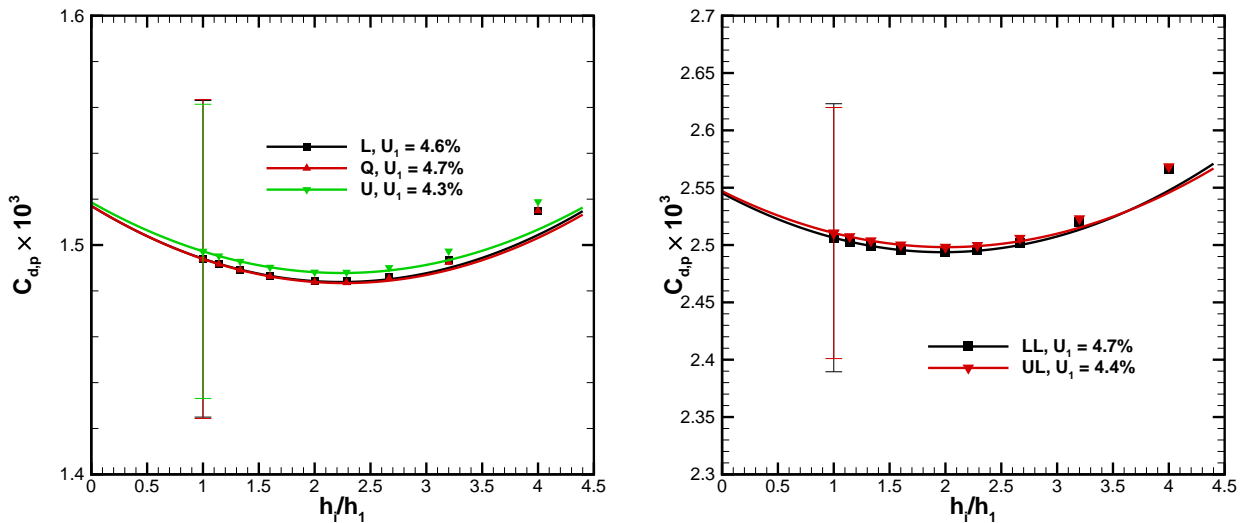


Figure 5.11: Effect of the discretization scheme used for the convection term of the $k-\omega$ SST turbulence model on $C_{d,p}$ for calculations without a transition model for the NACA 0012 (left) and the NLF₁-0416 (right) airfoils.

Considering now the calculations with the transition models, the C_f distribution for the two airfoils is presented in Figure 5.12. In both geometries, the transition region predicted by the AFT model is located much further upstream than that predicted by the $\gamma - Re_\theta$ and γ models. This is a consequence of the low value of N_{crit} used in this study. While in the NACA 0012 airfoil there is no flow separation, it occurs on the lower surface of the NLF₁-0416 for the $\gamma - Re_\theta$ and γ models and in the upper surface for the $\gamma - Re_\theta$ model. As such, the two airfoils exhibit different transition mechanisms.

Figures 5.13, 5.14 and 5.15 exhibit $C_{d,f}$ and $C_{d,p}$ with different schemes for the $\gamma - Re_\theta$, γ and AFT

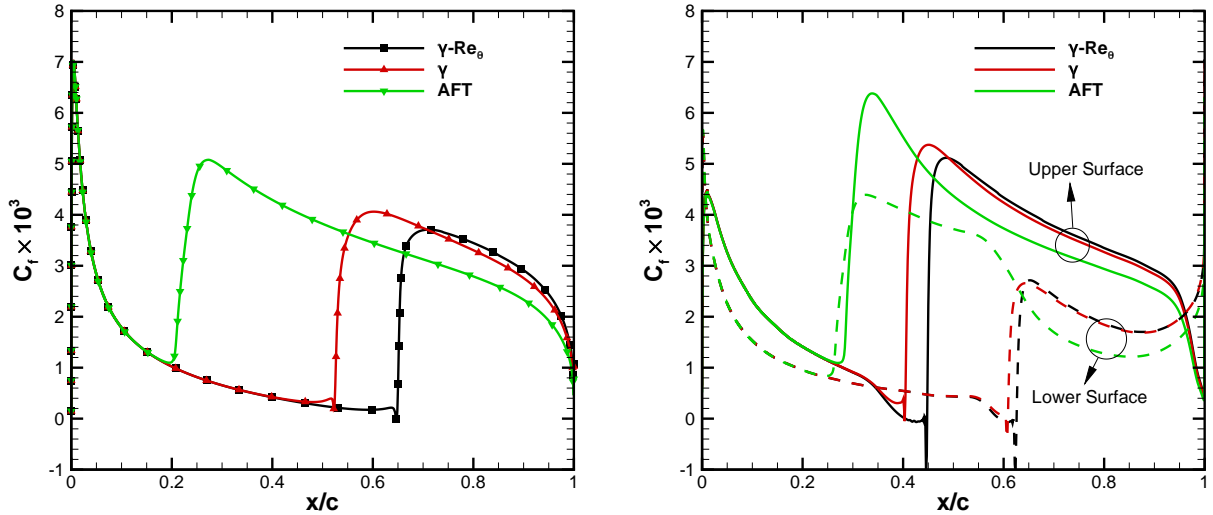


Figure 5.12: Skin friction coefficient distribution obtained with each transition model for the NACA 0012 (left) and the NLF₁-0416 (right) airfoils.

models respectively. Differences observed between each set of calculations are more pronounced in the friction component of the drag coefficient than in the pressure component. Regarding the scheme used in the transition transport equations, the use of flux limiters has a negligible impact. Additionally, only the $\gamma - Re_\theta$ model exhibits a small difference in the solution obtained between calculations using the first order upwind scheme or the QUICK scheme in the equations of the transition model.

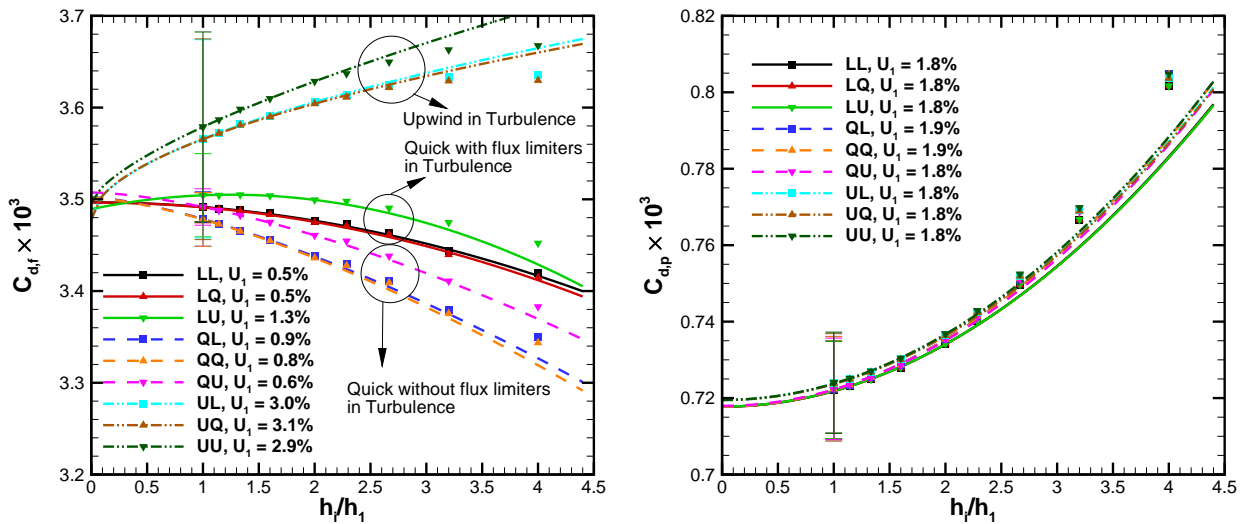


Figure 5.13: Effect of the discretization scheme used in the convection term of the transport equations of the turbulence and transition models using the $\gamma - Re_\theta$ model on the NACA 0012 airfoil: $C_{d,f}$ (left) and $C_{d,p}$ (right).

More important is the influence of the scheme used in the equations of the turbulence model. The use of flux limiters leads to a small difference in the calculations with the $\gamma - Re_\theta$ model. In the case of the γ model, there is no appreciable difference. Finally, for the AFT model, the solution on the coarse grids when a flux limiter is inactive is similar to the one obtained when using a first order upwind scheme. As the grid is refined, it starts to match the solution of the case where the flux limiters are active.

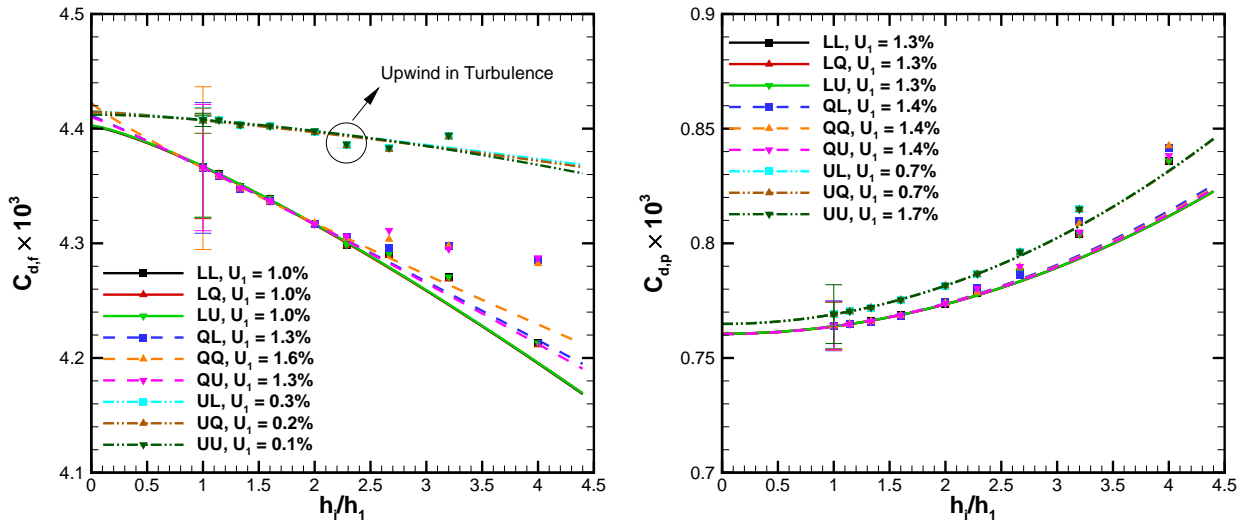


Figure 5.14: Effect of the discretization scheme used in the convection term of the transport equations of the turbulence and transition models using the γ model on the NACA 0012 airfoil: $C_{d,f}$ (left) and $C_{d,p}$ (right).

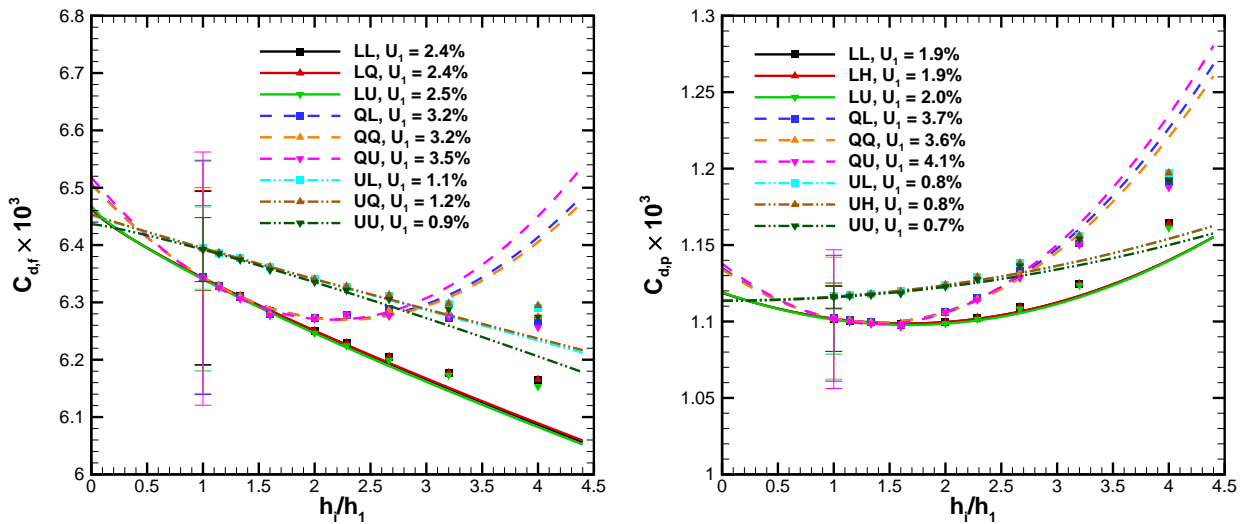


Figure 5.15: Effect of the discretization scheme used in the convection term of the transport equations of the turbulence and transition models using the AFT model on the NACA 0012 airfoil: $C_{d,f}$ (left) and $C_{d,p}$ (right).

The most significant difference comes from whether the first order upwind or QUICK scheme is used in the turbulence transport equations, which is a common trend displayed by all transition models and in disagreement with the trend observed in the calculations without transition model. For all models, the use of the first order upwind scheme leads to higher values for both $C_{d,f}$ and $C_{d,p}$. In the case of the γ model, transition takes place much further upstream in the coarsest grid than in the remaining grids, leading to significant numerical error.

Another worthwhile aspect is that $C_{d,f}$ increases as the grid is refined and the QUICK scheme is used for the transport equations of the turbulence model. However, if the first order upwind scheme is used instead, then the increase is smaller in the case of the γ and AFT models and, for the $\gamma - Re_\theta$ model, it decreases with grid refinement. Nevertheless, the extrapolated solution at $h_i/h_1 = 0$ is similar regardless of the scheme used. This shows that the comparison of numerical schemes can be misleading if the numerical uncertainty is not assessed. Furthermore, the different trends observed with the behaviour of $C_{d,f}$ with grid refinement hint at opposing effects as the grid is refined. This is further examined in Figure 5.16 where the C_f distribution in the vicinity of the transition region of every other grid for the LL and UL sets using the $\gamma - Re_\theta$ model is shown. In both sets, there is an increase of C_f in the turbulent region with grid refinement, leading to the increase in $C_{d,f}$ with grid refinement observed in the LL set.

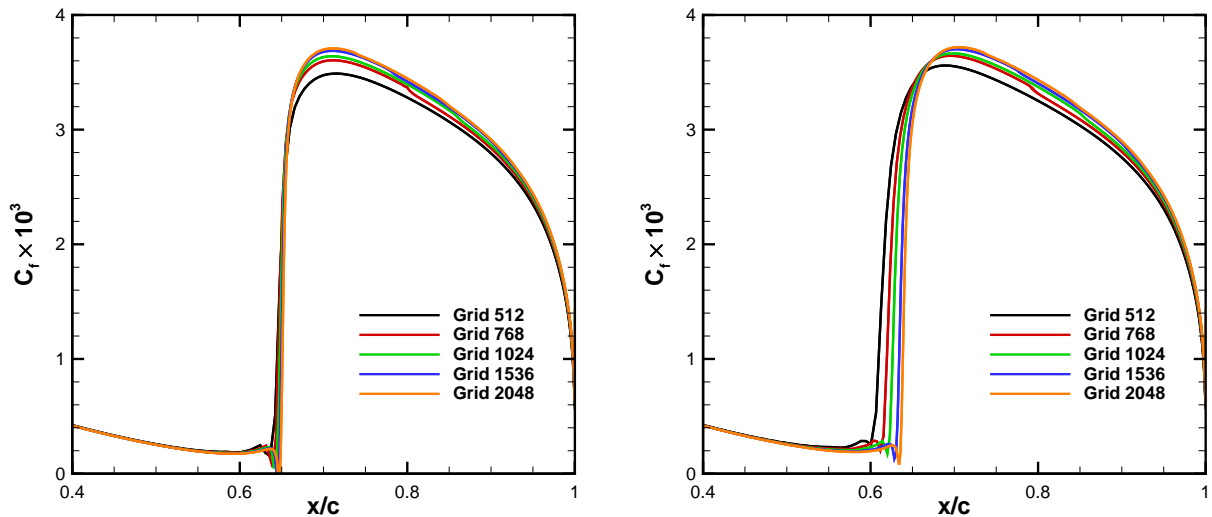


Figure 5.16: Skin friction coefficient distribution for the NACA 0012 airfoil and different grids using the $\gamma - Re_\theta$ model for the LL set (left) and for the UL set (right).

For the UL set, an additional effect occurs. The prediction of the transition region in the coarsest grids is located slightly upstream than that of the finest grids. The shift of transition downstream as the grid is refined promotes a higher extent of laminar flow, which acts as to decrease $C_{d,f}$. The different convergence behaviour exhibited by the UL set, and even the lower numerical uncertainty is then caused by the two opposing effects, which lead to an overall smaller change of $C_{d,f}$ as the grid is refined, even though the location of transition has a larger numerical error. This shows that the convergence of $C_{d,f}$ with grid refinement is affected by error cancelling.

The same effect is present in the γ model, but the shift of transition with grid refinement is not as pronounced, as illustrated in Figure 5.17. This explains why for this model there was still an increase

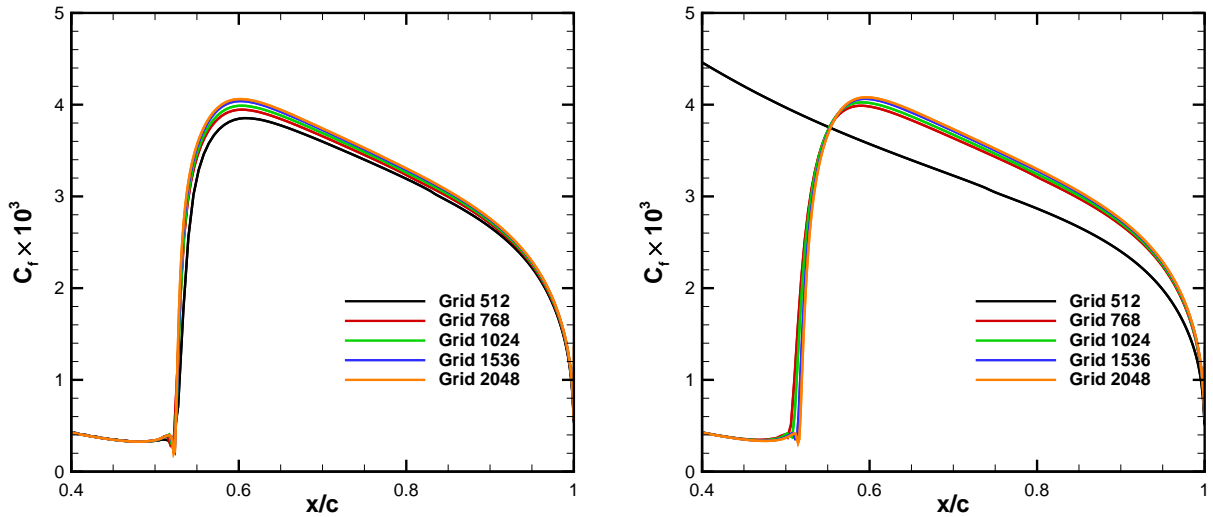


Figure 5.17: Skin friction coefficient distribution for the NACA 0012 airfoil and different grids using the γ model for the LL set (left) and for the UL set (right).

of $C_{d,f}$ with grid refinement for the UL set, albeit smaller than for the LL set. The most distinguishing feature however is the early transition in the coarsest grid for the UL set, incurring a significant numerical error.

The C_f distribution for the AFT model is presented in Figure 5.18. For both sets there is a slight difference on the prediction on the coarsest grid. Similarly to the $\gamma - Re_\theta$ model, the UL set exhibits the largest shift of the transition region with grid refinement. In this case, however, since transition happens much earlier for the AFT model, the increase of C_f in the turbulent region outweighs the increase of the extent of laminar flow. Thus, $C_{d,f}$ still increases with grid refinement, unlike what was observed for the $\gamma - Re_\theta$ model.

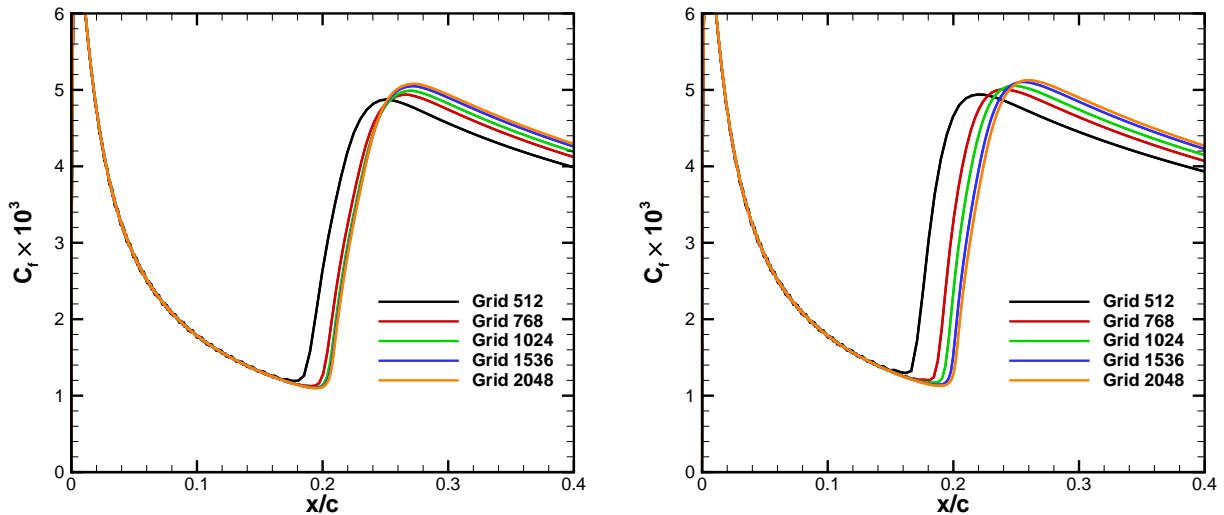


Figure 5.18: Skin friction coefficient distribution for the NACA 0012 airfoil and different grids using the AFT model for the LL set (left) and for the UL set (right).

The changes of the transition position with grid refinement when a first order upwind scheme is used in the convection term of the turbulence model equations is the most striking feature observed.

Moreover, there is a clear dependence on the transition model used. For the $\gamma - Re_\theta$ model, the shift in the transition region can be traced to the different level of turbulence intensity in the freestream, as displayed in Figure 5.19. The UL set shows a higher change in the freestream level of the turbulence intensity, which decreases as the grid is refined. This is directly related to the use of coarse grids in the freestream, which causes an underestimation of the decay. This effect is mitigated when the QUICK scheme is used. However, the change in the level of freestream turbulence intensity alone is not enough to justify the shift in the transition position, given that for the LL set there is also a decrease in the level of freestream turbulence with grid refinement. Since there are no appreciable gradients of the turbulence variables in the laminar region that would affect the transition location, it follows that the influence of the discretization scheme also impacts the transition process itself. This observation is also consistent with the fact that the AFT model also exhibits some dependence of the scheme used. The AFT model should show a minimal influence of turbulence on the location of transition, since it is mostly dependent on the value of N_{crit} .

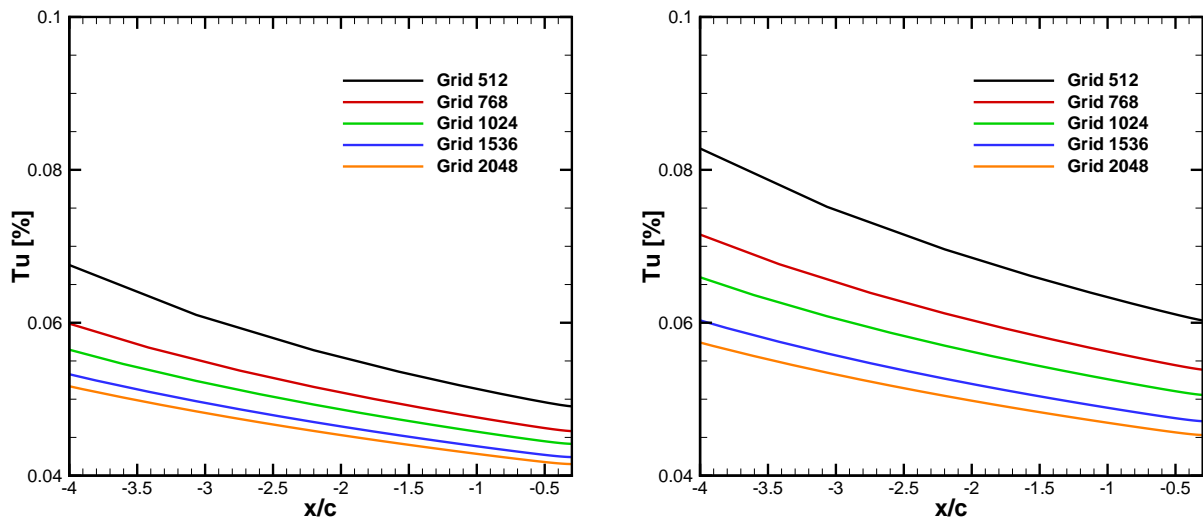


Figure 5.19: Evolution of the turbulence intensity in the region upstream of the NACA 0012 airfoil when using the $\gamma - Re_\theta$ model for the LL (left) and UL (right) sets.

The previous analysis is focused on the accuracy of the simulations. Naturally, it is not to be expected that the computations performed with the first order upwind scheme would be more accurate than those performed with the QUICK scheme. They should, however, be more robust. In the present case for the NACA 0012 airfoil, a total of $3 \times 9 \times 9 = 243$ simulations were performed, corresponding to 3 transition models, 9 grids and 9 combinations of discretization scheme. Out of the 243 simulations, 84 failed to attain the desired level of iterative convergence.

From these, 81 correspond to the cases where the QUICK scheme without flux limiters was used for the turbulence transport equations, regardless of the transition model used. An example of the convergence for this case for the $\gamma - Re_\theta$ and AFT models is shown in Figure 5.20. In spite of the stagnation of the residual of the k transport equation, the residuals of all other variables decrease down to machine precision. Furthermore, the stagnation of the residual of k takes place at the stagnation point of the airfoil. As such, this issue is not related to the transition phenomena, but to the turbulence model

itself.

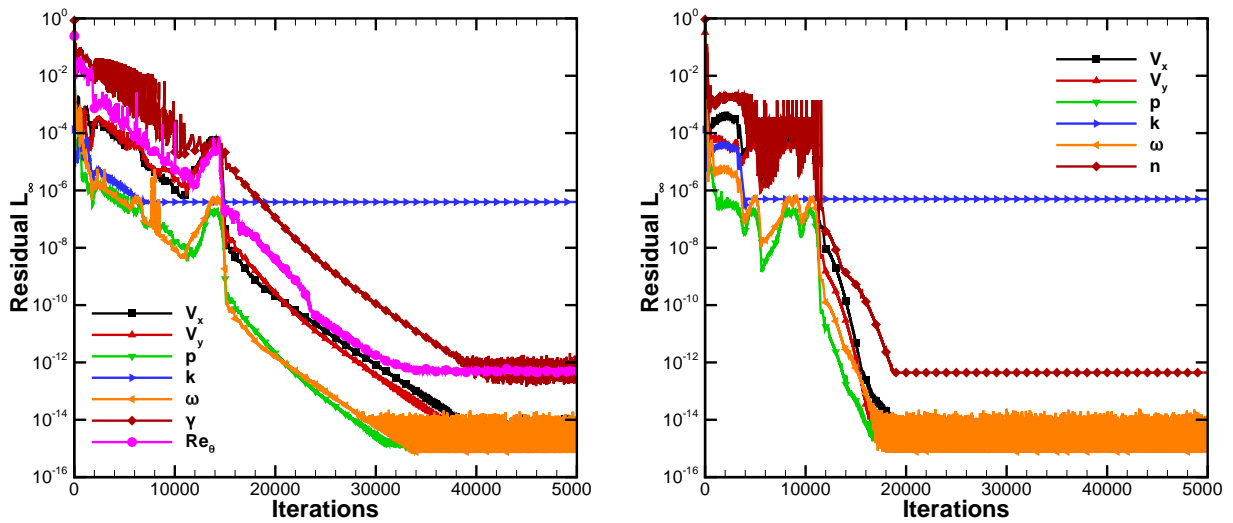


Figure 5.20: Iterative convergence evolution for the QL set and Grid 2048 using the $\gamma - Re_\theta$ model (left) and the AFT model (right).

As for the remaining three simulations that did not converge, all of these were done with the UU set, one with the $\gamma - Re_\theta$ model and two with the AFT model. Consequently, there was no added difficulty in the iterative convergence of the simulations due to the use of the QUICK scheme with flux limiters in either the turbulence or transition equations. This is further strengthened by Figure 5.21 which shows that the use of the QUICK scheme did not incur any significant increase in the number of iterations performed. Although only three grids are shown, the trends are representative of the entire grid set.

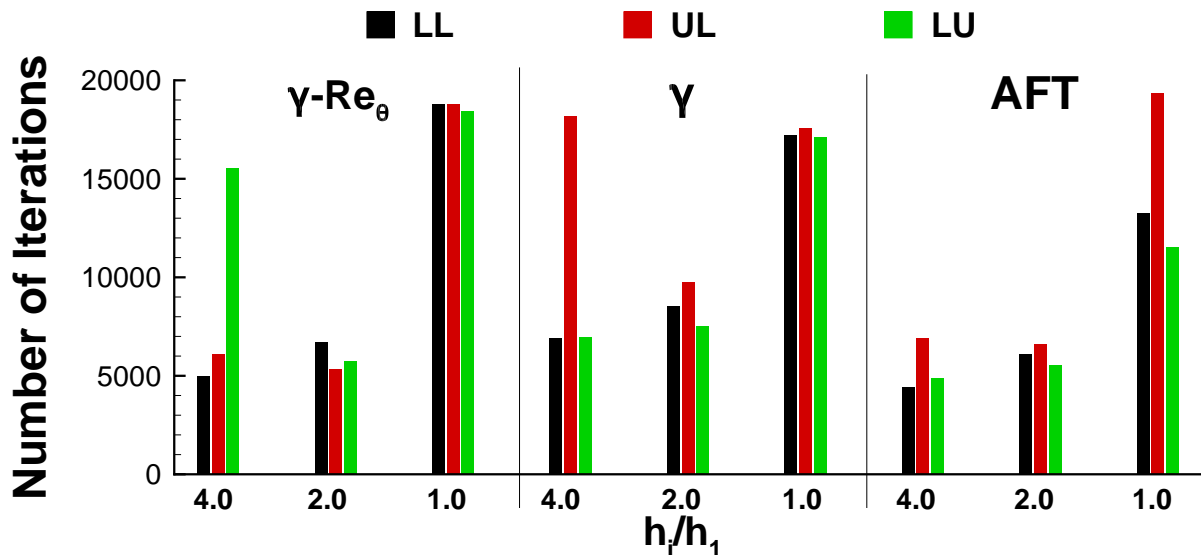


Figure 5.21: Number of iterations required to converge the numerical solution for the NACA 0012 using each transition model for different levels of grid refinement and different combinations of the discretization schemes.

All of the trends discussed for the NACA 0012 airfoil are also observed for the NLF₁-0416 airfoil, despite the different transition mechanism. Figures 5.22, 5.23 and 5.24 present the skin friction coefficient

cient distributions for each transition model. The use of the first order upwind scheme on the convection term of the turbulence model leads to larger changes with grid refinement for the $\gamma - Re_\theta$ model when compared to the calculations performed with the QUICK scheme. For the γ model, not only does the coarsest grid exhibit significant numerical error on the upper surface due to premature transition, but this also happens for the two following grids in the set. The coarsest grid also exhibits some numerical error for the AFT model, in a similar manner to the behaviour displayed in the NACA 0012 airfoil.

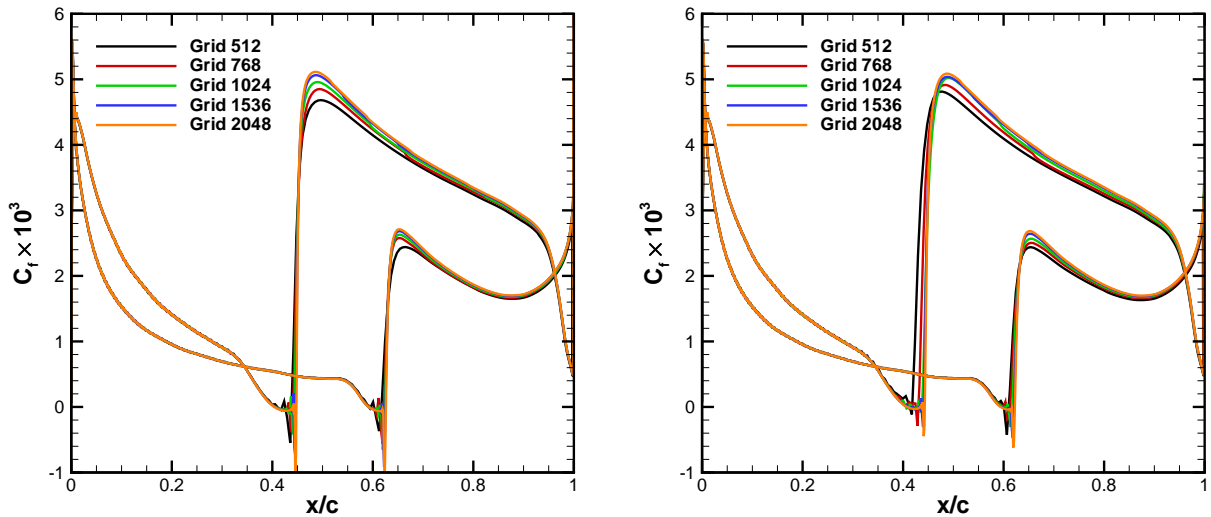


Figure 5.22: Skin friction coefficient distribution for the NLF₁-0416 airfoil and different grids using the $\gamma - Re_\theta$ model for the LL set (left) and for the UL set (right).

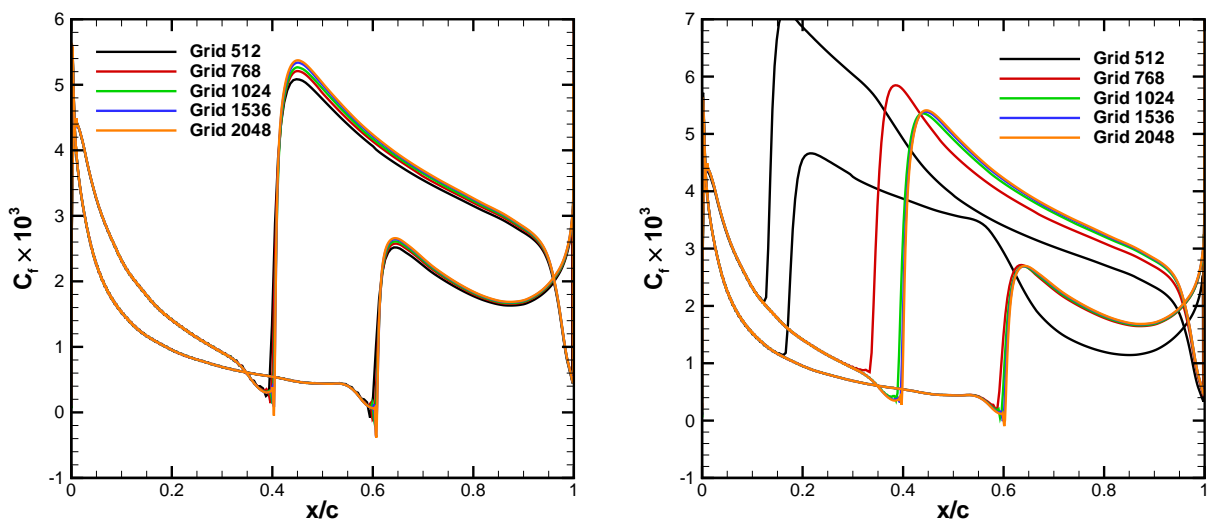


Figure 5.23: Skin friction coefficient distribution for the NLF₁-0416 airfoil and different grids using the γ model for the LL set (left) and for the UL set (right).

Regarding the iterative convergence, this test case proved to be much more difficult than the previous. A total of 144 simulations were performed and only 74 verified the set convergence criteria. All 27 calculations performed with the QUICK scheme without flux limiters on the turbulence equations did not converge. For the $\gamma - Re_\theta$ model, only two simulations converged. These correspond to the two coarsest grids, when using the first order upwind scheme on the transport equations for the turbulence model.

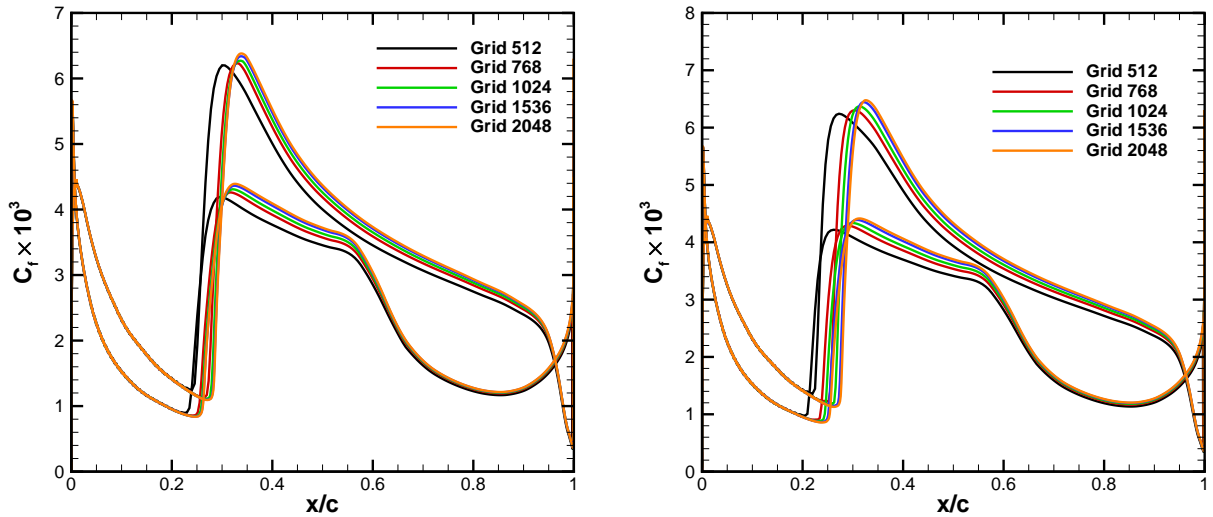


Figure 5.24: Skin friction coefficient distribution for the NLF₁-0416 airfoil and different grids using the AFT model for the LL set (left) and for the UL set (right).

This means that out of the 45 simulations performed with the $\gamma - Re_{\theta}$ model, 43 exhibited problems with the iterative convergence, although divergence never took place. On the other hand, for the γ model, all simulations achieved the desired level of iterative convergence with the exception of 4, besides the QL set. All of these were done using the coarsest grid. The only set for which the coarsest grid also converged was for the UL set. Finally, for the AFT model, a total of 6 simulations failed to converge, with the exception of the previously mentioned QL set. Out of the 6 simulations, two were in the LL set, two in the LQ set, and one each in the LU and UL sets. Additionally, these span grid 512 to grid 1024, the coarsest half of the set.

The significantly different robustness displayed by the $\gamma - Re_{\theta}$ model is due to the higher extent of separated flow predicted by this model. As discussed previously, flow separation is an obstacle to numerical robustness when considering steady flow, and the results of the $\gamma - Re_{\theta}$ model seem to indicate that using the QUICK scheme in the turbulence model for those conditions may prevent iterative convergence, although even most of the calculations using the first order upwind scheme also exhibited problems. On the contrary, the γ and AFT models exhibit little or no flow separation respectively, which makes iterative convergence easier. Considering the results of these two models, no significant advantage in terms of robustness is achieved through the use of the first order upwind scheme on either the turbulence or transition model for this case.

Figure 5.25 presents the number of iterations performed for each grid with the different sets. The $\gamma - Re_{\theta}$ model and the QL sets are not shown since those cases almost always hit the limit value of 50,000 iterations as previously mentioned. The behaviour of the γ model is straightforward: there is no significant influence of the discretization scheme used for the transition model. The use of the first order upwind scheme on the transport equations of the turbulence model only leads to a lower number of iterations for the coarsest and finest grids. For the AFT model, there are some slight changes due to the change of the discretization scheme used in the transition model. However, this does not occur for all grids. The trend is similar for the UL set as there is no noticeable decrease in the number of iterations

performed.

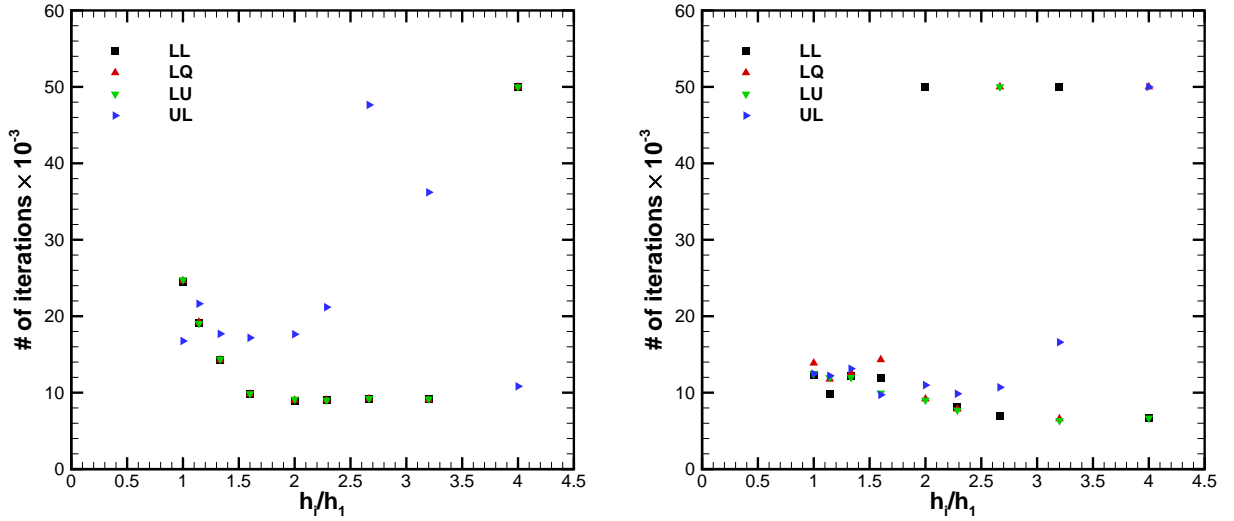


Figure 5.25: Number of iterations performed for the NLF₁-0416 airfoil with different combinations of discretization scheme and for each grid using the γ (left) and AFT (right) models.

Attention is now given to the flow around the 6:1 prolate spheroid. Figures 5.26, 5.27 and 5.28 present the convergence of $C_{d,f}$ and $C_{l,p}$ with grid refinement for the LL and UL sets for each transition model. In all cases, the effect of grid refinement is more significant in the UL set than in the LL set. Consequently, the estimated numerical uncertainty is also lower, with the exception of $C_{d,f}$ for the AFT model. Another relevant aspect is that for some cases, the solution at $h_i/h_1 = 0$ does not match for the two sets, indicating that the present level of grid refinement is not enough to make a reliable estimate of the exact solution. Furthermore, for the $\gamma - Re_\theta$ and γ models, the solution of the two coarsest grids does not appear to match that exhibited by the remaining grids. In the particular case of the AFT model, the pressure component of the lift coefficient exhibits a very strong variation with grid refinement. Although the evolution of $C_{d,p}$ is not shown, it also behaves in the same manner, showing that the effect of the discretization scheme on the turbulence transport equations is not limited to the friction component.

With regards to the iterative convergence of the calculations, difficulties for the LL set were observed at all grids for the $\gamma - Re_\theta$ model and for two intermediate grids when using the AFT model. The use of the first order upwind scheme in the turbulence model did not result in any significant improvement.

5.4 Size of the First Near Wall Cell

5.4.1 Introduction

For the study of the effect of the y^+ value, two test cases are considered: the flow over the flat plate and around the NLF₁-0416 airfoil. Angle of attack and inlet turbulence boundary conditions for each geometry are given in Table 5.3. All transition and turbulence model combinations are used here. A total of 45 grids are used for each case, organized into nine sets of five grids. While the level of grid refinement and cell count of each grid set follows that presented in Chapter 4, the size of the cells in the

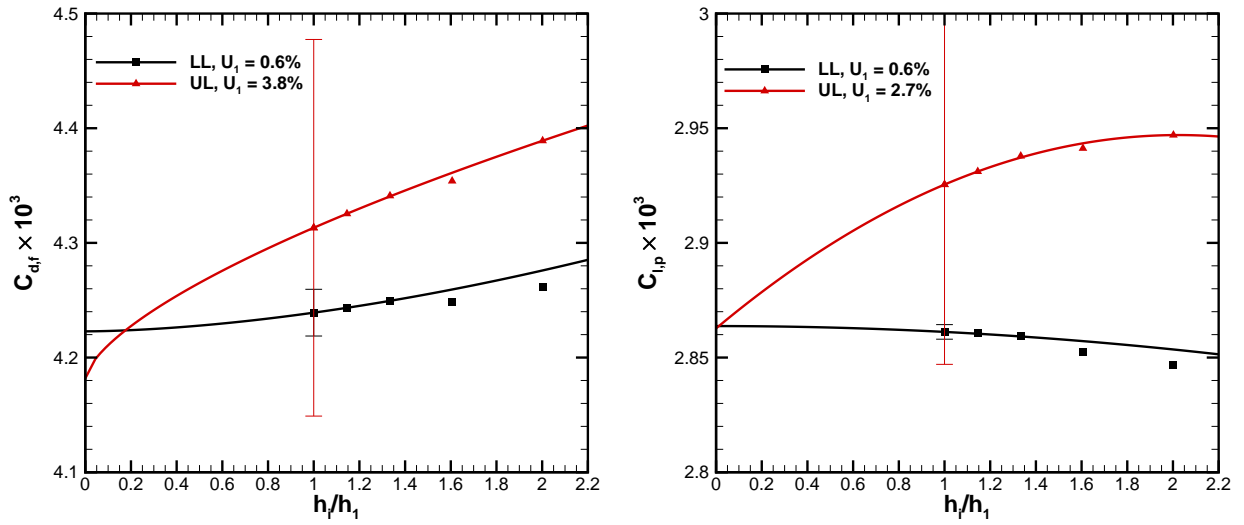


Figure 5.26: Effect of the discretization scheme used in the convection term of the transport equations of the turbulence and transition models using the $\gamma - Re_\theta$ model on the 6:1 prolate spheroid: $C_{d,f}$ (left) and $C_{l,p}$ (right).

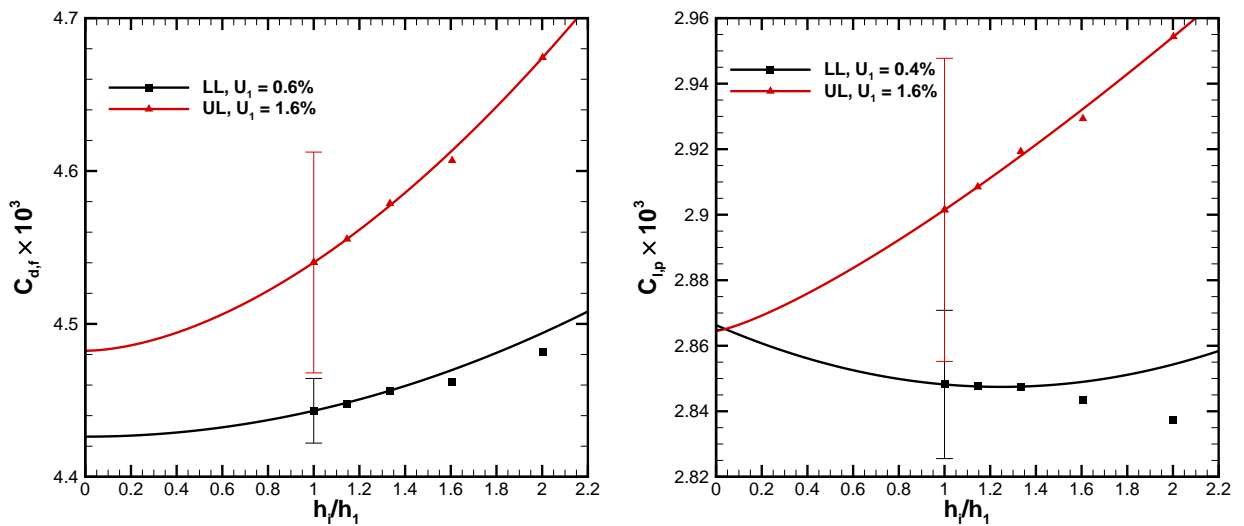


Figure 5.27: Effect of the discretization scheme used in the convection term of the transport equations of the turbulence and transition models using the γ model on the 6:1 prolate spheroid: $C_{d,f}$ (left) and $C_{l,p}$ (right).

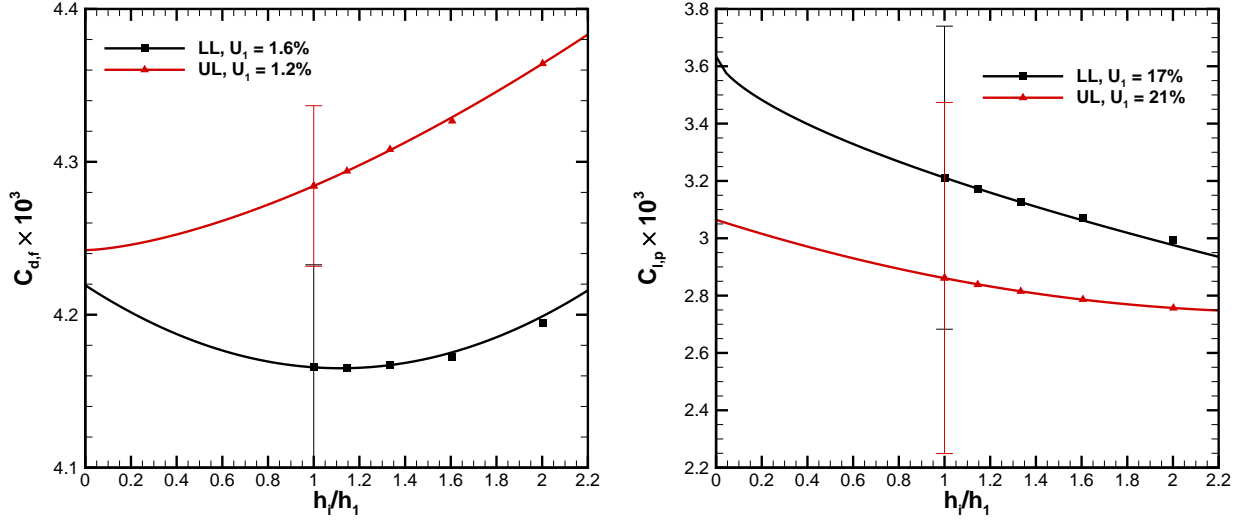


Figure 5.28: Effect of the discretization scheme used in the convection term of the transport equations of the turbulence and transition models using the AFT model on the 6:1 prolate spheroid: $C_{d,f}$ (left) and $C_{l,p}$ (right).

wall normal direction is varied.

The grid set with the highest y^+ value (grid set 9) is generated so that the coarsest grid of the set has an average value of $y_{avg}^+ \approx 1$. The intermediate set, grid set 5, is built such that for the coarsest grid the maximum value of y^+ follows $y_{max}^+ \approx 1$. The grid set with the lowest y^+ value, grid set 1, is created such that $y_{max}^+ \approx 0.1$. Finally, the remaining grid sets are made such that intermediate values of y^+ are obtained. This structure ensures that there are several grid sets that verify the commonly used criterion of $y_{max}^+ \approx 1$, exploring the effect of further decreasing the y_{max}^+ to levels that are rarely used.

Table 5.3: Angle of attack and inlet turbulence quantities for each test case for the calculations performed for the study of the effect of the size of the first near wall cell and corresponding y^+ value.

Case	Angle of Attack	Tu_{in}	$(\mu_t/\mu)_{in}$	x_F	N_{crit}	Tu_{LE}
Flat Plate (OH Grid)	-	1%	25.0	Not used	6.0	0.64%
NLF ₁ -0416	0°	3%	10.0	Not used	9.0	0.1%

This study follows that performed in Ref. [31], which was focused on the behaviour of the two turbulence models used here, the $k - \omega$ SST and the KSKL models, as well as the Spalart-Allmaras model, without any transition model. For that reason, calculations without transition model are not performed here, but the trends observed in Ref. [31] are mentioned throughout the text. This study has two main goals:

- To assess whether the influence of the size of the near-wall cell observed in Ref. [31] for calculations without transition model still holds when a transition model is included;
- To evaluate whether the prediction of the transition location is affected by y_{max}^+ .

Furthermore, the generation of the grids for the two test cases guarantees that, close to the wall, there are no differences in the streamwise direction for grids with the same number of volume cells. Thus, this study will also indirectly allow to qualitatively assess, for the present level of grid refinement, if

the prediction of the transition region is more influenced by grid refinement in the tangential or normal direction.

5.4.2 Results

Figure 5.29 presents the average and maximum values of y^+ obtained for the flat plate when using the $\gamma - Re_\theta$ model for each set of grids, showing the differences between each grid set. Although there are slight changes depending on the transition model, the values do not significantly differ from those here shown.

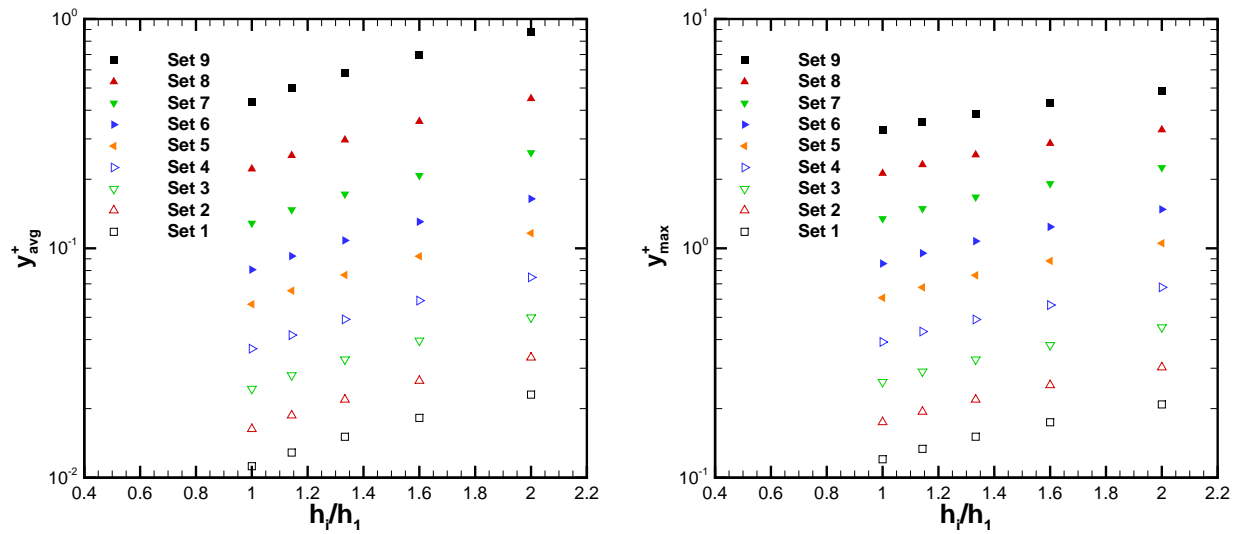


Figure 5.29: Average (left) and maximum (right) y^+ values obtained for the flat plate test case for each grid using the $k - \omega$ SST turbulence model combined with the $\gamma - Re_\theta$ transition model.

The friction resistance coefficient of the plate, C_F , obtained with the $k - \omega$ SST model coupled with each transition model is shown in Figure 5.30 both as a function of grid refinement and as the value of y_{max}^+ . Considering the $\gamma - Re_\theta$ model, from both plots it is clear that the obtained value of C_F is directly dependent on the value of y_{max}^+ . The extrapolated value of C_F for an infinitely fine grid ($h_i/h_1 = 0$) has significant variations for grid sets 9 through 6. Additionally there is a stronger reduction of the numerical error by decreasing the value of y^+ rather than through grid refinement. This is evidenced by the fact that the solution of the coarsest grid of grid set 1 is closer to the extrapolated solution at $h_i/h_1 = 0$ than the finest grids of the majority of the other grid sets. Small differences for the entire grid set are only obtained for sets 3 through to 1, for which $y_{max}^+ < 0.45$ for all grids. Furthermore, in general, there is always an increase in C_F as the grid is refined. Regarding the γ and AFT models, there is a clear influence of y_{max}^+ on the predicted value of C_F . However, there exists a larger influence of the grid refinement level than that which was observed for the $\gamma - Re_\theta$ model. In the case of the $k - \omega$ SST + γ formulation, this is visible in the absence of monotonic behaviour as the size of the first near wall cell is decreased, and the larger scatter in the data. With regards to the $k - \omega$ SST + AFT combination, whereas its behaviour follows closely that described for the $k - \omega$ SST + $\gamma - Re_\theta$ model, the coarsest grid of grid sets 1 through 6 appears to be off the trend of the remaining grids.

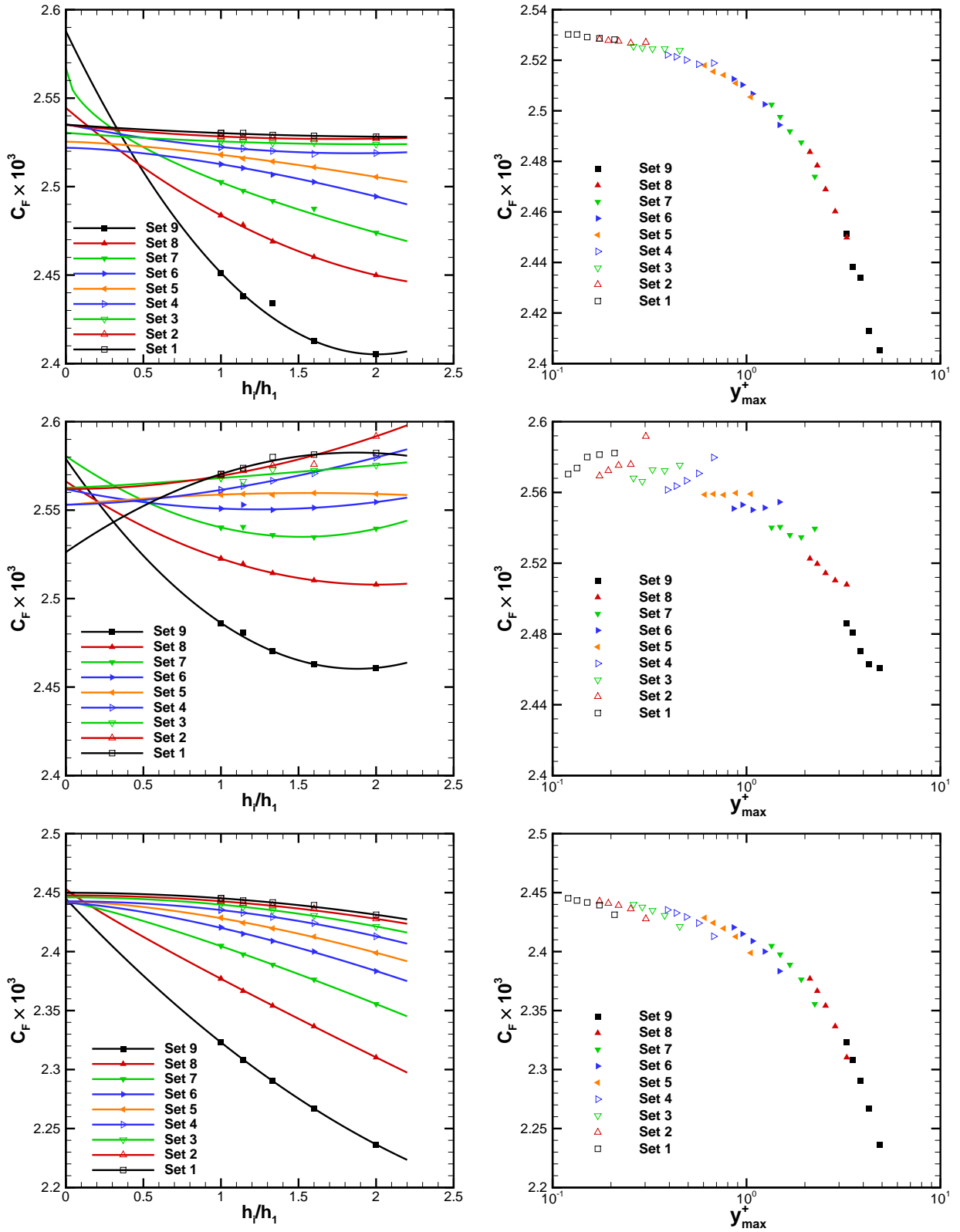


Figure 5.30: Convergence of the friction coefficient of the plate obtained with the $k - \omega$ SST model coupled with the $\gamma - Re_\theta$ (top), γ (middle) and AFT (bottom) models, with grid refinement (left) and with the maximum y^+ value (right).

Figure 5.31 presents a similar analysis but for the $\gamma - Re_\theta$ and γ models combined with the KSKL turbulence model. For these two cases there is no significant improvement in the decrease of y_{max}^+ , as all nine grid sets exhibit a similar behaviour. This means that the dominant source of the discretization error comes from the overall level of grid refinement. Moreover it can be seen that the KSKL + γ formulation possesses the highest sensitivity to the level of grid refinement.

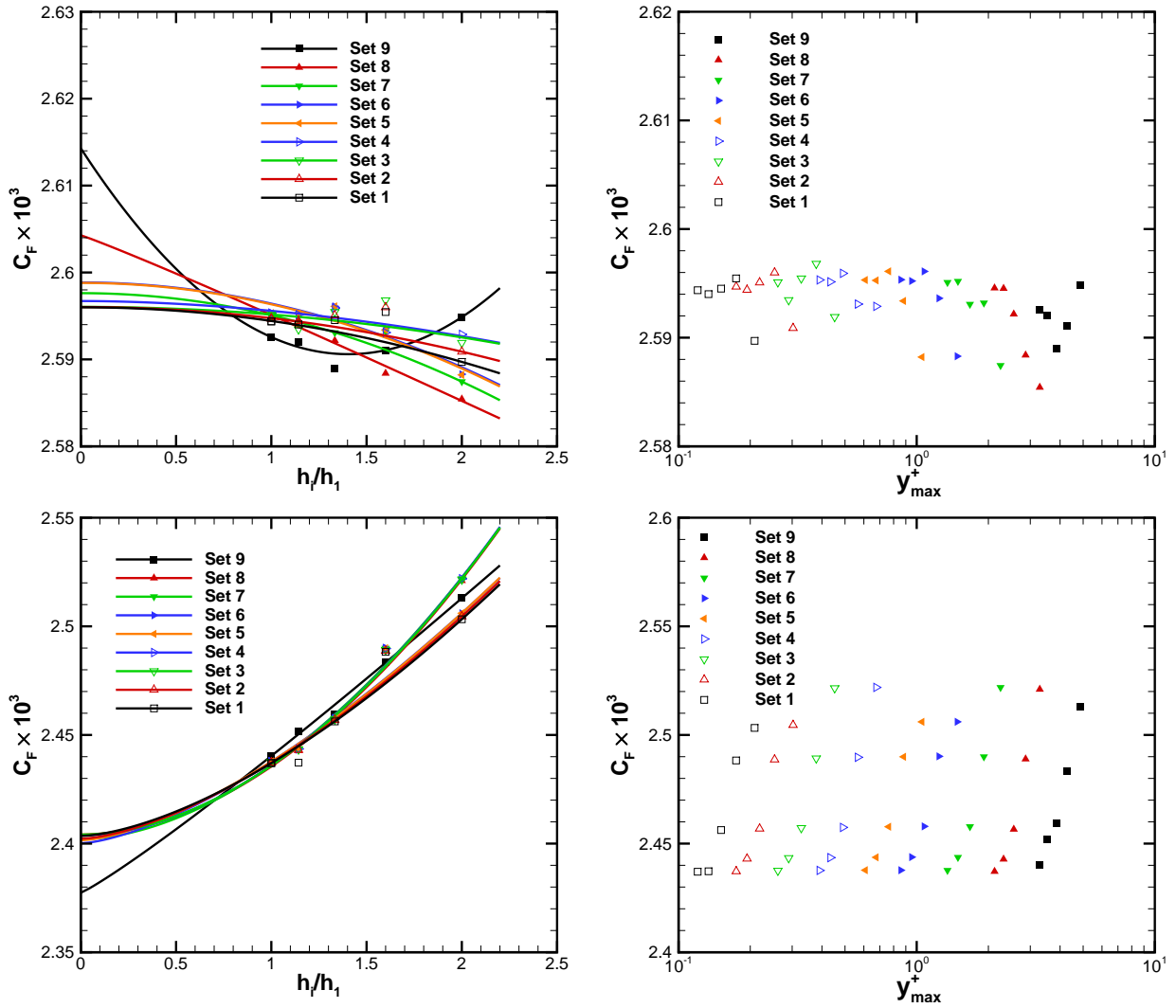


Figure 5.31: Convergence of the friction coefficient of the plate obtained with the KSKL model coupled with the $\gamma - Re_\theta$ (top) and γ (bottom) models, with grid refinement (left) and with the maximum y^+ value (right).

The comparison of all cases shows that the γ transition model is more dependent on the grid refinement level than the other two transition modelling options. In addition, for the same transition model, while the $k - \omega$ SST model is clearly more sensitive to the size of the first near wall cell than the KSKL model, the former does require finer grids. These trends match with those observed when no transition model is used [31]. Furthermore, comparing the estimate of the exact solution obtained for each grid set for the $k - \omega$ SST model, regardless of the transition model used, to that obtained in Ref. [31], shows that y_{max}^+ has more influence when a transition model is used.

A local analysis of the effect of y_{max}^+ is displayed in Figure 5.32 at $Re_x = 5 \times 10^5$ and $Re_x = 5 \times 10^6$.

The first location corresponds to laminar flow for all model combinations, while at the second one, the flow is already fully turbulent. Only the $\gamma - Re_\theta$ model is considered, as the trends exhibited with the γ or AFT models are similar, as observed in the grid convergence of C_F . Fig. 5.32 shows that only the set with the largest value of y_{max}^+ shows any sort of influence in the laminar region, as the remaining solutions are nearly coincident, although there is more scatter in the data when the KSKL model is used. The small effect of y^+ is to be expected, since in the laminar region the influence of the turbulence model should be minimal. At the turbulent region, the convergence of C_f with grid refinement follows closely that observed for the resistance coefficient of the plate. In the case of the $k - \omega$ SST model, there is an increase in C_f as the size of the first near wall cell is decreased, whereas this effect is minimal if the KSKL model is used.

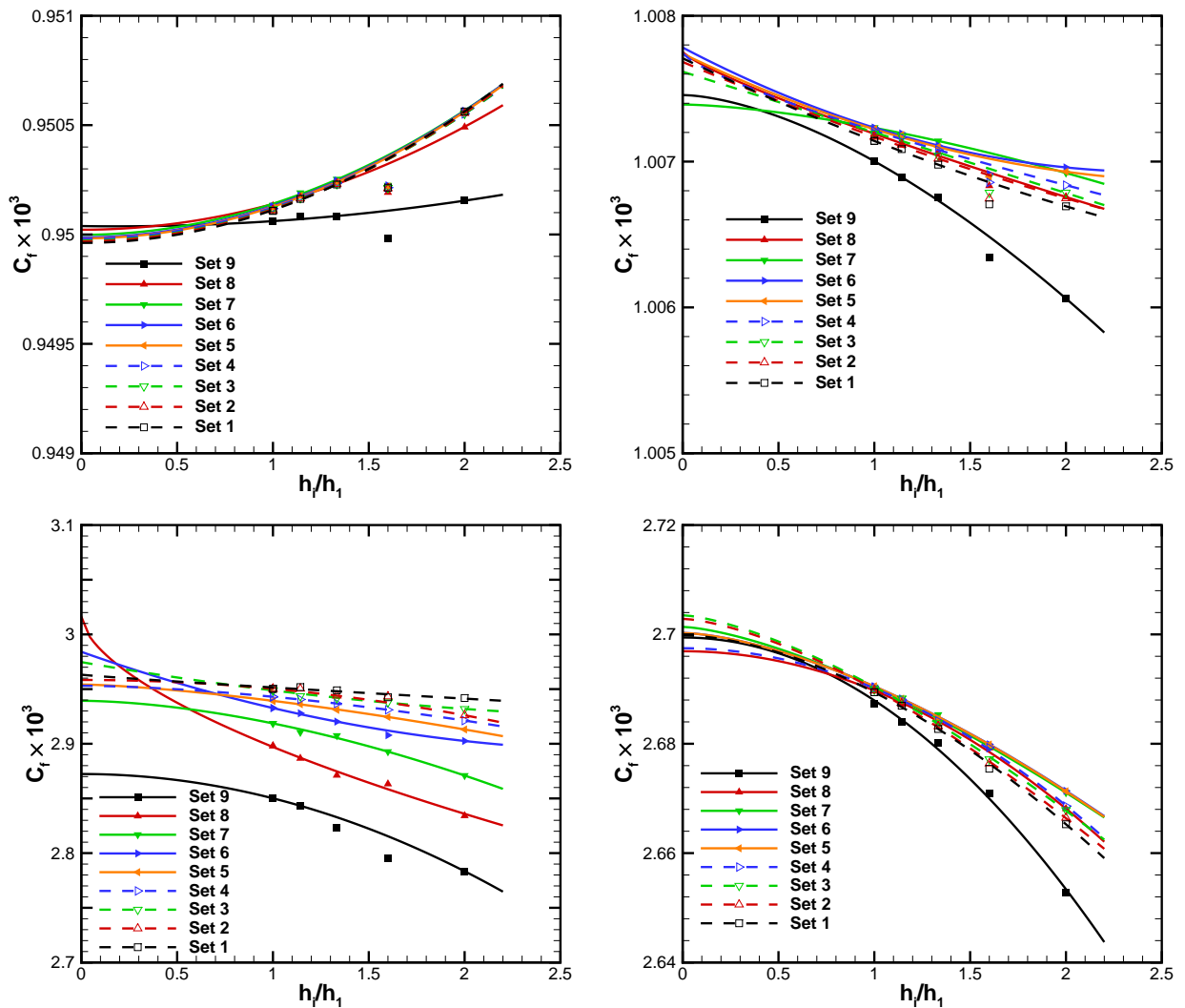


Figure 5.32: Convergence of the skin-friction coefficient with grid refinement at $Re_x = 5 \times 10^5$ (top) and at $Re_x = 6 \times 10^6$ (bottom) for the $k - \omega$ SST (left) and KSKL models combined with the $\gamma - Re_\theta$ transition model.

To conclude the flat-plate test case, the evolution of the skin friction coefficient in the vicinity of the transition region, which is depicted in Figure 5.33, is now considered. Once again, only the $\gamma - Re_\theta$ model is illustrated, as well as the finest and coarsest grids of the sets with highest (set 9) and lowest

(set 1) values of y^+ . For the $k-\omega$ SST + $\gamma-Re_\theta$ formulation, the start of transition is mostly independent of y^+ , as it is the same for both sets. This also hints at a negligible influence of the refinement in the wall normal direction, since if the streamwise spacing is constant the predicted location for transition is nearly the same. However, the evolution of C_f in the transition region is affected by y^+ . There is also a slight shift of transition downstream due to grid refinement, which takes place for both sets, possibly due to the refinement in the streamwise direction. The influence of the y^+ value is clearly seen in the turbulent region. Whereas there is an increase of the C_f level with grid refinement for set 9, there is no change in C_f in the turbulent region as the grid is refined for set 1. In the case of the KSKL + $\gamma-Re_\theta$, the influence of y^+ is minimal, as solution obtained in the finest grid of set 9 coincides with that of the finest grid of set 1. On the other hand, the shift of the transition location with grid refinement is more significant than that observed for the $k-\omega$ SST turbulence model.

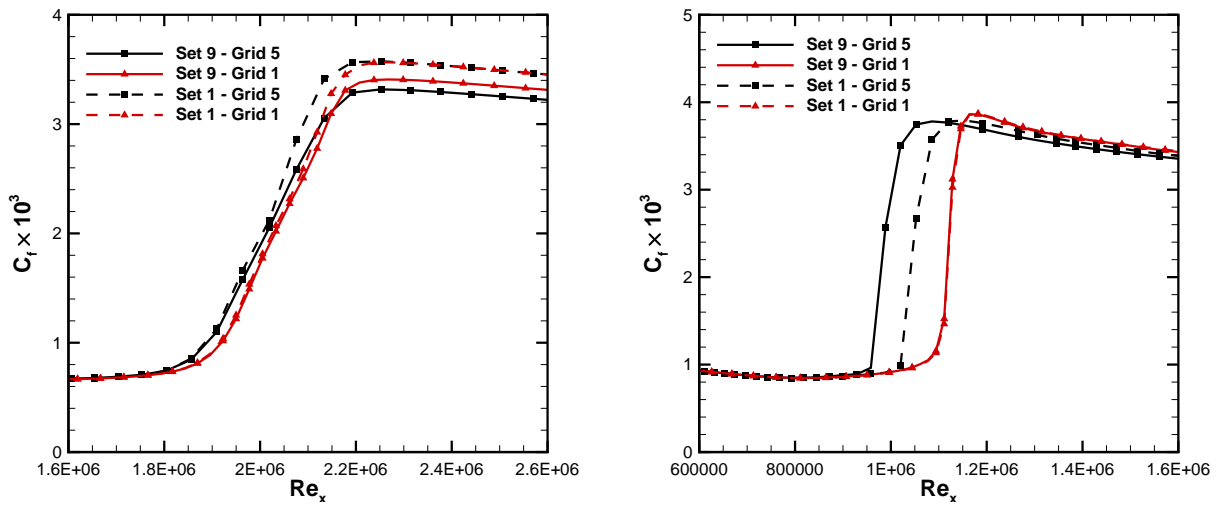


Figure 5.33: Skin friction coefficient distribution in the vicinity of the transition region for the coarsest and finest grids of set 9 and set 1 for the $k-\omega$ SST (left) and KSKL models combined with the $\gamma-Re_\theta$ transition model.

Attention is now given to the NLF₁-0416 airfoil, for which the maximum and average y^+ values obtained for the $k-\omega$ SST combined with the $\gamma-Re_\theta$ transition model are displayed in Figure 5.34. Due to the criteria selected for the generation of each grid set, the changes between each set are larger for grid sets 1 through 5 than for sets 5 through 9.

Figure 5.35 presents the convergence with grid refinement of $C_{d,f}$ and $C_{d,p}$ for the $k-\omega$ SST + $\gamma-Re_\theta$ formulation. The behaviour is similar to that observed in Figure 5.30 for the flat plate case, in that there is a reduction of the numerical error as y^+ is decreased, which is more pronounced for sets 5 through 1. This is again visible in the fact that the solution obtained at the coarsest grid of grid set 1 is closer to the extrapolated solution at $h_i/h_1 = 0$ than the finest grid of all other grid sets. It is also noted that this effect is not limited to the friction drag, but it also occurs for the pressure component. However, for the latter there is also a stronger sensitivity to the grid refinement level, as the solution at $h_i/h_1 = 0$ is different for each grid set. This shows that finer grids are required to estimate the exact solution of $C_{d,p}$. Equivalent plots are given in Figures 5.36 and 5.37 for the $k-\omega$ SST model along with the γ and AFT transition models. Similarly to the previous test case, the behaviour is the same

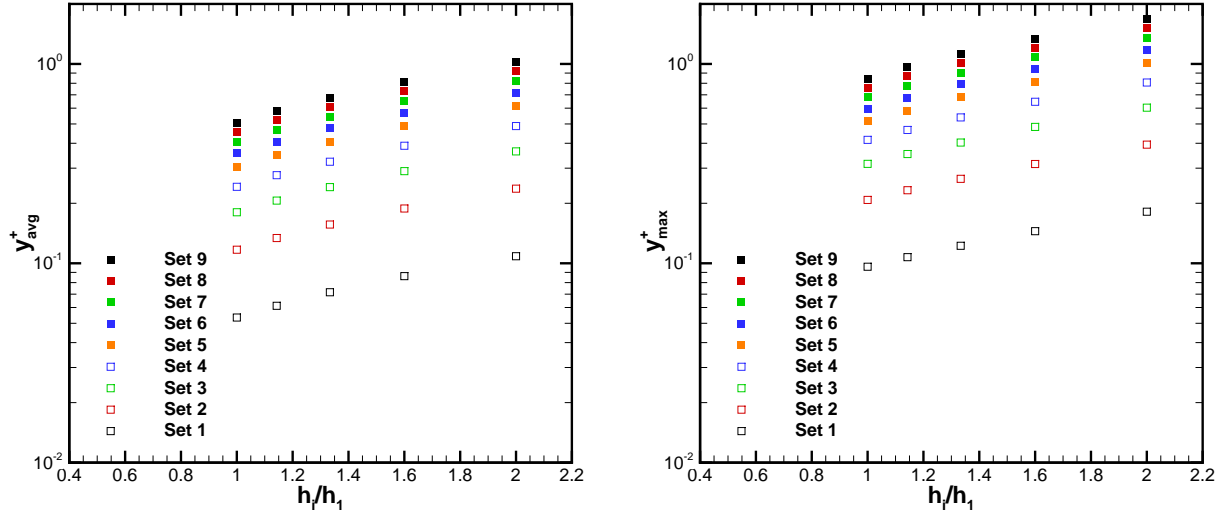


Figure 5.34: Average (left) and maximum (right) y^+ values obtained for the NLF₁-0416 airfoil test case for each grid using the $k - \omega$ SST turbulence model combined with the $\gamma - Re_\theta$ transition model.

regardless of the transition model used. Although not shown, the evolution of $C_{l,p}$ shows the same evolution as $C_{d,p}$, which is only natural since both are obtained from the pressure distribution. Once again, the γ model exhibits the highest dependency on the grid refinement level.

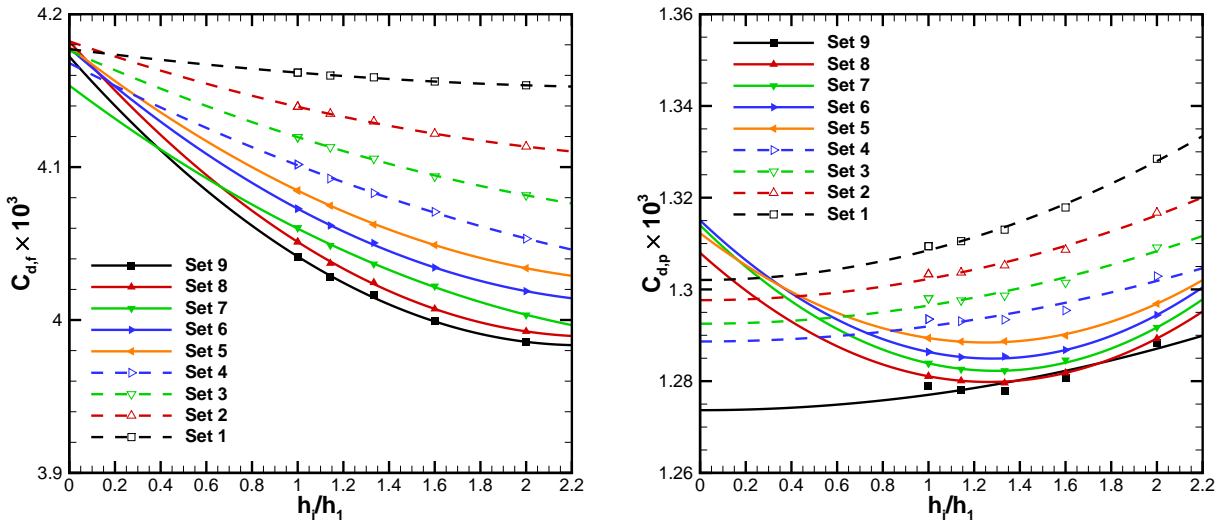


Figure 5.35: Convergence of the friction (left) and pressure (right) components of the drag coefficient obtained with the $k - \omega$ SST + $\gamma - Re_\theta$ formulation with grid refinement.

Changing the underlying turbulence model from the $k - \omega$ SST to the KSKL model, the strong sensitivity to y^+ becomes much smaller and the predominant effect becomes the level of grid refinement. This is shown in Figures 5.38 and 5.39. This trend matches exactly what was seen in the flat plate test case. The higher change of $C_{d,f}$ and $C_{d,p}$ in the formulations based on the $k - \omega$ SST model is again caused by the increasing level of C_f as y_{max}^+ is decreased. On the contrary, the KSKL model exhibits a very small change in C_f in the turbulent region.

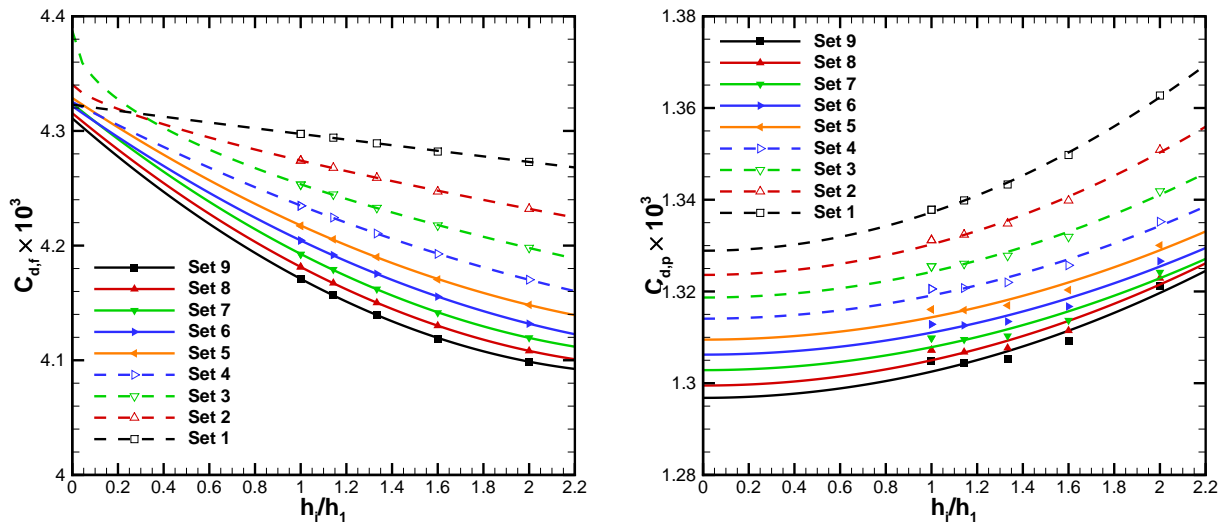


Figure 5.36: Convergence of the friction (left) and pressure (right) components of the drag coefficient obtained with the $k - \omega$ SST + γ formulation with grid refinement.

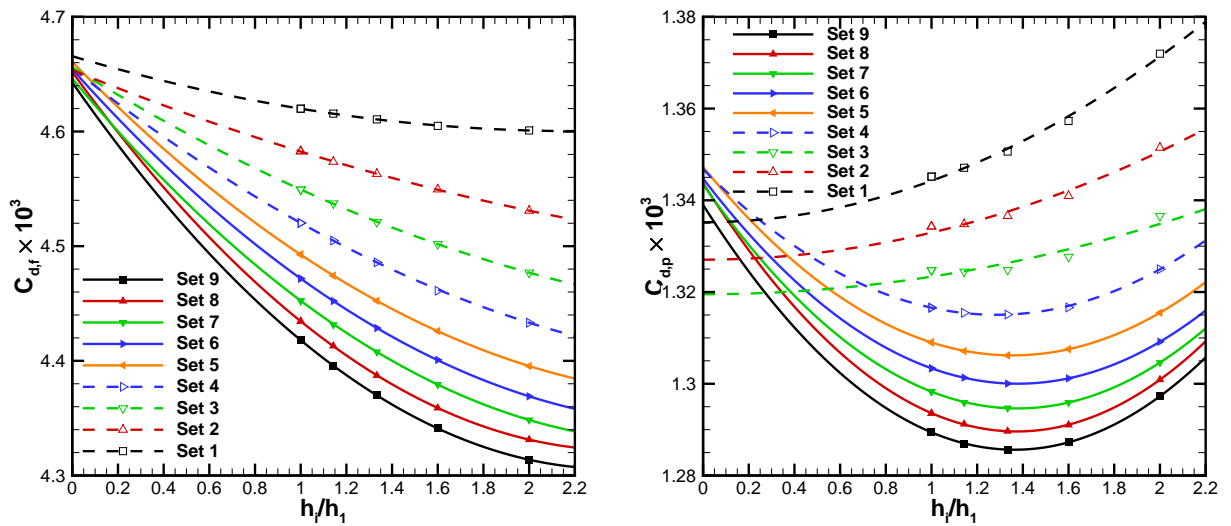


Figure 5.37: Convergence of the friction (left) and pressure (right) components of the drag coefficient obtained with the $k - \omega$ SST + AFT formulation with grid refinement.

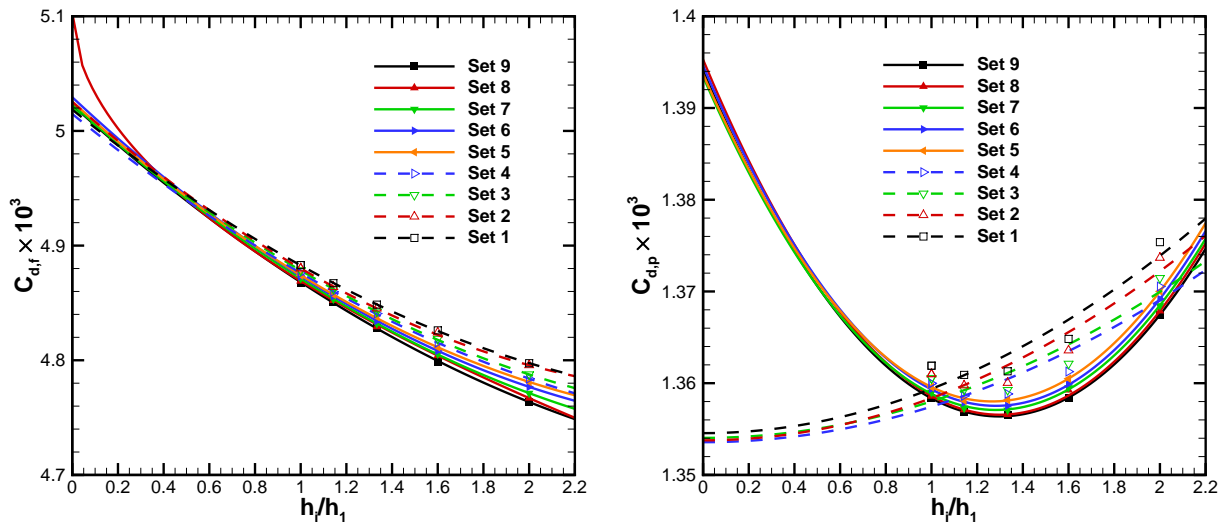


Figure 5.38: Convergence of the friction (left) and pressure (right) components of the drag coefficient obtained with the KSKL + $\gamma - Re_\theta$ formulation with grid refinement.

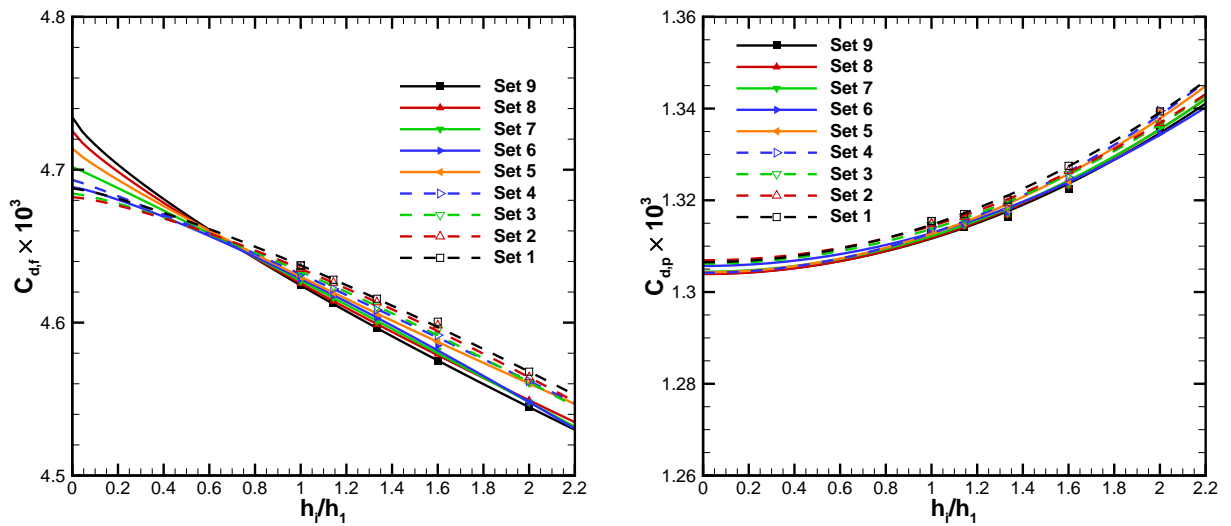


Figure 5.39: Convergence of the friction (left) and pressure (right) components of the drag coefficient obtained with the KSKL + γ formulation with grid refinement.

5.5 Main Remarks

The results presented in the previous section show that numerical solutions with transition models may behave significantly different from calculations that do not use a transition model. With respect to the numerical robustness, it is clear that the introduction of a transition model introduces more obstacles. There is a noisy iterative convergence, with significant residual oscillations. In many cases, residual stagnation may also occur. This is mainly due to either more challenging flow conditions, such as laminar flow separation, or due to the switches and limiters present in the formulation of each transition model through the form of \min and \max functions. The former situation is a consequence of the flow features that can be obtained through the use of transition models, while the latter can be addressed by using an alternative formulation for some of the limiters. While this approach greatly improves iterative convergence in the cases where residual stagnation took place, it is still a modification of the original model and leads to slightly earlier transition in the cases where it was tested.

In what concerns the influence of the convective discretization scheme, it is shown that for the cases studied, in calculations where a transition model is not used there is no noticeable difference in mean flow quantities between using a first or second order scheme in the transport equations pertaining to the turbulence model. This justifies the common approach undertaken of using first order schemes for these equations, in order to ensure numerical stability. The situation is much different when a transition model is used. In this case, the influence of the discretization of the convection term of the transport equations associated with the transition model is dependent on the transition model used. For the γ and AFT models, the influence is minimal, while for the $\gamma - Re_{\theta}$ model there is a small change. However, the influence of the scheme used in the transport equations of the turbulence model is far more significant, for all the transition models used. This is caused in part by the strong influence of the freestream values of the turbulence variables which undergo a steep decay that is generally underestimated due to insufficient grid refinement in the freestream. Moreover, for the particular case of the γ model, very large numerical errors caused by a wrong predicted location of transition can be obtained in coarse grids when a first order upwind scheme is used in the equations of the turbulence model.

While the study on the convective discretization scheme showed opposite trends between transitional flow calculations and those that rely solely on the turbulence model, the study on the effect of the maximum y^+ value showed a similar behaviour. In the test cases addressed, there is a clear influence of the size of the first near wall cell when the $k - \omega$ SST model is used as the underlying turbulence. This is verified in both friction and pressure forces, with the most noticeable change being the increase of C_f in the turbulent flow region as y^+ is decreased. In many cases, it appears to be more beneficial to reduce the y^+ value than to refine the grid in order to decrease the numerical error. There is no noticeable effect from the transition model used, as the three alternatives tested for the $k - \omega$ SST model displayed the same behaviour, although it is clear that the use of some transition models requires finer grids. Furthermore, it appears that for the present level of grid refinement, the refinement level in the streamwise direction is more important than in the wall normal direction, if y_{max}^+ is kept the same. On the other hand, the calculations with the KSKL model acting as the underlying turbulence model

show a minimal influence of the size of the first near wall cell, exactly matching the trends observed for calculations that do not use any transition model [31]. However, the use of the KSKL model is more affected by the grid refinement level.

Considering all of the above, it is apparent that the numerical side of transitional flow calculations is as challenging, if not more, than calculations that rely solely on a turbulence model. The now important effect of the convection discretization scheme matches unfavourably with the added iterative convergence difficulties, which may force the use of first order schemes on complex geometries. There is also a noteworthy aspect that the numerical error arises mostly from the turbulence model itself. Most trends observed are common and independent of the transition model used, and the discretization scheme is much more impactful on the equations of the turbulence model than of the transition model. However, this is only the case when a transition model is present, indicating that its use can result on a different behaviour of the underlying turbulence model than what is seen at high Reynolds numbers when transition modelling is not required.

Chapter 6

Results Part II: Modelling Aspects

6.1 Introduction

This chapter is dedicated to assessing modelling aspects that affect the prediction of the onset of transition. Section 6.2 is concerned with the effect of the limiter employed in the production term of the transport equation for the turbulent kinetic energy in the $k - \omega$ SST turbulence model. Two forms of the limiter are studied, the Kato-Launder limiter and the one based on the dissipation term, with three different values for the underlying constant. The effect of the inlet boundary conditions, which is of extreme importance for the predicted location of the transition region by any transition model, is considered in Section 6.3. The impact of the variation of the turbulence intensity or eddy-viscosity at the inlet is studied and the connection is made to the decay of the turbulence quantities in the freestream. A technique to control the decay without resorting to high values of the eddy-viscosity is also presented and assessed. The conclusions from the two studies are summarized in Section 6.4.

6.2 Turbulence Production Limiter

6.2.1 Introduction

The turbulence production limiter is a feature that is studied solely for the $k - \omega$ SST model coupled with the different transition models, since it is not present in the KSKL model. Two different forms of the production limiter are studied. The first is based on the dissipation term, as expressed in Eq. 3.17 and reproduced here in a general form

$$P_k = \min(\mu_t S^2, cD_k). \quad (6.1)$$

Three values are used for the constant c :

- 10, which is the proposed value of the 2003 version of the $k - \omega$ SST model [123];
- 15, as used for the remaining computations presented in this work in order to avoid the activation of the limiter outside of the stagnation region [126];

- 20, which corresponds to the original version of the $k - \omega$ SST model from 1994 [125].

The second form employed for the limiter is the Kato-Launder formulation, in which P_k is computed as

$$P_k = \mu_t S \Omega. \quad (6.2)$$

This approach uses the vorticity to prevent the excess of turbulence production in the stagnation region without resorting to the dissipation term.

The two test cases addressed for this study are the flow over the flat plate and around the NACA 0012 airfoil at $\alpha = 0^\circ$. The four variants of the production limiter are tested on the two geometries, for the $k - \omega$ SST model without any transition model and combined with the $\gamma - Re_\theta$, γ and AFT transition models. The inlet boundary conditions used for each case are given in Table 6.1.

Table 6.1: Angle of attack and inlet turbulence quantities for each test case for the calculations performed for the study of the effect of turbulence production limiter.

Case	Angle of Attack	Tu_{in}	$(\mu_t/\mu)_{in}$	x_F	N_{crit}	Tu_{LE}
Flat Plate (OH Grid)	-	5.37%	280	Not used	8	2.5%
NACA 0012	0°	3%	100	Not used	9	0.4%
NACA 0012	0°	3%	10	Not used	9	0.12%
NACA 0012	0°	3%	1	Not used	9	0.03%
NACA 0012	0°	3%	0.1	Not used	9	0.01%
6:1 Prolate Spheroid	5°	0.5%	250	Not used	-	0.15%

6.2.2 Results

The solution obtained for the skin-friction coefficient for each combination of the transition models with the $k - \omega$ SST model on the flat plate is given in Figure 6.1. The conclusions are the same regardless of the transition model used, as there appears to be no sensitivity to the limiter used for the production of k . However, the same does not hold true for the NACA 0012 calculations.

Figure 6.2 shows that, for the NACA 0012 case, the skin-friction coefficient obtained with the $k - \omega$ SST model is slightly dependent on the turbulence production limiter used. The simulation that employs the Kato-Launder formulation exhibits a larger value of C_f in the turbulent region, while also being the last one to exhibit transition. On the other hand, the calculations with the dissipation based limiter present the same level of C_f in the turbulent region. The solution for $c = 20$ displays transition earlier, with a gradual shift downstream as the constant of the limiter is decreased. In spite of the differences, the location of transition differs by less than 1% of the chord between all formulations, and no significant influence is shown by the inlet eddy-viscosity.

The usage of the $\gamma - Re_\theta$ transition model leads to a much stronger dependence on the turbulence production limiter, which is also influenced by the inlet eddy-viscosity. This is illustrated in Figure 6.3. Following the trend of the $k - \omega$ SST model, the Kato-Launder formulation leads the transition location being predicted further downstream than the other alternatives. For the case where $\mu_t/\mu = 100$, the transition locations predicted by the Kato-Launder formulation and the dissipation based approach using

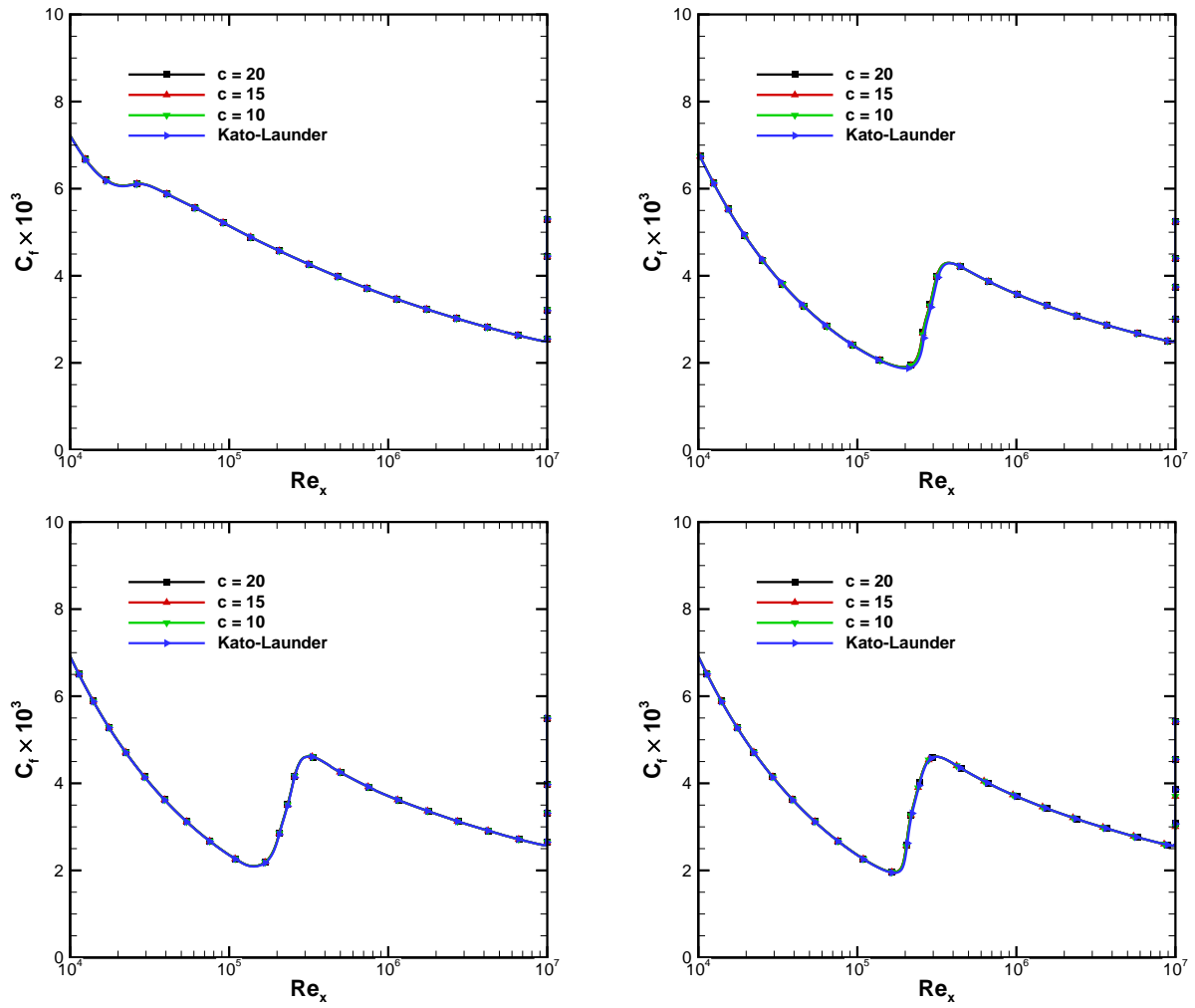


Figure 6.1: Skin-friction coefficient distribution for the flat plate test case using the $k - \omega$ SST model (top left) combined with the AFT model (top right), the $\gamma - Re_{\theta}$ model (bottom left) and the γ model (bottom right) for different formulations of the turbulence production limiter.

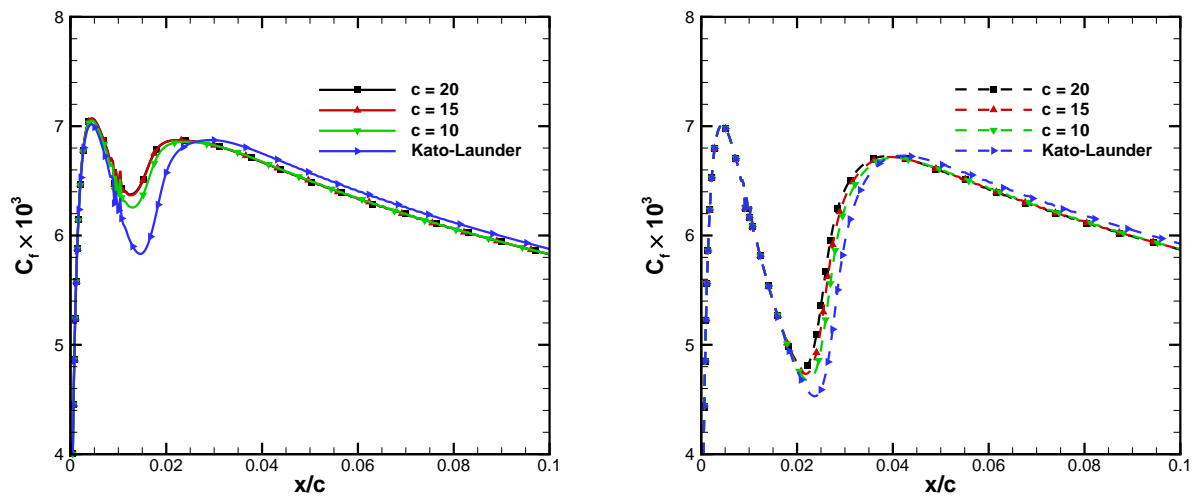


Figure 6.2: Skin-friction coefficient distribution for the NACA 0012 test case in the vicinity of the leading edge, using the $k - \omega$ SST model without a transition model, with different alternatives for the turbulence production limiter with inlet eddy-viscosity ratio of 100 (left) and 0.1 (right).

$c = 20$ differ by more than 10% of the chord. Across the range tested for the inlet eddy-viscosity, the gap between the solutions of each limiter reduces with the decrease of the eddy-viscosity. Considering only the approach based on the dissipation term, the solution for $c = 20$ and $c = 15$ are very similar when $\mu_t/\mu = 100$, with the transition location for $c = 10$ being predicted around 3% of the chord downstream of the others. As the eddy-viscosity is decreased to 10, the differences between $c = 10$, $c = 15$ and $c = 20$ increase. Considering that the decrease of the eddy-viscosity causes the production term to decrease as well, this should lead to smaller differences between each solution and less impact from the limiter. Since that is not the case, that means that the predominant effect comes from a decrease of the dissipation term, making the limiter more strict and providing different solutions for each value of c . As the inlet eddy-viscosity is lowered to 1 and 0.1, the solutions for each limiter become more similar, and the difference in the location of transition also decreases.

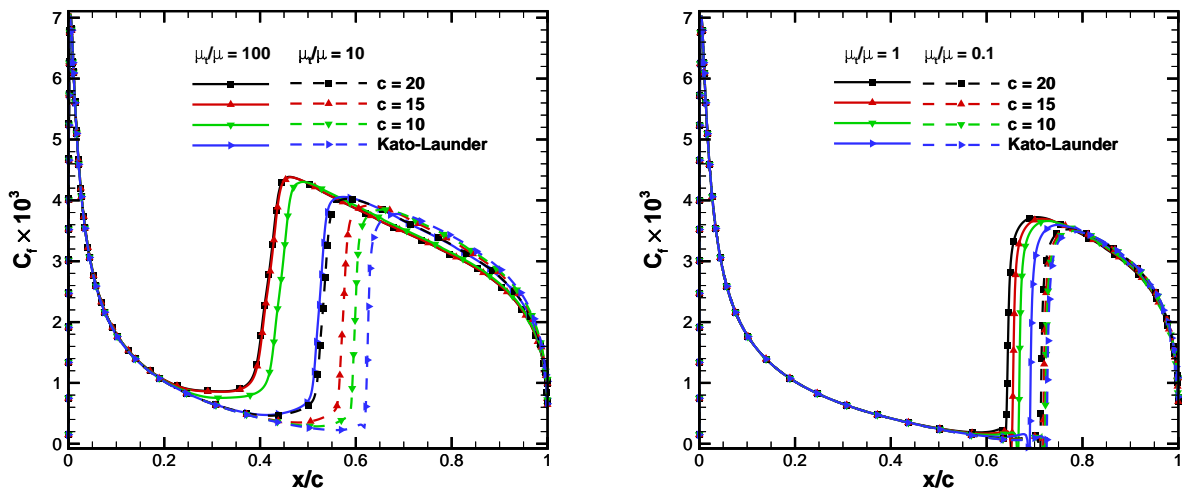


Figure 6.3: Skin-friction coefficient distribution for the NACA 0012 test case, using the $k - \omega$ SST + $\gamma - Re_\theta$ model with different alternatives for the turbulence production limiter with inlet eddy-viscosity ratios of 100 and 10 (left) and 1 and 0.1 (right).

The γ model shows a smaller sensitivity to the production limiter employed. As seen in Figure 6.4, the difference in the location of transition is around 8% of the chord for $\mu_t/\mu = 100$ and under 2% for $\mu_t/\mu = 10$. As for the remaining two cases, the difference is negligible, as the skin-friction coefficient distributions are visually coincident. Thus, the γ model shows a smaller sensitivity to the turbulence production limiter employed, although there is still a significant effect when higher values are used for the inlet eddy-viscosity. Even less sensitive is the AFT model, for which there is no apparent influence of the formulation used for the turbulence production limiter. This is given in Figure 6.5, which shows that for any given value of the inlet eddy-viscosity, the solution is virtually independent of the limiter used.

From the C_f distribution for the four different model combinations tested, it is evident that the $\gamma - Re_\theta$ model is the most affected by the turbulence production limiter. In the case of the $k - \omega$ SST model without any transition model, the influence of the limiter on the location of transition is not very strong. This is mostly due to transition occurring close to the leading edge of the airfoil, where the effects of different limiters should be more evident. However, when a transition model is employed, transition does not occur upstream of $x/c = 0.35$, which is a considerable distance away from the stagnation region,

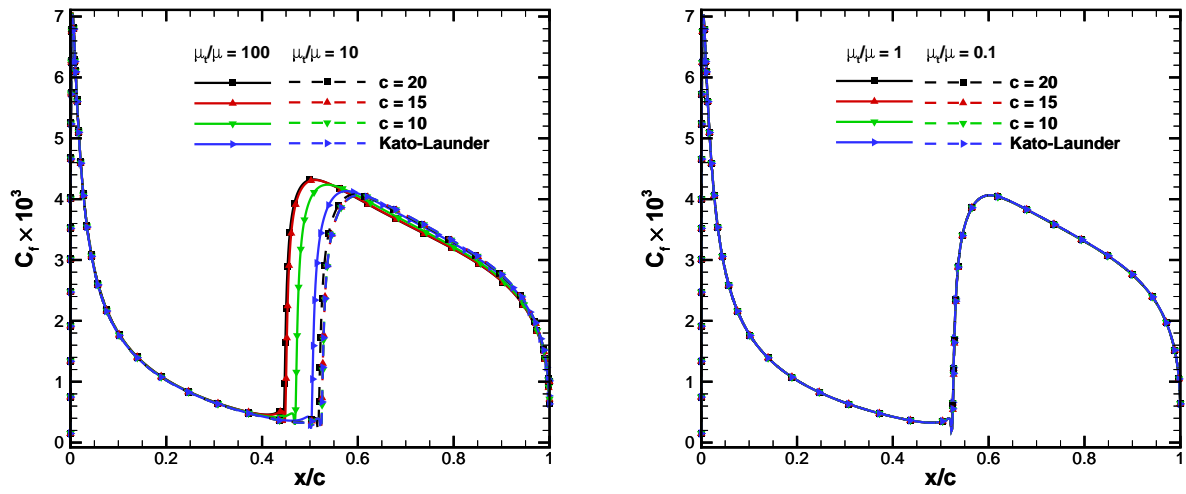


Figure 6.4: Skin-friction coefficient distribution for the NACA 0012 test case, using the $k - \omega$ SST + γ model with different alternatives for the turbulence production limiter with inlet eddy-viscosity ratios of 100 and 10 (left) and 1 and 0.1 (right).

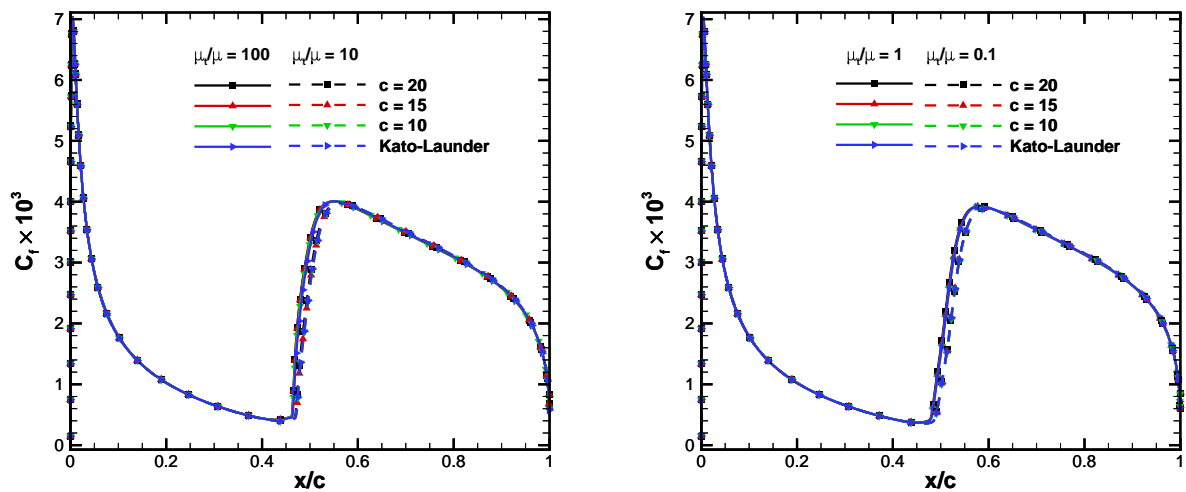


Figure 6.5: Skin-friction coefficient distribution for the NACA 0012 test case, using the $k - \omega$ SST + AFT model with different alternatives for the turbulence production limiter with inlet eddy-viscosity ratios of 100 and 10 (left) and 1 and 0.1 (right).

such that the limiter should not be active.

To further clarify the issue, the $\gamma - Re_\theta$ model with inlet eddy-viscosity set to 10 is considered, as it was the case that exhibited the strongest dependence on the production limiter employed. Figure 6.6 presents $\hat{Re}_{\theta t}$ at the leading edge of the airfoil for each formulation of the production limiter. The case where $c = 20$ presents the lowest values for $\hat{Re}_{\theta t}$, which are responsible for the earlier transition. As the constant of the dissipation based limiter is reduced, $\hat{Re}_{\theta t}$ increases, presenting its maximum values when the Kato-Launder formulation is used.

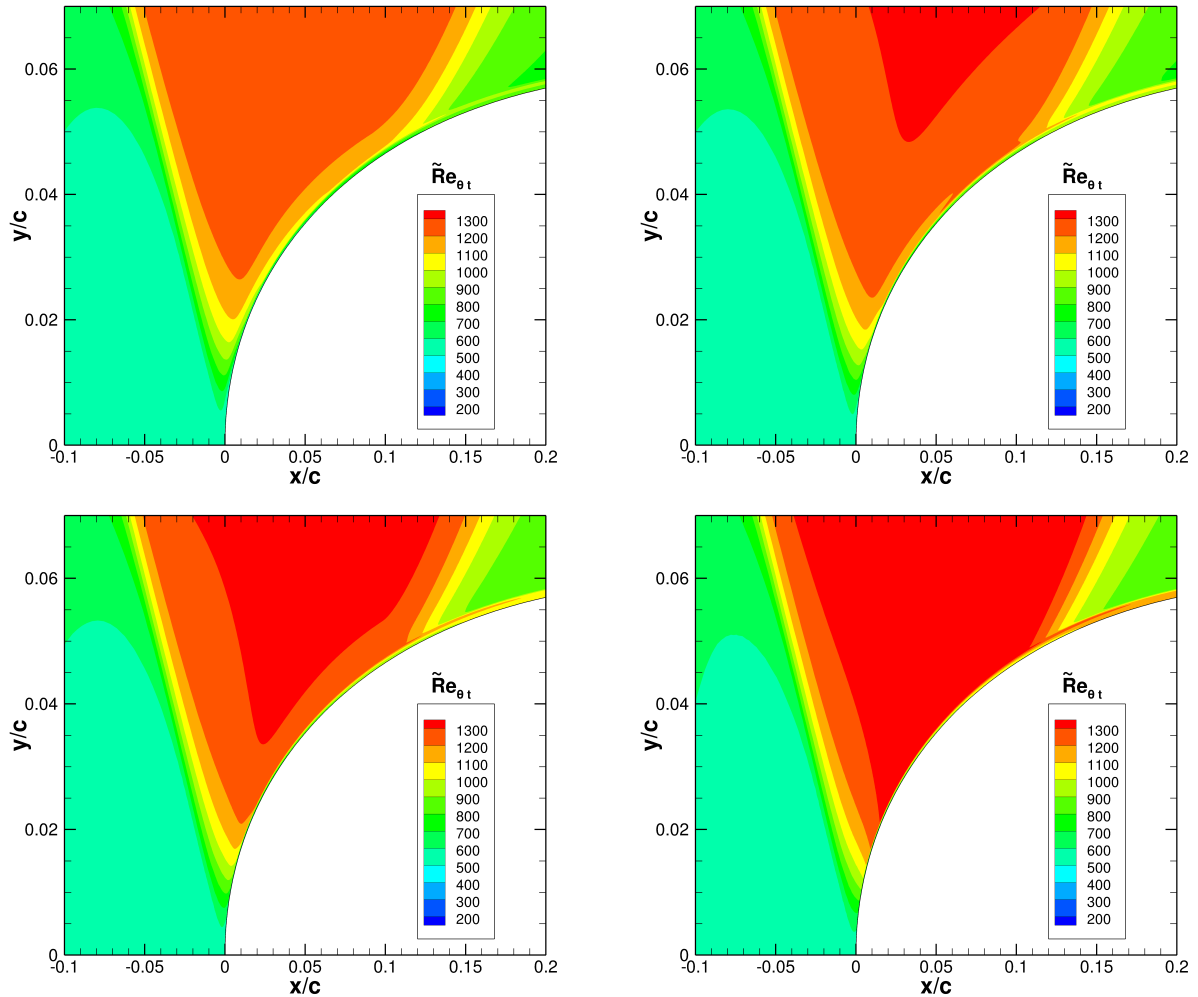


Figure 6.6: Evolution of $\hat{Re}_{\theta t}$ obtained in the vicinity of the leading edge of the NACA 0012 airfoil when using the $k - \omega$ SST + $\gamma - Re_\theta$ model for different approaches of the turbulence production limiter: $c = 20$ (top left), $c = 15$ (top right), $c = 10$ (bottom left) and the Kato-Launder formulation (bottom right).

As shown in Figure 6.7, the behaviour of $\hat{Re}_{\theta t}$ is a direct consequence of the evolution of the turbulence kinetic energy, the variable to which the production limiter is applied. For $c = 20$, the highest values of k in the freestream are obtained, which result in the lowest $\hat{Re}_{\theta t}$ field seen in Figure 6.6. As the constant of the limiter is decreased, making it more strict, the turbulence kinetic energy decreases as well. However, the effect of production at the stagnation region only completely disappears for the Kato-Launder formulation. The overall influence of the limiter is not limited to the freestream, as it affects the boundary layer as well, according to that displayed in Figure 6.8. Ultimately, the changes in $\hat{Re}_{\theta t}$ due

to the different growth of k are the cause of the differences in the location of transition.

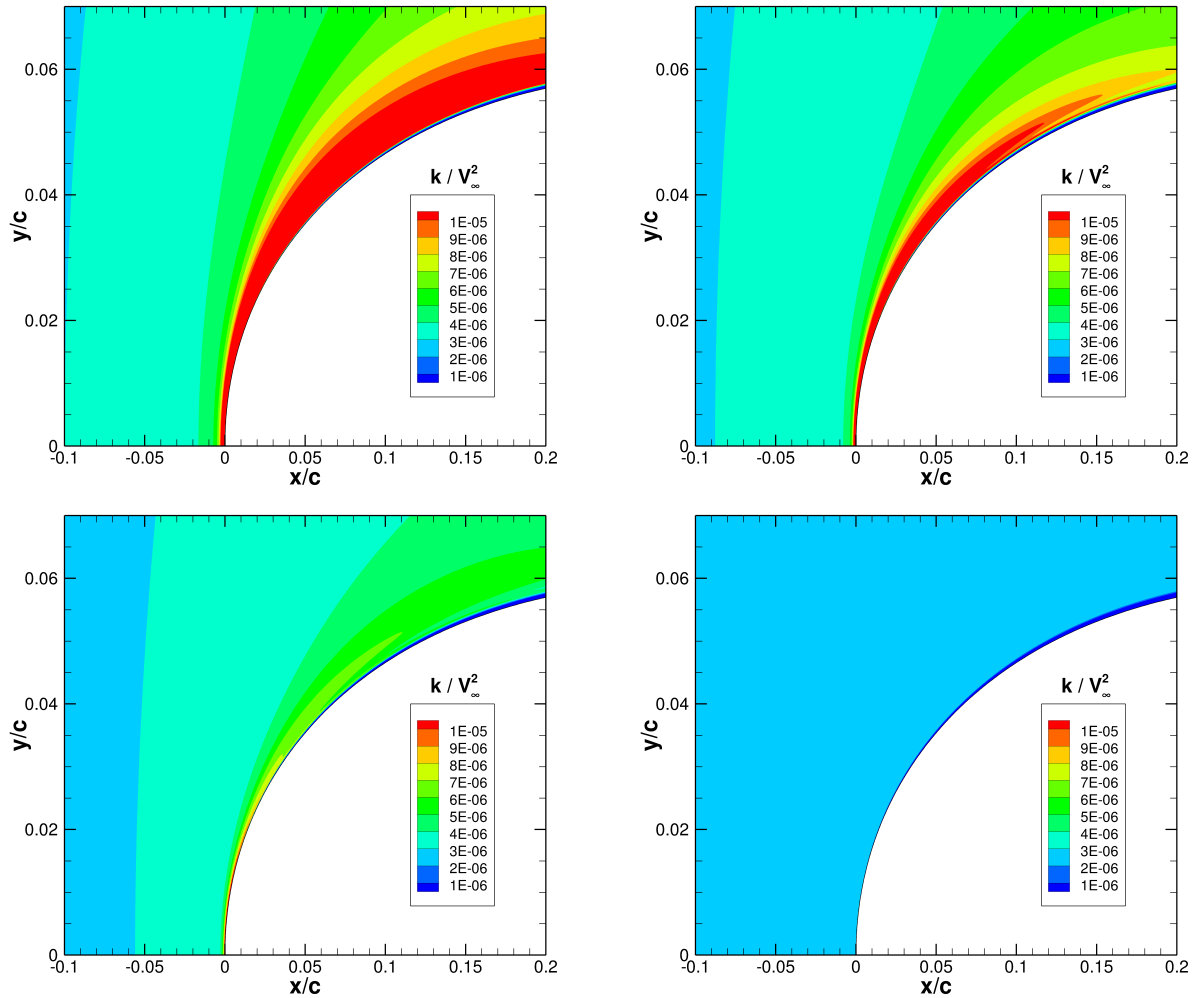


Figure 6.7: Evolution of the turbulence kinetic energy obtained in the vicinity of the leading edge of the NACA 0012 airfoil when using the $k - \omega$ SST + $\gamma - Re_\theta$ model for different approaches of the turbulence production limiter: $c = 20$ (top left), $c = 15$ (top right), $c = 10$ (bottom left) and the Kato-Lauder formulation (bottom right).

The skin-friction coefficient distribution on the surface of the prolate spheroid obtained with the $k - \omega$ SST + $\gamma - Re_\theta$ model is shown in Figure 6.9 for each different option of the turbulence production limiter. The effect of the limiter employed is more noticeable on the leeward side, close to the symmetry plane. For higher values of c , transition occurs further upstream, as a consequence of the increased production in the stagnation region. At the symmetry plane, a difference of around 8% of the spheroid's length is observed for the location of the transition region between the solutions obtained using $c = 20$ and $c = 10$. The solution with the Kato-Lauder limiter exhibits transition even further downstream than the one with $c = 10$. As the azimuthal angle is decreased, the differences between each alternative decrease. There is no significant effect of the turbulence production limiter in the windward side of the spheroid, which exhibits mostly laminar flow for all of the numerical solutions.

The trends observed for the prolate spheroid match those previously discussed for the NACA 0012 airfoil. The location of transition exhibits a strong sensitivity to the production limiter employed in the

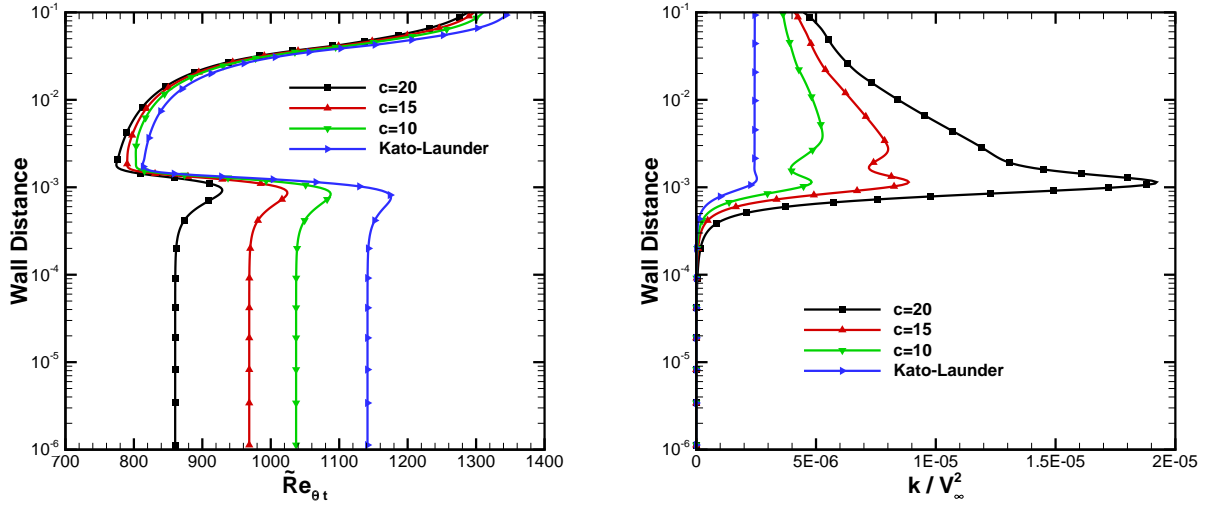


Figure 6.8: Boundary-layer profiles at $x/c = 0.2$ of $\tilde{Re}_{\theta t}$ (left) and k (right) in the upper surface of the NACA 0012 airfoil for different approaches of the turbulence production limiter.

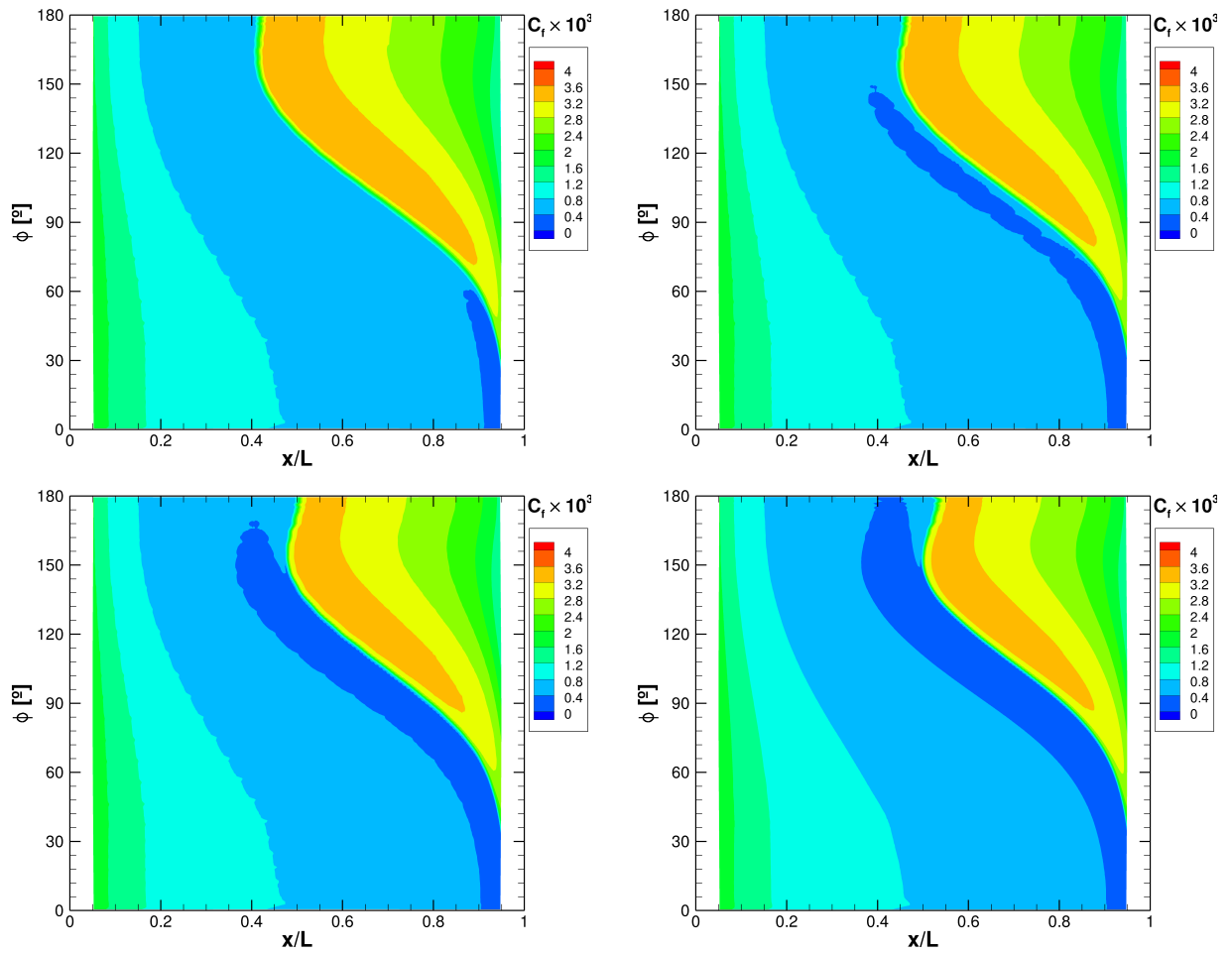


Figure 6.9: Skin-friction coefficient distribution on the surface of the prolate spheroid using the $k-\omega$ SST model combined with the $\gamma-Re_{\theta}$ model for different approaches of the turbulence production limiter: $c = 20$ (top left), $c = 15$ (top right), $c = 10$ (bottom left) and the Kato-Lauder formulation (bottom right).

$k - \omega$ SST turbulence model both in two and three dimensional flows. This is especially true when high values are used for the inlet eddy-viscosity, which is generally the case for simulations employing transition models.

6.3 Influence of Inlet Boundary Conditions & Turbulence Decay

6.3.1 Introduction

Four test cases are considered for this study. These are the flat plate, the NACA 0012 airfoil and the sickle wing. For the flat plate, the two different grid sets described in Chapter 4 are used. Table 6.2 presents the base conditions used with the Cartesian grids. A total of nine different sets of boundary conditions is used. These are divided in groups of three, each group corresponding to one of the designations used in the ERCOFTAC experiments, T3AM, T3A, and T3B. Within each group, three variants of the boundary conditions are used, labeled BC1, BC2 and BC3. Table 6.2 only presents the BC1 set, which is built to ensure that the decay of turbulence in the freestream obtained with the $k - \omega$ SST model matches that of the experimental data. The conditions for the BC2 set are the same as of the BC1 set, with the exception that x_F is not used, and so the decay starts at the inlet of the domain. Finally, the BC3 set is obtained from the BC2 conditions by reducing the eddy-viscosity ratio to 0.1.

Table 6.2: Base inlet boundary conditions used with the H grids for the flat plate test case.

Designation	Tu_{in}	$(\mu_t/\mu)_{in}$	x_F	N_{crit}	Tu_{LE}
T3AM - BC1	1.0%	7.55	$-0.05L$	2.6	0.72%
T3A - BC1	5.37%	12.7	$-0.05L$	-	1.2%
T3B - BC1	7.21%	99.2	$-0.05L$	-	3.3%

The AFT transition model is only tested for the T3AM set of cases. The reason behind this choice is related to the specification of N_{crit} according to the value of the inlet turbulence intensity following Eq. 3.117. For the Tu_{in} values used in the T3A and T3B cases, this would lead to a negative N_{crit} which has no physical meaning, and the mathematical model would be that of the $k - \omega$ SST turbulence model with the modification to the $F1$ blending function.

The second and third test cases consist of the NACA 0012 airfoil at an angle of attack of 0° and the 6:1 prolate spheroid at $\alpha = 5^\circ$. For the NACA 0012, the inlet turbulence intensity is kept constant at 3% and x_F is not used. The eddy-viscosity ratio is varied from 100 to 0.1 as described in Table 6.3. For the prolate spheroid, two sets of boundary conditions are tested, given in Table 6.4.

Table 6.3: Inlet boundary conditions used for the NACA 0012 airfoil test case.

Tu_{in}	$(\mu_t/\mu)_{in}$	x_F	N_{crit}	Tu_{LE}
3%	100	Not used	9.0	0.4%
3%	10	Not used	9.0	0.12%
3%	1	Not used	9.0	0.03%
3%	0.1	Not used	9.0	0.01%

Table 6.4: Inlet boundary conditions used for the prolate spheroid test case.

Designation	Tu_{in}	$(\mu_t/\mu)_{in}$	x_F	N_{crit}	Tu_{LE}
Set A	0.1917%	5.2	$-1.5L$	-	0.15%
Set B	0.5%	250	Not used	-	0.15%

Each of the three initial test cases serves a different purpose. The flat plate test case represents an ideal situation where enough information is known to specify the inlet conditions, through the matching of the freestream decay with the experimental measurements. Furthermore, since there is no pressure gradient, it is a good case to evaluate directly the influence of freestream turbulence. The NACA 0012 airfoil represents a case where no information is known and thus the conditions are chosen arbitrarily. In both of these test cases, variations are performed which allow a qualitative assessment of the uncertainty associated with the inlet boundary conditions for turbulence. Finally, the prolate spheroid test case represents a common situation in which a single data point is known, usually the freestream turbulence intensity at a given point in the domain. In fact, the two different conditions given in Table 6.4 have both been built so that a turbulence intensity of 0.15% is obtained at the nose of the spheroid, a general guideline used for this case [9]. Since this is the only information known, then the eddy-viscosity is not restricted and neither is the decay of turbulence.

Upon addressing the three previously described test cases, a modification to the $k - \omega$ SST model is introduced, allowing for the control of the freestream turbulence decay without resorting to the eddy-viscosity at the inlet. This modification is then tested in the three geometries addressed before. It does not solve the lack of information in the specification of the eddy-viscosity, but it allows for it to be uncoupled from controlling the freestream turbulence decay.

6.3.2 Sensitivity studies

The skin-friction coefficient distribution obtained for the flat plate with the different boundary conditions is illustrated in Figure 6.10. Calculations using only the underlying $k - \omega$ SST model are performed as well, showing that even the turbulence model itself exhibits some slight changes in the position of transition depending on the inlet conditions used. Unlike the other alternatives, the AFT model exhibits only a slight sensitivity to the change in the eddy-viscosity or turbulence decay. This effect is due to the reliance of the model on N_{crit} , meaning that all freestream information is contained in a single quantity, which in this case is related to the turbulence intensity and constant for the entire domain.

The $\gamma - Re_\theta$ and γ models exhibit very similar trends. For each group of boundary conditions, the set with the less intense decay (BC1) always predicts transition further upstream than the others, which is to be expected. With the removal of x_F (BC2 set), which causes the decay to start at the inlet of the domain rather than close to the leading edge of the plate, the position of transition moves downstream. The effect becomes stronger when the eddy-viscosity is lowered to 0.1 (BC3) in such a way that regardless of the inlet turbulence intensity, the solution is nearly the same. This behaviour is also displayed by the solutions of the $k - \omega$ SST model without any transition model. The same analysis is shown in Figure 6.11 for the $\gamma - Re_\theta$ and γ models combined with the KSKL model. The dependence

on the freestream boundary conditions is similar to that exhibited in the previous case.

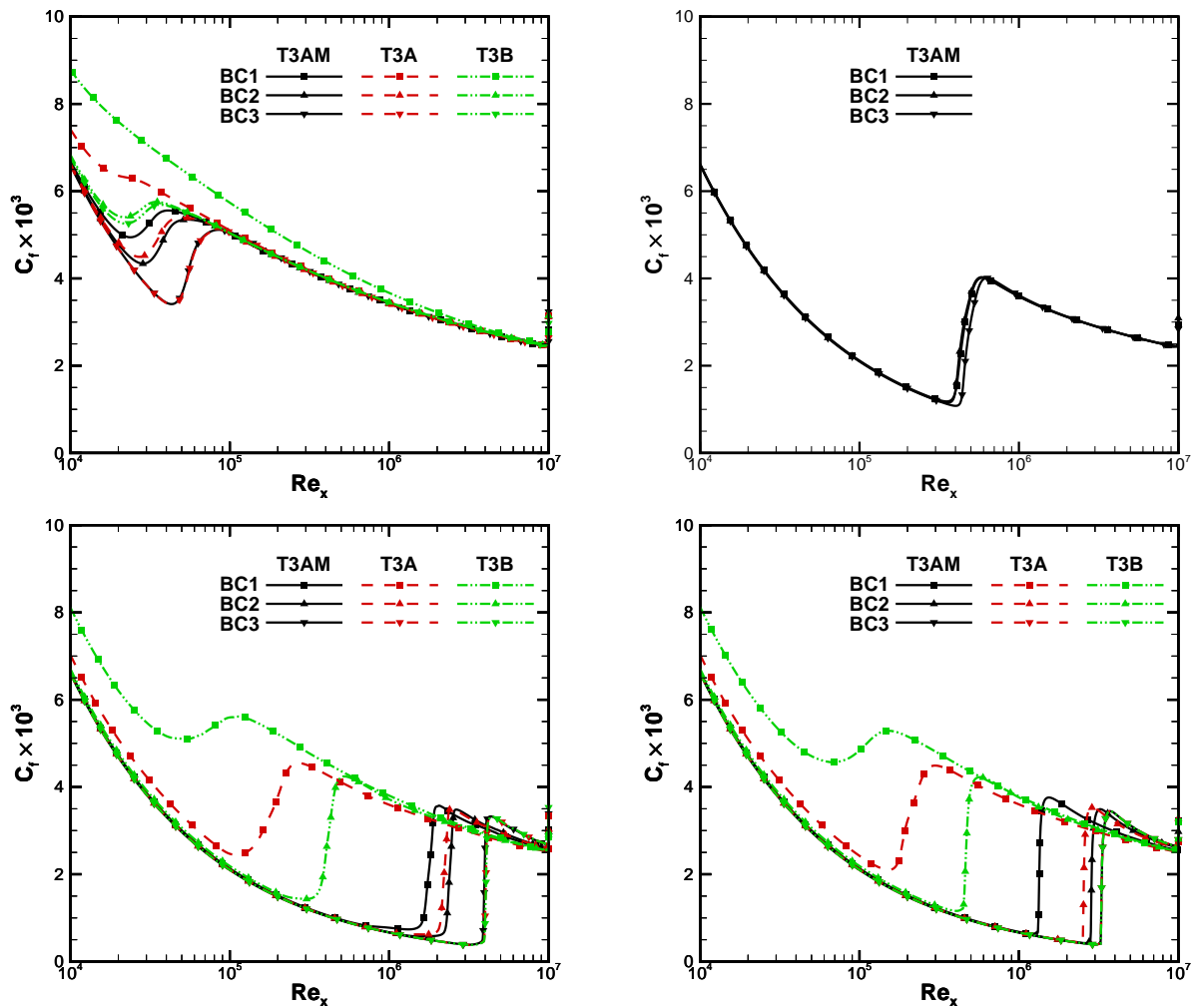


Figure 6.10: Skin-friction coefficient distribution for the flat plate test case using the $k - \omega$ SST model (top left) combined with the AFT model (top right), the $\gamma - Re_{\theta}$ model (bottom left) and the γ model (bottom right).

Another common aspect between the $\gamma - Re_{\theta}$ and γ transition models is the overprediction of C_f in the laminar region. As the freestream turbulence intensity and eddy-viscosity are increased, the C_f level predicted in the laminar region becomes higher than that of the remaining conditions and of the Blasius solution. This behaviour is undesirable and troublesome in the sense that eddy-viscosity ratios in the order of 100 are generally required to maintain a reasonable decay of the freestream turbulence. This is even more critical in practical applications in which the inlet is placed much further away from the body, leading to a larger region for turbulence to decay. While for simple geometries the use of x_F alleviates this issue, its application in complex geometries may be troublesome.

The overprediction of C_f can be traced to a deviation of the velocity profile in the laminar boundary-layer, as indicated in Figure 6.12. This is most noticeable in case T3B-BC1, and is a direct consequence of the significant value of the eddy-viscosity in the upper part of the boundary-layer. Due to the high value in the freestream, the eddy-viscosity does not decrease quickly enough in the upper part of the boundary-layer causing a distortion of the velocity profile. The non-negligible value of the eddy-viscosity

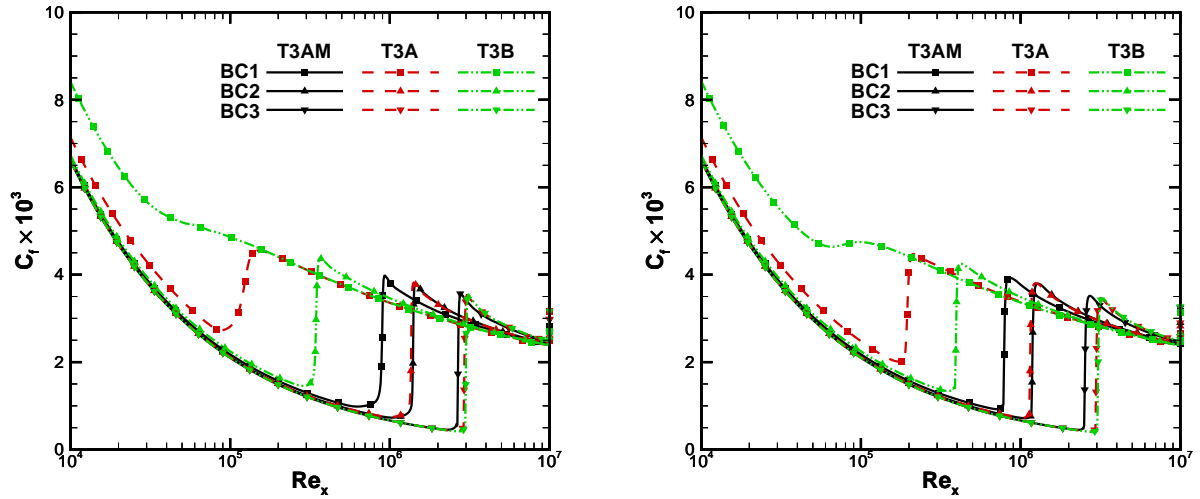


Figure 6.11: Skin-friction coefficient distribution for the flat plate test case using the KSKL model combined with the $\gamma - Re_\theta$ model (left) and the γ model (right).

can be seen as a reduction of the effective Reynolds number, which leads to the larger C_f value.

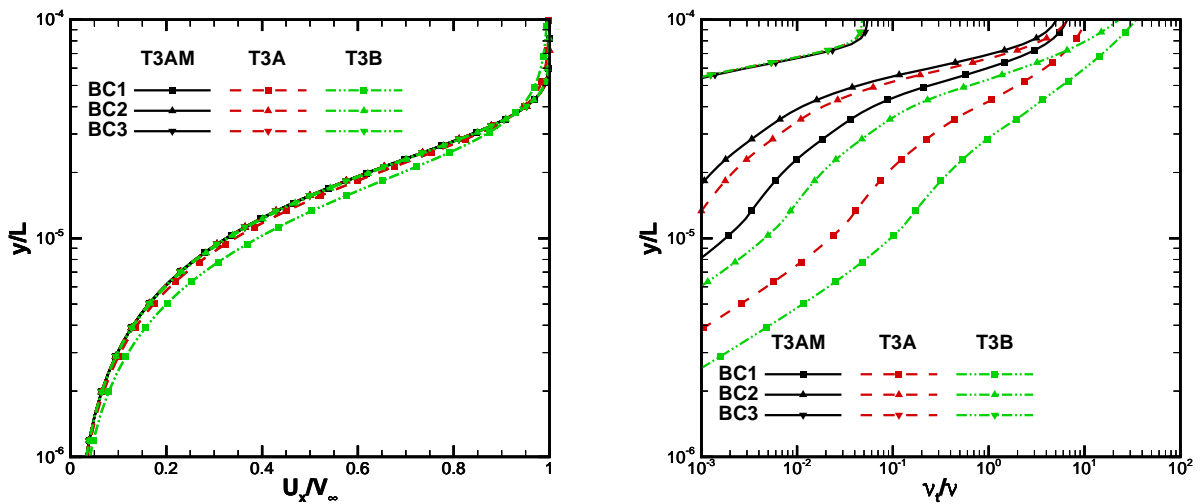


Figure 6.12: Velocity (left) and eddy-viscosity (right) profiles for the flat plate test case obtained with the $k - \omega$ SST + $\gamma - Re_\theta$ model at $Re_x = 10^4$ for varying inlet boundary conditions.

The evolution of the turbulence intensity and eddy-viscosity in the freestream is portrayed in Figure 6.13. Conditions BC3 show that if the eddy-viscosity is not high enough, then the level of turbulence in the freestream quickly decays in such a way that the value specified at the inlet has a very small impact. All three sets of conditions (T3AM, T3A and T3B) have a nearly coincident turbulence intensity evolution along the freestream when the eddy-viscosity ratio is set to 0.1 (BC3 set) despite the significantly different turbulence intensity set at the inlet. Furthermore, in the region upstream of the plate, Tu decreases by over an order of magnitude, showing the difficulty in using low values for the eddy-viscosity. As this quantity is increased, the decay becomes less steep, and differences in the evolution of the turbulence intensity are now visible depending on the value set at the inlet. The use of x_F simply keeps the turbulence quantities fixed until the desired location, changing the location at which the decay starts but not its magnitude. A much smaller decrease is exhibited by the eddy-viscosity in the freestream, never

exceeding one order of magnitude even along the entire domain.

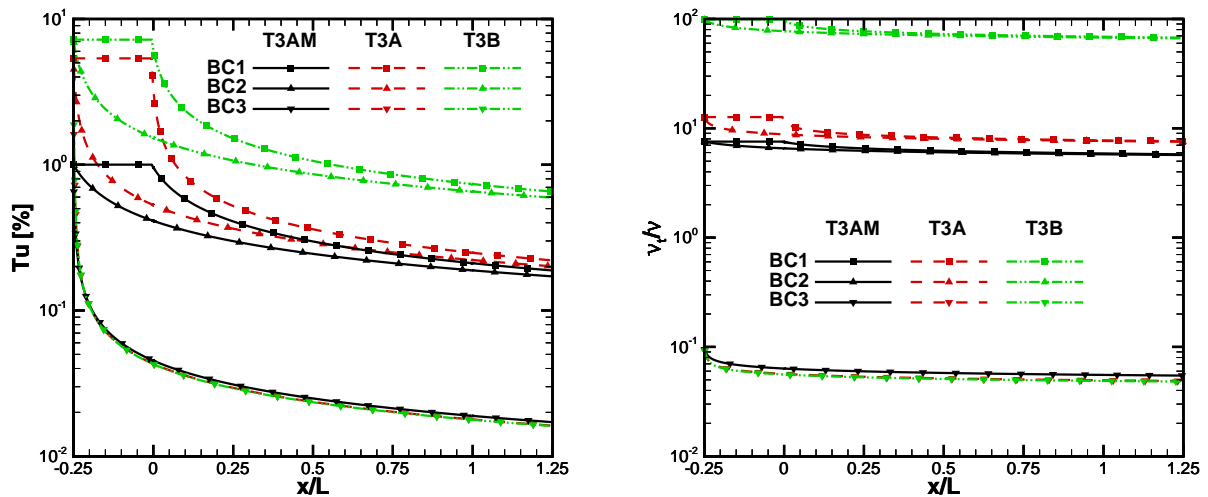


Figure 6.13: Evolution of the turbulence intensity (left) and eddy-viscosity ratio (right) in the freestream for the flat plate test case obtained when using the $k - \omega + \gamma - Re_\theta$ model for varying inlet boundary conditions.

Figure 6.14 presents the skin-friction coefficient distribution obtained in the finest grid for the NACA 0012 airfoil. For the $k - \omega$ SST model without the use of a transition model, the selected value for the inlet eddy-viscosity has a minimal influence. When the $\gamma - Re_\theta$ model is used, the location of the transition region ranges from $x/c = 0.35$ to $x/c = 0.7$, which naturally has a significant impact on the friction component of the drag coefficient. On the other hand, the γ model, which presented nearly the same behavior as $\gamma - Re_\theta$ in the flat plate test case, shows a much smaller influence of the inlet eddy-viscosity, as the solutions for $\mu_t/\mu = 10$, $\mu_t/\mu = 1$ and $\mu_t/\mu = 0.1$ are nearly coincident. This indicates this model to be more sensitive to the pressure gradient than the $\gamma - Re_\theta$ model. Regarding the AFT model, the impact of the high eddy-viscosity is felt on the evolution of C_f through the transition region rather than on the onset of transition itself.

An illustration of the velocity and $\tilde{Re}_{\theta t}$ profiles obtained with the $\gamma - Re_\theta$ model at $x/c = 0.31$ are depicted in Figure 6.15. At this location, the solution for $\mu_t/\mu = 100$ exhibits a slight shift of the velocity profile, signifying the pre-transitional boundary-layer and the corresponding increase of γ and k . The remaining solutions have a nearly coincident velocity profile in the still laminar flow. The influence of the eddy-viscosity is seen in the profiles of $\tilde{Re}_{\theta t}$. Outside of the boundary layer, there is a difference on the level of $\tilde{Re}_{\theta t}$ for each solution, with the simulation with the lowest value of the inlet eddy-viscosity exhibiting the highest level of the $\tilde{Re}_{\theta t}$ on the freestream. A noteworthy aspect is the fact that for the simulation with $\mu_t/\mu = 100$, the value of $\tilde{Re}_{\theta t}$ in the boundary layer is lower than the value on the freestream. On the contrary, for the remaining solutions, $\tilde{Re}_{\theta t}$ is higher inside the boundary layer than in the freestream. This does not match with the diffusion mechanism that is responsible for the value of $\tilde{Re}_{\theta t}$ in the boundary layer, as there is no production in this region. It follows then that the higher value of $\tilde{Re}_{\theta t}$ in the boundary layer is being convected from upstream.

Further investigation is done through Figure 6.16, which shows $\tilde{Re}_{\theta t}$ in the region around the leading edge of the airfoil for the solutions obtained with $\mu_t/\mu = 10$ and $\mu_t/\mu = 1$. Downstream of the stagnation

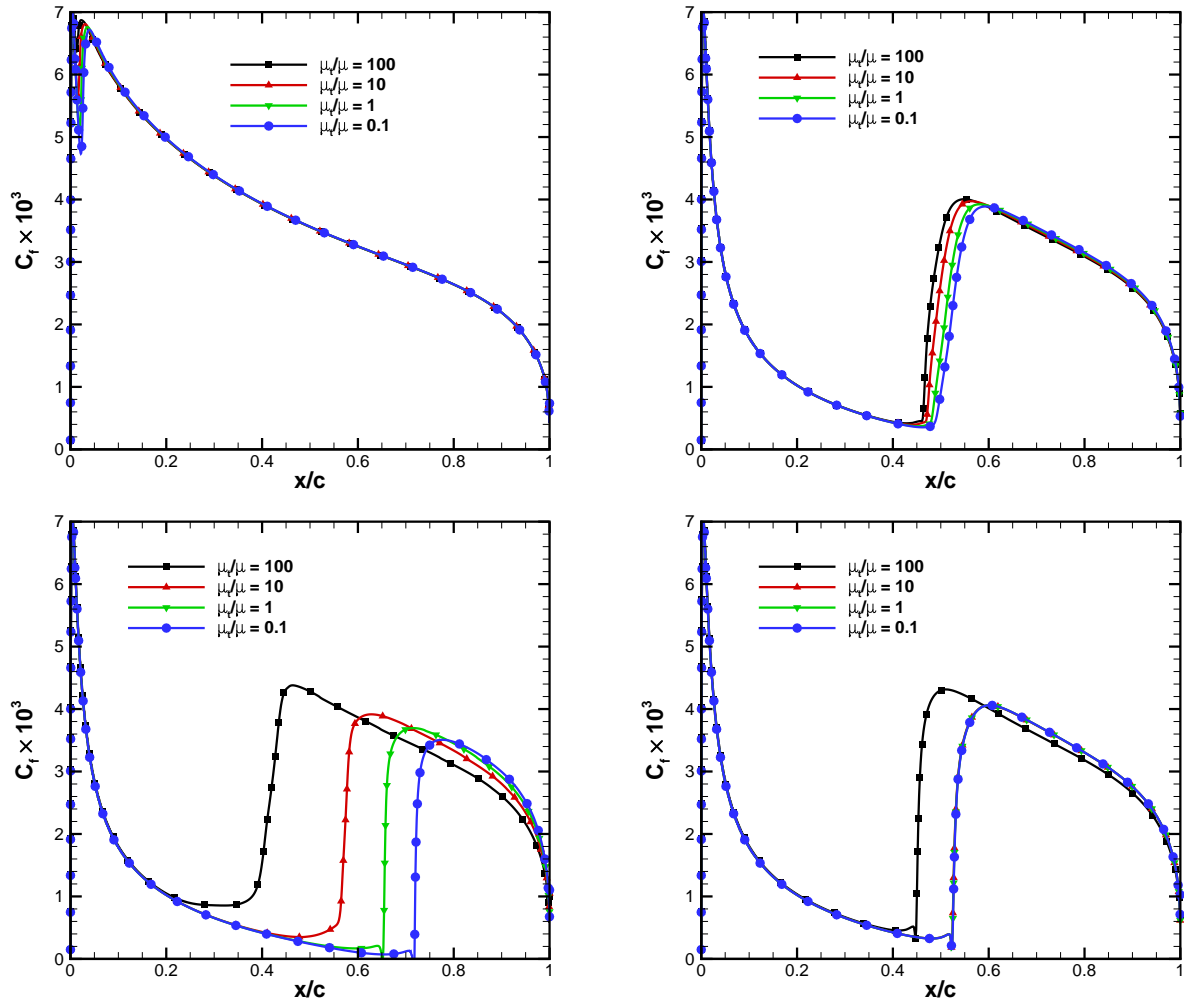


Figure 6.14: Skin-friction coefficient distribution for the NACA 0012 test case using the $k - \omega$ SST model (top left) combined with the AFT model (top right), the $\gamma - Re_{\theta}$ model (bottom left) and the γ model (bottom right) for varying inlet boundary conditions.

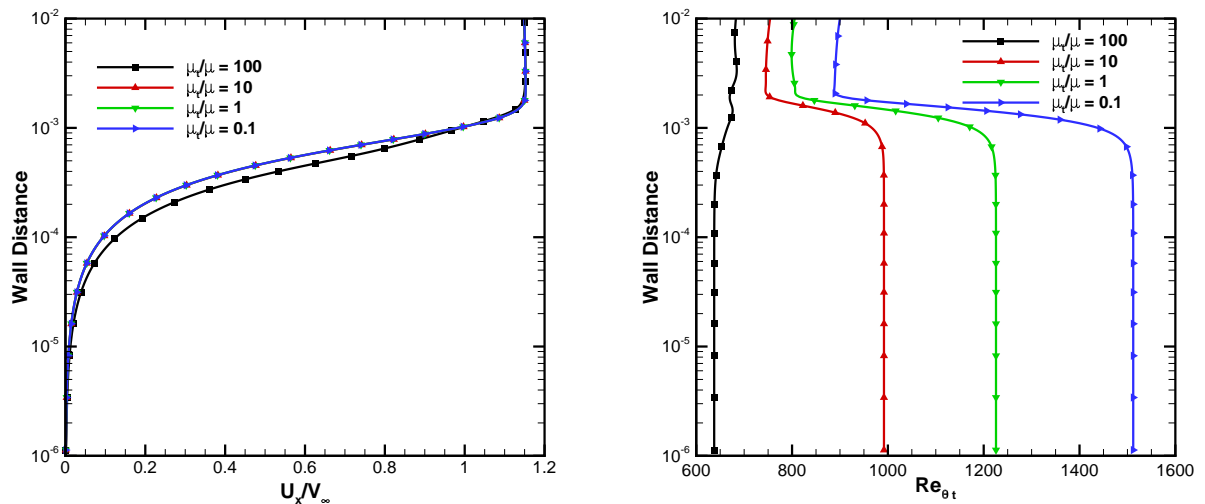


Figure 6.15: Boundary-layer profiles of the streamwise velocity (left) and $\tilde{Re}_{\theta t}$ (right) obtained with the $k - \omega$ SST + $\gamma - Re_{\theta}$ model at $x/c = 0.31$ for varying inlet boundary conditions.

there is a significant increase of $\tilde{Re}_{\theta t}$ in the freestream, a consequence of the favourable pressure gradient, which is diffused into the boundary layer. However, the solution for $\mu_t/\mu = 1$ exhibits a much higher value of $\tilde{Re}_{\theta t}$ in the freestream, a consequence of the lower value of k and its production which is proportional to μ_t . In spite of the lower eddy-viscosity, diffusion is strong enough that the high value of $\tilde{Re}_{\theta t}$ spreads into the boundary layer in this region and propagates downstream as well. This leads to the higher values of $\tilde{Re}_{\theta t}$ observed at $x/c = 0.31$.

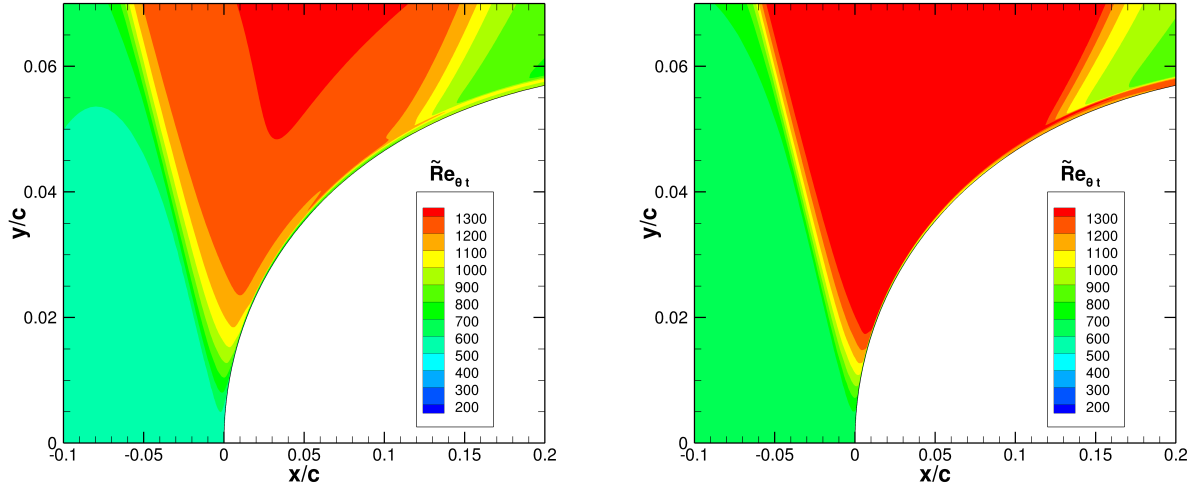


Figure 6.16: Evolution of $\tilde{Re}_{\theta t}$ obtained with the $k - \omega$ SST + $\gamma - Re_{\theta}$ model at the vicinity of the leading edge of the NACA 0012 airfoil for an inlet eddy-viscosity ratio of 10 (left) and 1 (right).

In the absence of the transport equation for $\tilde{Re}_{\theta t}$ and the diffusion mechanism, it follows that the influence of the eddy-viscosity ought to be lower. This matches the behaviour displayed by the γ model previously. More details are given in Figure 6.17, again for $x/c = 0.31$. For this model, the velocity profiles match visually regardless of the inlet value of the eddy-viscosity. Since there is no equation for $\tilde{Re}_{\theta t}$, the critical momentum thickness Reynolds number $Re_{\theta c}$ which is present in the source term of the γ equation is considered instead. The solution for the highest inlet eddy-viscosity exhibits a slightly lower value of $Re_{\theta c}$ inside the boundary layer than the remaining cases, thus justifying the earlier transition. The remaining cases have a very similar profile of $Re_{\theta c}$, which matches well with the fact that transition is exhibited in nearly the same location for those simulations.

In the case of the AFT transition model, the evolution of \tilde{n} along the boundary layer is considered in Figure 6.18 for the cases with highest and lowest inlet eddy-viscosity. While no appreciable differences exist in the laminar region where \tilde{n} is increasing, the two solutions exhibit different behaviours once it reaches the limiting value of 9. In the case of the calculation with $\mu_t/\mu = 100$, the decrease of \tilde{n} along the boundary layer is faster than in the simulation with $\mu_t/\mu = 0.1$.

Figure 6.19 presents the lift and drag coefficients obtained with each model for three different angles of attack, showing that the trends are the same regardless of the angle of attack considered. In all cases, the drag coefficient is most influenced quantity. For the $k - \omega$ SST model, there is a smaller scatter of the results, and the numerical uncertainty associated with the discretization error has a larger impact than the specification of the turbulence eddy-viscosity at the inlet. In the calculations where transition models

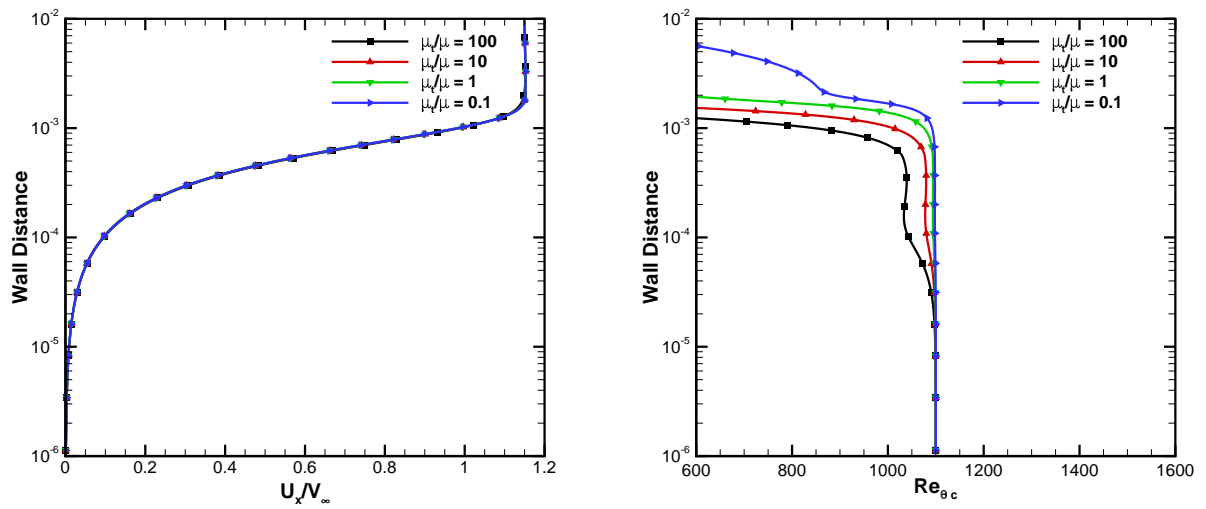


Figure 6.17: Boundary-layer profiles of the streamwise velocity (left) and $Re_{\theta c}$ (right) obtained with the $k - \omega$ SST + γ model at $x/c = 0.31$ for varying inlet boundary conditions.

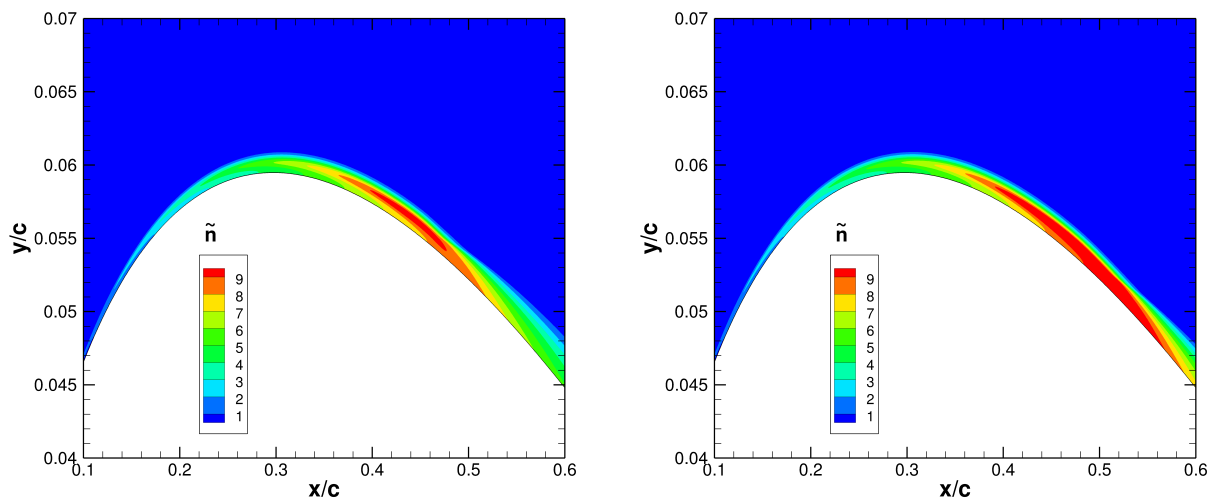


Figure 6.18: Evolution of \tilde{n} for the $k - \omega$ SST + AFT model in the upper surface of the NACA 0012 airfoil for an inlet eddy-viscosity ratio of 100 (left) and 0.1 (right).

are used there are larger differences in the drag coefficient due to different values for the inlet eddy-viscosity. In the case of the $\gamma - Re_\theta$ transition model, this effect is clearly dominant over the numerical uncertainty.

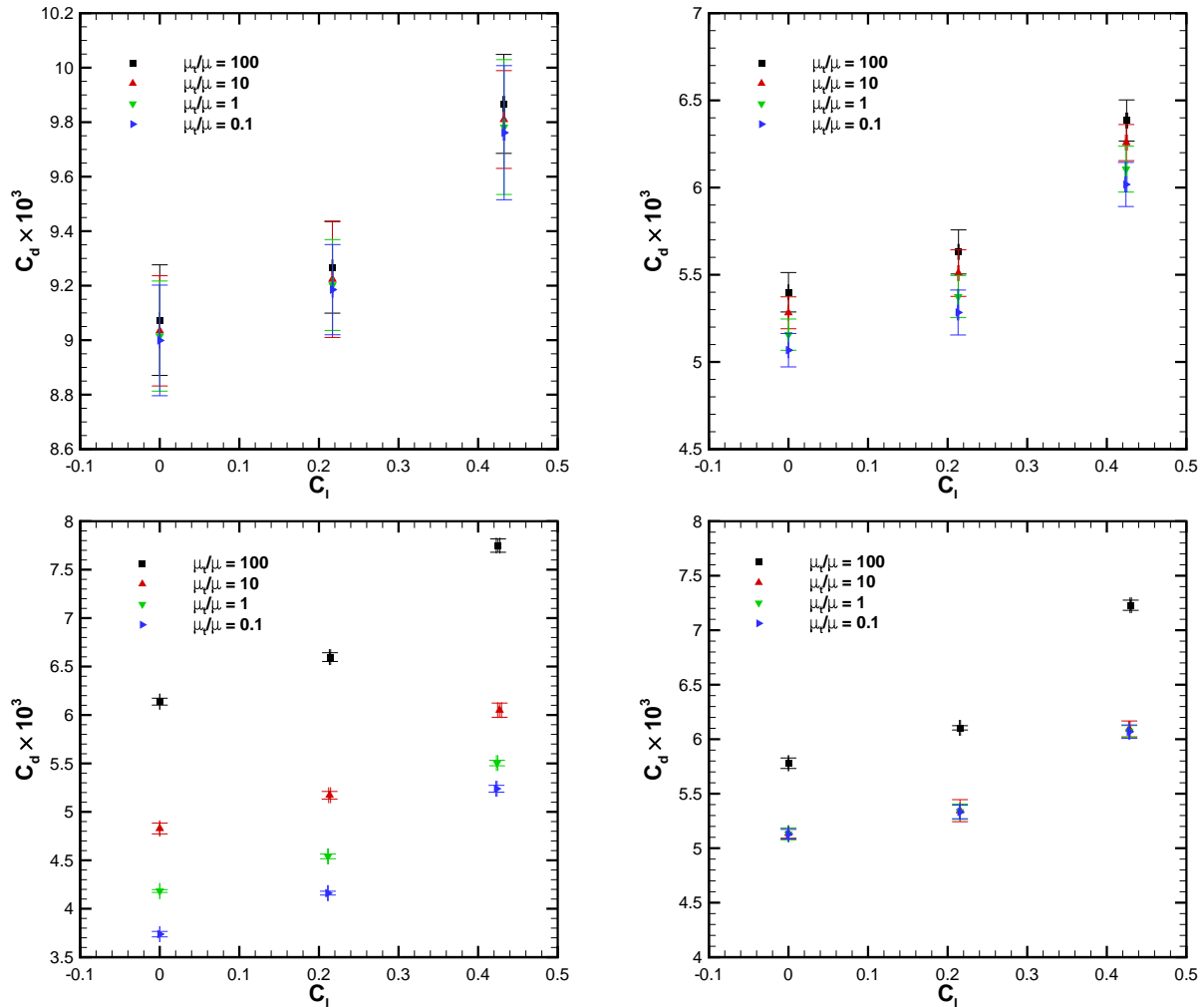


Figure 6.19: Drag polar for the NACA 0012 test case using the $k - \omega$ SST model (top left) combined with the AFT model (top right), the $\gamma - Re_\theta$ model (bottom left) and the γ model (bottom right) for varying inlet boundary conditions.

The skin-friction coefficient on the surface of the spheroid obtained with the $\gamma - Re_\theta$ model is displayed in Figure 6.20. The two sets of conditions tested are designed in such a way that the turbulence intensity at the nose of the spheroid is 0.15%. In spite of this, the transition front along the spheroid is not the same for the two cases. Set A exhibits transition further upstream than that given by set B by approximately 5%. Furthermore, set A predicts the lowest level of turbulence intensity in the freestream around the spheroid, as the eddy-viscosity is much lower for these conditions. This shows that a single freestream turbulence intensity level is not enough to fully characterize the problem, as different combinations of inlet conditions can match that requirement but provide different solutions. In addition, the control of the decay via the eddy-viscosity does not always work as expected. In the present case, conditions A have a lower level of the eddy-viscosity and consequently have the highest decay. Nevertheless, the calculation using those conditions exhibited transition further upstream, due to the role of the eddy-viscosity in

diffusing the value of Re_θ from the freestream inside the boundary layer.

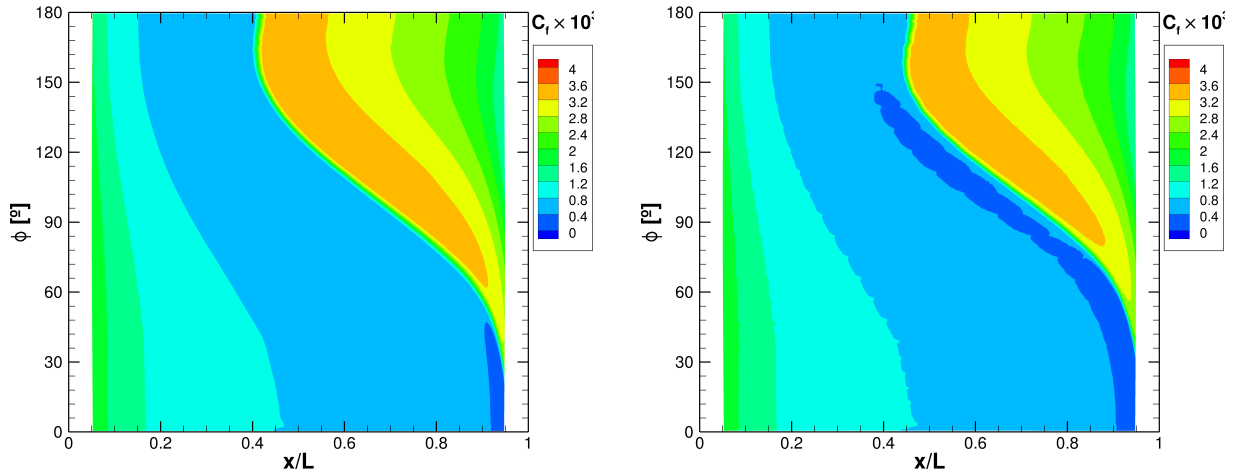


Figure 6.20: Skin friction coefficient on the surface of the prolate spheroid with the $\gamma - Re_\theta$ transition model using set of boundary conditions A (left) and B (right).

6.3.3 New approach for the control of turbulence decay

The role of the eddy-viscosity in the control of the turbulence decay arises as an undesirable feature. The main reason for this is the extremely large value required to overcome the steep decay predicted by the underlying turbulence model. This issue is further amplified by the large distances at which inlet boundaries are placed on the computational domain. As an example, in the present case of the prolate spheroid, an eddy-viscosity ratio of 250 was required in order to obtain the desired level of 0.15% at the nose of the spheroid, without using any further measures to control the decay. As seen in the flat-plate test case, the use of a high eddy-viscosity may also impact the laminar solution. The importance of the eddy-viscosity in controlling the decay of turbulence makes it so that the transition models, with the exception of the AFT model, appear to be more sensitive to the inlet eddy-viscosity rather than to the inlet turbulence intensity. In addition the true role of the eddy-viscosity in the transition model becomes more difficult to assess, since most of its influence is felt on the freestream turbulence level.

In order to avoid using excessively high values for the inlet eddy-viscosity, alternative approaches are required. While the use of x_F is helpful, as it acts as a reduction of the size of the region along which turbulence will decay, its application is restricted to simple flows. In a wing-body configuration, x_F would have to be located upstream of the fuselage, meaning that a significant decay can take place before the flow encounters the wings. A similar situation can take place in the case of a propeller, where the presence of the hub prevents x_F from being located close to the propeller's blades. A more general approach is the use of sustaining terms in the transport equations of the turbulence model, which impose base values for the turbulence variables. This variant of the $k - \omega$ SST model is usually denominated as SST-sust [142]. However, this alternative was not built with a focus on transitional flows, but rather on establishing consistency on calculations that employ only a turbulence model. Furthermore, the use of the additional terms is active everywhere in the flowfield, including in the boundary-layer. This means

that the sustaining terms are not allowed to take significant values, as they could corrupt the solution of the turbulence model, restricting their use to very low turbulence intensity environments.

An analysis of the equations for the decay of k and ω in the freestream (Eqs. 4.19 and 4.20) shows that the decay of both variables is controlled by five distinct quantities. These are: the constants of the dissipation term in the turbulence model (β and β^*), the Reynolds number of the flow, the distance from the inlet, the inverse of the eddy-viscosity ratio at the inlet and turbulence kinetic energy at the inlet. Naturally, the Reynolds number of the flow is not a viable option to control the decay. The eddy-viscosity ratio at the inlet is the most common approach and the one for which a suitable alternative would be desirable, while the distance to the inlet is already considered in the use of x_F . Using the turbulent kinetic energy to control its own decay does not solve the issue. This leaves the constants β and β^* as the only option.

Following this approach, β and β^* are redefined as

$$\begin{aligned}\beta &= (1 - F_{FS})\beta_o + F_{FS}\beta_{FS} \\ \beta^* &= (1 - F_{FS})\beta_o^* + F_{FS}\beta_{FS}^*,\end{aligned}\tag{6.3}$$

where β_o and β_o^* are the original constants of the SST model while β_{FS} and β_{FS}^* are given by

$$\begin{aligned}\beta_{FS} &= \lambda\beta_o \\ \beta_{FS}^* &= \lambda\beta_o^*\end{aligned}\tag{6.4}$$

with $0 < \lambda < 1$. The function F_{FS} switches from 0 inside the boundary layer to 1 in the freestream, ensuring that the new constants of the dissipation terms are only active in the freestream, so that the model works as intended inside the boundary layer. The formulation of F_{FS} is based on the dimensionless total pressure loss Δp_t^*

$$\Delta p_t^* = \frac{p + \frac{1}{2}\rho V^2 - (p_{max} + \frac{1}{2}\rho V_\infty^2)}{\frac{1}{2}\rho V_\infty^2}.\tag{6.5}$$

An auxiliary variable ϕ is built so that $0 < \phi < 1$:

$$\phi = \min\left(\max\left(\frac{\Delta p_t^* - \Delta_{min}}{\Delta_{max} - \Delta_{min}}, 0\right), 1\right),\tag{6.6}$$

where Δ_{min} and Δ_{max} represent limiting values for Δp_t^* . For $\Delta p_t^* < \Delta_{min}$, which represents a pressure loss more intense than Δ_{min} , ϕ is set to 0, which enforces the original constants of the $k-\omega$ SST model. If $\Delta p_t^* > \Delta_{max}$, which signifies a small pressure loss, then ϕ is set to 1 and the modified constants are used. The blending function F_{FS} is given by

$$F_{FS} = -2\phi^3 + 3\phi^2,\tag{6.7}$$

which ensures a smooth behaviour of the blending function in the vicinity of $F_{FS} = 0$ and $F_{FS} = 1$.

Considering the application of this technique, the decay equations for k and ω in the freestream are

now written as

$$k^* = \frac{k_{in}^*}{\left(1 + \lambda\beta (x^* - x_{in}^*) k_{in}^* \left(\frac{\mu}{\mu_t}\right)_{in} Re\right)^{\frac{\beta^*}{\beta}}}, \quad (6.8)$$

and

$$\omega^* = \frac{\omega_{in}^*}{1 + \lambda\beta (x^* - x_{in}^*) k_{in}^* \left(\frac{\mu}{\mu_t}\right)_{in} Re}. \quad (6.9)$$

It is worth noting that this approach does not solve the lack of knowledge regarding how to set the decay. In fact, it adds a new degree of freedom to the problem through the introduction of λ . However, this approach allows for the control of the decay to be uncoupled from the inlet eddy-viscosity. If $\lambda = 1$, the original $k - \omega$ SST model is recovered. For $\lambda < 1$, the decay becomes less intense. Keeping all other quantities constant, the decay of turbulence becomes determined by the quantity $\lambda \frac{\mu}{\mu_t}$. This means that the decay obtained when using $\lambda = 1$ and $\frac{\mu_t}{\mu} = 10$ is the same as that obtained if $\lambda = 0.1$ and $\frac{\mu_t}{\mu} = 1$. Thus, using this approach, it is possible to mitigate the use of high values for the inlet eddy-viscosity.

This approach is tested for the flow over the flat plate, for two different values of the inlet turbulence intensity, $I = 1.0\%$, which corresponds to the T3AM case, and $I = 5.5\%$ for the T3A conditions. The different combinations of the inlet eddy-viscosity and λ are given in Table 6.5. The skin-friction coefficient and the evolution of the freestream turbulence intensity for the T3AM case are displayed in Figure 6.21. The results show that the control of the decay of turbulence via the modified constants leads to the same location of transition as the calculation where the control of the decay is done through the inlet eddy-viscosity. The evolution of the freestream turbulence intensity is also the same for the two cases.

Table 6.5: Inlet boundary conditions used for the OH grids for the flat plate test case to assess the performance of the approach to control the decay of turbulence.

Case	Tu_{in}	$(\mu_t/\mu)_{in}$	λ	x_F	Tu_{LE}
T3AM	1%	25	1	Not used	0.64%
T3AM	1%	0.1	1/25 = 0.004	Not used	0.64%
T3A	5.37%	280	1	Not used	2.46%
T3A	5.37%	1.0	1/280	Not used	2.46%
T3A	5.37%	0.1	0.1/280	Not used	2.46%

Similar plots are given in Figure 6.22 for the runs corresponding to the T3A conditions. This case is more challenging, as a consequence of the higher freestream turbulence intensity, which causes a stronger decay and thus requires a higher inlet eddy-viscosity. The evolution of the freestream turbulence intensity is the same for all the three cases, and the location of transition is also very similar. In addition, the use of λ to control the decay avoids the overprediction of C_f in the laminar region. However, the level of C_f in the turbulent region is slightly affected, becoming dependent on the value of λ . While this seems to indicate that this approach cannot be used for high values of the turbulence intensity, it is worth noting that this approach is modifying the constants of the dissipation terms in the freestream by at least a factor of around 280. This also means that in the region where the constants return to the original values of the $k - \omega$ SST model, which corresponds to a thin area at the edge of the boundary layer, there is a change in these constants by the same factor. This sudden change, especially if not done outside

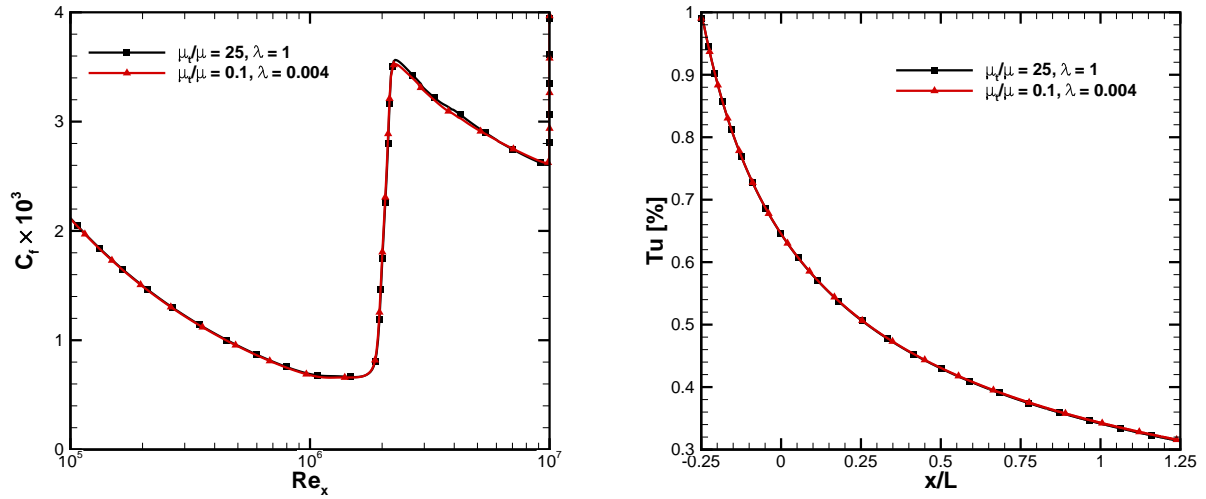


Figure 6.21: Skin friction coefficient distribution (left) and turbulence intensity evolution on the freestream (right) on the flat plate test case for the T3AM conditions using the $k - \omega$ SST + $\gamma - Re_{\theta}$ model.

of the boundary layer, can be responsible by the changes in the turbulent region.

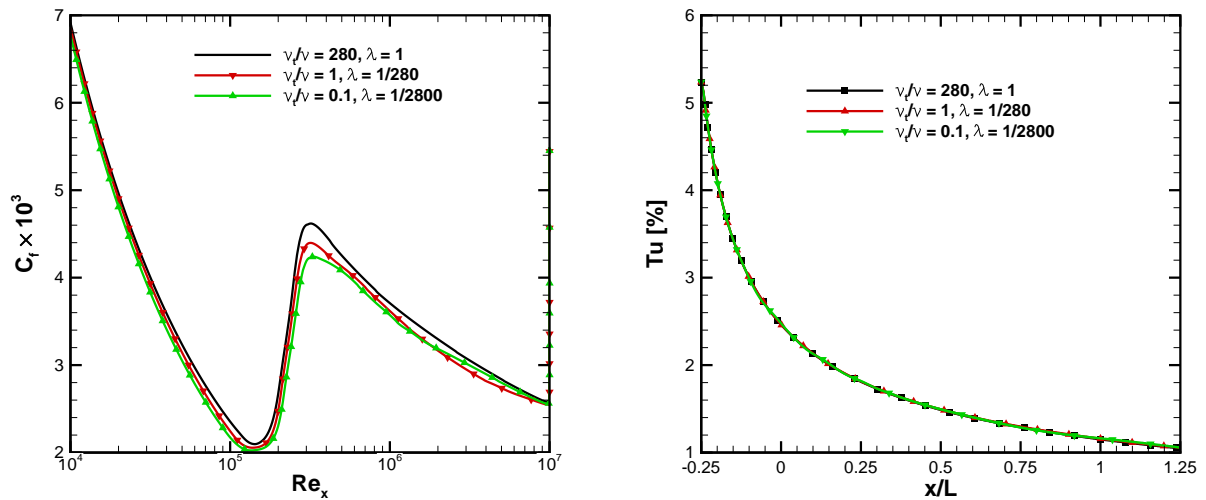


Figure 6.22: Skin friction coefficient distribution (left) and turbulence intensity evolution on the freestream (right) on the flat plate test case for the T3A conditions using the $k - \omega$ SST + $\gamma - Re_{\theta}$ model.

Further testing of this alternative to control the decay of turbulence is performed on the NACA 0012 airfoil at $\alpha = 0^\circ$. The selected combinations of the boundary conditions at the inlet for turbulence and the value of λ are given in Table 6.5. The base combinations with $\lambda = 1$ correspond to those analysed previously and given in Table 6.3. The results for the skin friction coefficient are shown in Figure 6.23, where only the first three conditions of Table 6.3. The calculation using the modified constants with $\mu_t/\mu = 10$ and $\lambda = 0.1$ does not predict the same location for transition as the solution with $\mu_t/\mu = 100$ and $\lambda = 1$, even though the freestream decay of the two conditions is the same. Instead, transition is predicted much further upstream. A comparison of the turbulence kinetic energy profiles at $x/c = 0.05$, where the flow is still laminar for all conditions is shown as well. The condition that corresponds to the control of turbulence via λ exhibits the largest value of k both inside and outside of the boundary layer.

Given that the capability of the modified constants to reproduce the freestream decay has been es-

Table 6.6: Inlet boundary conditions used for the NACA 0012 test case to assess the performance of the approach to control the decay of turbulence.

Tu_{in}	$(\mu_t/\mu)_{in}$	λ	x_F	Tu_{LE}
3%	100	1	Not used	0.4%
3%	10	1	Not used	0.12%
3%	10	0.1	Not used	0.4%
3%	1	1	Not used	0.03%
3%	1	0.01	Not used	0.4%

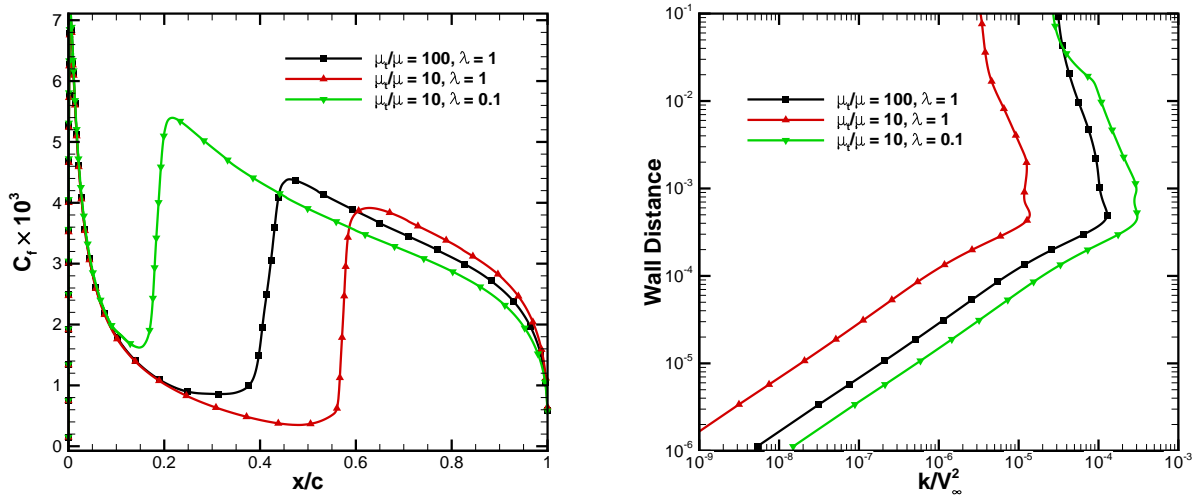


Figure 6.23: Skin friction coefficient distribution (left) and turbulence kinetic energy profile in the boundary layer (right) on the NACA 0012 test case using the $k - \omega$ SST + $\gamma - Re_\theta$ model for the dissipation based turbulence production limiter with $c = 15$.

established in the previous case, it follows that the increased level of turbulence kinetic energy must follow from another cause other than the dissipation term. The culprit lies in the production of k associated with the stagnation region, as shown in Figure 6.24. A much stronger increase of k outside of the boundary layer is observed in the case where $\mu_t/\mu = 10$ and $\lambda = 0.1$ than in the case with $\mu_t/\mu = 100$ and $\lambda = 1$. Noting that the production term has the same form in the two simulations, and that it is proportional to μ_t , the cause for the higher value of k for $\mu_t/\mu = 10$ lies in the production limiter. In the case of $\mu_t/\mu = 100$, even though the eddy-viscosity is higher, the smaller dissipation term forces the limiter to be active. On the contrary, for the case with $\mu_t/\mu = 10$ and $\lambda = 0.1$, despite the lower eddy-viscosity, the dissipation term as seen in the production limiter uses the original constant of the model, which results in a higher value for the limiter.

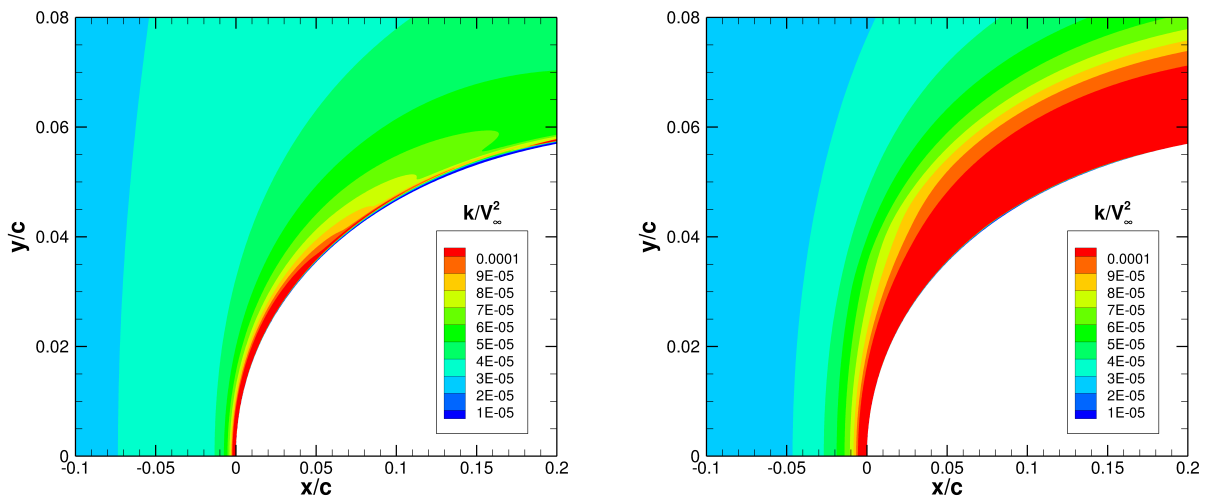


Figure 6.24: Evolution of the turbulence kinetic energy in the vicinity of the leading edge of the NACA 0012 airfoil for the $k - \omega$ SST + $\gamma - Re_\theta$ model with an inlet eddy-viscosity ratio of 100 and $\lambda = 1$ (left) and inlet eddy-viscosity ratio of 10 and $\lambda = 0.1$ (right) for the dissipation based turbulence production limiter with $c = 15$.

One apparent solution to this issue would be to employ the modified dissipation constant in the turbulence production limiter as well. However that does not solve the problem, since while that guarantees that the dissipation as seen in the limiter would be the same for the two cases, the eddy-viscosity would not be the same, thus still originating a different growth of k in the stagnation region. Thus, it would also be required to modify the production term itself so that its magnitude would match that of the case where the turbulence decay is controlled solely by the eddy-viscosity.

A simpler option is to change the limiter used on the production term. Instead of being dependent on the dissipation term, the Kato-Launder formulation is applied instead. This guarantees that differences in the dissipation term do not affect the behaviour of k close to the stagnation region. Furthermore, it should also prevent the difference in the value of the eddy-viscosity to have any meaningful influence over the production term and consequently over the evolution of the turbulence kinetic energy. The conditions given on Table 6.6 are run again for the $k - \omega$ SST model using the Kato-Launder production limiter and the $\gamma - Re_\theta$ model.

A comparison of the k field in the vicinity of the stagnation region is shown in Figure 6.25. With the

use of the Kato-Launder formulation, there is no significant growth of the turbulence kinetic energy in the stagnation region. Furthermore, there are no differences due to the use of different values for the eddy-viscosity at the inlet as observed in the previous case. As a consequence, the transition location is no longer affected by the stagnation region as shown in Figure 6.26. It becomes solely dependent on the decay of freestream turbulence and is not influenced by the eddy-viscosity.

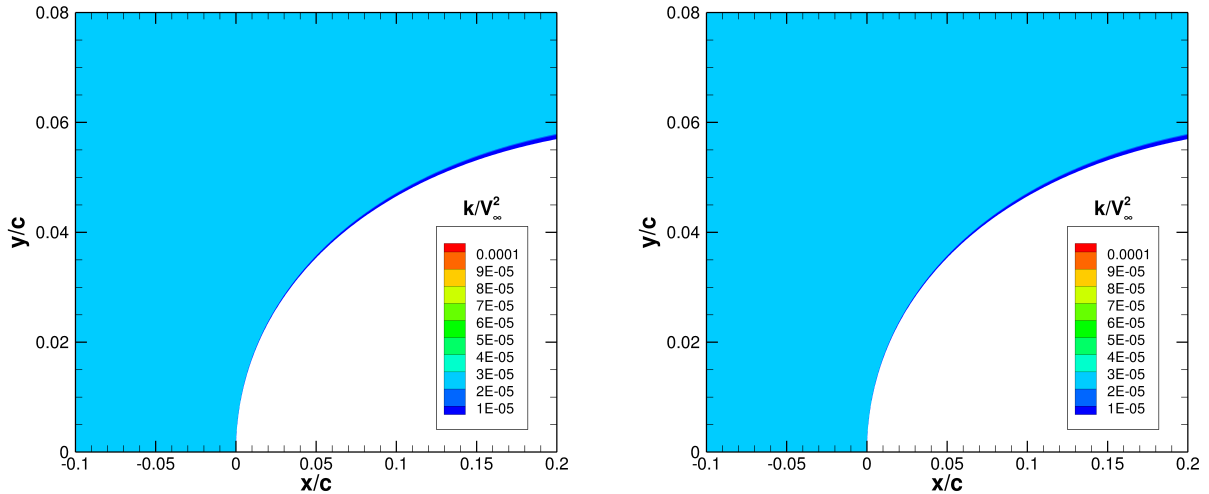


Figure 6.25: Evolution of the turbulence kinetic energy in the vicinity of the leading edge of the NACA 0012 airfoil for the $k - \omega$ SST + $\gamma - Re_\theta$ model with an inlet eddy-viscosity ratio of 100 and $\lambda = 1$ (left) and inlet eddy-viscosity ratio of 10 and $\lambda = 0.1$ (right) for the Kato-Launder limiter.

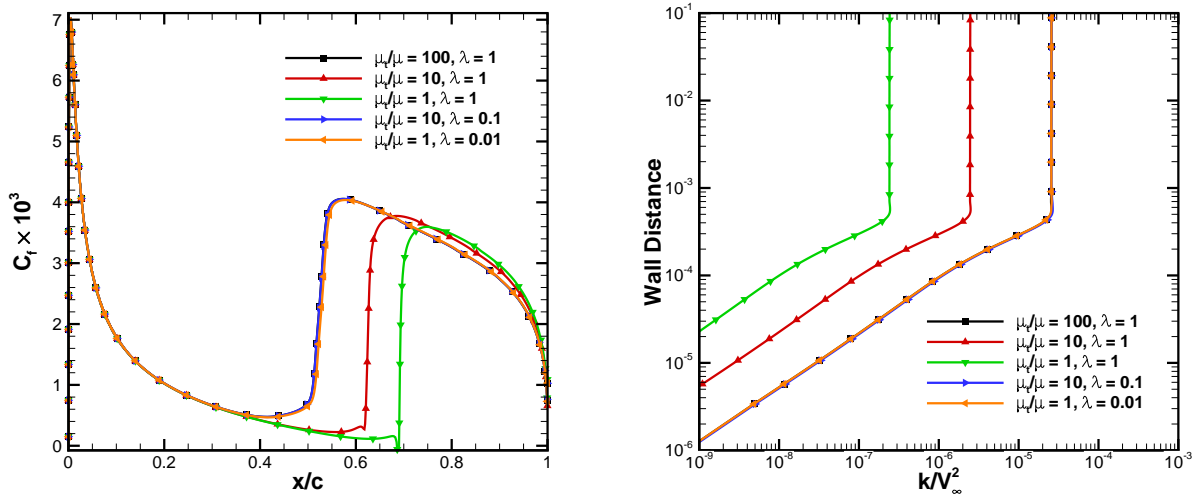


Figure 6.26: Skin friction coefficient distribution (left) and turbulence kinetic energy profile in the boundary layer (right) on the NACA 0012 test case using the $k - \omega$ SST + $\gamma - Re_\theta$ model for the Kato-Launder limiter.

In order to further test the new approach to control the decay of turbulence in the freestream, additional calculations are performed for the prolate spheroid at an angle of attack of 5° . The combination of inlet boundary conditions and the value of the λ for each simulation are given in Table 6.7. The calculation with $(\mu_t/\mu)_{in} = 250$ and $\lambda = 1$ acts as the reference solution. The modification is the decay is employed for two calculations with $(\mu_t/\mu)_{in} = 25$ and $(\mu_t/\mu)_{in} = 2.5$, guaranteeing the same turbulence decay than that of the reference solution. A simulation with $(\mu_t/\mu)_{in} = 25$ without any decay modification

is also performed, to ensure that changing the eddy-viscosity in this range produces a significant effect if it fully controls the decay. The Kato-Launder formulation is employed for the turbulence production limiter, based upon the behaviour observed for the NACA 0012 airfoil.

Table 6.7: Inlet boundary conditions used for the 6:1 prolate spheroid test case to assess the performance of the approach to control the decay of turbulence.

Tu_{in}	$(\mu_t/\mu)_{in}$	λ	x_F	Tu_{LE}
0.5%	250	1	Not used	0.15%
0.5%	25	1	Not used	0.05%
0.5%	25	0.1	Not used	0.15%
0.5%	2.5	0.01	Not used	0.15%

Figure 6.27 presents the skin-friction coefficient distribution on the surface of the prolate spheroid for each of conditions previously discussed. As a first point of note, reducing the eddy-viscosity ratio from 250 to 25 has a significant effect on the location of transition, in particular close to the symmetry plane on the leeward side. However, upon activating the modification to the decay of freestream turbulence, the overall evolution of C_f is nearly identical between each case that displays the same decay. This confirms that the developed approach is a suitable alternative to control the decay of turbulence, allowing the use of lower values for the inlet eddy-viscosity, fully applicable in three-dimensional flows.

6.4 Main Remarks

The results from this chapter illustrate and explore the difficulties and challenges in the usage of transition models. The first analyzed aspect, the influence of the limiter used in the production term of the transport equation for the turbulence kinetic energy is mostly irrelevant for simulations in which a transition model is not used. On the other hand, depending on the transition model used, its importance can range from negligible to significant, as a difference of over 10% of the chord was observed on the transition location. The effect of the turbulence production limiter is also amplified by the high inlet eddy-viscosity which is not required for calculations using only a turbulence model, but is typically used in calculations with transition models. Out of the three models studied, the $\gamma - Re_\theta$ model presented the highest sensitivity to the turbulence production limiter, a consequence of the second variable of the model and the importance of the freestream evolution of the turbulence kinetic energy. The influence of the limiter was much smaller on the γ model, which agrees with the formulation of the model that possesses a different mechanism in its sensitization to the freestream conditions, and negligible for the AFT model.

Also addressed was the overall influence of each transition model to the inlet boundary conditions for turbulence. An appropriate setting of these is crucial for the correct prediction of transition. Unfortunately, there is very rarely enough information to fully characterize the evolution of freestream turbulence. In many cases, only a single data point is given, usually in the form of the value of the turbulence intensity at a given point in the domain. This is insufficient to completely describe turbulence in the numerical calculation, for it is unknown how it will decay from that point on. The example for the prolate spheroid

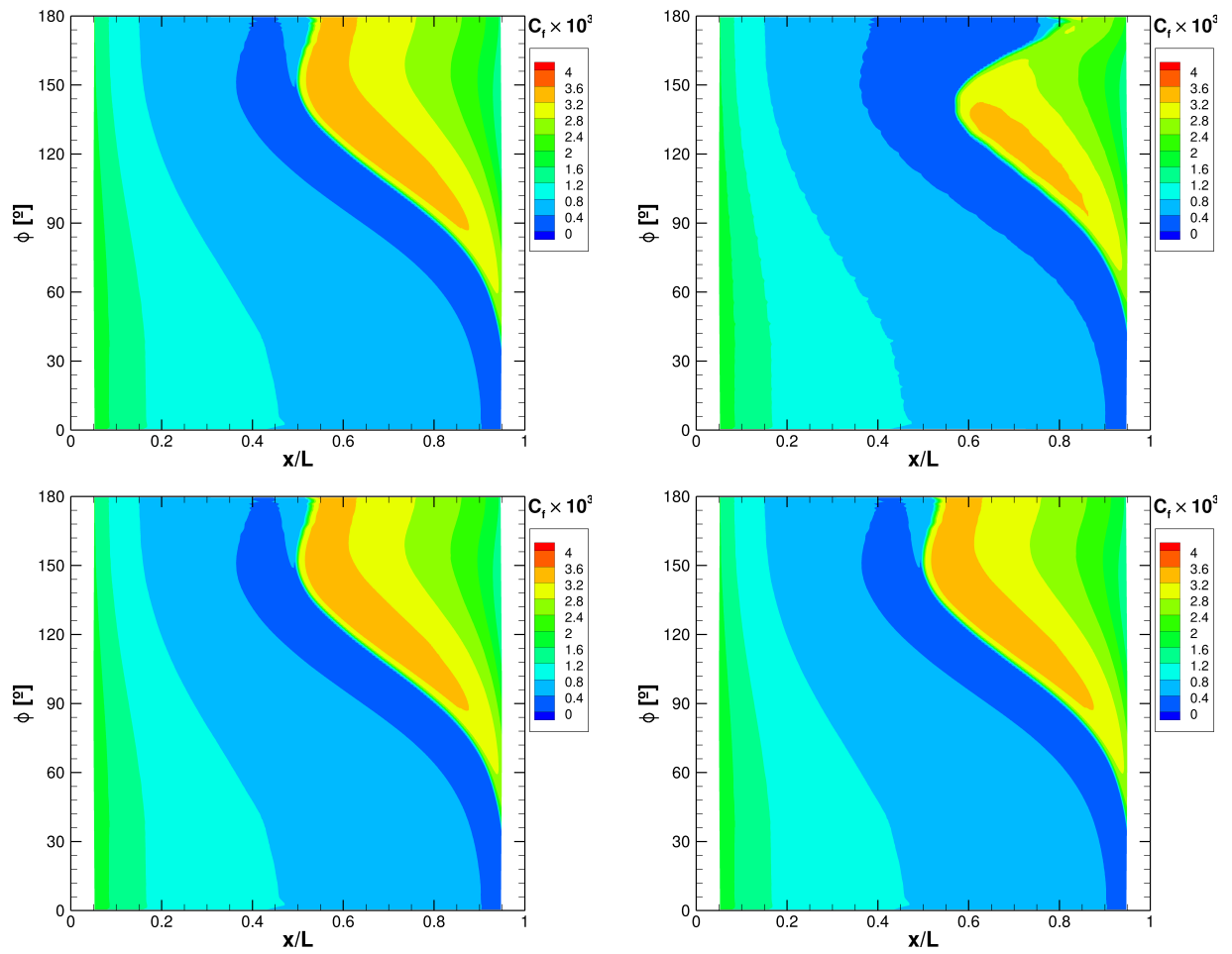


Figure 6.27: Skin-friction coefficient distribution on the surface of the prolate spheroid using the $k - \omega$ SST model combined with the $\gamma - Re_\theta$ model with an inlet eddy viscosity ratio of 250 and $\lambda = 1$ (top left), an inlet eddy-viscosity ratio of 25 and $\lambda = 1$ (top right), an inlet eddy-viscosity ratio of 25 and $\lambda = 0.1$ (bottom left) and an inlet eddy-viscosity ratio of 2.5 and $\lambda = 0.01$ (bottom right).

illustrates that different solutions can be obtained while still matching the constraint of a single turbulence intensity level.

Each model also reacts differently to the inlet quantities. In the case of the AFT model, where most of the information regarding the level of freestream turbulence is contained in a single variable, N_{crit} , changing the inlet boundary conditions for the turbulence variables has a small impact as long as N_{crit} remains constant. If N_{crit} is related to the inlet turbulence intensity, then naturally this variable acquires a significant influence over the location of transition. Meanwhile, the $\gamma - Re_\theta$ model is strongly dependent on the freestream evolution of k and its decay. Therefore, the model is very sensitive to both the inlet turbulence intensity as well as the inlet eddy-viscosity, since the latter controls the decay in the freestream of the former. This constitutes the reason why extremely high eddy-viscosity ratios are generally used for transitional flow calculations, as a way to ensure a small decay of the turbulence kinetic energy. Finally, the γ model is also sensitive to the inlet boundary conditions for turbulence, as its formulation is similar to that of the $\gamma - Re_\theta$. However, the absence of the second transport equation makes this model less dependent on the freestream evolution of k than its predecessor.

An alternative to control the decay of turbulence in the freestream is presented and explored. This approach is built on the total pressure in order to identify the freestream, and modifies the constants of the dissipation terms of the turbulence transport equations. Thus, the usage of high eddy-viscosity ratios at the inlet is avoided and replaced by a single parameter that only changes the turbulence model in the freestream. The testing of this methodology showed that a reduction of two orders of magnitude of the eddy-viscosity is possible without compromising the solution. However, due to the effect of turbulence production at the stagnation region, the use of the Kato-Launder formulation is required for the predicted location of transition to be only dependent on the freestream decay.

Chapter 7

Results Part III: Comparison with Experimental Data

7.1 Introduction

This Chapter presents a comparison between the numerical solution and experimental data for several test cases, some of which have not been addressed so far. Two-dimensional flows are addressed in Section 7.2 and three-dimensional cases are discussed in Section 7.3. The conditions tested for each geometry are given in Table 7.1. It should be mentioned that this does not correspond to a formal validation exercise for any of the models. A proper validation exercise would entail full characterization of both numerical and experimental uncertainty, with the latter not being given in the reports associated with either test case. Furthermore, information to characterize the turbulence quantities would also be required and the available measurements are generally insufficient to set the two turbulence variables in the numerical calculations.

Table 7.1: Angle of attack and inlet turbulence quantities for each test case for the comparison with experimental data study.

Geometry	Angle of Attack	Tu_{in}	$(\mu_t/\mu)_{in}$	x_F	N_{crit}	Tu_{LE}
NACA 0015	5°, 10°	0.5%	0.0018	Not used	-	0.01%
Eppler 387	1°, 7°	1%	0.003	Not used	2.6	0.01%
S809	0°, 1°, 3°, 5°, 6°, 7°	1%	1.65	Not used	-	0.06%
NLF ₁ -0416	-2°, 0°, 2°, 4°, 6°	1%	1.65	Not used	-	0.04%
SD 7003	4°	0.1%	0.1	Not used	-	0.09%
6:1 Prolate Spheroid	5°, 10°, 15°	0.1917%	5.2	-1.5L	6.6	0.15%
Sickle Wing	-2.6°	0.066%	1.04	Not used	-	0.04%

7.2 Two-dimensional Flows

7.2.1 NACA 0015

The first case to be considered is that of the flow around the NACA 0015 airfoil. The skin-friction coefficient distribution is presented in Figure 7.1 for $\alpha = 5^\circ$ and in Figure 7.2 for $\alpha = 10^\circ$. This case is the only two-dimensional test case for which experimental data for C_f is available [146], obtained through Temperature Sensitive Paint coating. The C_f line for the experimental data was obtained from averaging along the spanwise direction, and the uncertainty exhibited corresponds to the standard deviation of the average. Comparing the results obtained with the $\gamma - Re_\theta$ and the γ model shows slight differences starting at the separation point, and extending through the separated flow region. However, the end of transition is nearly coincident between the two numerical solutions, and so is the turbulent region. When compared to the measurements, the numerical solutions underpredict the skin-friction coefficient throughout most of the airfoil's surface, a difference that is not justified by either experimental or numerical uncertainty. Nevertheless, good agreement is observed in the obtained location and extent of the transition region. These trends are observed at both angles of attack.

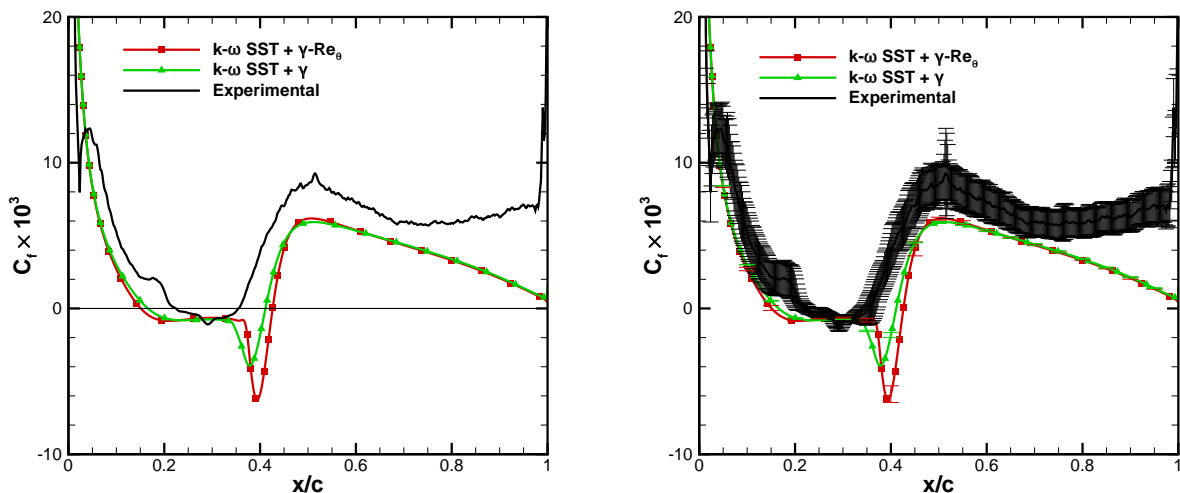


Figure 7.1: Skin friction coefficient distribution on the upper surface of the NACA 0015 airfoil at $\alpha = 5^\circ$ with the $\gamma - Re_\theta$ and γ models combined with the $k - \omega$ SST turbulence model without uncertainty (left) and with uncertainty (right).

This test case is also a good example to illustrate the importance of considering the experimental uncertainty, making it clear that it can be substantial. For this particular flow, it is even larger than the numerical uncertainty, which only assumes non-negligible levels during the transition region, a consequence of the steep gradients of C_f in this region. Another noteworthy aspect is the increase of C_f displayed by the experimental data for $\alpha = 5^\circ$, starting at around $x/c = 0.7$. This effect is not reproduced by the numerical simulations. Since there is no favourable pressure gradient that would justify this increase, this casts some doubt on the validity of the experimental data in this region. This is confirmed in Ref. [146], as in this region it is not possible to maintain the the heat flux uniform along the surface, therefore affecting the estimation of C_f . For the higher angle of attack ($\alpha = 10^\circ$, Figure 7.2), although

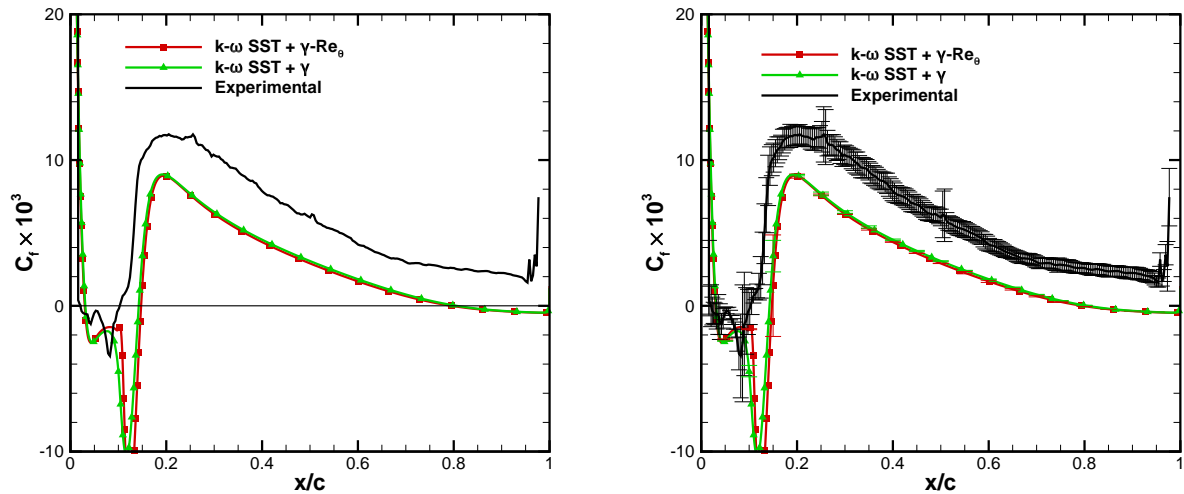


Figure 7.2: Skin friction coefficient distribution on the upper surface of the NACA 0015 airfoil at $\alpha = 10^\circ$ with the $\gamma - Re_{\theta}$ and γ models combined with the $k - \omega$ SST turbulence model without uncertainty (left) and with uncertainty (right).

there is no increase of C_f , a change in its slope is visible at $x/c = 0.7$.

7.2.2 S809

Figure 7.3 presents the skin friction coefficient on the surface of the S809 airfoil for an angle of attack of 0° . Results are given for the $k - \omega$ SST and KSKL models combined with the $\gamma - Re_{\theta}$ and γ models. For this angle of attack only, results without any transition model are given as well. All transition models predict transition to take place at around $x/c = 0.5$ on the upper surface and at $x/c = 0.55$ on the lower surface with small differences in the transition region. On the turbulent regime, the solutions with transition model do not match the fully turbulent solution of the same turbulence model. Interestingly enough, in the lower surface there is also a strong match in the turbulent region of all calculations done with a transition model included, regardless of the underlying turbulence model.

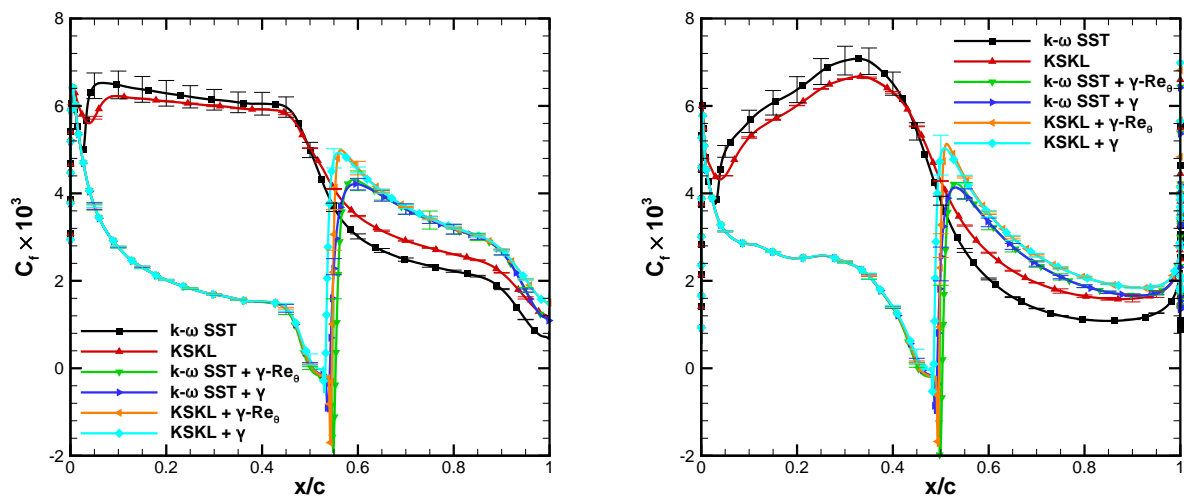


Figure 7.3: Skin friction coefficient distribution on the upper (left) and lower (right) surfaces of the S809 airfoil at $\alpha = 0^\circ$ with different turbulence and transition model combinations.

Transition is caused by the adverse pressure gradient that begins near $x/c = 0.4$ in the upper surface and downstream of $x/c = 0.45$ in the lower surface, as illustrated in Figure 7.4. This also leads to a small region of separated flow in both surfaces. Overall the numerical results match well with the experimental measurements in the upper and lower surfaces. The predicted location of transition is visible in the abrupt pressure recovery that leads to a sharp increase of C_p , a feature that is not captured by simulations without a transition model. The details on the pressure recovery vary between each model combination, but the visual comparison suggests that a good agreement between the numerical solution and the experimental data is obtained. The lower surface always exhibits a laminar separation bubble which moves slightly downstream as the angle of attack is increased and as such the ensuing results focus on the upper surface.

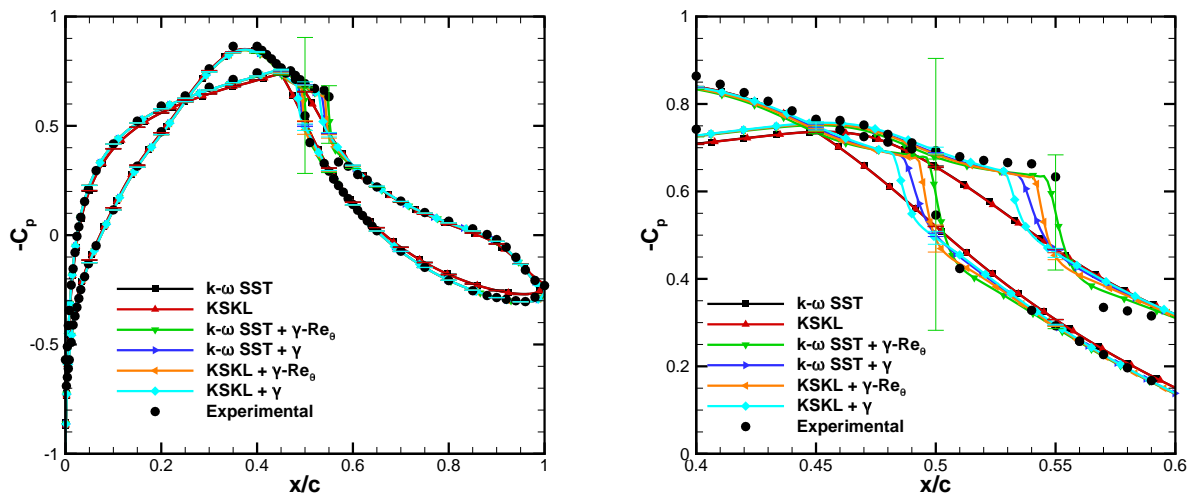


Figure 7.4: Pressure coefficient distribution on the surface of the S809 airfoil at $\alpha = 0^\circ$ with different turbulence and transition model combinations. Entire view (left), close-up of the transition region (right). Experimental data from [152].

The observed trends remain as the angle of attack is increased up until $\alpha = 5^\circ$. At these conditions, displayed in Figure 7.5, the KSKL model combined with the $\gamma - Re_\theta$ transition model exhibits transition much further upstream than the remaining formulations in the upper surface. However, at this angle of attack, a laminar separation bubble was still observed in the experiments. As a result of the earlier transition at around $x/c = 0.3$, the KSKL + $\gamma - Re_\theta$ formulation exhibits a small increase of C_p at this location and a smoother evolution around $x/c = 0.5$ where the laminar separation bubble ought to be located. The prediction of the remaining models still matches well with the experimental data.

As the angle of attack is increased to 6° , only the formulations that rely on the γ transition model still exhibit a laminar separation bubble at $x/c = 0.5$. This is depicted in Figure 7.6. At this angle of attack, the laminar separation bubble was no longer detected in the experiments, which agrees to both the $k - \omega$ SST and KSKL models combined with the $\gamma - Re_\theta$ model. Even though experimental data is not shown in this case, it is clear that the predictions given by the combinations with the γ transition model are incorrect, since these still exhibit laminar flow separation. However, given the findings of Section 6.3, these comparisons could be significantly different if the boundary conditions at the inlet for the turbulence variables were slightly different than those used. Finally, at $\alpha = 7^\circ$, the $k - \omega$ SST + γ

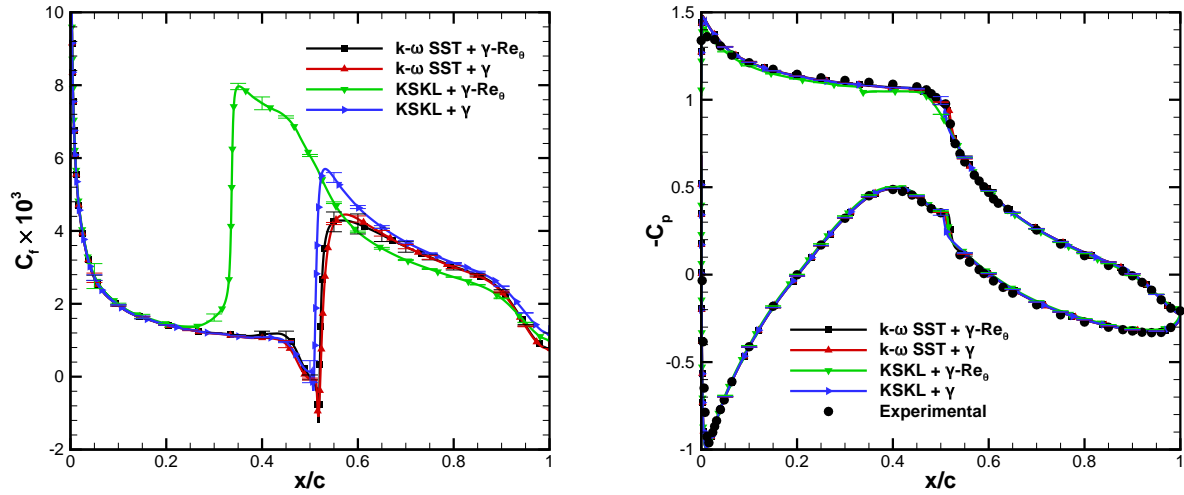


Figure 7.5: Skin friction coefficient (left) and pressure coefficient (right) distributions on the surface of the S809 airfoil at $\alpha = 5^\circ$ with different turbulence and transition model combinations. Experimental data from [152].

formulation still exhibits a small region of separated flow at $x/c = 0.5$ in anticipation of transition. The location of transition predicted by the remaining model combinations ranges from around $x/c = 0.1$ to $x/c = 0.4$. The pressure coefficient distribution, given in Figure 7.7 still shows strong agreement with the experimental data, including in the region around $x/c = 0.5$, with the exception of the $k - \omega$ SST + γ model combination.

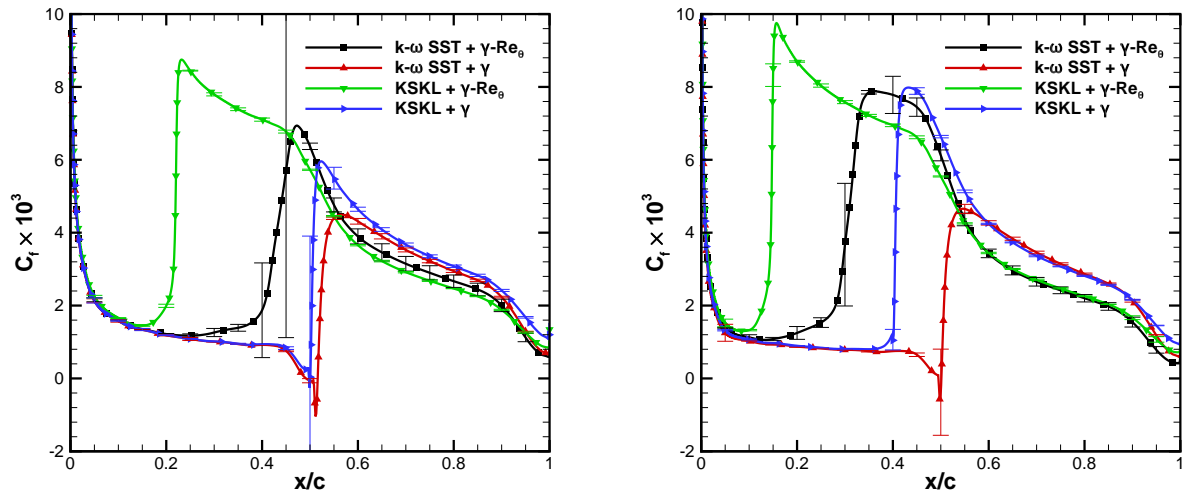


Figure 7.6: Skin friction coefficient distribution on the upper surface of the S809 airfoil at $\alpha = 6^\circ$ (left) and $\alpha = 7^\circ$ (right) with different turbulence and transition model combinations.

The drag polar obtained for the previously discussed angles of attack is shown in Figure 7.8. For the lower angles of attack there is an underprediction of the drag coefficient and overprediction of the lift coefficient which are not covered by the numerical uncertainty. Furthermore, the solution of all models is fairly coincident. As the angle of attack is increased up to $\alpha = 3^\circ$, the difference in the drag coefficients based on the experimental data and the numerical solutions decreases. However, for $\alpha \leq 5^\circ$, as the transition mechanism is no longer the laminar separation bubble for all models, significant differences

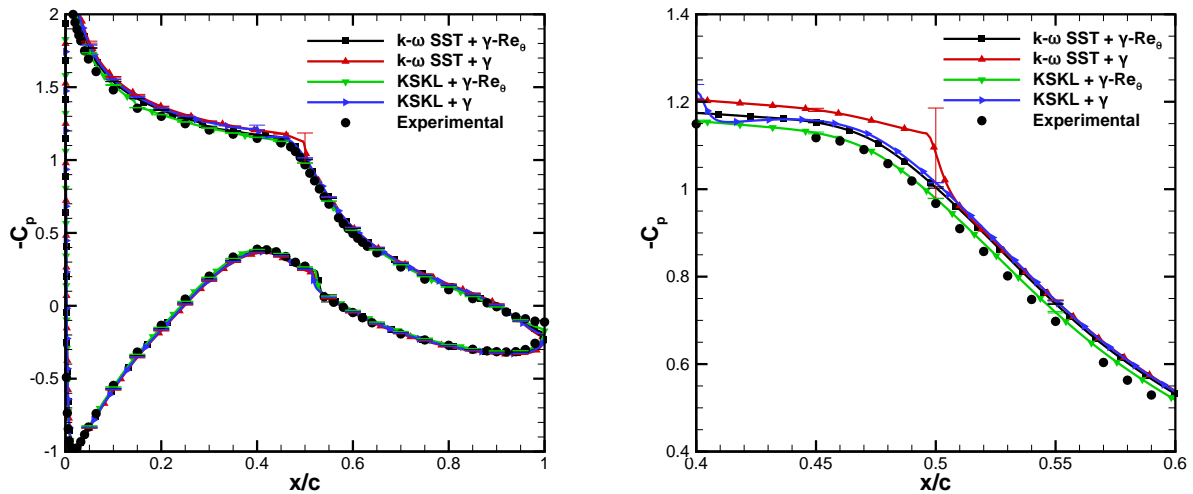


Figure 7.7: Pressure coefficient distribution on the surface of the S809 airfoil at $\alpha = 7^\circ$ with different turbulence and transition model combinations. Entire view (left), close-up of the transition region (right). Experimental data from [152].

show up on the prediction of the drag coefficient. For $\alpha = 5^\circ$ the $KSKL + \gamma - Re_\theta$ model exhibits a much higher drag coefficient which clearly exceeds the experimental data, a natural consequence of the increased friction drag due to transition taking place much further upstream than the remaining formulations. For the higher angles of attack, there is a clear underprediction of drag by most models, with the solution that best matches the experiments being the one provided by the $KSKL + \gamma - Re_\theta$ formulation. As the laminar separation bubble becomes absent in the solution for each model due to transition taking place further upstream, significant differences in the drag coefficient are observed.

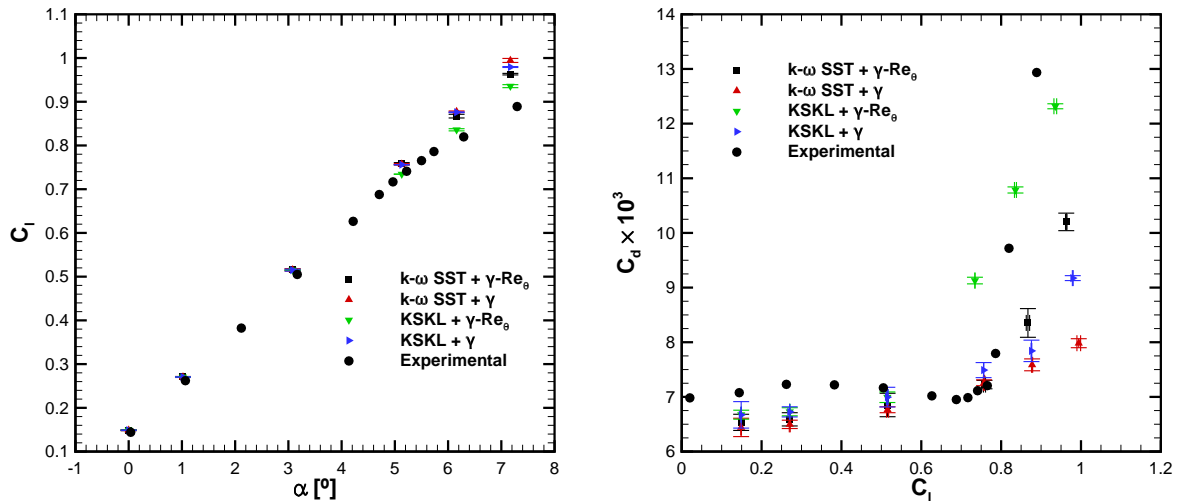


Figure 7.8: Lift coefficient as a function of the angle of attack (left) and drag polar (right) for the S809 airfoil at varying angle of attack with each transition model and experimental data from [152].

Figure 7.9 presents a comparison of the experimental and numerical locations of transition obtained with each model in the upper and lower surface. For the numerical calculations, the uncertainty in the estimation of the start and end of transition are shown as well in the form of the error bars. These are determined by obtaining the locations of the start and end of transition for each grid, and applying

the procedure described in Section 4.3. For each surface, the first symbol corresponds to the start of transition and the second to the end of transition as obtained by the C_f distribution. All models exhibit a good agreement in the lower surface, a consequence of the presence of the laminar separation bubble at all angles of attack. Meanwhile for the upper surface the trends are similar to those discussed for the drag coefficient. At the lower angles of attack there is a strong agreement between all models and the experimental data. As α is increased and each model no longer predicts the laminar separation bubble as the triggering mechanism for transition, much different predictions for the location of transition are obtained.

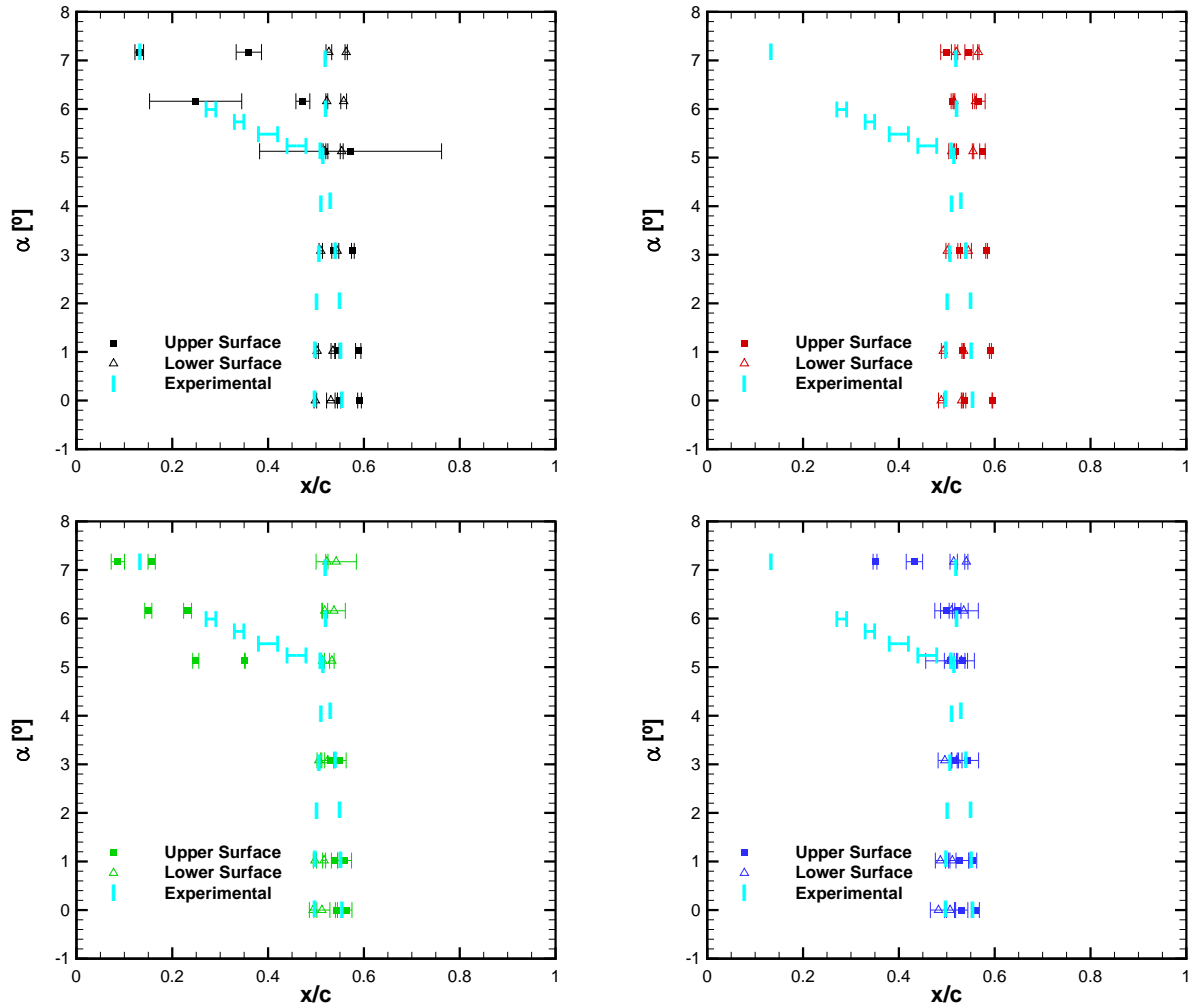


Figure 7.9: Start and end locations of transition on the upper and lower surface of the S809 airfoil for varying angle of attack obtained with the $k-\omega$ SST + $\gamma - Re_\theta$ model (top left), $k-\omega$ SST + γ model (top right), KSKL + $\gamma - Re_\theta$ model (bottom left) and KSKL + γ model (bottom right).

7.2.3 NLF₁-0416

The next geometry to be considered is the NLF₁-0416 airfoil. The C_f distribution for $\alpha = -2^\circ$ is presented in Figure 7.10. On the upper surface, there is moderate agreement between the predicted location of transition for most models, with the $k-\omega$ SST + $\gamma - Re_\theta$ model predicting it slightly further downstream than the rest. As a consequence, and due to the sudden drop in C_f as transition starts, this

is the only formulation that exhibits laminar flow separation. On the lower surface the transition location shows a larger scatter, from $x/c = 0.35$ to $x/c = 0.52$, depending on the model used. The solutions for the γ model are much more similar than those for the $\gamma - Re_\theta$ model, considering the different underlying turbulence models.

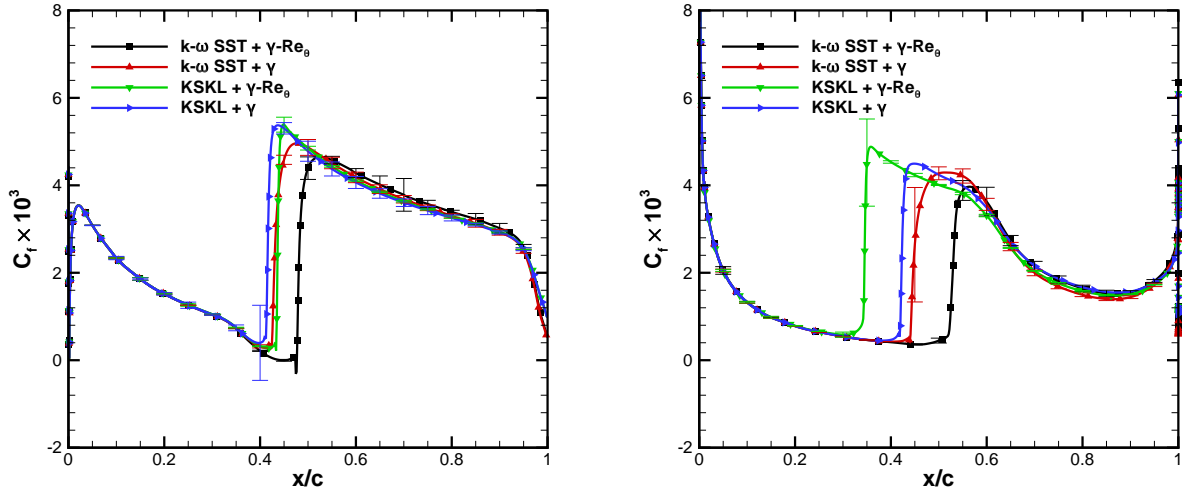


Figure 7.10: Skin friction coefficient distribution on the upper (left) and lower (right) surfaces of the NLF₁-0416 airfoil at $\alpha = -2^\circ$ with different turbulence and transition model combinations.

The pressure coefficient distribution along the surface of the airfoil is plotted in Figure 7.11 for the lowest and highest angles of attack tested. At $\alpha = -2^\circ$ there is an underprediction of C_p in the lower surface. The agreement is better on the upper surface, although there is also a slight underprediction close to the suction peak. The $k - \omega$ SST + $\gamma - Re_\theta$ model exhibits the pressure recovery associated with flow transition, mismatching with the experimental data. For $\alpha = 6^\circ$ the distribution of C_p in the lower surface now matches well with the experimental data. On the other hand, all models now overpredict the pressure coefficient in the region around the suction peak. As the flow solution for each model undergoes transition, the agreement with the experimental data improves.

Figure 7.12 presents the drag polar of the NLF₁-0416 airfoil. For all angles of attack there is an overprediction of the lift coefficient which becomes more noticeable as the angle of attack is increased. At the lower angles the $k - \omega$ SST model exhibits the lowest prediction for C_d , as a consequence of the delayed transition, resulting in an underprediction of the drag coefficient when compared to the other models. The predictions of these are similar throughout the tested range of α .

The comparison between the experimental and numerical prediction for the location of the transition region is given in Figure 7.13. Experimental results for the upper surface are only available for $\alpha = -2^\circ, 0^\circ$ and 2° . For the lower surface, the only angle of attack out of those tested for which experimental data is not given is -2° . The $k - \omega$ SST model combined with the $\gamma - Re_\theta$ model predicts transition further downstream than the experiments in both the lower and upper surfaces for the lower angles of attack. As the angle of attack increases, the experimental position of transition on the lower surface moves downstream. This effect is barely reproduced in the numerical solutions and leads to the better agreement in the lower surface for the higher angles. When the $k - \omega$ SST model is used with the γ

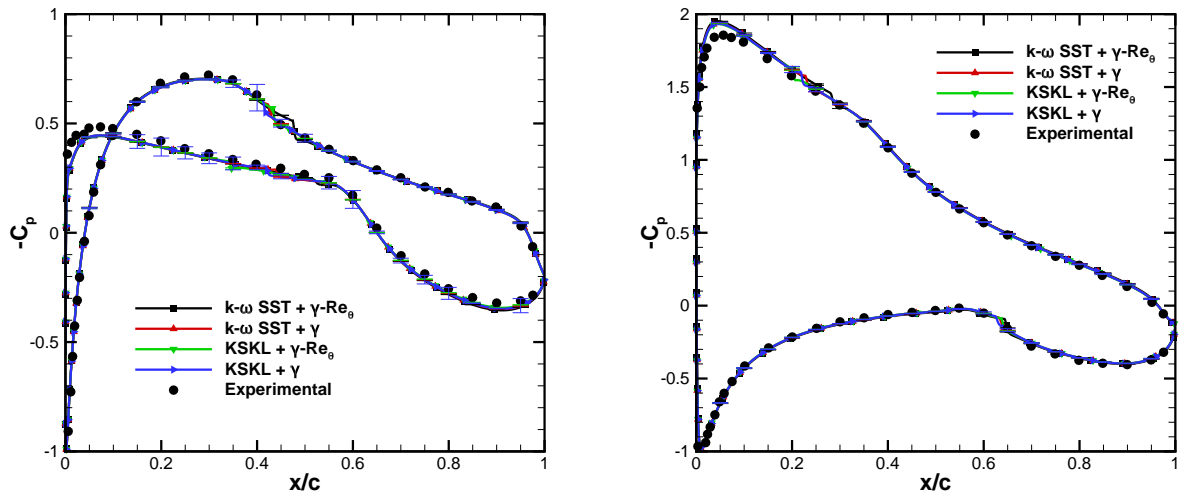


Figure 7.11: Pressure coefficient distribution on the surface of the NLF₁-0416 airfoil at $\alpha = -2^\circ$ (left) and $\alpha = 6^\circ$ (right) with different turbulence and transition model combinations. Experimental data from [147].

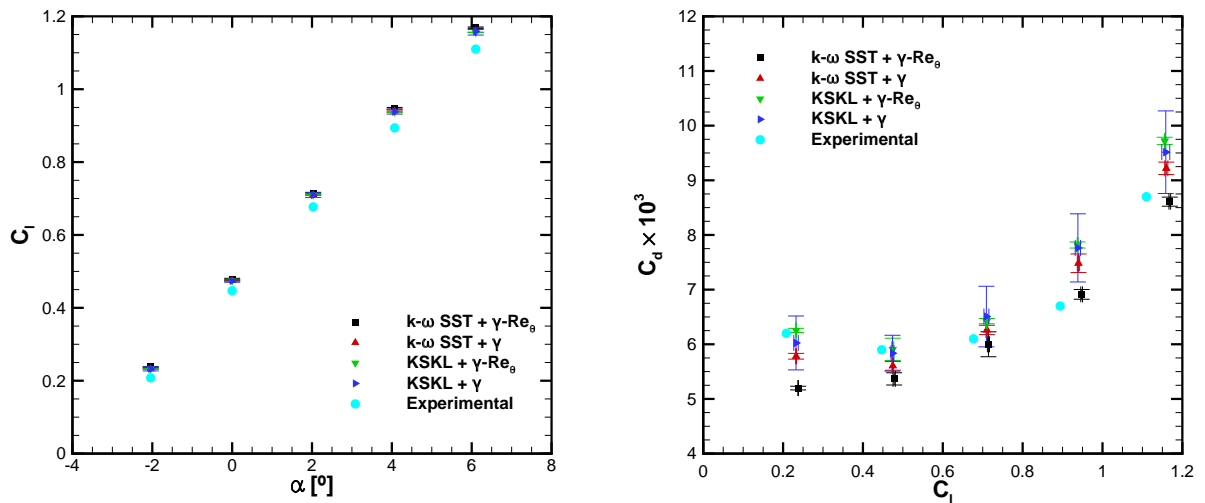


Figure 7.12: Lift coefficient as a function of the angle of attack (left) and drag polar (right) for the NLF₁-0416 airfoil at varying angle of attack with each transition model and experimental data from [147].

transition model the trends are similar, although the late prediction of transition is not as strong as before. The solutions using the KSKL model follow the same trends, but exhibit a larger numerical uncertainty.

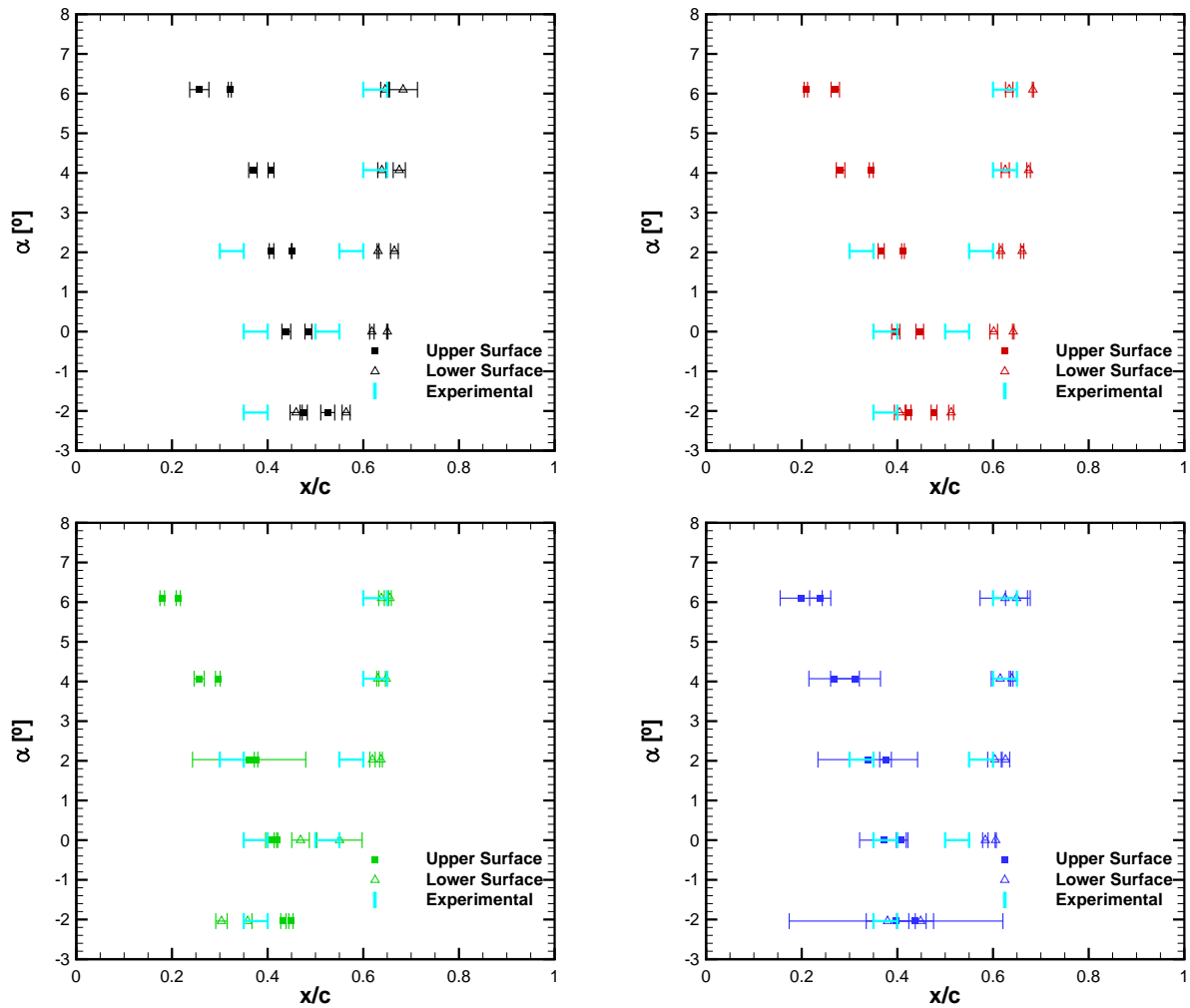


Figure 7.13: Start and end locations of transition on the upper and lower surface of the NLF₁-0416 for varying angle of attack obtained with the $k-\omega$ SST + $\gamma - Re_\theta$ model (top left), $k-\omega$ SST + γ model (top right), KSKL + $\gamma - Re_\theta$ model (bottom left) and KSKL + γ model (bottom right).

7.2.4 Eppler 387

The results for the Eppler 387 airfoil are given in Figures 7.14 and 7.15 for $\alpha = 1^\circ$ and $\alpha = 7^\circ$ respectively. For both angles of attack, the use of a transition model results on laminar flow on the entire lower surface. On the contrary, if no transition model is used, transition takes place at around $x/c = 0.2$ for $\alpha = 1^\circ$ and $x/c = 0.4$ for $\alpha = 7^\circ$. As there is no flow separation in the lower surface, the pressure distribution is not affected by the use of a transition model. On the upper surface at $\alpha = 1^\circ$, all transition models predict a laminar separation bubble whose length exceeds 20% of the chord. Slight differences are observed in the C_f distribution starting from the separation point depending on the transition model used. Differences are observed in the pressure coefficient as well until the flow has transitioned and becomes fully turbulent. The solution of the $k-\omega$ SST model without a transition model is unable to predict the laminar separation bubble and results in a much different and incorrect pressure distribution.

For $\alpha = 7^\circ$, there is no laminar separation in the experiments, which is also seen in the absence of the corresponding pressure plateau. However both the $\gamma - Re_\theta$ and γ models still predict flow separation, with a shorter bubble length than for the lower angle of attack. The solution of the AFT model predicts transition at around $x/c = 0.2$, preventing laminar flow separation. As a consequence, the $k - \omega$ SST + AFT formulation presents the best match with the experimental pressure coefficient distribution.

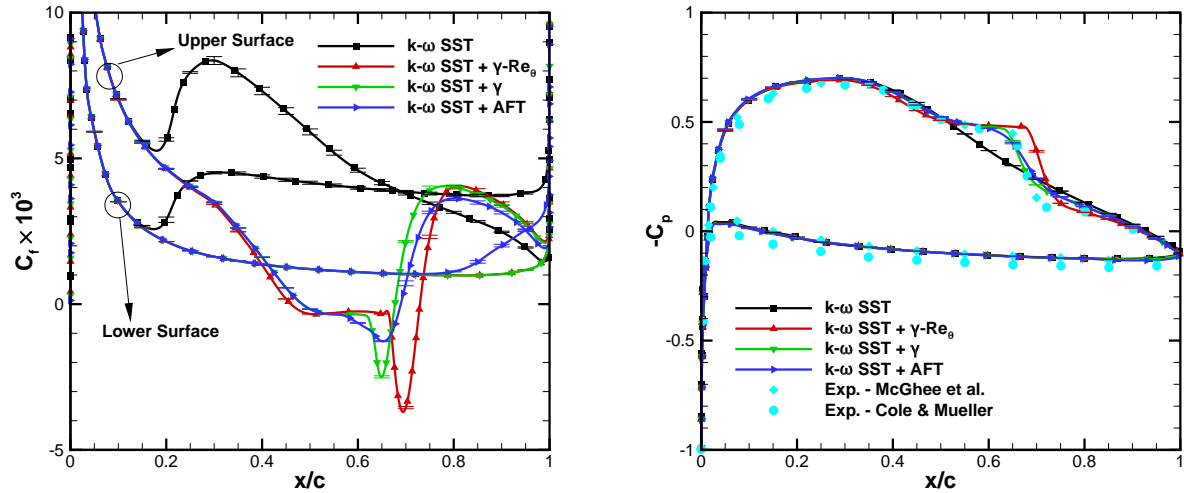


Figure 7.14: Skin-friction (left) and pressure (right) coefficient distributions on the surface of the Eppler 387 airfoil at $\alpha = 1^\circ$ for different transition models and experimental data from [149] and [148].

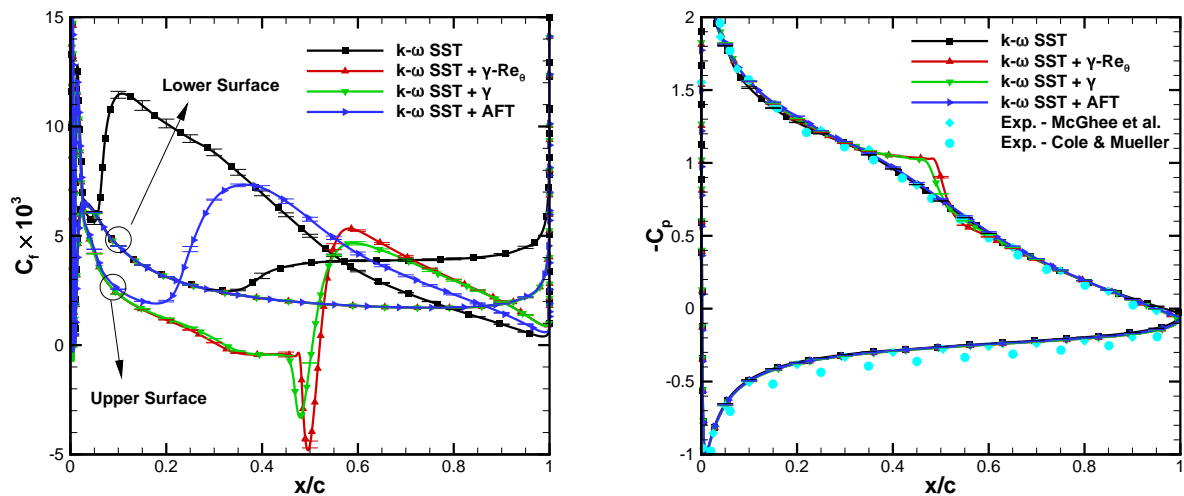


Figure 7.15: Skin-friction (left) and pressure (right) coefficient distributions on the surface of the Eppler 387 airfoil at $\alpha = 7^\circ$ for different transition models and experimental data from [149] and [148].

The lift and drag coefficients are displayed in Figure 7.16. Good agreement is obtained between the numerical solutions and the experimental data for the lift coefficient, regardless of the transition model used. However, a significant improvement is seen in the drag coefficient when a transition model is used, as the solution without it greatly overestimates the drag coefficient. This is naturally related to the laminar flow prediction on the lower surface and the laminar separation bubble on the upper surface. Different measurements exist for this airfoil at this Reynolds number, which results in some scatter and serves as an example of possible experimental uncertainty. At $\alpha = 1^\circ$ the $\gamma - Re_\theta$ model predicts a

higher drag coefficient than the remaining models, a direct consequence of the pressure distribution, since it was the model that predicted transition the furthest downstream. At $\alpha = 7^\circ$ there seems to be a slight overprediction of the drag coefficient on the simulations with a transition model. The highest drag coefficient is that obtained with the AFT model, due to the higher friction component caused by the earlier transition. Even though the pressure distribution of the solutions obtained with the AFT model and the $k - \omega$ SST model are visually similar, the larger extent of turbulent flow in both surfaces leads to a much higher drag coefficient for the latter model.

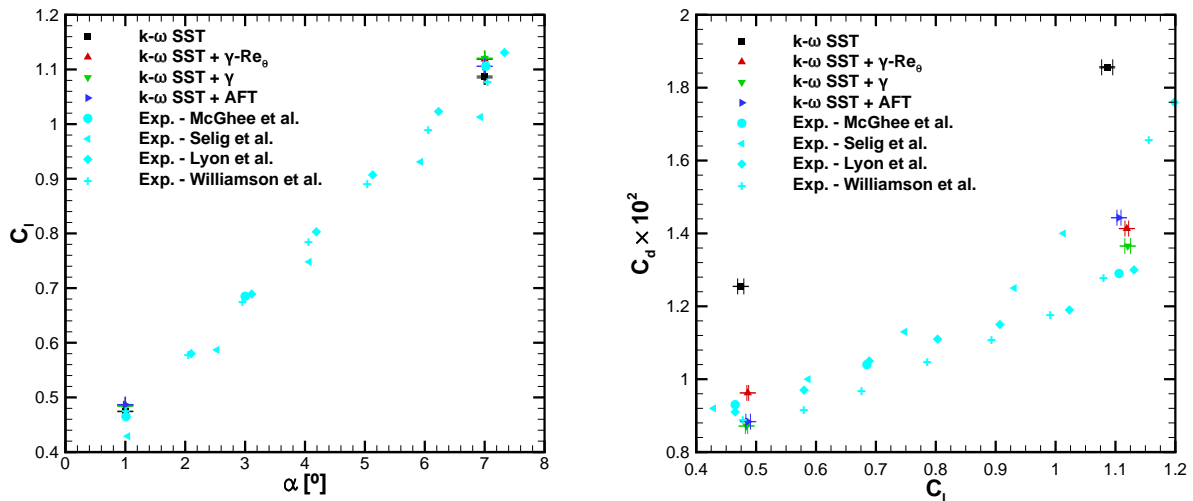


Figure 7.16: Lift coefficient as a function of the angle of attack (left) and drag polar (right) for the Eppler 387 airfoil at varying angle of attack with each transition model and experimental data [35, 148–151].

Figure 7.17 presents the locations at which the flow undergoes separation, reattachment, and the start and end of transition. Good agreement for the flow separation and reattachment locations at $\alpha = 1^\circ$ is observed. Although numerical uncertainty is very small due to the much higher level of grid refinement used for this geometry, there is no information regarding the experimental uncertainty, making it difficult to judge if any one SST model is better than the others. As mentioned before, no flow separation was detected for $\alpha = 7^\circ$, unlike the predictions of the $\gamma - Re_\theta$ and γ models. With regards to the transition location, the experimental location is always contained within the interval defined by the start and end positions of the numerical solutions.

7.3 Three-dimensional Flows

7.3.1 SD7003 wing

The SD7003 wing comprises the first three dimensional test case. For this geometry, only the formulations using the $k - \omega$ SST model coupled with the $\gamma - Re_\theta$ and γ transition models are considered. Figure 7.18 presents the C_f and C_p distributions on the surface of the wing for the two formulations. Regardless of the transition model used, the flow on the lower surface is always laminar. On the upper surface, both models predict a large region of separated laminar flow that starts at around $x/c = 0.18$.

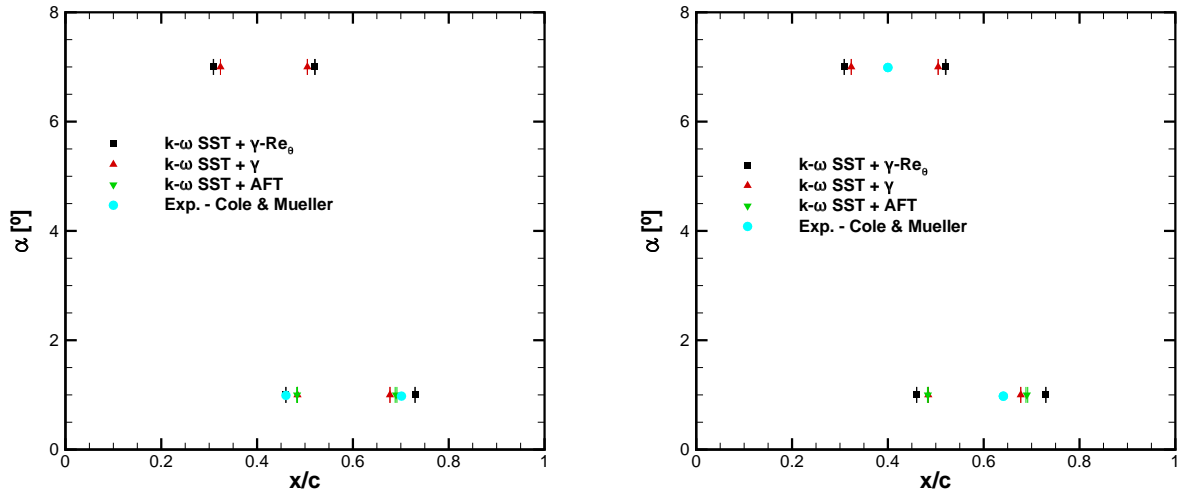


Figure 7.17: Location for flow separation and reattachment (left) and transition (right) for the Eppler 387 airfoil at varying angle of attack for different transition models and experimental data from [149].

The flow only reattaches close to $x/c = 0.6$ for the $\gamma - Re_{\theta}$ model and at around $x/c = 0.7$ for the γ model.

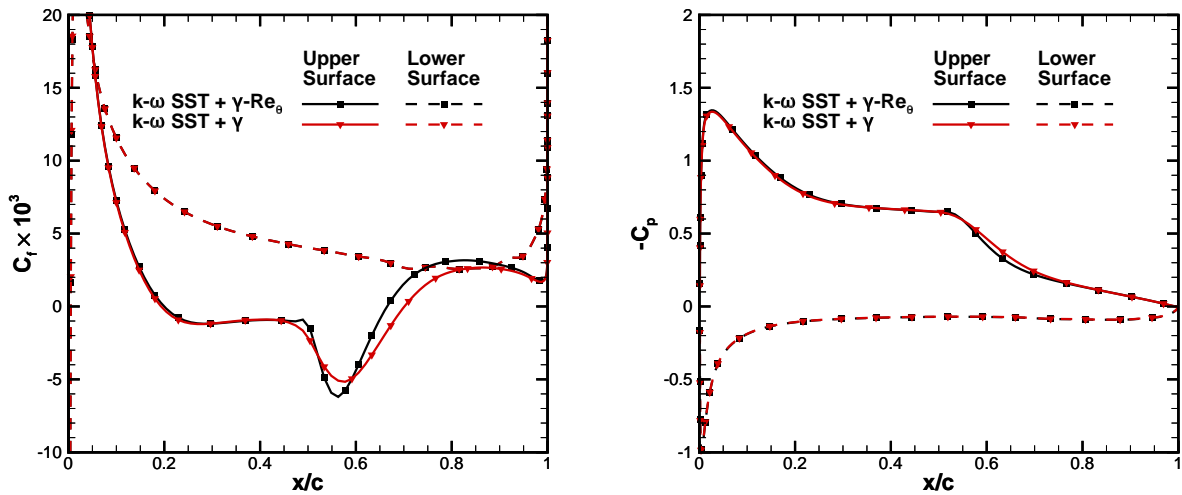


Figure 7.18: Skin-friction (left) and pressure (right) coefficient distributions on the surface of the SD7003 wing at the symmetry plane for the $k - \omega$ SST + $\gamma - Re_{\theta}$ and $k - \omega$ SST + γ models for the slipwall boundary condition case.

Under the setup with the boundary at the root of the wing being treated with a slipwall boundary conditions, the flow is nearly two-dimensional. as the velocity component and gradients in the spanwise direction are negligible. Upon introducing a no-slip wall boundary condition at the plane where the root of the wing is located, the flow changes significantly, due to the boundary layer that now develops along the wall. If a transition model is not used, the wall boundary layer is turbulent starting from the inlet, and the flow on the wing also quickly becomes turbulent. As a consequence, no flow separation is observed, and the only challenging feature becomes the interaction between the boundary layer developing on the wall and on the wing. Figure 7.19 illustrates the skin-friction coefficient on the surface of the wing and at the symmetry plane obtained in a calculation with the $k - \omega$ SST model.

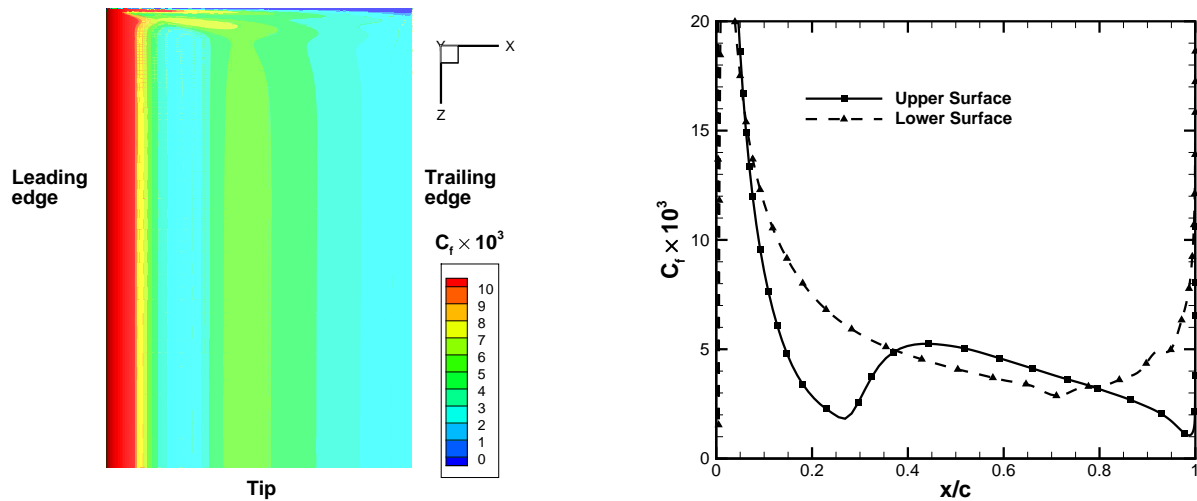


Figure 7.19: Skin-friction coefficient on the upper surface of the wing (left) and on the symmetry plane (right) at the surface of the SD7003 wing for the $k - \omega$ SST model for the no-slip wall boundary condition case.

The inclusion of a transition model is much more challenging. In this case, the boundary layer developing in the tunnel wall is still laminar, and the interaction with the laminar separation of the boundary layer at the wing causes difficulties for the statistically steady approach. As such, for this test case and using only one grid, unsteady simulations were performed. The computations were performed in two stages. In the first stage, the unconverged steady solution was used as the initial condition, and a total of 100 dimensionless time units were computed. For this stage, the iterative convergence criteria was set so that at each time step, the L_∞ norm of the normalised residuals was under 10^{-4} . For the second stage, the simulation time corresponded to 10 dimensionless time units, and the iterative criteria was decreased to 10^{-6} . The final solution of the first stage was used as the initial solution of the second stage.

Figure 7.20 presents the evolution of the friction and pressure components of the drag coefficient for the second run. Significant oscillations are observed in both quantities, regardless of the transition model used. More importantly, even though there is a clear high frequency oscillation which corresponds to vortex shedding on the upper surface, a periodic behaviour is not observed, i.e, there is more than one frequency with significant amplitude.

The skin-friction coefficient over the upper surface of the wing is plotted in Figure 7.21. The unconverged solution of the steady simulations with the no-slip wall boundary condition is presented as well. As mentioned, the cases with the freeslip boundary condition result in a quasi-2d solution, with a higher extent of separated flow being predicted by the γ model. This trend is observed as well close to the symmetry plane for the steady solution of the case with the no-slip wall boundary condition. In fact, the solution at the symmetry plane is very similar to that of the case with the freeslip boundary condition, showing that this region is not significantly affected by the boundary layer of the tunnel wall. Close to the root of the wing significant flow separation can be detected, which prevents the steady calculation from converging. The time-averaged unsteady solution shows some differences to the steady solution across the entire surface of the wing, a consequence from the difficulty in properly establishing the averaging

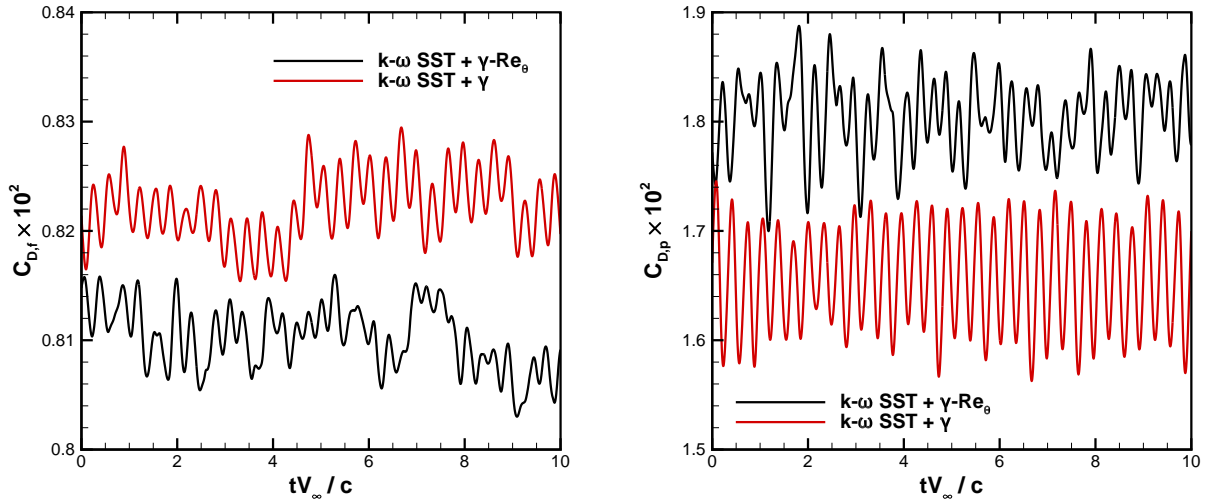


Figure 7.20: Time evolution of the friction (left) and pressure (right) components of the drag coefficient for the unsteady calculations of the SD7003 wing using the $k - \omega$ SST + $\gamma - Re_{\theta}$ and $k - \omega$ SST + γ models for the no-slip wall boundary condition case.

time given the irregular evolution of the flow. Most notably, the extent of flow separation close to the root wing is smaller than in the steady solution.

A depiction of the time-averaged velocity field at the symmetry plane is given in Figure 7.22. Experimental data from [161] and the numerical solutions of the $\gamma - Re_{\theta}$ and γ models are presented. Uncertainty is not given for either case, for it was not provided in the experimental data, and only a single grid was used in the numerical simulations, preventing its estimation through the procedure described in Section 4.3. Regardless of the transition model used, no significant differences are visible between the steady solution of the simulation with the no-slip boundary condition and the simulation using the freeslip boundary condition. On the contrary, the time averaged solution of the unsteady calculation exhibits a larger separation bubble than the steady simulations, with this effect being stronger for the $\gamma - Re_{\theta}$ model. All numerical calculations exhibit a laminar separation bubble that is considerably larger than that from the experimental data. Furthermore, the velocity increase at the suction peak predicted by each transition model is smaller than that observed for the experimental data. Despite the differences observed in the velocity field, significant improvement of the solution is obtained when either the $\gamma - Re_{\theta}$ or γ transition models are used when compared to the solution of the $k - \omega$ SST model.

7.3.2 6:1 prolate spheroid

The second three-dimensional case consists of the 6:1 prolate spheroid. Figure 7.23 presents the skin friction coefficient on the unrolled surface of the prolate spheroid for $\alpha = 5^\circ$. x/L represents the axial position along the surface, while the azimuthal angle Φ is considered as 0° at the symmetry plane on the pressure side of the spheroid and $\Phi = 180^\circ$ at the symmetry plane on the suction side. Experimental data as well as the results obtained with different turbulence and transition modelling approaches are shown. Not the entire surface of the spheroid is shown, as the areas corresponding to the extremities of the spheroid are blanked out. This is done in order to achieve consistency between the experiments

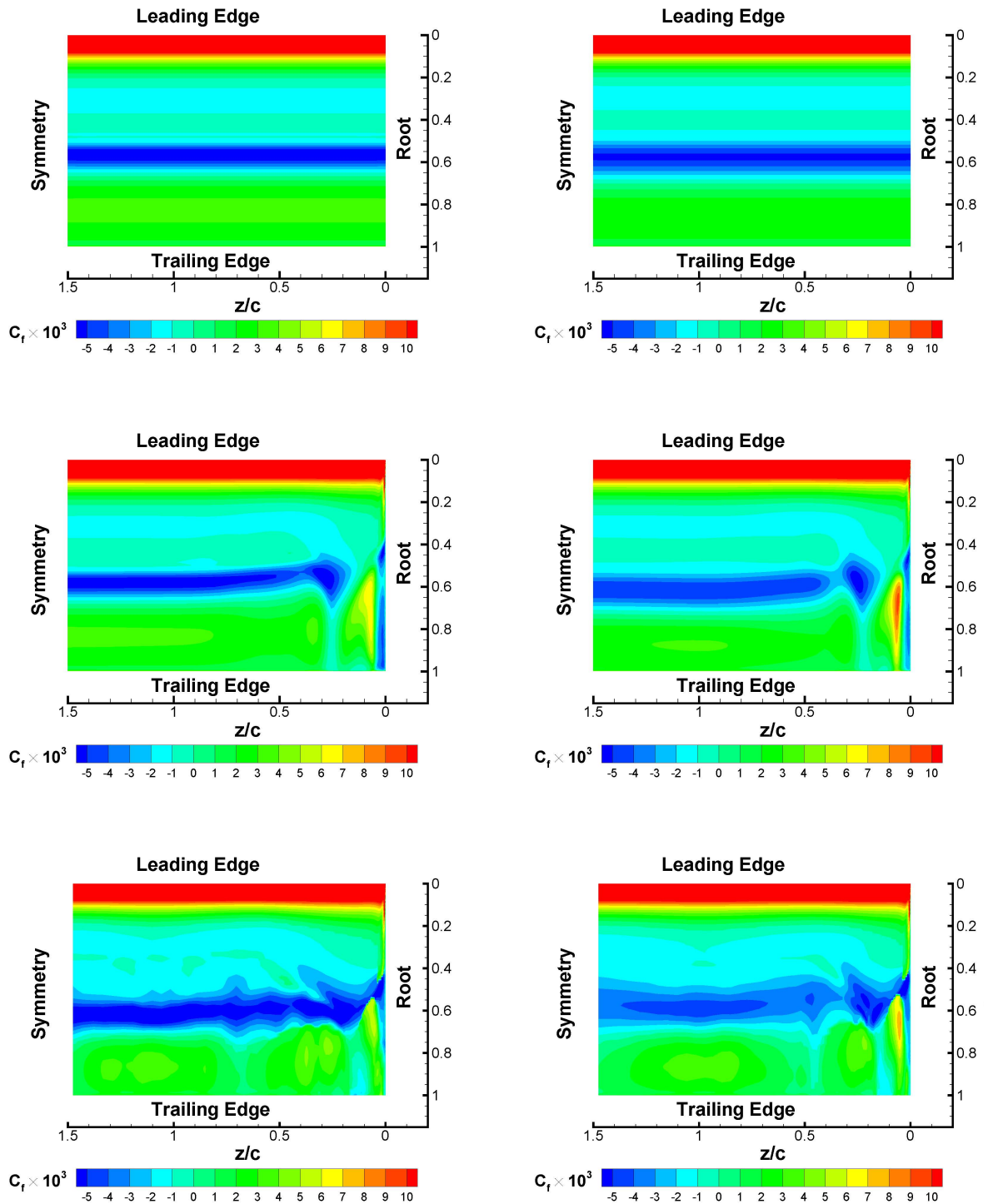


Figure 7.21: Skin-friction coefficient distribution on the upper surface of the SD7003 wing. Slipwall boundary condition using the $\gamma - Re_\theta$ (top left) and the γ (top right) model. Steady solution of the no-slip wall boundary condition using the $\gamma - Re_\theta$ (middle left) and the γ (middle right) model. Time-averaged unsteady solution of the no-slip wall boundary condition using the $\gamma - Re_\theta$ (bottom left) and the γ (bottom right) model.

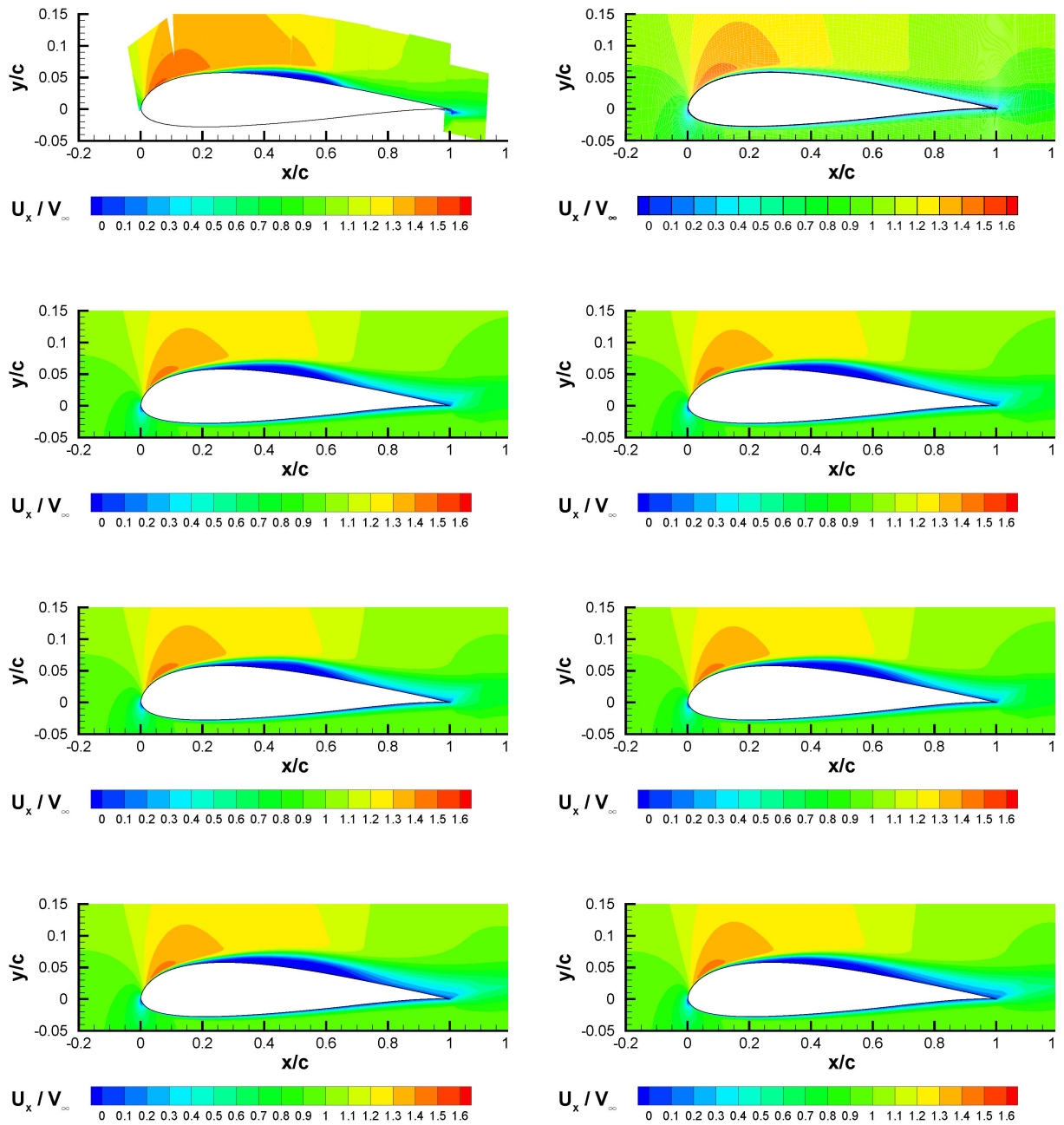


Figure 7.22: Velocity field around the SD7003 wing at the symmetry plane. First row: experimental data (left) and wall boundary condition using only the $k-\omega$ SST model (right). Second row: slipwall boundary condition using the $\gamma - Re_\theta$ (left) and the γ (right) model. Third row: steady solution of the no-slip wall boundary condition using the $\gamma - Re_\theta$ (left) and the γ (right) model. Fourth row: time-averaged unsteady solution of the no-slip wall boundary condition using the $\gamma - Re_\theta$ (left) and the γ (right) model.

and the numerical solutions, as there was no measured data on those regions.

The experimental data shows a well defined transition front at around $x/L = 0.5$ for most azimuthal angles from the suction side up to the pressure side, with transition corresponding to the region with the sharp increase of C_f . None of the five modelling approaches presented is able to reproduce the trends exhibited by the experiments. On the symmetry plane at the suction side ($\Phi = 180^\circ$) all models predict transition further upstream than the measured data. Furthermore, the C_f increase associated with flow transition is also much faster in the numerical calculations than in the experiments. In the range $\Phi = 180^\circ$ to $\Phi = 150^\circ$, as the azimuthal angle is increased, the solutions using the $k - \omega$ SST turbulence model and the KSKL + γ formulations predict a slight shift upstream of the transition front. For the AFT transition model the transition region always moves downstream with decreasing azimuthal angle, whereas the KSKL + $\gamma - Re_\theta$ combination, displays a small region where the transition region remains at the same streamwise location, and then starts to decrease. All models are consistent in the transition region moving downstream for $\Phi < 150^\circ$ as the azimuthal angle is lowered, resulting in transition being predicted much further downstream for most of the surface of the spheroid than the experimental data, resulting in large modelling errors on the pressure side of the spheroid. The solution that displays the least worst agreement with the experiments is the one obtained with the KSKL + $\gamma - Re_\theta$ combination. At the lower azimuthal angles there is still a significant portion of the flow that is turbulent, with a strong reduction of that region when the transition model is changed to the γ model. The solutions obtained using the other formulations do not exhibit transition in the displayed area of the surface of the spheroid.

As a matter of fact, none of the attempted formulations is suitable for this case as all lack the capability to model crossflow transition. To overcome this obstacle the crossflow extension described in Appendix A is implemented on the $\gamma - Re_\theta$ and γ models. The results for the new model combinations using the crossflow extension are presented in Figure 7.24. The usage of the crossflow extension is seen in the range $60^\circ < \Phi < 150^\circ$, where it leads to the transition region moving upstream. This results in a better agreement with the experimental distribution than the previous cases where the crossflow extension was not used. Nonetheless for $\Phi < 30^\circ$, there is no effect from the crossflow extension, and transition again takes place much further upstream than that seen in the experimental data. The new modelling approach results in a smoother distribution when used with the γ model than with the $\gamma - Re_\theta$ model. This is attributed to the differences in the coupling with each model, since the extension itself is the same. When used with the same transition model but with different underlying turbulence models, the crossflow extension is triggered at different streamwise locations. This is visible for the $\gamma - Re_\theta$ model, where the effect of the crossflow extension is seen at $x/c = 0.45$ at $\Phi = 90^\circ$. At the same azimuthal angle and transition model but using the KSKL turbulence model instead, the crossflow extension leads to transition at around $x/c = 0.3$.

For the simulations at the angle of attack of $\alpha = 10^\circ$ the KSKL turbulence model and the AFT transition model are no longer employed. Figure 7.25 presents the experimental skin-friction coefficient distribution, as well as the one obtained from the numerical solutions using the $k - \omega$ SST turbulence model with the $\gamma - Re_\theta$ and γ models. With the increase in the angle of attack the transition front moves upstream throughout the entire surface of the spheroid, being located at around $x/L = 0.25$ in the range

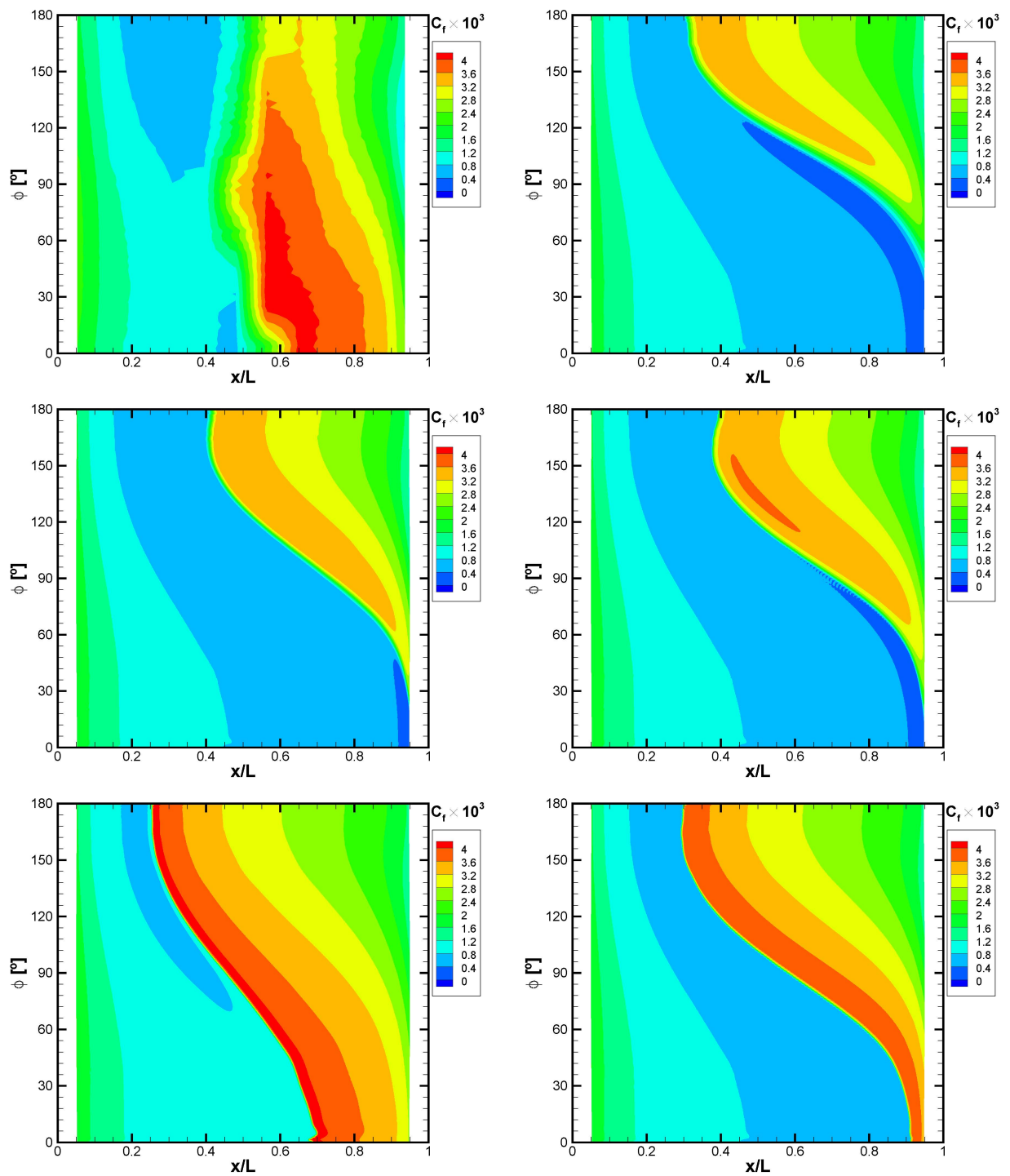


Figure 7.23: Skin friction coefficient on the surface of the prolate spheroid at $\alpha = 5^\circ$. Experimental data [154](top left), $k - \omega$ SST + AFT model (top right), $k - \omega$ SST + $\gamma - Re_\theta$ model (middle left), $k - \omega$ SST + γ model (middle right), KSKL + $\gamma - Re_\theta$ model (bottom left) and KSKL + γ model (bottom right).

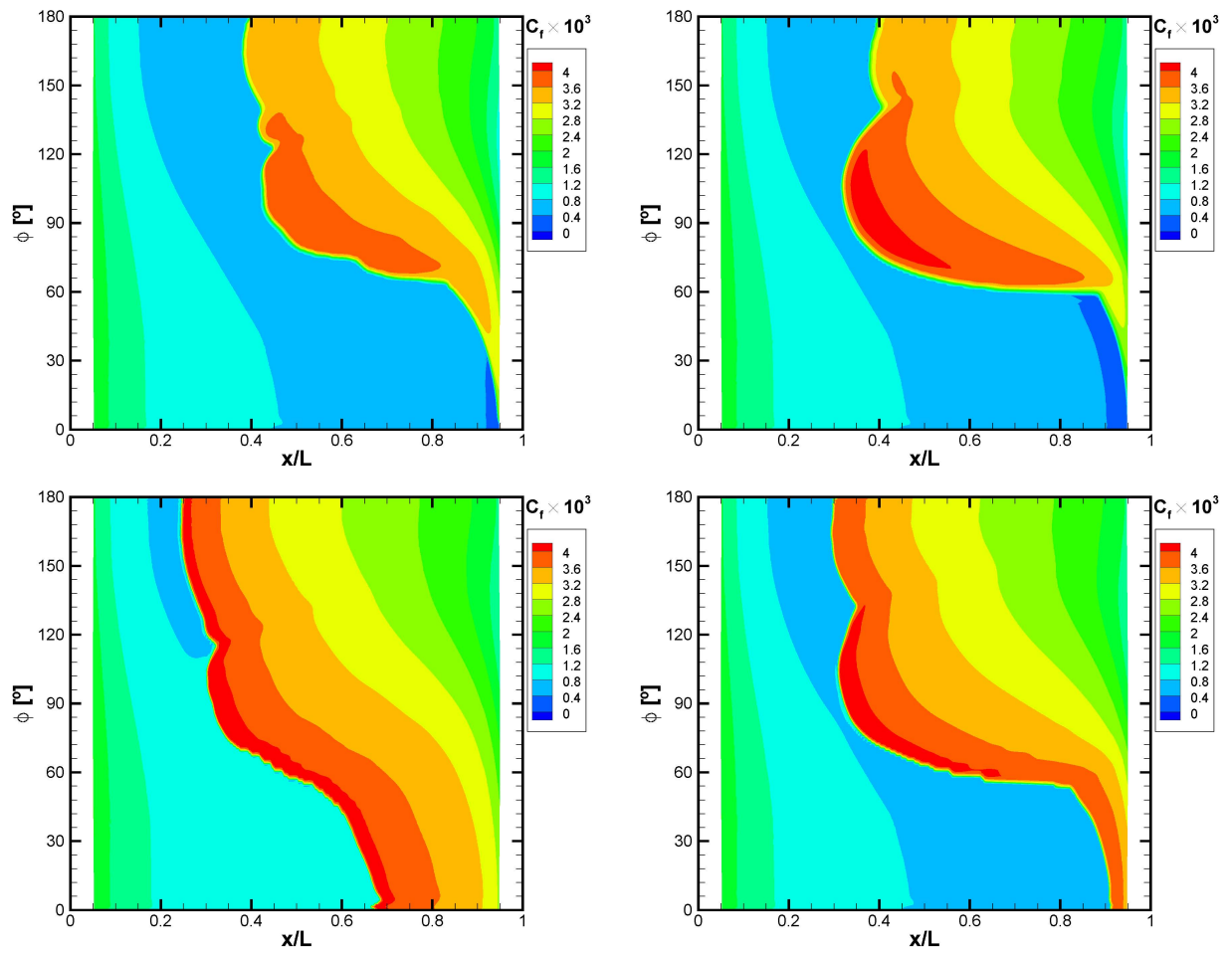


Figure 7.24: Skin friction coefficient on the surface of the prolate spheroid at $\alpha = 5^\circ$ with the usage of the crossflow extension. $k - \omega$ SST + $\gamma - Re_\theta$ model (top left), $k - \omega$ SST + γ model (top right), KSKL + $\gamma - Re_\theta$ model (bottom left) and KSKL + γ model (bottom right).

$75^\circ < \Phi < 150^\circ$. For $\Phi < 75^\circ$, the transition front reaches around $x/L = 0.6$ at $\Phi = 0^\circ$, which is similar to the measurements at $\alpha = 5^\circ$. Once again, the simulations where the crossflow extension is not employed show large discrepancies with the experimental data. The $k - \omega$ SST + $\gamma - Re_\theta$ formulation now predicts transition to start downstream of the experimental data for $\Phi = 180^\circ$. Once again, with the decrease of the azimuthal angle the transition front moves upstream, close to around $x/L = 0.25$ at $\Phi = 150^\circ$, where it is in good agreement with the experimental data. However, further decreasing the azimuthal angle down to $\Phi = 90^\circ$ leads to the transition front to significantly shift downstream, such that for lower azimuthal angles the flow is almost entirely laminar. Using the γ model instead of the $\gamma - Re_\theta$ model simply leads to an overall shift upstream of the transition front, which is more pronounced close to $\Phi = 180^\circ$.

With the use of the crossflow extension, the solutions of both transition models change significantly. At the symmetry plane on the suction side, there is now a much closer agreement between the two models. Once again, the transition front moves upstream as the azimuthal angle is decreased in the range $150^\circ < \Phi < 180^\circ$. However, past $\Phi = 150^\circ$, the transition front keeps shifting upstream, a direct consequence of the crossflow correlations. This effect is also seen in the experimental data, although it is much less pronounced. The region of turbulent flow extends all the way down to $\Phi = 60^\circ$, where the transition front now moves downstream, such that in the region $\Phi < 45^\circ$ the flow is laminar, unlike what is observed in the experimental distribution. Nonetheless, the use of the crossflow extension does result in some improvement and better agreement with the experimental data.

The results for the angle of attack of 15° are depicted in Figure 7.26. Only calculations using the crossflow extension are performed. The kink in the transition front that is observed on the experimental data at $\Phi = 130^\circ$ corresponds to the location where the transition mechanism changes, as crossflow transition is dominant for $\Phi < 130^\circ$. This feature is also observed in the simulations, although the kink is located at a higher azimuthal angle, and slightly upstream. In the region $\Phi > 130^\circ$ the agreement between the numerical solutions and the measured data is good, although at $\Phi = 180^\circ$, transition is predicted downstream of the experimental location. As a consequence of the earlier transition in the simulations, the turbulent region with lower C_f is larger in the simulations. In the range $60^\circ < \Phi < 120^\circ$ the numerical transition front matches well with that from the experiments. However, for the lower azimuthal angles, the flow is laminar, while the experiments show a steady shift downstream of transition, stopping at $x/L = 0.8$ at $\Phi = 0^\circ$.

It is clear that the use of the crossflow extension improves the agreement between the numerical solution and the experimental measurements, and is nearly indispensable for this case. However, the nearly entirely laminar flow at the pressure side of the spheroid across all angles of attack is still an incorrect feature that highlights some deficiencies in this formulation. In particular, there is no interaction between crossflow and the other modes of transition in the crossflow extension used, which might contribute to the discrepancies observed in the pressure side of the spheroid.

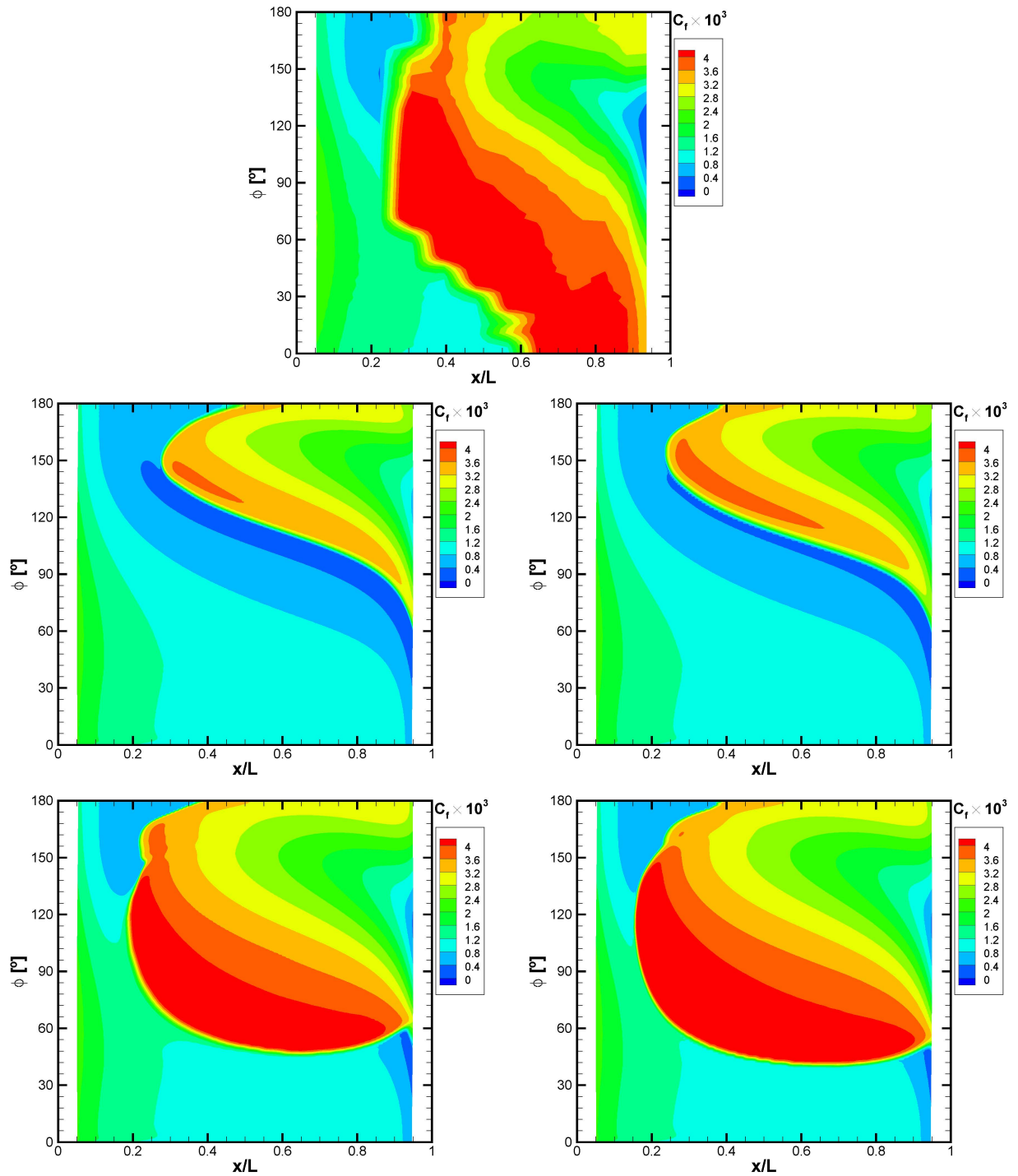


Figure 7.25: Skin friction coefficient on the surface of the prolate spheroid at $\alpha = 10^\circ$. Experimental data [154](top), $k - \omega$ SST + $\gamma - Re_\theta$ model (top left), $k - \omega$ SST + γ model (top right), $k - \omega$ SST + $\gamma - Re_\theta$ model with crossflow extension (bottom left) and $k - \omega$ SST + γ model with crossflow extension (bottom right).

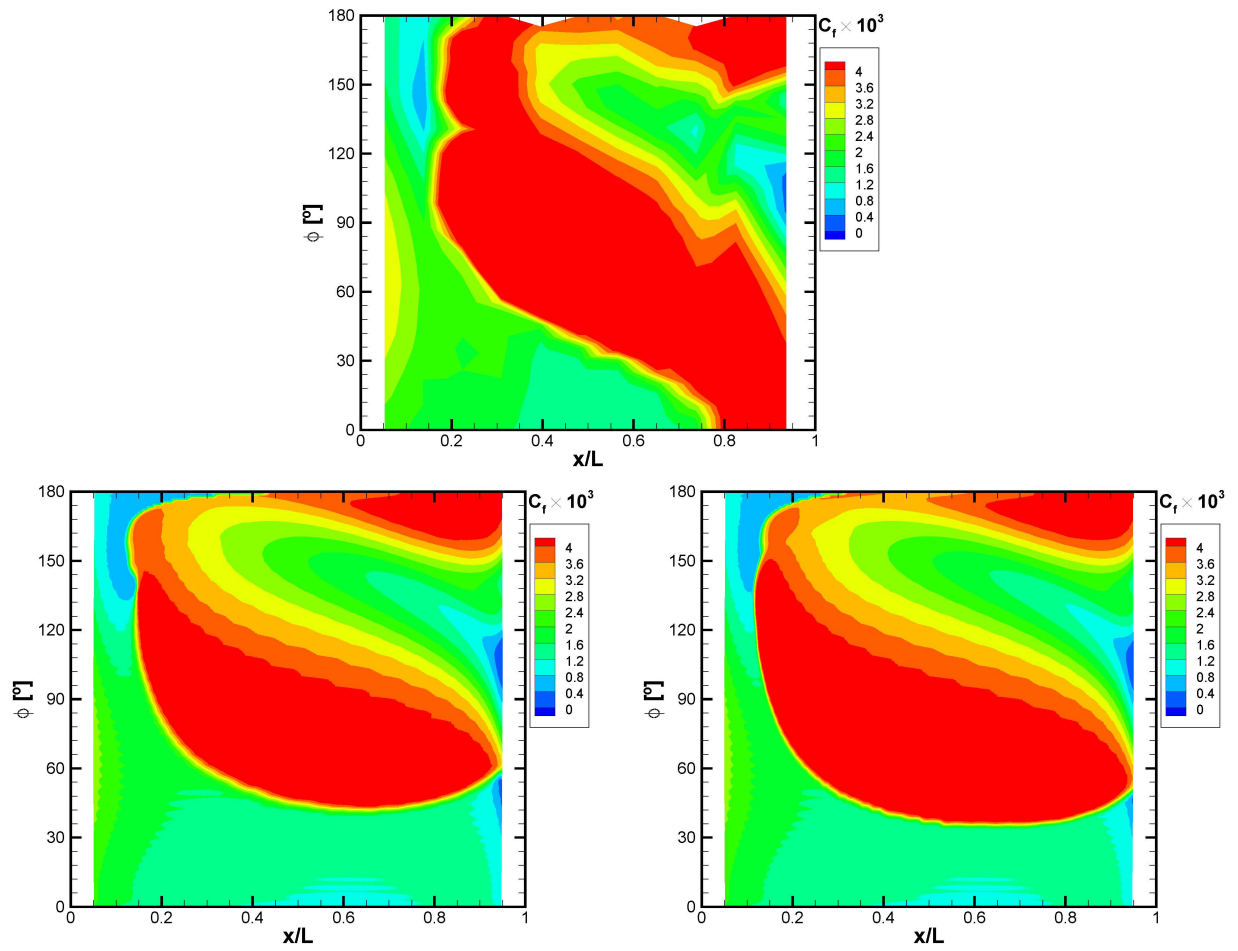


Figure 7.26: Skin friction coefficient on the surface of the prolate spheroid at $\alpha = 15^\circ$. Experimental data [154](top), $k-\omega$ SST + $\gamma - Re_{\theta}$ model with crossflow extension (bottom left) and $k-\omega$ SST + γ model with crossflow extension (bottom right).

7.3.3 Sickle wing

The final test case addressed is the flow around the sickle wing, starting with the unstructured grid set. The skin friction coefficient distribution obtained with the $k - \omega$ SST model is shown in Figure 7.27, as well as the transition line obtained from the experimental data. In both the upper and lower surfaces of the wing, the $k - \omega$ SST model predicts transition at the leading edge of the wing, resulting in turbulent flow across the entire surface. Naturally, the model is incapable of matching the experimental transition front. In addition, several oscillations are observed in the skin friction coefficient, particularly in the upper surface. This is a consequence of the unstructured grid topology used for this geometry and the hanging nodes that occur in the grid close to the boundary layer.

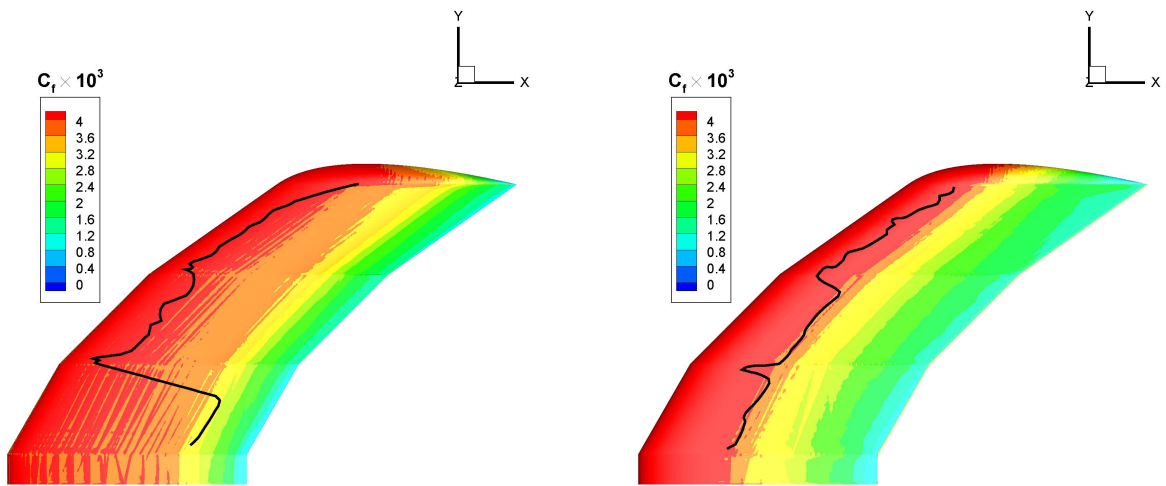


Figure 7.27: Skin friction coefficient on the upper (left) and lower (right) surface of the sickle wing for the $k - \omega$ SST model on the Hexpress grid set and experimental transition line [163, 164].

The next formulation to be considered is the $k - \omega$ SST + γ combination. Figure 7.28 presents the results obtained for every other grid for this model. The solution for this model combination exhibits large changes as the grid is refined. In the coarsest grid, the upper surface exhibits early transition in the section corresponding to $\Psi = 30^\circ$, evidenced by the rapid increase of C_f . Moving away from the root of the wing, the transition front moves downstream, and now most of the surface experiences laminar flow. This trend is exactly the opposite of that displayed by the experimental data, where a large portion of laminar flow is only seen in the first section, and the transition front moves upstream as one moves towards the tip of the wing. The prediction on the lower surface is better. On the first section transition is predicted slightly upstream of the experimental data, and slightly downstream in the final section.

However, as the grid is refined, there is a drastic change in both surfaces. For the intermediate grid, transition now takes place soon after the leading edge, across the entire span of the wing, in both the lower and upper surfaces. This heavily contrasts to the late transition predicted in the coarsest grid on the upper surface, being similar to calculation without a transition model. Further refining the grid causes additional changes in the transition front. In the upper surface there appears to be what resembles a turbulent spot in the first section, while the outboard part of the wing is immersed in turbulent flow. This

solution is nearly the opposite of the one obtained in the coarsest grid with regards to the regions of the flow that are laminar or turbulent. Meanwhile, a steady shift of transition downstream is obtained in the lower surface.

These results show the deficiencies of the γ model highlighted in Section 5.3. In this particular case, the combination of the first order upwind scheme and the unstructured grid topology leads to drastic changes with grid refinement, which compromise the numerical accuracy of the simulations. For this reason, the γ model is no longer considered for this case.

Figure 7.29 presents the solution for the $k - \omega$ SST + $\gamma - Re_\theta$ formulation. In the upper surface, there is a good agreement between the numerical results and the transition line obtained from the experiments at the first section, where natural transition takes place. Moving towards the tip of the wing, the solution of the $k - \omega$ SST + $\gamma - Re_\theta$ model shows no significant change in the position of transition along the chordwise direction, whereas the experimental transition line moves upstream due to crossflow transition. In a similar way to the prolate spheroid test case, this shows the inability of the $\gamma - Re_\theta$ model to account for crossflow transition without the use of additional correlations. In the lower surface there is a better agreement between the calculations and the experimental data throughout the entire span of the wing, although the differences get larger close to the tip of the wing with transition being predicted downstream of the experimental location.

The next logical step is to employ the crossflow extension, which is done for the $\gamma - Re_\theta$ model. The results are given in Figure 7.30. The inclusion of the crossflow effects leads to remarkable agreement between the numerical solution and the experimental data throughout most of the entire upper surface, with the exception of the first section. In this region, which was correctly predicted in the absence of the crossflow extension due to it occurring via the natural transition mechanism, transition in the numerical results is now located upstream of the experimental transition line. On the lower surface, the numerical transition front is now located upstream of the experimental one, whereas it was downstream of it when no crossflow extension was used. Nevertheless, for the first and third regions of the wing, good agreement between the calculations and the measurements is obtained.

To conclude the discussion of this test case with the unstructured grids, Figure 7.31 presents a comparison of the pressure coefficient obtained with each model with available experimental data at three different sections of the wing. These correspond to cuts at the middle of each section at constant sweep angle. In the first section there is a strong waviness of the numerical pressure coefficient, a consequence of the unstructured grid used. This behaviour is consistent across the solutions of the three models displayed. Nonetheless, in the first section there is a good agreement with experimental data, irrespective of which formulation is employed. In the remaining two sections, the best agreement to the experimental results is given by the $k - \omega$ SST model solution without a transition model, and by the solution where the crossflow correlations were used. The C_p distribution obtained with the $\gamma - Re_\theta$ model without the crossflow extension seems to underpredict the pressure coefficient in the lower surface in the range $0.6 < x/c < 0.8$ and to overpredict it for $x/c > 0.7$ in the upper surface. The latter effect is likely caused by the late transition predicted in the upper surface.

The usage of the multiblock structured grids generated with GridPro is now considered. The skin-

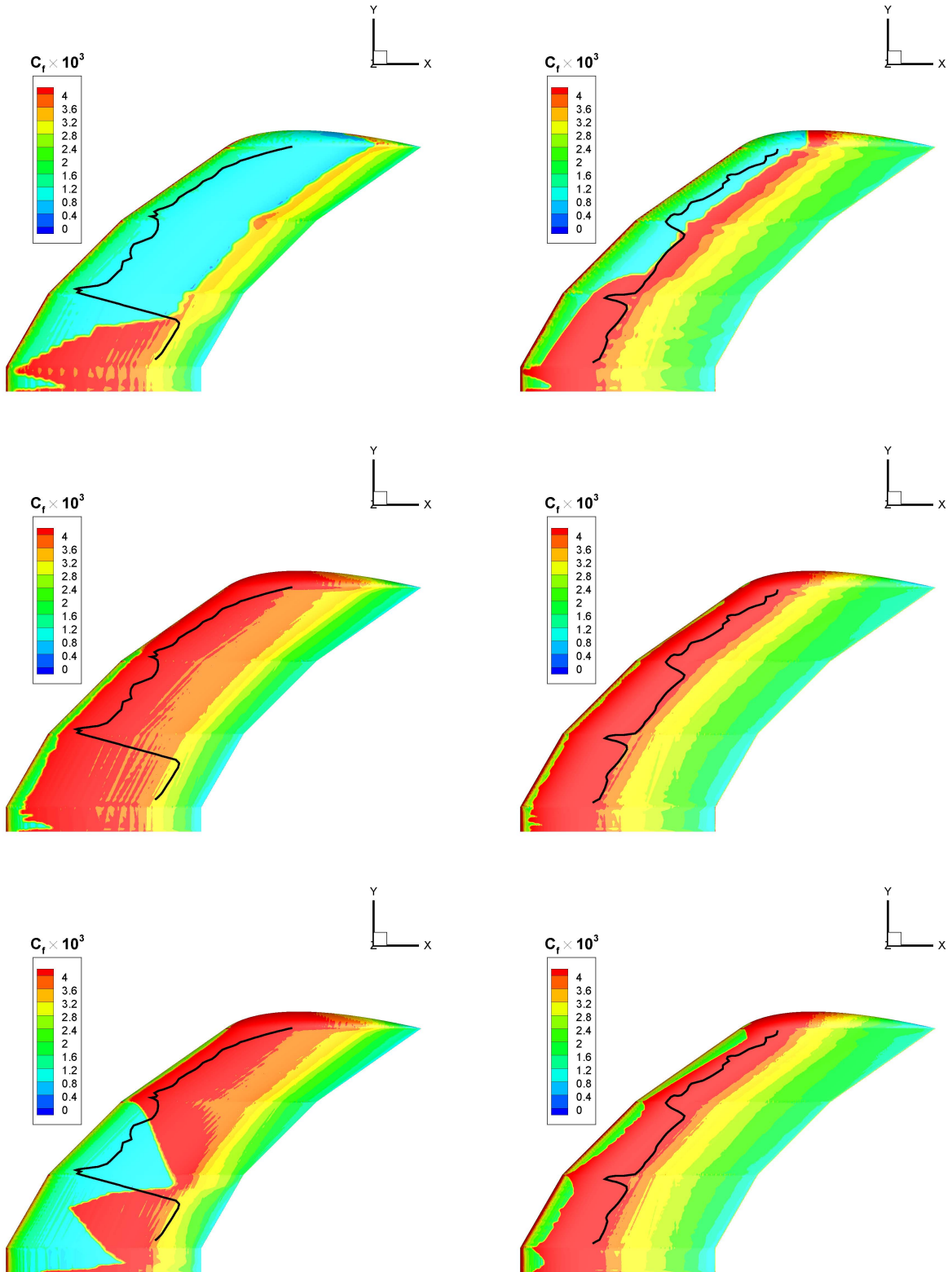


Figure 7.28: Skin friction coefficient on the surface of the sickle wing for the $k - \omega$ SST + γ model on the Hexpress grid set and experimental transition line [163, 164]. Upper surface of the coarsest grid (top left), lower surface of the coarsest grid (top right), upper surface of an intermediate grid (middle left), lower surface of an intermediate grid (middle right), upper surface of the finest grid (bottom left), lower surface of the finest grid (bottom right).

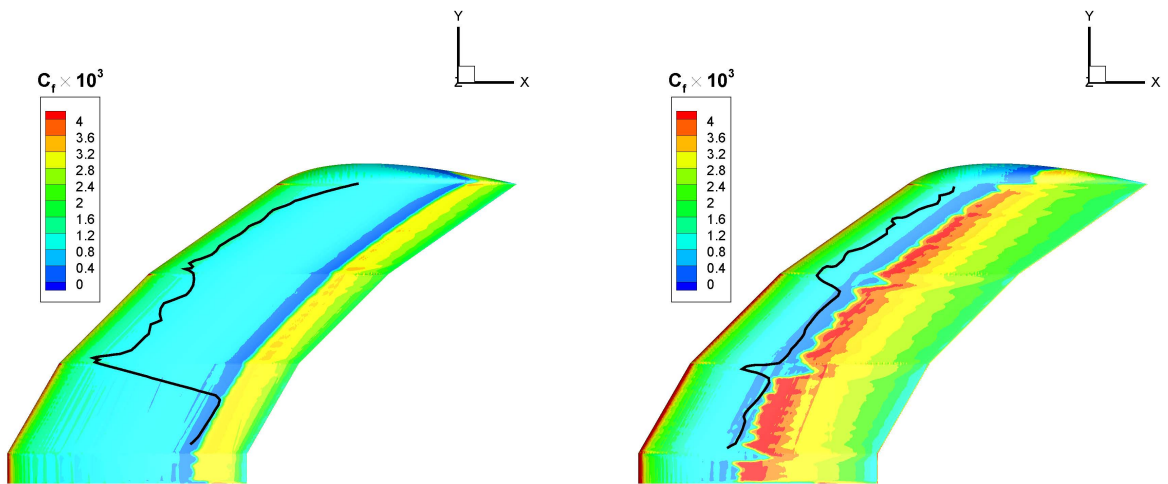


Figure 7.29: Skin friction coefficient on the upper (left) and lower (right) surfaces of the sickle wing for the $k - \omega$ SST + $\gamma - Re_\theta$ model on the Hexpress grid set and experimental transition line [163, 164].

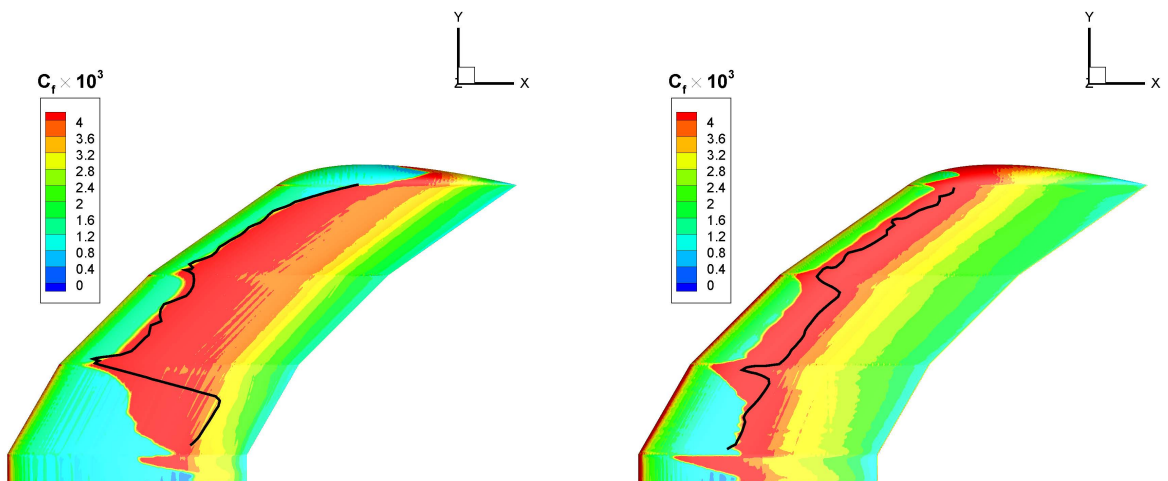


Figure 7.30: Skin friction coefficient on the upper (left) and lower (right) surfaces of the sickle wing for the $k - \omega$ SST + $\gamma - Re_\theta$ model using the crossflow extension on the Hexpress grid set and experimental transition line [163, 164].

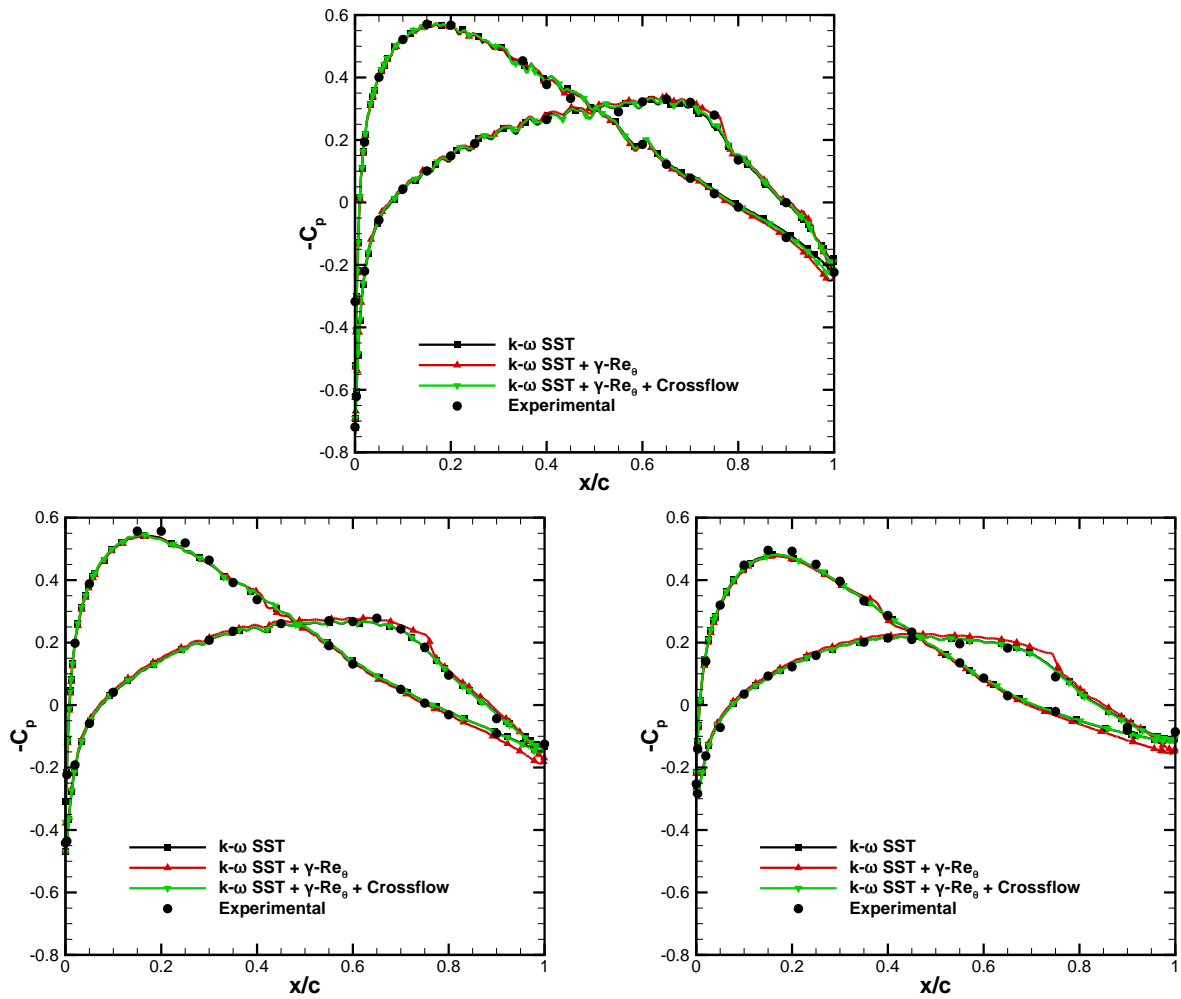


Figure 7.31: Pressure coefficient distribution on the surface of the prolate spheroid obtained with the different modelling approaches on the Hexpress grid set and experimental data [163, 164] at the middle of the first section (top), middle of the second section (bottom left) and middle of the third section (bottom right).

friction coefficient distribution obtained with the $k - \omega$ SST turbulence model is exhibited in Figure 7.32 for the finest grid. Due to the grid quality, C_f displays a smooth evolution, unlike what was observed for the unstructured grids. Aside from that, the behaviour of the skin-friction coefficient is similar throughout the surface of the wing, exhibiting transition at the leading edge for both the upper and lower surfaces, since no transition model is employed.

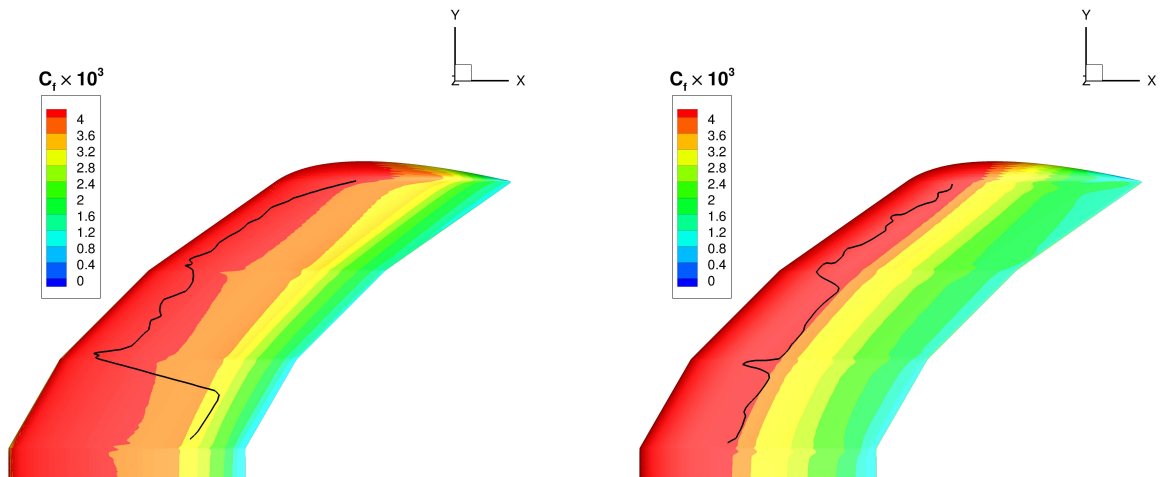


Figure 7.32: Skin-friction coefficient distribution on the upper (left) and lower (right) surface of the sickle wing for the $k - \omega$ SST model on the GridPro grid set and experimental transition line [163, 164].

Following the same order as presented for the Hexpress grid set, Figure 7.33 presents the C_f distribution on the surface of the sickle wing obtained with the $k - \omega + \gamma$ model for the coarsest and finest grids of the set. The effect of grid refinement introduces some slight changes in C_f , particularly at the tip of the wing on the lower surface. This case contrasts heavily with solutions obtained for the Hexpress grid set, in which grid refinement led to extreme changes in the location of transition. This highlights the sensitivity of the γ transition model to the quality of grid used.

The convergence of the γ model for this grid set allows for its solution to be compared against the experimental data. In the upper surface, the numerical solution exhibits transition slightly upstream than the experimental measurement at the first constant sweep section. Moving along the span of the wing towards the tip, there is only a small shift downstream of the transition location predicted by the γ model, missing the onset of transition due to crossflow transition that takes place much closer to the leading edge. On the lower surface, the γ model initially predicts transition upstream of the measured data. At the second constant sweep section, the agreement with experimental data is better, but as the sweep angle is again increased, the numerical solution now exhibits transition downstream of the experimental line.

Since the $k - \omega$ SST + γ model exhibits a proper behaviour with grid refinement, simulations using the crossflow extension for this model were also performed for the GridPro grid set. The solution for the finest grid is exhibited in Figure 7.34. In the upper surface, there is a good agreement between the numerical solution and the experimental data for the higher sweep angles. However, the crossflow extension causes transition to occur much further upstream at the first section, which exhibited better

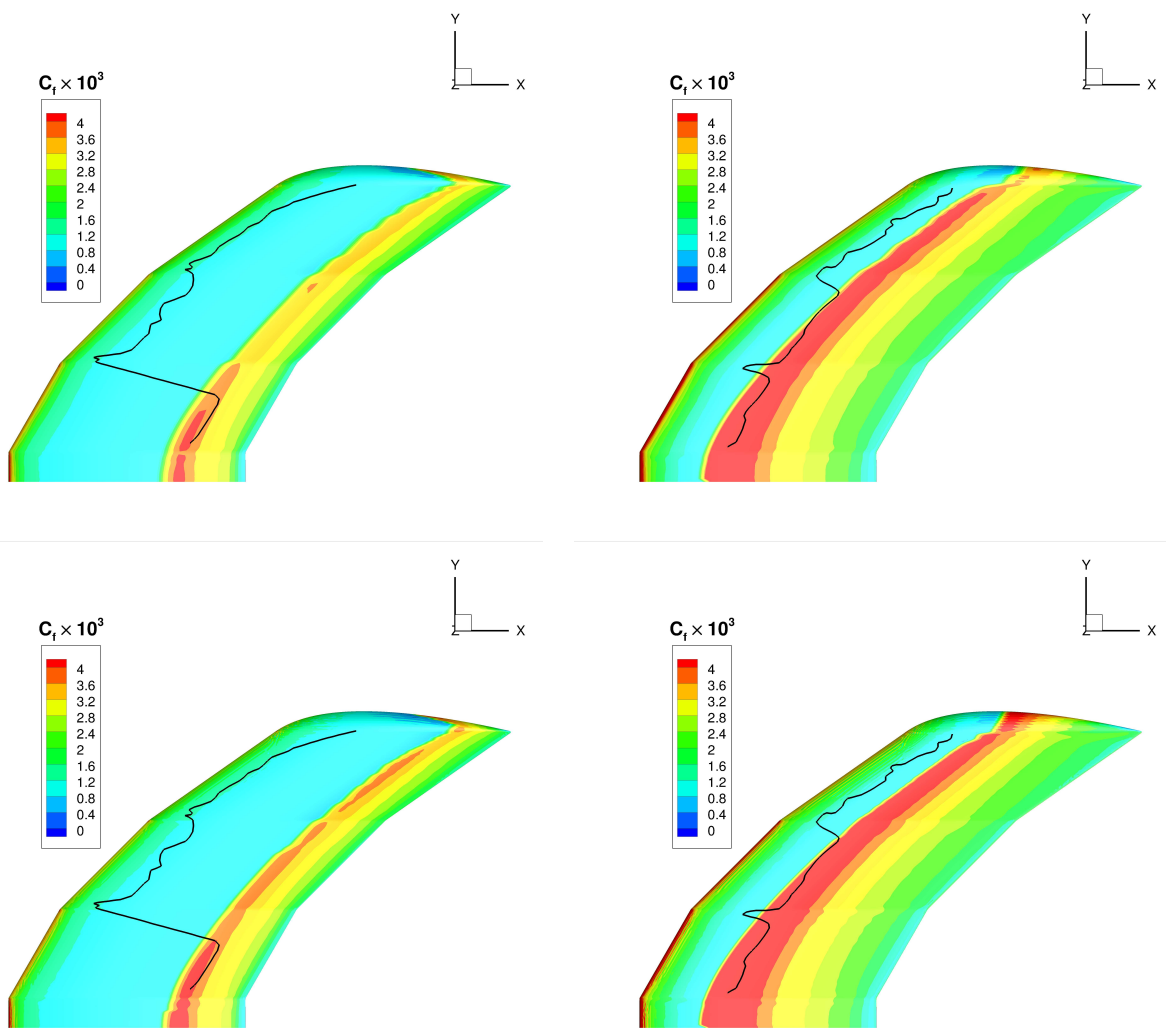


Figure 7.33: Skin-friction coefficient distribution on the upper (left) and lower (right) surface of the sickle wing for the $k - \omega$ SST + γ model on the GridPro grid set and experimental transition line [163, 164]. Coarsest grid (top) and finest grid (bottom).

agreement for the previous case where the crossflow extension was not used. A similar effect takes place in the lower surface, where the crossflow extension causes transition much further upstream for most of the surface of the wing. However, the section with the highest sweep angle now exhibits very good agreement with the experimental data.

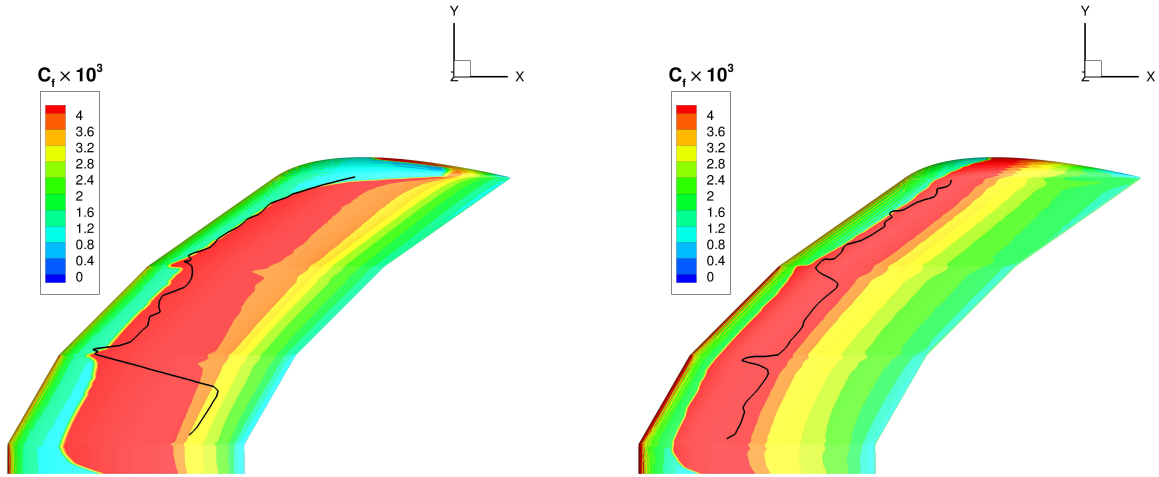


Figure 7.34: Skin-friction coefficient distribution on the upper (left) and lower (right) surface of the sickle wing for the $k-\omega$ SST + γ model using the crossflow extension on the GridPro grid set and experimental transition line [163, 164].

Figure 7.35 presents the results obtained with the $k-\omega$ SST + $\gamma - Re_\theta$ model. Across the entire surface, the numerical solution is similar to that which was obtained for the Hexpress grid set, although it is much smoother. Again, since no crossflow extension is present, the location of transition is mostly insensitive to the increase of the sweep angle, and only displays good agreement with the experimental measurements at the first section, which has the lowest sweep angle.

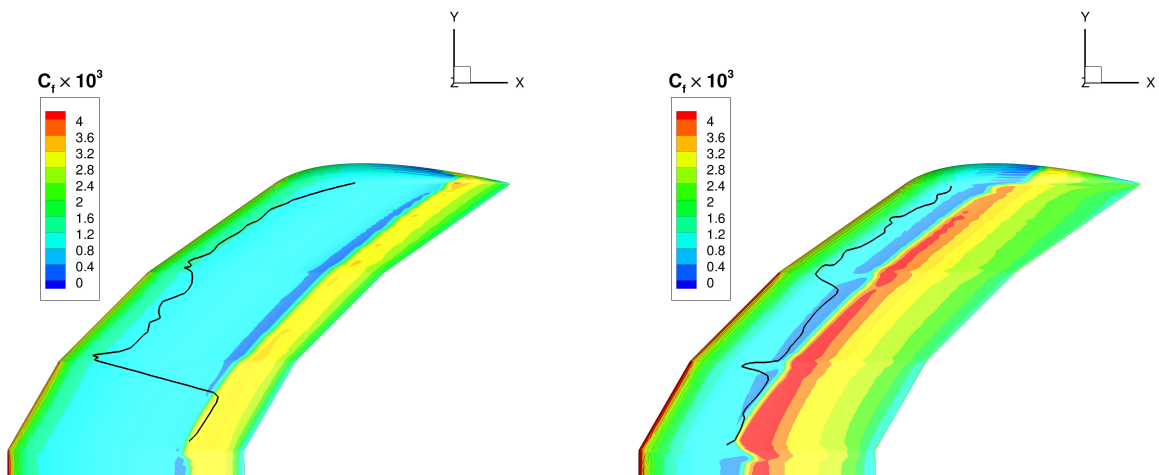


Figure 7.35: Skin-friction coefficient distribution on the upper (left) and lower (right) surface of the sickle wing for the $k-\omega$ SST + $\gamma - Re_\theta$ model on the GridPro grid set and experimental transition line [163, 164].

The solution obtained for the $k-\omega$ SST + $\gamma - Re_\theta$ model with the inclusion of the crossflow extension

is illustrated in Figure 7.36. Excellent agreement is observed in the upper surface with the exception of the section with the lowest sweep angle, in which the crossflow extension causes transition much further upstream than the measured data. On the lower surface, only the section with the highest sweep angle matches well with the experimental data, with the crossflow extension leading to earlier transition in the remaining sections of the wing. This trend is similar to that observed for the γ model, although the shift of transition upstream due to the crossflow extension is not as strong for the $\gamma - Re_\theta$ model. A comparison of these results with the solutions obtained for the Hexpress grid set shows that there are some differences at the regions where the sweep angle changes between each section and at the tip of the wing. At the section with the lowest sweep angle, the solution obtained in the GridPro grid set also exhibits transition slightly upstream than the solution obtained for the Hexpress grid set.

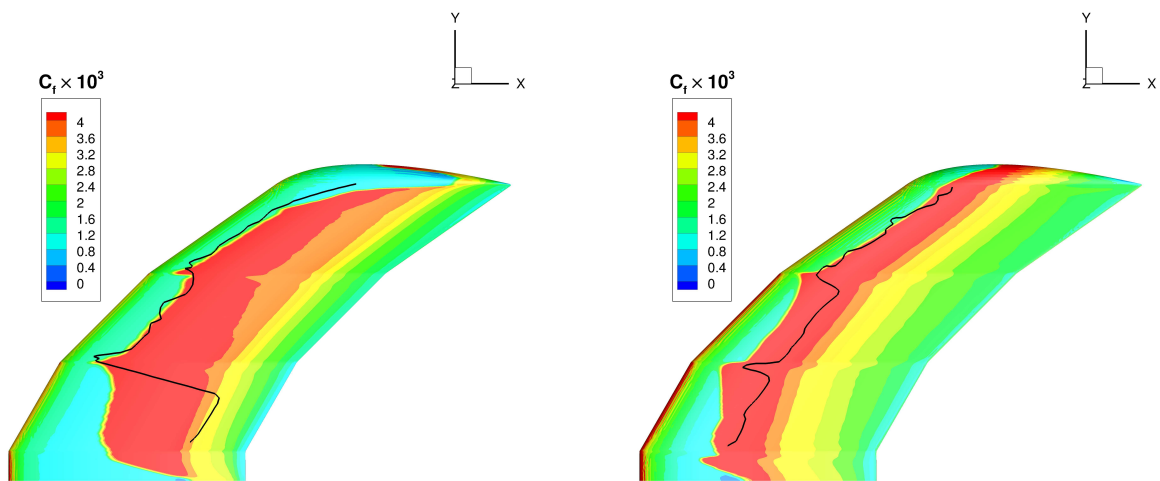


Figure 7.36: Skin-friction coefficient distribution on the upper (left) and lower (right) surface of the sickle wing for the $k - \omega$ SST + $\gamma - Re_\theta$ model using the crossflow extension on the GridPro grid set and experimental transition line [163, 164].

7.4 Main Remarks

The comparison with experimental data shows that when transition is caused by laminar separation or is located in regions of strong adverse pressure gradient, different modelling approaches lead to very similar solutions, which tend to agree well with experimental measurements. However, outside of these conditions, the prediction of the location of the transition region varies significantly, depending not only on the transition model employed, but on the underlying turbulence model as well. Nonetheless, the usage of transition models, even on the absence of sufficient information to uniquely set the inlet boundary conditions for turbulence, generally leads to an improvement of the force predictions, namely on the drag coefficient. For more complex three dimensional flows, the deficiencies of the models and the inability to handle crossflow transition become evident. The latter can be solved through the use of extensions to the models to account for crossflow, which result in much more accurate predictions for the location of transition, albeit some discrepancies are still observed.

The present comparison does not fit the requirements of a formal validation exercise for several reasons. On one hand, the experimental data available does not have details on the uncertainty of the measurements. On the other hand, the lack of detailed information for setting the turbulence quantities at the inlet do not fully determine the boundary conditions for the problem. Furthermore, the computational domain in most cases does not match the experimental setup, introducing additional discrepancies. While the latter could have been easily solved, the remaining issues are due to lack of information from the experiments, a common trend among most of the available data.

Chapter 8

Conclusions

This work presents a detailed assessment of RANS compatible formulations to account for laminar-to-turbulent transition modelling. This is an area where considerable attention has been devoted in the recent years by both researchers and industry alike, with new models being proposed, studied, and applied. These new transition models act as a complement to existing turbulence modelling approaches that are unable to accurately predict the onset of transition to turbulent flow, resulting in largely inaccurate solutions for flows at moderate Reynolds numbers. Thus, with the maturity of transition models so fades the general idea that RANS modelling is not appropriate for low Reynolds numbers flows, where there are non-negligible portions of both laminar and turbulent flow.

The first step consisted of an introduction to the physics of transition, where the classical division of different transition mechanisms is presented. Focus is given on the transition mechanisms that are addressed throughout this work such as natural transition, bypass transition, separation-induced transition and crossflow transition. A review of existing methods to predict transition is also performed, covering the high fidelity methodologies such as Direct Numerical Simulation and Large Eddy Simulation, historical approaches based on linear stability theory such as the e^N method, empirical correlations for the prediction of the onset of transition and transport equation based models, which are the main subject of study. The three transition models used are the $\gamma - Re_\theta$ model, the γ model and the AFT model. They are chosen based on their widespread usage and due to covering different modelling perspectives. The coupling to different underlying turbulence models is assessed as well. The $k_T - k_L - \omega$ model was also included in preliminary studies. However, its inability to accurately predict separation induced transition and weaker numerical robustness led to the choice of leaving it out of this work.

The selected combinations of turbulence and transition models are tested for a wide range of flows. The simplest one is the flow over a flat plate, typically used to calibrate the transition models, and a prime candidate to assess the sensitivity to the inlet boundary conditions for turbulence, due to the absence of a pressure gradient and surface curvature. The flow around several airfoils is considered as well. These are the NACA 0012, NACA 0015, Eppler 387, S809 and NLF₁-0416. Besides covering different transition mechanisms, the availability of experimental data at moderate Reynolds numbers for most of these geometries makes them good test cases to evaluate transition models. The three dimensional

test cases consist of the SD 7003 wing, a very low Reynolds number case ($Re_c = 4 \times 10^6$), the 6:1 prolate spheroid, and the sickle wing, with the last two being excellent geometries to address crossflow transition.

Rather than focusing on each geometry in particular, emphasis is given to the features of the transition models that are being studied. These are divided into two different categories. The first is that of numerical aspects, which affect the accuracy of the solution with regards to the exact solution of the mathematical model being solved. Within this group, three factors are considered: numerical robustness, the discretization scheme used in the convection term of the transport equations associated with the turbulence and transition models and the size of the first near wall cell and corresponding y^+ value. The second category is related to the location of transition predicted by the models and the factors that influence it. These factors consist on the turbulence production limiter for stagnation regions, which is inherent to the underlying turbulence model and not to the transition model, but can still impact the location of transition, and on the overall influence of the inlet boundary conditions for the turbulence variables. A comparison with the experimental data available for each test case is also performed within this environment.

Regarding the numerical features, the following was concluded:

- The use of a transition model, regardless of which one is used, entails significant numerical challenges when compared to simulations that employ only a turbulence model. On one hand, the existence of laminar flow that is more prone to flow separation can lead to difficulties, and the tight coupling between transition and turbulence model causes a higher computational cost. Furthermore, the formulation of all transition models includes several limiters and switches which are not continuous or do not have continuous derivatives, which can result in residual stagnation. While the first few mentioned aspects are unavoidable, the latter can be solved by introducing smooth variants of the functions that cause issues. This approach prevents residual stagnation in many cases, although it can lead to transition moving slightly upstream due to the change in the model formulation.
- In simulations without a transition model, the discretization of the convection term of the turbulence transport equations showed a negligible impact on the accuracy of the mean flow field solution for the tested cases. However, this is no longer the case when a transition model is added, due to several factors. The first is that significant streamwise gradients take place in the transition region, which may not be significantly refined since its location is generally unknown during the grid generation process. This effect is not present in simulations without a transition model. Furthermore, the prediction of transition is heavily dependent on the freestream turbulence, which in turn depends on the decay which starts and is steeper right upstream of the inlet. At this location, grids are generally coarse, which results in an underestimation of the decay, particularly if first order schemes are used. The combination of these two factors causes transitional flow calculations to be much more sensitive to the discretization scheme used in the convection term of the turbulence transport equations. On the contrary, the discretization scheme employed for the convection term

on the transport equations of the transition model has a negligible impact.

- In what concerns the size of the first near wall cell, there is a close match between the trends observed for simulations with and without a transition model. In both cases, there is a significant influence of the y^+ value on the predicted level of C_f on the turbulent region for the $k - \omega$ SST model. In addition, it appears that the calculations with a transition model are more sensitive to the size of the near wall cell. When the KSKL model is used as the underlying turbulence model, the rule of thumb of $y^+ \approx 1$ leads to a much smaller influence. Furthermore, no significant sensitivity of the transition location to the size of the first near wall cell was detected. While these trends are equivalent to those obtained without transition model, for the $k - \omega$ SST model, a reliable estimation of the exact solution based on grid refinement studies is more affected by y^+ when a transition model is used.

Overall, the use of a transition model leads to more challenges than calculations that use only a turbulence model, a consequence of the wider range of flows that can be properly reproduced. Numerical error, as a consequence from both the iterative and discretization components is likely to be larger than the one obtained for a simulation without a transition model. Although recommended, the use of second order schemes for the convection term of the turbulence transport equations may be difficult in complex flows, thus becoming the dominant source of error. As a result, significant care must be taken in the application of transition models, as the experience from simulations without a transition model may not be directly translated for calculations with transition models.

In fact, this last point was also observed in the study of the modelling aspects. Both the effect of the turbulence production limiter and the influence of the inlet boundary conditions exhibit different trends depending on whether or not a transition model is used. The main observations are:

- The growth of turbulence in stagnation regions can affect the evolution of the turbulence kinetic energy at the edge of the boundary layer, as well as some of the variables of the transition models. In particular for the $\gamma - Re_\theta$ model, differences of over 10% of the chord were observed in the location of the transition region depending on the limiter used. While differences between the different approaches to limit turbulence production in stagnation regions are very small in simulations without a transition model, the same does not necessarily hold true in calculations with transition models.
- The influence of the turbulence boundary conditions at the inlet is the most crucial aspect in the use of transition models. Simulations using only a turbulence model and the reproduction of flows where trip wires or other mechanisms are used to induce turbulent flow are almost immune to this sensitivity. On the other hand, for transitional flow simulations, this corresponds to a physical behaviour and a desirable property of all transition models, as it represents the response of a flow. However, in most cases, there is insufficient information to set the inlet turbulence quantities. When information regarding the turbulence level is available, it is usually in the form of a single data point, a turbulence intensity level at a given location in the domain. This is not enough to fully characterize turbulence in the computations, as two variables need to be specified for the

models used herein. Therefore, while one may know the level of turbulence at a certain location, its evolution upstream and downstream of that location is unknown and still has some impact on the prediction of the transition region.

- To control the decay of turbulence that is predicted by the underlying turbulence model, the general approach is to use extremely high values of the inlet eddy-viscosity. While this approach prevents modifications to the turbulence model, it results in eddy-viscosity profiles that attain their maximum value outside of the boundary layer. Furthermore, if high turbulence intensity values are desired, the required level of the eddy-viscosity may be high enough to affect the laminar boundary layer, causing a deviation of the velocity profile and an overprediction of the skin-friction coefficient. The approach developed to control the decay of turbulence in the freestream by modifying the constants of the underlying turbulence model allows for lower eddy-viscosity values, but does not seem appropriate for conditions corresponding to high levels of freestream turbulence. Furthermore, due to the effect of stagnation regions, its applicability requires the use of the Kato-Launder production limiter.

With regards to each individual model, the $\gamma - Re_\theta$ model is the most all around robust approach from a modelling standpoint. Unlike the AFT model, it is capable of dealing with a multitude of transition triggering mechanisms, although the ability to simulate crossflow transition requires an extension to the original model. On the numerical side, it suffers from the disadvantage of being the only transition model with two transport equations, which makes iterative convergence slower. Nonetheless, it generally leads to lower numerical errors than the other models. The closely related γ model is also appropriate for most transition mechanisms. Despite generally exhibiting easier iterative convergence than the $\gamma - Re_\theta$ model, and being apparently less sensitive to the inlet boundary conditions, it shows tremendous sensitivity to spatial discretization. As observed in both the two dimensional test cases and for the sickle wing, the solution of the model can become dominated by the discretization error, resulting in inaccurate predictions for transition. While this is easily solved in two dimensional cases, for complex flows the application of this model can become troublesome. The intermittency based models contrast with the AFT model in their applicability. The latter is restricted to low turbulence intensity scenarios, and does not have any terms to handle separation induced transition. However, this model is less dependent on freestream turbulence and its influence can be translated in a single variable, making it easier to set up.

As mentioned in the introduction to this thesis, the work developed during this thesis has been a part of groups investigating the topic of transition modelling. In particular, calculations for the flat-plate, the Eppler 387 and NACA 0015 airfoils and the 6:1 prolate spheroid have been presented at workshops organized by the AVT-313 panel. Results for the flat plate, the NLF₁-0416 airfoil and the prolate spheroid have also been presented at the 1st AIAA Transition Modeling and Prediction Workshop. Given the similar test cases employed, the trends observed in the two workshops were very similar. Nevertheless, they led to significantly different outcomes in terms of the decision of the next steps to be undertaken. On one hand, the workshop organized by the AIAA will focus on simpler cases in the near future. This was motivated by the disparity of the numerical solutions, which in some cases corresponded to the same

model on the same grid. On the other hand, the lack of agreement displayed on the prolate spheroid between the experimental data and the numerical simulations, even when using crossflow extensions, led the AVT-313 group into focusing on these differences.

Considering the results presented and discussed throughout this thesis, it is difficult to justify an immediate focus on new or improved extensions or corrections to the transition models. The main reason for this is that the level of maturity of the models is still low. As shown in this work, the application of a transition model can be strongly influenced by the turbulence production limiter, by the discretization scheme for the convection term of the transport equations of the turbulence model, and by the inlet boundary conditions for turbulence. While this is not an impediment to the use of the models, it raises difficulties in the consistency of the results. As an example, the turbulence production limiter was not fixed in any of the workshops, and it was seldom mentioned. This omission also occurs in the literature, and sometimes even for the inlet boundary conditions. Detailed studies are required on how each of the mentioned features, and any others that may not have been addressed herein, influence the predictions of the transition models. Naturally, comparisons of results by different groups such as those organized in the previously mentioned workshops can contribute to this end.

Another path for future work consists of formal validation of the transition models. Throughout the test cases assessed in this dissertation, the use of a transition model always resulted in a better overall agreement with experimental data when compared to the solutions that do not employ them. This clearly demonstrates the potential of transition models, but is not enough. Detailed experimental data, which is not available for any of the test cases that have been explored here, is required to make proper evaluations of the modelling error. This includes not only a quantification of the experimental uncertainty, but also enough information to set both variables of the turbulence model at the inlet, eliminating any free parameters in the computational setup. In this regard, it would be beneficial to examine geometries in which the most common transition mechanisms play a role, in order to fully cover the range of applicability of the models. Therefore, an ideal validation data set ought to include cases with natural transition, bypass transition, separation-induced transition and crossflow transition. While the latter is suitable to be addressed by either the prolate spheroid or the sickle wing, the remaining mechanisms can easily be considered in the flow around an airfoil. In particular, the NLF₁-0416 airfoil is a good candidate, as depending on the angle of attack, it can cover both natural and separation-induced transition.

References

- [1] J. Slotnick, A. Khodadoust, J. Alonso, D. Darmofal, W. Gropp, E. Lurie, and D. Mavriplis. CFD Vision 2030 Study: A Path to Revolutionary Computational Aerosciences. *NASA/CR-2014-218178*, 2014.
- [2] Y. Lian and W. Shyy. Laminar-Turbulent Transition of a Low Reynolds Number Rigid or Flexible Airfoil. *AIAA Journal*, 45(7):1501–1513, 2007. doi: 10.2514/1.25812.
- [3] D. Kim, Y. Kim, J. Li, R. V. Wilson, J. E. Martin, and P. M. Carrica. Boundary Layer Transition Models for Naval Applications: Capabilities and Limitations. *Journal of Ship Research*, 63(4): 294–307, 2019.
- [4] C. J. Axten and M. D. Maughmer. Demonstrating the Potential of CFD Transition Modeling for Racing Sailplane Design. In *AIAA Aviation 2020 Forum*, page 2710, 2020.
- [5] R. Lanzafame, S. Mauro, and M. Messina. Wind Turbine CFD Modeling Using a Correlation-Based Transitional Model. *Renewable Energy*, 52:31–39, 2013. doi: 10.1016/j.renene.2012.10.007.
- [6] J. Baltazar, D. Rijpkema, and J. F. de Campos. On the Use of the γ - $\tilde{R}e_{\theta_t}$ Transition Model for the Prediction of the Propeller Performance at Model-Scale. *Ocean Engineering*, 170:6–19, 2018.
- [7] J.-D. Lee and A. Jameson. Natural-Laminar-Flow Airfoil and Wing Design by Adjoint Method and Automatic Transition Prediction. In *47th AIAA Aerospace Sciences Meeting including The New Horizons Forum and Aerospace Exposition*, page 897, 2009.
- [8] NASA Transition Modeling Workshop 2017. https://turbmodels.larc.nasa.gov/transition_workshop2017.html. Last Accessed in 02/04/2021.
- [9] J. G. Coder. Standard Test Cases for Transition Model Verification and Validation in Computational Fluid Dynamics. AIAA Paper No. 2018-0029, 2018. doi: 10.2514/6.2018-0029.
- [10] 1st AIAA CFD Transition Modeling and Prediction Workshop. <https://transitionmodeling.larc.nasa.gov>. Last accessed in 02/04/2021.
- [11] D. C. Wilcox. *Turbulence Modeling for CFD*. DCW Industries La Canada, CA, second edition, 1998.

- [12] C. L. Rumsey. Apparent Transition Behavior of Widely-used Turbulence Models. *International Journal of Heat and Fluid Flow*, 28(6):1460–1471, 2007.
- [13] C. L. Rumsey and J. P. Slotnick. Overview and Summary of the Second AIAA High-Lift Prediction Workshop. *Journal of Aircraft*, 52(4):1006–1025, 2015.
- [14] R. E. Mayle. The Role of Laminar-Turbulent Transition in Gas Turbine Engines. In *ASME 1991 International Gas Turbine and Aeroengine Congress and Exposition*, 1991. doi: 10.1115/91-GT-261.
- [15] E. Dick and S. Kubacki. Transition Models for Turbomachinery Boundary Layer Flows: A Review. *International Journal of Turbomachinery, Propulsion and Power*, 2(2):4, 2017.
- [16] P. R. Spalart. Strategies for Turbulence Modelling and Simulations. *International Journal of Heat and Fluid Flow*, 21(3):252–263, 2000.
- [17] S. Lardeau, M. Leschziner, and T. Zaki. Large Eddy Simulation of Transitional Separated Flow over a Flat Plate and a Compressor Blade. *Flow, Turbulence and Combustion*, 88(1-2):19–44, 2012.
- [18] J. L. van Ingen. A Suggested Semi-Empirical Method for the Calculation of the Boundary Layer Transition Region. *Report VTH-74, Delft University of Technology*, 1956.
- [19] A. M. O. Smith and N. Gamberoni. Transition, Pressure Gradient and Stability Theory. *Douglas Aircraft Co., Report ES 26388*, 1956.
- [20] W. P. Jones and B. E. Launder. The Calculation of Low-Reynolds-Number Phenomena with a Two-Equation Model of Turbulence. *International Journal of Heat and Mass Transfer*, 16(6):1119–1130, 1973.
- [21] V. C. Patel, W. Rodi, and G. Scheuerer. Turbulence Models for Near-Wall and Low Reynolds Number Flows - A Review. *AIAA journal*, 23(9):1308–1319, 1985.
- [22] C. L. Rumsey, B. A. Pettersson Reif, and T. B. Gatski. Arbitrary Steady-State Solutions with the $K-\epsilon$ Model. *AIAA Journal*, 44(7):1586–1592, 2006.
- [23] R. B. Langtry and F. R. Menter. Correlation-Based Transition Modeling for Unstructured Parallelized Computational Fluid Dynamics Codes. *AIAA Journal*, 47(12):2894–2906, December 2009. doi: 10.2514/1.42362.
- [24] D. K. Walters and D. Cokljat. A Three-Equation Eddy-Viscosity Model for Reynolds-Averaged Navier-Stokes Simulations of Transitional Flow. *Journal of Fluids Engineering*, 130(12):121401, 2008. doi: 10.1115/1.2979230.
- [25] J. G. Coder and M. D. Maughmer. Computational Fluid Dynamics Compatible Transition Modeling Using an Amplification Factor Transport Equation. *AIAA Journal*, 52(11):2506–2512, 2014. doi: 10.2514/1.J052905.

- [26] W. Elsner and P. Warzecha. Numerical Study of Transitional Rough Wall Boundary Layer. *Journal of Turbomachinery*, 136(1), 09 2013. doi: 10.1115/1.4023467.
- [27] S. Medida and J. Baeder. A New Crossflow Transition Onset Criterion for RANS Turbulence Models. In *21st AIAA Computational Fluid Dynamics Conference*, page 3081, 2013. doi: 10.2514/6.2013-3081.
- [28] K. Suluksna, P. Dechaumphai, and E. Juntasaro. Correlations for Modeling Transitional Boundary Layers Under Influences of Freestream Turbulence and Pressure Gradient. *International Journal of Heat and Fluid Flow*, 30(1):66–75, 2009.
- [29] F. R. Menter, P. E. Smirnov, T. Liu, and R. Avancha. A One-Equation Local Correlation-Based Transition Model. *Flow, Turbulence and Combustion*, 95(4):583–619, December 2015. doi: 10.1007/s10494-015-9622-4.
- [30] J. G. Coder and M. D. Maughmer. Application of the Amplification Factor Transport Transition Model to the Shear Stress Transport Model. In *53rd AIAA Aerospace Sciences Meeting*. AIAA Paper 2015-0588, 2015. doi: 10.2514/6.2015-0588.
- [31] L. Eça, F. S. Pereira, and G. Vaz. Viscous Flow Simulations at High Reynolds Numbers Without Wall Functions: Is $y^+ \approx 1$ Enough for the Near-wall Cells? *Computers & Fluids*, 170:157–175, 2018.
- [32] S. Nie, N. Krimmelbein, A. Krumbein, and C. Grabe. Coupling of a Reynolds Stress Model with the $\gamma - Re_{\theta t}$ Transition Model. *AIAA Journal*, 56(1):146–157, 2018.
- [33] R. Lopes, L. Eça, and G. Vaz. On the Numerical Behavior of RANS-Based Transition Models. *Journal of Fluids Engineering*, 142(5), 2020.
- [34] ERCOFTAC Classic Database. <http://cfd.mace.manchester.ac.uk/ercoftac>. Last accessed in 02/04/2021.
- [35] M. S. Selig, J. J. Guglielmo, A. P. Broeren, and P. Giguère. *Summary of Low Speed Airfoil Data*, volume 1. SoarTech Publications, 1995.
- [36] C. J. Lloyd, J. Peakall, A. D. Burns, G. M. Keevil, and R. M. Dorrell. Numerical Errors at Walls: on the Sensitivity of RANS Models to Near-wall Cell Size. *International Journal of Computational Fluid Dynamics*, 34(3):204–225, 2020.
- [37] B. S. Venkatachari, P. Paredes, J. M. Derlaga, P. G. Buning, M. M. Choudhari, F. Li, and C. Chang. Assessment of Transition Modeling Capability in OVERFLOW with Emphasis on Swept-Wing Configurations. In *AIAA Scitech 2020 Forum*, page 1034, 2020.
- [38] P. J. Roache. *Verification and Validation in Computational Science and Engineering*. Hermosa Albuquerque, NM, 1998.
- [39] H. Schlichting and K. Gersten. *Boundary-Layer Theory*. Springer, ninth edition, 2016.

- [40] C. P. Ellington. The Novel Aerodynamics of Insect Flight: Applications to Micro-Air Vehicles. *Journal of Experimental Biology*, 202(23):3439–3448, 1999.
- [41] G. M. Whitesides. The Origins and the Future of Microfluidics. *Nature*, 442(7101):368–373, 2006.
- [42] F. M. White. *Viscous Fluid Flow*. McGraw-Hill New York, third edition, 2006.
- [43] W. S. Saric, H. L. Reed, and E. J. Kerschen. Boundary-Layer Receptivity to Freestream Disturbances. *Annual Review of Fluid Mechanics*, 34(1):291–319, 2002. doi: 10.1146/annurev.fluid.34.082701.161921.
- [44] W. S. Saric. Görtler Vortices. *Annual Review of Fluid Mechanics*, 26(1):379–409, 1994.
- [45] P. Hall, M. R. Malik, and D. I. A. Poll. On the Stability of an Infinite Swept Attachment Line Boundary Layer. *Proceedings of the Royal Society of London. A. Mathematical and Physical Sciences*, 395(1809):229–245, 1984.
- [46] R. B. Langtry. *A Correlation-Based Transition Model Using Local Variables for Unstructured Parallelized CFD Codes*. PhD thesis, University of Stuttgart, 2006.
- [47] G. B. Schubauer and H. K. Skramstad. Laminar Boundary-Layer Oscillations and Transition on a Flat Plate. *Journal of Research of the National Bureau of Standards*, 38:251, 1947.
- [48] T. Herbert. Parabolized Stability Equations. *Annual Review of Fluid Mechanics*, 29(1):245–283, 1997.
- [49] F. P. Bertolotti, T. Herbert, and P. R. Spalart. Linear and Nonlinear Stability of the Blasius Boundary Layer. *Journal of Fluid Mechanics*, 242:441–474, 1992. doi: 10.1017/S0022112092002453.
- [50] Klebanoff P. S. Effects of Free-Stream Turbulence on a Laminar Boundary Layer. *Bulletin of the American Physical Society*, 16(11):1323, 1971.
- [51] T. J. Mueller and J. D. DeLaurier. Aerodynamics of Small Vehicles. *Annual Review of Fluid Mechanics*, 35(1):89–111, 2003.
- [52] W. Shyy, Y. Lian, J. Tang, D. Viieru, and H. Liu. *Aerodynamics of Low Reynolds Number Flyers*, volume 22. Cambridge University Press Cambridge, 2007.
- [53] J. M. Russell. Length and Bursting of Separation Bubbles: A Physical Interpretation. *Science and Technology of Low Speed Motorless Flight, NASA Conference Publication 2085*, 1979.
- [54] W. S. Saric, H. L. Reed, and E. B. White. Stability and Transition of Three-Dimensional Boundary Layers. *Annual Review of Fluid Mechanics*, 35(1):413–440, 2003.
- [55] R. G. Jacobs and P. A. Durbin. Simulations of Bypass Transition. *Journal of Fluid Mechanics*, 428:185–212, 2001.

- [56] J. Wissink and W. Rodi. DNS of Separation-Induced Transition Influenced by Free-Stream Fluctuations. In *IUTAM Symposium on Laminar-Turbulent Transition*, pages 389–394. Springer Netherlands, 2006. ISBN 978-1-4020-4159-4.
- [57] S. Hosseinverdi and H. F. Fasel. Numerical Investigation of Laminar-Turbulent Transition in Laminar Separation Bubbles: The Effect of Free-Stream Turbulence. *Journal of Fluid Mechanics*, 858: 714–759, 2019.
- [58] L. Chen, X. Liu, M. Oliveira, and C. Liu. DNS for Late Stage Structure of Flow Transition on a Flat-Plate Boundary Layer. In *48th AIAA Aerospace Sciences Meeting Including the New Horizons Forum and Aerospace Exposition*, 2010. doi: 10.2514/6.2010-1470.
- [59] L. H. von Deyn, P. Forooghi, B. Frohnepfel, P. Schlatter, A. Hanifi, and D. S. Henningson. Direct Numerical Simulations of Bypass Transition over Distributed Roughness. *AIAA Journal*, 58(2): 702–711, 2020. doi: 10.2514/1.J057765.
- [60] H. B. E. Kurz and M. J. Kloker. Mechanisms of Flow Tripping by Discrete Roughness Elements in a Swept-Wing Boundary Layer. *Journal of Fluid Mechanics*, 796:158–194, 2016.
- [61] U. Piomelli, T. A. Zang, C. G. Speziale, and M. Y. Hussaini. On the Large-Eddy Simulation of Transitional Wall-Bounded Flows. *Physics of Fluids A: Fluid Dynamics*, 2(2):257–265, 1990.
- [62] P. Schlatter, S. Stolz, and L. Kleiser. LES of Transitional Flows Using the Approximate Deconvolution Model. *International Journal of Heat and Fluid Flow*, 25(3):549–558, 2004.
- [63] A. Monokrousos, L. Brandt, P. Schlatter, and D. S. Henningson. DNS and LES of Estimation and Control of Transition in Boundary Layers Subject to Free-Stream Turbulence. *International Journal of Heat and Fluid Flow*, 29(3):841–855, 2008.
- [64] V. Michelassi, J. G. Wissink, J. Frohlich, and W. Rodi. Large-Eddy Simulation of Flow around Low-Pressure Turbine Blade with Incoming Wakes. *AIAA Journal*, 41(11):2143–2156, 2003.
- [65] S. K. Roberts and M. I. Yaras. Large-Eddy Simulation of Transition in a Separation Bubble. *Journal of Fluids Engineering*, 128(2):232–238, 08 2006. doi: 10.1115/1.2170123.
- [66] J. L. van Ingen. The e^N Method for Transition Prediction. Historical Review of Work at TU Delft. In *38th Fluid Dynamics Conference and Exhibit*, page 3830, 2008.
- [67] J. M. M. Sousa and L. M. G. Silva. Transition Prediction in Infinite Swept Wings Using Navier-Stokes Computations and Linear Stability Theory. *Computers and Structures*, 82(17-19):1551–1560, 2004.
- [68] H. W. Stock and W. Haase. Navier-Stokes Airfoil Computations with e^N Transition Prediction Including Transitional Flow Regions. *AIAA Journal*, 38(11):2059–2066, 2000.
- [69] G. Schrauf, J. Perraud, D. Vitiello, and F. Lam. Comparison of Boundary-Layer Transition Predictions Using Flight Test Data. *Journal of Aircraft*, 35(6):891–897, 1998.

- [70] J. Perraud, D. Arnal, G. Casalis, J.-P. Archambaud, and R. Donelli. Automatic Transition Predictions Using Simplified Methods. *AIAA Journal*, 47(11):2676–2684, 2009.
- [71] L. M. Mack. Boundary-Layer Linear Stability Theory. AGARD Report No. 709, Part 2. Technical report, California Institute of Technology, 1984.
- [72] T. S. Haynes and H. L. Reed. Simulation of Swept-Wing Vortices Using Nonlinear Parabolized Stability Equations. *Journal of Fluid Mechanics*, 405:325–349, 2000.
- [73] G. L. O. Halila, G. Chen, Y. Shi, K. J. Fidkowski, J. R. R. A. Martins, and M. T. de Mendonça. High-Reynolds Number Transitional Flow Simulation Via Parabolized Stability Equations with an Adaptive RANS Solver. *Aerospace Science and Technology*, 91:321–336, 2019.
- [74] H. W. Stock. Airfoil Validation Using Coupled Navier-Stokes and e^N Transition Prediction Methods. *Journal of Aircraft*, 39(1):51–58, 2002.
- [75] N. Tanouti. Coupling of e^N Transition Prediction Method with Reynolds-Averaged Navier-Stokes Solver ENFLOW. Master’s thesis, Delft University of Technology, 2017.
- [76] B. J. Abu-Ghannam and R. Shaw. Natural Transition of Boundary Layers — The Effects of Turbulence, Pressure Gradient, and Flow History. *Journal of Mechanical Engineering Science*, 22(5):213–228, 1980.
- [77] J. Perraud, H. Deniau, and G. Casalis. Overview of Transition Prediction Tools in the elsA Software. In *6th European Conference on Computational Fluid Dynamics*, 2014.
- [78] D. Arnal, R. Houdeville, A. Seraudie, and O. Vermeersch. Overview of Laminar-Turbulent Transition Investigations at ONERA Toulouse. In *41st AIAA Fluid Dynamics Conference and Exhibit*, page 3074, 2011.
- [79] S. J. Dhawan and R. Narasimha. Some Properties of Boundary Layer Flow During the Transition from Laminar to Turbulent Motion. *Journal of Fluid Mechanics*, 3(4):418–436, 1958.
- [80] W. Rodi and G. Scheuerer. Calculation of Heat Transfer to Convection-Cooled Gas Turbine Blades. *Journal of Engineering for Gas Turbines and Power*, 107(3):620–627, 1985.
- [81] R. C. Schmidt and S. V. Patankar. Simulating Boundary Layer Transition with Low-Reynolds-Number $k-\varepsilon$ Turbulence Models: Part 1 — An Evaluation of Prediction Characteristics. *Journal of Turbomachinery*, 113(1):10–17, 1991.
- [82] R. C. Schmidt and S. V. Patankar. Simulating Boundary Layer Transition with Low-Reynolds-Number $k-\varepsilon$ Turbulence Models: Part 2 — An Approach to Improving the Predictions. *Journal of Turbomachinery*, 113(1):18–26, 1991.
- [83] C. K. G. Lam and K. Bremhorst. A Modified Form of the $k-\varepsilon$ Model for Predicting Wall Turbulence. *Journal of Fluids Engineering*, 103(3):456–460, 1981.

- [84] D. C. Wilcox. Simulation of Transition with a Two-Equation Turbulence Model. *AIAA Journal*, 32(2):247–255, 1994.
- [85] D. Biswas and Y. Fukuyama. Calculation of Transitional Boundary Layers with an Improved Low-Reynolds-Number Version of the k - ε Turbulence Model. *Journal of Turbomachinery*, 116(4):765–773, 1994.
- [86] X. Zheng, C. Liu, F. Liu, and C. Yang. Turbulent Transition Simulation Using the k - ω Model. *International Journal for Numerical Methods in Engineering*, 42(5):907–926, 1998.
- [87] L. Eça, R. Lopes, G. Vaz, J. Baltazar, and D. Rijpkema. Validation Exercises of Mathematical Models for the Prediction of Transitional Flows. In *Proceedings of the 31st Symposium on Naval Hydrodynamics*. Monterey, CA, 2016.
- [88] J. Steelant and E. Dick. Modelling of Bypass Transition with Conditioned Navier–Stokes Equations Coupled to an Intermittency Transport Equation. *International Journal for Numerical Methods in Fluids*, 23(3):193–220, 1996.
- [89] Y. B. Suzen and P. G. Huang. Modeling of Flow transition Using an Intermittency Transport Equation. *Journal of Fluids Engineering*, 122(2):273–284, 2000.
- [90] J. R. Cho and M. K. Chung. A k - ε - γ Equation Turbulence Model. *Journal of Fluid Mechanics*, 237:301–322, 1992.
- [91] R. Pecnik, W. Sanz, A. Gehrler, and J. Woisetschläger. Transition Modeling Using Two Different Intermittency Transport Equations. *Flow, Turbulence and Combustion*, 70(1-4):299–323, 2003.
- [92] J. Steelant and E. Dick. Modeling of Laminar-Turbulent Transition for High Freestream Turbulence. *Journal of Fluids Engineering*, 123(1):22–30, 2001.
- [93] F. R. Menter, T. Esch, and S. Kubacki. Transition Modelling Based on Local Variables. In *Engineering Turbulence Modelling and Experiments 5*, pages 555–564. Elsevier, 2002.
- [94] F. R. Menter, R. B. Langtry, S. R. Likki, Y. B. Suzen, P. G. Huang, and S. Völker. A Correlation-Based Transition Model Using Local Variables—Part I: Model Formulation. *Journal of Turbomachinery*, 128(3):413–422, 03 2006. doi: 10.1115/1.2184352.
- [95] R. B. Langtry, F. R. Menter, S. R. Likki, Y. B. Suzen, P. G. Huang, and S. Völker. A Correlation-Based Transition Model Using Local Variables—Part II: Test Cases and Industrial Applications. *Journal of Turbomachinery*, 128(3):423–434, 03 2006. doi: 10.1115/1.2184353.
- [96] E. R. Van Driest and C. B. Blumer. Boundary Layer Transition - Freestream Turbulence and Pressure Gradient Effects. *AIAA Journal*, 1(6):1303–1306, 1963.
- [97] C. Content and R. Houdeville. Application of the γ - r_θ Laminar-Turbulent Transition Model in Navier-Stokes Computations. In *40th Fluid Dynamics Conference and Exhibit*, page 4445, 2010.

- [98] Ü. Kaynak and E. Gürdamar. Boundary-layer Transition Under the Effect of Compressibility for the Correlation Based Transition Model. In *46th AIAA Aerospace Sciences Meeting and Exhibit*, page 774, 2008.
- [99] T. Misaka and S. Obayashi. Application of Local Correlation-Based Transition Model to Flows Around Wings. In *44th AIAA Aerospace Sciences Meeting and Exhibit*, page 918, 2006.
- [100] N. N. Sørensen. CFD Modelling of Laminar-Turbulent Transition for Airfoils and Rotors Using the γ Model. *Wind Energy: An International Journal for Progress and Applications in Wind Power Conversion Technology*, 12(8):715–733, 2009.
- [101] W. Piotrowski, W. Elsner, and S. Drobniak. Transition Prediction on Turbine Blade Profile with Intermittency Transport Equation. *Journal of Turbomachinery*, 132(1), 2010.
- [102] P. Malan, K. Suluksna, and E. Juntasaro. Calibrating the $\gamma - Re_\theta$ Transition Model for Commercial CFD. In *47th AIAA Aerospace Sciences Meeting Including The New Horizons Forum and Aerospace Exposition*, page 1142, 2009.
- [103] K. Pettersson and S. Crippa. Implementation and Verification of a Correlation Based Transition Prediction Method. In *38th Fluid Dynamics Conference and Exhibit*, page 4401, 2008.
- [104] C. Seyfert and A. Krumbein. Evaluation of a Correlation-Based Transition Model and Comparison with the e^n Method. *Journal of Aircraft*, 49(6):1765–1773, 2012.
- [105] P. L. Delafin, F. Deniset, and J.-A. Astolfi. Effect of the Laminar Separation Bubble Induced Transition on the Hydrodynamic Performance of a Hydrofoil. *European Journal of Mechanics-B/Fluids*, 46:190–200, 2014.
- [106] J. Babajee and T. Arts. Investigation of the Laminar Separation-Induced Transition with the $\gamma - re_{\theta t}$ Transition Model on Low-Pressure Turbine Rotor Blades at Steady Conditions. In *Turbo Expo: Power for Land, Sea, and Air*, volume 44748, pages 1167–1178. American Society of Mechanical Engineers, 2012.
- [107] C. Sheng, J. Wang, and Q. Zhao. Improved Rotor Hover Predictions Using Advanced Turbulence Modeling. *Journal of Aircraft*, 53(5):1549–1560, 2016.
- [108] D. Riedeberger and U. Rist. Numerical Simulation of Laminar-Turbulent Transition on a Dolphin Using the $\gamma - Re_\theta$ Model. In *High Performance Computing in Science and Engineering'11*, pages 379–391. Springer, 2012.
- [109] A. Minot, J. Marty, J. Perraud, and G. Casalis. Implementation of a Surface Roughness-Based Transition Onset Correction in the $\gamma - Re_\theta$ Transition Model. volume 2B: Turbomachinery of *Turbo Expo: Power for Land, Sea, and Air*, 06 2017. doi: 10.1115/GT2017-63237.
- [110] R. Langtry. *Extending the $\gamma - Re_\theta$ Correlation Based Transition Model for Crossflow Effects (Invited)*. 2015. doi: 10.2514/6.2015-2474.

- [111] C. Grabe, N. Shengyang, and A. Krumbein. Transport Modeling for the Prediction of Crossflow Transition. *AIAA Journal*, 56(8):3167–3178, 2018. doi: 10.2514/1.J056200.
- [112] A. Mosahebi and E. Laurendeau. Introduction of a Modified Segregated Numerical Approach for Efficient Simulation of $\gamma - Re_\theta$ Transition Model. *International Journal of Computational Fluid Dynamics*, 29(6-8):357–375, 2015.
- [113] J. Coder and M. Maughmer. *One-Equation Transition Closure for Eddy-Viscosity Turbulence Models in CFD*. 2012. doi: 10.2514/6.2012-672.
- [114] S. Medida and J. Baeder. Application of the Correlation-based $\gamma - Re_\theta$ Transition Model to the Spalart-Allmaras Turbulence Model. In *20th AIAA Computational Fluid Dynamics Conference*, page 3979, 2011.
- [115] S. Medida. *Correlation-based Transition Modeling for External Aerodynamic Flows*. PhD thesis, University of Maryland, 2014.
- [116] S. Medida, D. A. Corson, and M. Barton. Implementation and Validation of Correlation-based Transition Models in AcuSolve. In *46th AIAA Fluid Dynamics Conference*, page 3478, 2016.
- [117] D. K. Walters and J. H. Leylek. A New Model for Boundary Layer Transition Using a Single-point RANS Approach. *Journal of Turbomachinery*, 126(1):193–202, 2004.
- [118] R. E. Mayle and A. Schulz. The Path to Predicting Bypass Transition. volume 119, pages 405–411, 07 1997. doi: 10.1115/1.2841138.
- [119] J. G. Coder. Enhancement of the Amplification Factor Transport Transition Modeling Framework. In *55th AIAA Aerospace Sciences Meeting*, page 1709, 2017.
- [120] J. G. Coder, T. H. Pulliam, and J. C. Jensen. Contributions to HiLiftPW-3 Using Structured, Overset Grid Methods. In *2018 AIAA Aerospace Sciences Meeting*, page 1039, 2018.
- [121] S. C. Cakmakcioglu, O. Bas, and U. Kaynak. A Correlation-based Algebraic Transition Model. *Proceedings of the Institution of Mechanical Engineers, Part C: Journal of Mechanical Engineering Science*, 232(21):3915–3929, 2018.
- [122] P. Ströer, N. Kimmelbein, A. Krumbein, and C. Grabe. Stability-Based Transition Transport Modeling for Unstructured Computational Fluid Dynamics Including Convection Effects. *AIAA Journal*, 58(4):1506–1517, 2020.
- [123] F. R. Menter, M. Kuntz, and R. Langtry. Ten Years of Industrial Experience with the SST Turbulence Model. *Turbulence, Heat and Mass Transfer*, 4(1):625–632, 2003.
- [124] F. R. Menter, Y. Egorov, and D. Rusch. Steady and Unsteady Flow Modelling Using the $k - \sqrt{k}l$ Model. In *Fifth International Symposium on Turbulence, Heat and Mass Transfer*. Dubrovnik, Croatia, 2006. doi: 10.1615/ICHMT.2006.TurbulHeatMassTransf.800.

- [125] F. R. Menter. Two-Equation Eddy-Viscosity Turbulence Models for Engineering Applications. *AIAA Journal*, 32(8):1598–1605, 1994.
- [126] L. Eça. On the Limiter of the Production Term of the k Transport Equation in the SST $k - \omega$ Eddy-viscosity Turbulence Model. Technical report, Instituto Superior Tecnico - Universidade de Lisboa, 2008.
- [127] R. Lopes, E. Fernandes, L. Eça, G. Vaz, and M. Kerkvliet. Coupling Two Correlation-Based Transition Models to the $k - \sqrt{k}L$ Eddy Viscosity Turbulence Model. *AIAA Journal*, 59(5):1735–1748, 2021.
- [128] M. Drela and M. B. Giles. Viscous-Inviscid Analysis of Transonic and Low Reynolds Number Airfoils. *AIAA Journal*, 25(10):1347–1355, 1987.
- [129] L. M. Mack. Transition and Laminar Instability. *Jet Propulsion Laboratory Publication*, 78, 1977.
- [130] G. Vaz, F. Jaouen, and M. Hoekstra. Free-Surface Viscous Flow Computations: Validation of URANS Code FreSCo. In *ASME 2009 28th International Conference on Ocean, Offshore and Arctic Engineering*, pages 425–437, 2009. doi: 10.1115/OMAE2009-79398.
- [131] C. M. Klaij. On the Stabilization of Finite Volume Methods with Co-located Variables for Incompressible Flow. *Journal of Computational Physics*, 297:84–89, 2015.
- [132] J. H. Ferziger, M. Perić, and R. L. Street. *Computational Methods for Fluid Dynamics*. Springer, fourth edition, 2020.
- [133] L. Eça and F. S. Pereira. Verification of ReFRESCO Non-orthogonality Correctors Using the Method of Manufactured Solutions. Technical report, Instituto Superior Tecnico - Universidade de Lisboa, 2012.
- [134] M. Hoekstra. *Numerical Simulation of Ship Stern Flows with a Space-marching Navier–Stokes Method*. PhD thesis, Delft University of Technology, 1999.
- [135] P. J. Roache. Verification and Validation in Fluids Engineering: Some Current Issues. *Journal of Fluids Engineering*, 138(10), 2016.
- [136] P. J. Roache. Code Verification by the Method of Manufactured Solutions. *Journal of Fluids Engineering*, 124(1):4–10, 2002.
- [137] L. Eça, C. M. Klaij, G. Vaz, M. Hoekstra, and F. S. Pereira. On Code Verification of RANS Solvers. *Journal of Computational Physics*, 310:418–439, 2016.
- [138] C. J. Roy. Review of Code and Solution Verification Procedures for Computational Simulation. *Journal of Computational Physics*, 205(1):131–156, 2005.
- [139] L. Eça and M. Hoekstra. A Procedure for the Estimation of the Numerical Uncertainty of CFD Calculations Based on Grid Refinement Studies. *Journal of Computational Physics*, 262:104–130, April 2014. doi: 10.1016/j.jcp.2014.01.006.

- [140] J. Brouwer, J. Tukker, and M. van Rijsbergen. Uncertainty Analysis and Stationarity Test of Finite Length Time Series Signals. In *4th International Conference on Advanced Model Measurement Technology for the Maritime Industry (AMT'15)*, 2015.
- [141] D. C. Wilcox. *Turbulence Modeling for CFD*. 2nd Edition, DCW Industries, Inc., 2004.
- [142] P. R. Spalart and C. L. Rumsey. Effective Inflow Conditions for Turbulence Models in Aerodynamic Calculations. *AIAA Journal*, 45(10):2544–2553, October 2007. doi: 10.2514/1.29373.
- [143] L. Eça, M. Hoekstra, and J. Windt. Practical Grid Generation Tools with Applications to Ship Hydrodynamics. In *Proceedings of the Eight International Conference on Grid Generation in Computational Field Simulations*, 2002.
- [144] L. Eça. Grid Generation Tools for Structured Grids. Technical report, Instituto Superior Tecnico - Universidade de Lisboa, 2003.
- [145] V. Brederode. *Fundamentos de Aerodinâmica Incompressível*. Author's Edition, 1997.
- [146] M. Miozzi, F. Di Felice, C. Klein, and M. Costantini. Taylor Hypothesis Applied to Direct Measurement of Skin Friction Using Data from Temperature Sensitive Paint. *Experimental Thermal and Fluid Science*, 110:109913, 2020.
- [147] D. M. Somers. Design and Experimental Results for a Natural-Laminar-Flow Airfoil for General Aviation Applications. Technical report, Langley Research Center, Hampton, VA, NASA TP-1861, 1981.
- [148] R. J. Mcghee, B. S. Walker, and B. F. Millard. Experimental Results for the Eppler 387 Airfoil at Low Reynolds Numbers in the Langley Low-Turbulence Pressure Tunnel. *NASA Technical Memorandum 4062*, 1988.
- [149] G. M. Cole and T. J. Mueller. Experimental Measurements of the Laminar Separation Bubble on an Eppler 387 Airfoil at Low Reynolds Numbers. *UNDAS-1419-FR*, University of Notre Dame, 1990.
- [150] M. S. Selig, C. A. Lyon, A. P. Broeren, P. Giguère, and A. Gopalarathnam. *Summary of Low Speed Airfoil Data*, volume 3. SoarTech Publications, 1997.
- [151] G. A. Williamson, B. D. McGranahan, B. A. Broughton, R. W. Deters, J. B. Brandt, and M. S. Selig. *Summary of Low Speed Airfoil Data*, volume 5. 2012.
- [152] D. M. Somers. Design and Experimental Results for the S809 Airfoil. Technical report, National Renewable Energy Laboratory, Golden, CO, NREL/SR-440-6918, 1997.
- [153] H. U. Meier and H.-P. Kreplin. Experimental Investigation of the Boundary Layer Transition and Separation on a Body of Revolution. *Zeitschrift für Flugwissenschaften und Weltraumforschung*, 4:65–71, 1980.

- [154] H.-P. Kreplin, H. Meier, and A. Maier. Wind Tunnel Model and Measuring Techniques for the Investigation of Three-dimensional Turbulent Boundary Layers. In *10th Aerodynamic Testing Conference*, page 781, 1978.
- [155] T. C. Fu, A. Shekarriz, J. Katz, and T. T. Huang. The Flow Structure in the Lee of an Inclined 6:1 Prolate Spheroid. *Journal of Fluid Mechanics*, 269:79–106, 1994. doi: 10.1017/S0022112094001497.
- [156] K. M. Barber and R. L. Simpson. Mean Velocity and Turbulence Measurements of Flow Around a 6:1 Prolate Spheroid. In *29th Aerospace Sciences Meeting*, page 255, 1991. doi: 10.2514/6.1991-255.
- [157] GridPro. www.gridpro.com. Last accessed in 02/04/2021.
- [158] M. Galbraith and M. Visbal. Implicit Large Eddy Simulation of Low Reynolds Number Flow Past the SD7003 Airfoil. In *46th AIAA Aerospace Sciences Meeting and Exhibit*, page 225, 2008.
- [159] P. Catalano and R. Tognaccini. Influence of Free-stream Turbulence on Simulations of Laminar Separation Bubbles. In *47th AIAA Aerospace Sciences Meeting Including The New Horizons Forum and Aerospace Exposition*, page 1471, 2009.
- [160] P. Catalano and R. Tognaccini. RANS Analysis of the Low-Reynolds Number Flow Around the SD7003 Airfoil. *Aerospace Science and Technology*, 15(8):615–626, 2011.
- [161] M. Ol, B. R. McCauliffe, E. S. Hanff, U. Scholz, and C. Kähler. Comparison of Laminar Separation Bubble Measurements on a Low Reynolds Number Airfoil in Three Facilities. In *35th AIAA Fluid Dynamics Conference and Exhibit*. No. AIAA-2005-0029, 2005.
- [162] R. Petzold and R. Radespiel. Transition on a Wing with Spanwise Varying Crossflow Evaluated with Linear Stability Theory. In *43rd AIAA Fluid Dynamics Conference*, page 2466, 2013.
- [163] R. Petzold and R. Radespiel. Transition on a Wing with Spanwise Varying Crossflow and Linear Stability Analysis. *AIAA Journal*, 53(2):321–335, 2015.
- [164] M. Kruse, F. Munoz, R. Radespiel, and C. Grabe. Transition Prediction Results for Sickle Wing and NLF (1)-0416 Test Cases. In *2018 AIAA Aerospace Sciences Meeting*, page 0537, 2018.
- [165] Hexpress. www.numeca.com/product/omnis-hexpress. Last accessed in 02/04/2021.
- [166] M. Piotrowski and D. W. Zingg. Investigation of a Local Correlation-based Transition Model in a Newton-Krylov Algorithm. In *AIAA Scitech 2019 Forum*, page 2299, 2019.
- [167] A. L. Rocha, L. Eça, and G. Vaz. On the Numerical Convergence Properties of the Calculation of the Flow Around the KVLCC2 Tanker in Unstructured Grids. In *MARINE VII: Proceedings of the VII International Conference on Computational Methods in Marine Engineering*, pages 336–352. CIMNE, 2017.

- [168] C. G. Speziale, S. Sarkar, and T. B. Gatski. Modelling the Pressure-Strain Correlation of Turbulence: An Invariant Dynamical Systems Approach. *Journal of Fluid Mechanics*, 227:245–272, 1991.
- [169] B. E. Launder, G. J. Reece, and W. Rodi. Progress in the Development of a Reynolds-Stress Turbulence Closure. *Journal of Fluid Mechanics*, 68(3):537–566, 1975.
- [170] B. Eisfeld, C. Rumsey, and V. Togiti. Verification and Validation of a Second-moment-closure Model. *AIAA Journal*, 54(5):1524–1541, 2016.

Appendix A

Crossflow Extension

The crossflow extension applied to the $\gamma - Re_\theta$ and γ models is mainly dependent on the local Helicity Reynolds number Re_{He}

$$Re_{He} = \frac{\rho d^2 He}{\mu U} \quad (\text{A.1})$$

with the Helicity calculated as

$$He = \vec{u} \cdot (\nabla \times \vec{u}). \quad (\text{A.2})$$

The velocity at the edge of the boundary layer, U_e is estimated locally by

$$U_e = \sqrt{V_\infty^2 + \frac{p_\infty - p}{\frac{1}{2}\rho}}, \quad (\text{A.3})$$

and its streamwise derivative is obtained through

$$\frac{dU_e}{ds} = \frac{U_i}{U} \frac{dU_e}{dx_i}. \quad (\text{A.4})$$

The derivative in each cartesian direction can be related to the derivative of the pressure by

$$\frac{\partial U_e}{\partial x_i} = -\frac{1}{\rho U_e} \frac{\partial p}{\partial x_i}. \quad (\text{A.5})$$

A pressure gradient parameter is given by

$$\lambda^+ = \frac{\rho l^2}{\mu} \frac{dU_e}{ds}, \quad (\text{A.6})$$

where

$$l = \frac{1}{C_{He,max}} \frac{2}{15} d, \quad (\text{A.7})$$

with the constant $C_{He,max} = 0.6944$.

The local shape factor is estimated by

$$H_{12}^+ = 4.02923 - \sqrt{-8838.4\lambda^{+4} + 1105.1\lambda^{+3} - 67.962\lambda^{+2} + 17.574\lambda^+ + 2.0593}, \quad (\text{A.8})$$

and it is used to compute the Helicity Reynolds number at transition onset, $Re_{He,t}^+$, using

$$Re_{He,t}^+ = \max(-456.83 H_{12}^+ + 1332.7, 150.0). \quad (\text{A.9})$$

Having the local Helicity Reynolds number and the one at transition onset, a structure of functions similar to that used in the production term of the γ transport equation in the $\gamma - Re_\theta$ and γ models is built:

$$F_{onset1,CF} = \frac{Re_{He}}{0.7 Re_{He,t}^+}, \quad (\text{A.10})$$

$$F_{onset2,CF} = \min(\max(F_{onset1,CF}, F_{onset1,CF}^4), 2.0), \quad (\text{A.11})$$

$$F_{onset3,CF} = \max\left(1 - \left(\frac{R_T}{2}\right)^3, 0.0\right), \quad (\text{A.12})$$

$$F_{onset,CF} = \max(F_{onset2,CF} - F_{onset3,CF}, 0.0). \quad (\text{A.13})$$

The coupling to the $\gamma - Re_\theta$ model is performed by changing P_γ to

$$P_\gamma = (F_{length}[\gamma F_{onset}]^{0.5} + F_{length,CF}[\gamma F_{onset,CF}]^{0.5}) c_{a1} \rho S (1 - c_{e1} \gamma). \quad (\text{A.14})$$

In the case of the γ model, since the form of the original production term is different than that of the $\gamma - Re_\theta$ model, the coupling is also performed differently. Thus, for the γ model, P_γ becomes

$$P_\gamma = (F_{length} F_{onset} + F_{length,CF} F_{onset,CF}) \rho S \gamma (1 - \gamma). \quad (\text{A.15})$$

In both cases, the triggering functions F_{onset} and $F_{onset,CF}$ are independent from each other, meaning that there is no coupling between crossflow transition and natural or bypass transition.

Appendix B

Preliminary Results for the SSG-LRR Reynolds Stress Model

B.1 Model Equations

This model is a blend between the formulation of Speziale-Sarkar-Gatski (SSG) [168] with an ε equation and the Launder-Reece-Rodi formulation (LRR) [169] with an ω equation. The model solves 7 transport equations [170], one for each component of the Reynolds stress tensor, identified as $R_{ij} = \overline{\rho u_i' u_j'}$, and an equation for ω which can be written for steady flow as:

$$\frac{\partial(\rho U_k R_{ij})}{\partial x_k} = \rho P_{ij} + \rho \Pi_{ij} - \rho \varepsilon_{ij} + \rho M_{ij} + \frac{\partial}{\partial x_k} \left[\left(\mu + \frac{D}{C_\mu} \mu_t \right) \frac{\partial R_{ij}}{\partial x_k} \right], \quad (\text{B.1})$$

$$\frac{\partial(\rho U_k \omega)}{\partial x_k} = \frac{\alpha_\omega \omega}{k} \frac{\rho P_{kk}}{2} - \beta_\omega \rho \omega^2 + \frac{\partial}{\partial x_k} \left[\left(\mu + \sigma_\omega \frac{\rho k}{\omega} \right) \frac{\partial \omega}{\partial x_k} \right] + \sigma_d \frac{\rho}{\omega} \max \left(\frac{\partial k}{\partial x_j} \frac{\partial \omega}{\partial x_j}, 0 \right). \quad (\text{B.2})$$

The source terms of the Reynolds stress equations are comprised of four different contributions. P_{ij} is the production term, Π_{ij} is the pressure-strain correlation, ε_{ij} is the dissipation term, and M_{ij} is the fluctuating mass flux. This last term is neglected, thus $M_{ij} = 0$.

The production term is

$$P_{ij} = -R_{ik} \frac{\partial U_j}{\partial x_k} - R_{jk} \frac{\partial U_i}{\partial x_k} \quad (\text{B.3})$$

and the dissipation term is modelled by

$$\varepsilon_{ij} = \frac{2}{3} \varepsilon \delta_{ij}, \quad (\text{B.4})$$

with

$$\varepsilon = C_\mu k \omega, \quad (\text{B.5})$$

$$k = R_{ii} / 2. \quad (\text{B.6})$$

The pressure-strain correlation is

$$\begin{aligned} \Pi_{ij} = & - \left(C_1 \varepsilon + \frac{1}{2} C_1^* P_{kk} \right) a_{ij} + C_2 \varepsilon \left(a_{ik} a_{kj} - \frac{1}{3} a_{kl} a_{kl} \delta_{ij} \right) + (C_3 - C_3^* \sqrt{a_{kl} a_{kl}}) k S_{ij}^* \\ & + C_4 k \left(a_{ik} S_{jk} + a_{jk} S_{ik} - \frac{2}{3} a_{kl} S_{kl} \delta_{ij} \right) + C_5 k (a_{ik} W_{jk} + a_{jk} W_{ik}) \end{aligned} \quad (\text{B.7})$$

where

$$a_{ij} = \frac{R_{ij}}{k} - \frac{2}{3} \delta_{ij}. \quad (\text{B.8})$$

The quantity S_{ij}^* is the compressible strain rate tensor and it is given by

$$S_{ij}^* = S_{ij} - \frac{1}{3} S_{kk} \delta_{ij}. \quad (\text{B.9})$$

It is worth noting that in the case of an incompressible flow, $S_{kk} = 0$ and therefore $S_{ij}^* = S_{ij}$. The diffusion coefficient D can be written as

$$D = 0.5 C_\mu F_1 + \frac{2}{3} 0.22 (1 - F_1). \quad (\text{B.10})$$

The vast majority of the model's coefficients are blended in a manner similar to that of the $k - \omega$ SST model. For any generic constant ϕ :

$$\phi = F_1 \phi^{(\omega)} + (1 - F_1) \phi^{(\varepsilon)} \quad (\text{B.11})$$

where the F_1 blending function is

$$F_1 = \tanh(\zeta^4) \quad (\text{B.12})$$

$$\zeta = \min \left[\max \left(\frac{\sqrt{k}}{C_\mu \omega d}, \frac{500 \mu}{\rho \omega d^2} \right), \frac{4 \sigma_\omega^{(\varepsilon)} \rho k}{(CD) d^2} \right] \quad (\text{B.13})$$

$$(CD) = \sigma_d^{(\varepsilon)} \frac{\rho}{\omega} \max \left(\frac{\partial k}{\partial x_k} \frac{\partial \omega}{\partial x_k}, 0 \right) \quad (\text{B.14})$$

All model constants are presented in table B.1.

Table B.1: Model constants of the SSG-LRR Reynolds stress model [170].

$\alpha_\omega^{(\omega)} = 0.5556$	$\beta_\omega^{(\omega)} = 0.075$	$\sigma_\omega^{(\omega)} = 0.5$	$\sigma_d^{(\omega)} = 0$
$C_1^{(\omega)} = 1.8$	$C_1^{*(\omega)} = 0$	$C_2^{(\omega)} = 0$	$C_3^{(\omega)} = 0.8$
$C_3^{*(\omega)} = 0$	$C_4^{(\omega)} = 0.5(18C_2^{(LRR)} + 12)/11$	$C_5^{(\omega)} = 0.5(-14C_2^{(LRR)} + 20)/11$	$C_2^{LRR} = 0.52$
$\alpha_\omega^{(\varepsilon)} = 0.44$	$\beta_\omega^{(\varepsilon)} = 0.0828$	$\sigma_\omega^{(\varepsilon)} = 0.856$	$\sigma_d^{(\varepsilon)} = 1.712$
$C_1^{(\varepsilon)} = 1.7$	$C_1^{*(\varepsilon)} = 0.9$	$C_2^{(\varepsilon)} = 1.05$	$C_3^{(\varepsilon)} = 0.8$
$C_3^{*(\varepsilon)} = 0.65$	$C_4^{(\varepsilon)} = 0.625$	$C_5^{(\varepsilon)} = 0.2$	

B.2 Coupling with the $\gamma - Re_\theta$ Transition Model

The coupling between the SSG-LRR Reynolds stress model is fully detailed in [32]. Starting with the changes on the turbulence model, the production, dissipation and pressure strain terms of the Reynolds stresses transport equations are changed to

$$P_{ij} = \gamma_{eff} P_{ij,SSG-LRR}, \quad (B.15)$$

$$\varepsilon_{ij} = \min(\max(\gamma_{eff}, 0.1), 1.0) \varepsilon_{ij,SSG-LRR}, \quad (B.16)$$

$$\Pi_{ij} = \gamma_{eff} \Pi_{ij,SSG-LRR}. \quad (B.17)$$

$P_{ij,SSG-LRR}$, $\varepsilon_{ij,SSG-LRR}$ and $\Pi_{ij,SSG-LRR}$ are the original production, dissipation and the pressure strain correlation of the SSG-LRR model given in Equations B.3, B.4 and B.7.

As the SSG-LRR model makes use of the F_1 function of the $k - \omega$ SST model, it is changed in the same way as before:

$$F_1 = \max(F_{1,SSG-LRR}, F_3) \quad (B.18)$$

where $F_{1,SSG-LRR}$ is the original definition of F_1 and F_3 is given by

$$F_3 = \exp\left[-\left(\frac{R_y}{120}\right)^8\right] \quad (B.19)$$

$$R_y = \frac{\rho d \sqrt{k}}{\mu}. \quad (B.20)$$

In the laminar boundary layer, the production of ω vanishes for the SSG-LRR model, unlike what happens for the SST model. In order to match the ω profile of the two conditions in the laminar boundary layer, the production of ω is changed to

$$P_\omega = (1 - C_{lam}) \alpha_\omega S^2 + C_{lam} \left(-\alpha_\omega \frac{\omega}{k} R_{ik} \frac{\partial U_i}{\partial x_k}\right) \quad (B.21)$$

with C_{lam} defined as

$$C_{lam} = \begin{cases} 0, & c_\omega > \gamma \\ \frac{\gamma - c_\omega}{1 - c_\omega}, & c_\omega \leq \gamma \end{cases} \quad (B.22)$$

$$c_\omega = \left(\exp\left(-\left(\frac{420}{Re_{\theta t}}\right)^4\right)\right)^2. \quad (B.23)$$

This modification ensures that in the laminar boundary layer ($\gamma \approx 0.02$) the production of ω matches that of the SST model and reverts to the SSG-LRR formulation when the flow becomes turbulent ($\gamma = 1$). There is an additional effect taking into account the value of $Re_{\theta t}$ in order to improve the behaviour of the model in flows with a high level of freestream turbulence.

Some modifications on the transition model are performed as well. The first two correspond to new

correlations for $F_{length,1}$ and Re_{θ_c} which are now determined as

$$F_{length,1} = 0.48 + 40.0 \exp\left(\frac{-\left(\hat{Re}_{\theta t}\right)^2}{32000}\right) + 0.46 \exp\left(-0.5 \left(\frac{\hat{Re}_{\theta t} - 330}{130}\right)^2\right). \quad (\text{B.24})$$

$$Re_{\theta c1} = 1.1097\hat{Re}_{\theta t} - 1.7072 \times 10^{-3}\hat{Re}_{\theta t}^2 + 6.5245 \times 10^{-6}\hat{Re}_{\theta t}^3 - 9.5545 \times 10^{-9}\hat{Re}_{\theta t}^4 - 6.0 \exp\left(-\frac{\hat{Re}_{\theta t}}{55}\right), \quad (\text{B.25})$$

$$Re_{\theta c2} = 100.467 + 0.3615\hat{Re}_{\theta t} + 9.80618 \times 10^{-4}\hat{Re}_{\theta t}^2 - 1.58628 \times 10^{-6}\hat{Re}_{\theta t}^3 + 16.1474 \times 10^{-10}\hat{Re}_{\theta t}^4, \quad (\text{B.26})$$

$$Re_{\theta c} = \begin{cases} Re_{\theta c1}, & \hat{Re}_{\theta t} < 271.38; \\ \min(Re_{\theta c2}, 1500), & \hat{Re}_{\theta t} \geq 271.38. \end{cases} \quad (\text{B.27})$$

The final modification consists in a new definition for F_{onset2}

$$F_{onset2} = f_{bp}F_{onsetn} + (1 - f_{bp})F_{onset2_original} \quad (\text{B.28})$$

with $F_{onset2_original}$ corresponding to equation 3.46 and

$$f_{bp} = \exp\left(-\left(\frac{\hat{Re}_{\theta t}}{120}\right)^4\right) \quad (\text{B.29})$$

$$F_{onsetn} = \begin{cases} 0, & F_{onset1} < 1.0 \\ F_{onset2}, & F_{onset1} \geq 1.0 \end{cases} \quad (\text{B.30})$$

B.3 Results

The results for the SSG-LRR + $\gamma - Re_{\theta}$ formulation are only given for three aspects. The first is the iterative convergence of the simulations, one of the most challenging aspects in the use of any Reynolds stress model, which naturally does not become easier with the inclusion of the transition model. The second aspect concerns the effect of the size of the first near wall cell and corresponding y^+ value. The final feature is the influence of the inlet boundary conditions, which is even more important considering some of the correlations of the transition model are changed in its coupling with the SSG-LRR model. All results are given for the flat-plate geometry.

B.3.1 Iterative convergence

A single set of calculations for the flat plate is considered to discuss the iterative convergence of the calculations with the SSG-LRR + $\gamma - Re_{\theta}$ formulation. The inlet boundary conditions for turbulence follow those used for the the study of the effect of the y^+ given in Section 5.4. The calculations discussed here correspond to those of grid set 5. A depiction of the number of iterations required to achieve the desired iterative convergence level is shown in Figure B.1 as well as the evolution of the residuals for the finest grid. As expected, when the SSG-LRR model is used as the underlying turbulence model for

the $\gamma - Re_\theta$ model, there is a significant increase in the number of iterations performed compared to the original coupling with the $k - \omega$ SST model, in particular for the finer grids. In terms of the evolution of the residuals, all variables exhibit a decrease of the residuals down to 10^{-8} with the exception of the shear component R_{12} , which stagnates at a higher level.

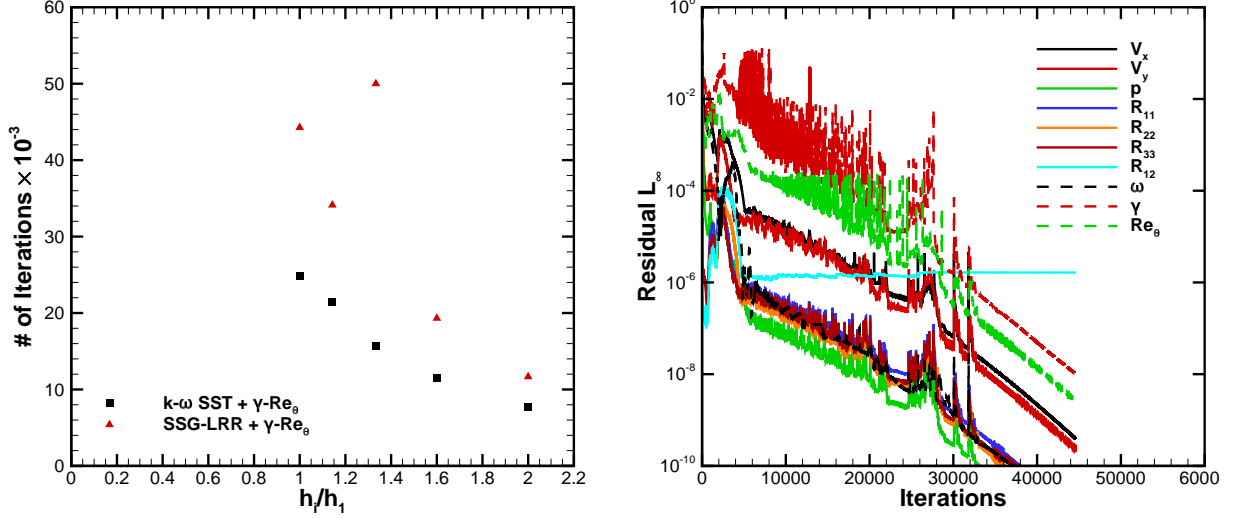


Figure B.1: Number of iterations performed for each grid of grid set 5 (left) and residual evolution on the finest grid (right) for the flat plate case using the SSG-LRR Reynolds stress model combined with the $\gamma - Re_\theta$ transition model.

This residual stagnation is due to the realizability constraints enforced in the code after the solution of the transport equations. These constraints are

$$R_{ij} \geq 0, \quad i = j \quad (\text{B.31})$$

and

$$|R_{ij}| \leq \sqrt{R_{ii}R_{jj}}, \quad i \neq j \quad (\text{B.32})$$

In this particular case, the solution of the SSG-LRR + $\gamma - Re_\theta$ model fails to meet the second condition in the laminar boundary-layer. This results in stagnation of the residual for R_{12} since at every iteration, its value is imposed through the realizability constraint and not by the transport equation. Naturally, the influence of this change is minimal since the Reynolds stress model is not impactful in the laminar boundary layer. For this reason, the variables of the turbulence model are not considered for the iterative convergence criteria when the SSG-LRR + $\gamma - Re_\theta$ formulation is used.

B.3.2 Effect of the size of the first near wall cell

The setup for the study of the size of the first near wall cell follows that described in Section 5.4. In a similar way to the other models tested, the maximum and average y^+ values obtained with the SSG-LRR + $\gamma - Re_\theta$ model are given in Figure B.2. The values obtained for each grid comply with the intended setting for each grid set.

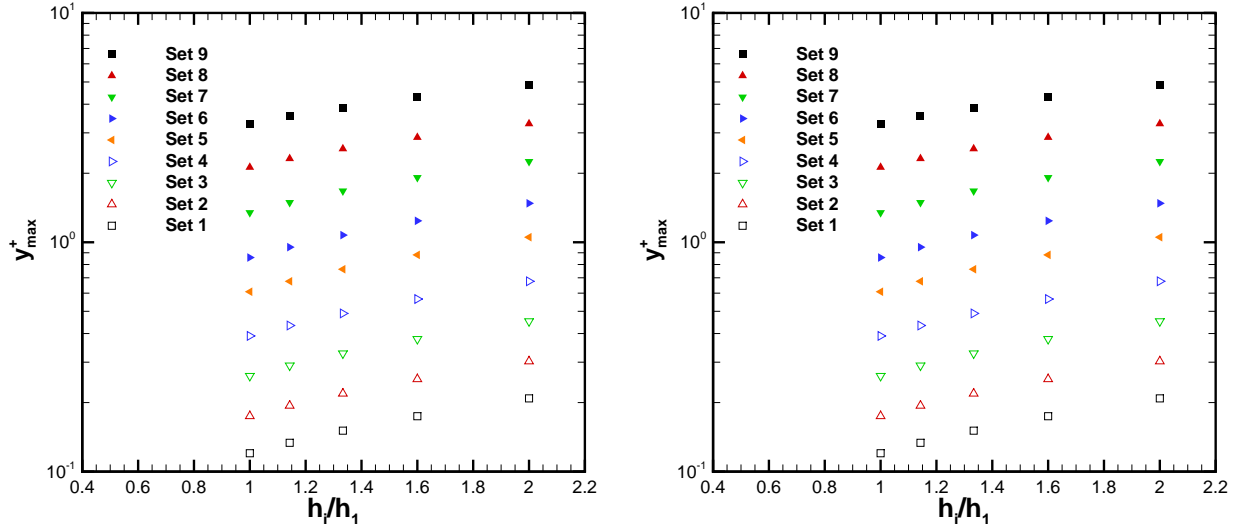


Figure B.2: Average (left) and maximum (right) y^+ values obtained for the flat plate test case for each grid using the SSG-LRR turbulence model combined with the $\gamma - Re_\theta$ transition model.

The convergence of the plate's resistance coefficient with grid refinement is shown in Figure B.3. Again, there is a considerable dependence of the solution on the value of the maximum y^+ . This is unsurprising considering that the SSG-LRR model solves an equation for ω that is similar to that of the $k - \omega$ SST model. Therefore, it inherits the singular behaviour of ω at the wall which is the cause for the sensitivity to the maximum y^+ . However, for the SSG-LRR model there is also some influence of grid refinement, as the two coarsest grids of each set exhibit a different trend than the remaining five. This illustrates the need for higher grid refinement when the SSG-LRR model is used.

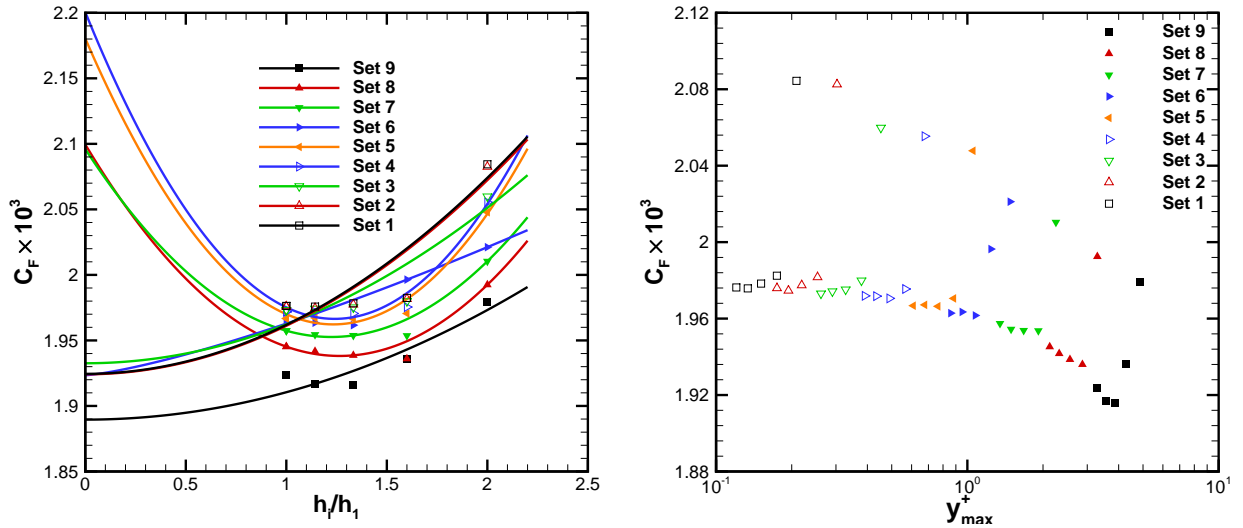


Figure B.3: Convergence of the friction coefficient of the plate obtained with the SSG-LRR + $\gamma - Re_\theta$ formulation with grid refinement (left) and with the maximum y^+ value (right).

The influence of the size of the first near wall cell is naturally more significant in the turbulent region than in the laminar region, as evidenced in Figure B.4. There are some changes in the extrapolated solution at $h_i/h_1 = 0$ even at the finest grid set, a consequence of the non-monotonic behaviour observed in the convergence of the skin-friction coefficient in the turbulent region.

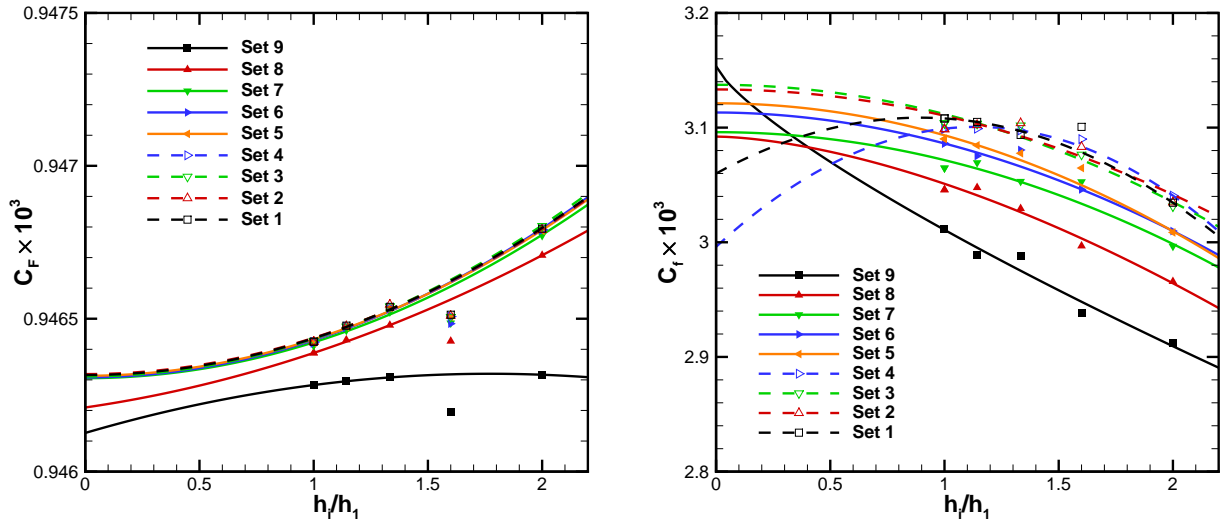


Figure B.4: Convergence of the skin-friction coefficient with grid refinement at $Re_x = 5 \times 10^5$ (left) and $Re_x = 7 \times 10^6$ (right) for the SSG-LRR model combined with the $\gamma - Re_\theta$ transition model.

Finally, a comparison of the skin-friction coefficient distribution for the coarsest and finest grids of the sets with highest and lowest y^+ values is performed in Figure B.5. Unlike what was observed for the $k - \omega$ SST + $\gamma - Re_\theta$ formulation in Section 5.4, the location of transition is slightly affected by the size of the first near wall cell when the SSG-LRR is used as the underlying turbulence model. Despite this, the strongest effect is still that of grid refinement. In contrast to the solution of the $k - \omega$ SST model, the coarsest and finest grids of grid set 1 do not exhibit the same level of C_f in the turbulent region. This again shows the stronger influence of overall grid refinement on the SSG-LRR model.

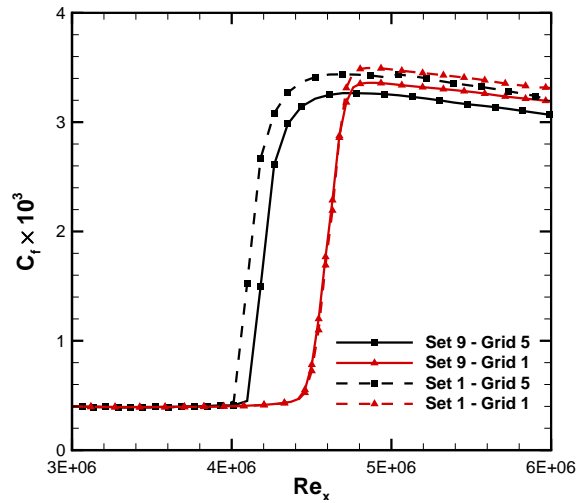


Figure B.5: Skin friction coefficient distribution in the vicinity of the transition region for the coarsest and finest grids of set 9 and set 1 for the SSG-LRR model combined with the $\gamma - Re_\theta$ transition model.

B.3.3 Influence of the inlet boundary conditions

The settings for the study of the influence of the inlet boundary conditions follow those described in Table 6.2. However, only the BC2 and BC3 sets are used, as X_F is not used with the SSG-LRR

model. The resulting skin-friction coefficient distribution for each case is presented in Figure B.6. The numerical solution of all BC3 conditions leads to laminar flow, as transition does not occur on the surface of the plate. This shows the SSG-LRR + $\gamma - Re_\theta$ formulation to be more dependent on the turbulence quantities at the inlet than the remaining alternatives addressed in this thesis, as none of the other model combinations exhibited laminar flow on the entire plate for this test case. Furthermore, even for the BC2 conditions, transition is located much further downstream than the locations predicted by all of the other models. It is then evident that to achieve the same location of transition, the SSG-LRR model requires higher inlet turbulence intensity and/or eddy-viscosity at the inlet.

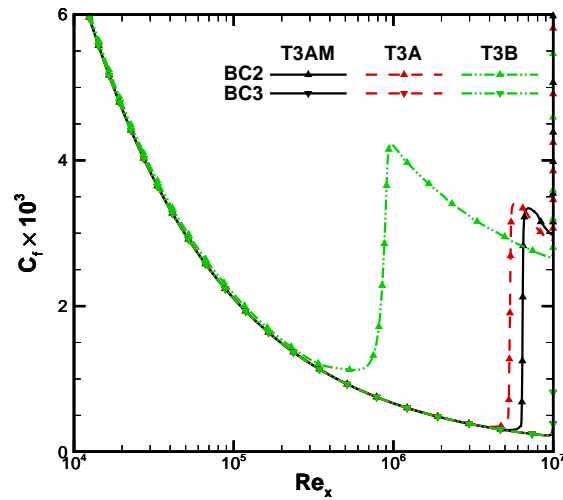


Figure B.6: Skin-friction coefficient distribution for the flat plate test case using the SSG-LRR model combined with the $\gamma - Re_\theta$ model for varying inlet boundary conditions.

The previous results seem counter-intuitive, considering that the decay of turbulence of the SSG-LRR and the $k - \omega$ SST model ought to be similar, as shown in Appendix C. In the case of the KSKL model, a direct comparison cannot be made since the decay is different. Figure B.7 presents the profiles of $Re_{\theta,t}$ and $Re_{\theta,c}$ at $x/L = 0.1$ for the finest grid of the T3AM-BC3 case, the one that corresponds to the lowest turbulence in the freestream. At this location, the solution of both models is laminar. The profiles of $Re_{\theta,t}$ are similar on the outside and inside the boundary layer, as expected by the similar decay of turbulence. Some differences are observed at the edge of the boundary layer, but not to the extent that would justify the different transition prediction. However, the $Re_{\theta,c}$ profiles are much different, with the solution of the SSG-LRR + $\gamma - Re_\theta$ formulation exhibiting a constant value of 1500. This is a consequence of the different correlation between $Re_{\theta,c}$ and $Re_{\theta,t}$ that is part of the coupling between the SSG-LRR and the $\gamma - Re_\theta$ models. As this variable is used in the production term of the intermittency, it follows that this is the cause for the delayed transition observed for the SSG-LRR+ $\gamma - Re_\theta$ formulation.

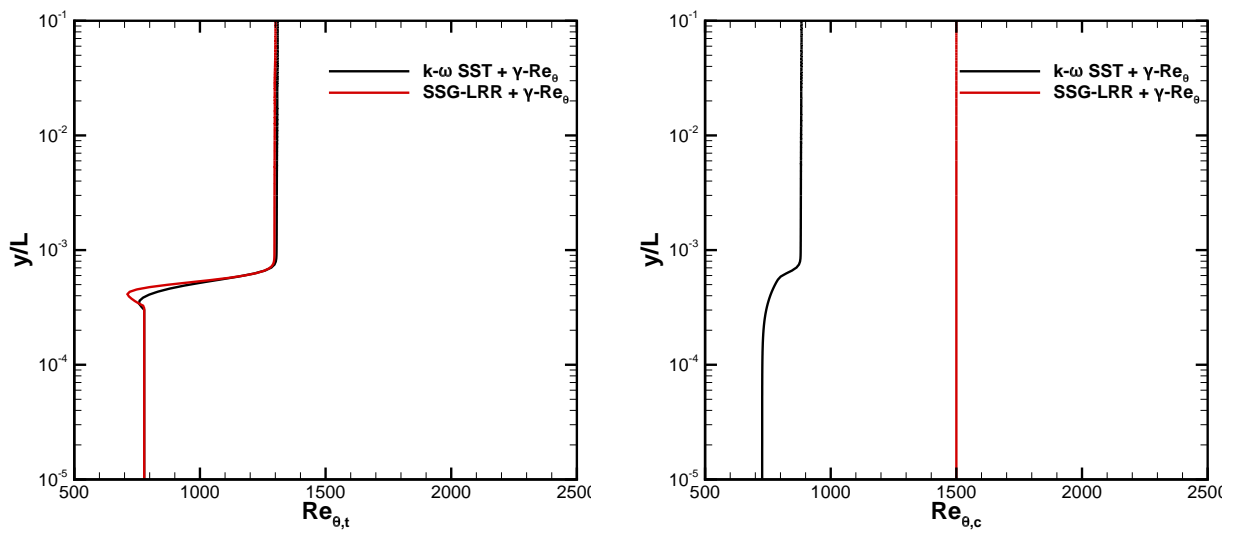


Figure B.7: Boundary-layer profiles at $x/L = 0.1$ of $\hat{Re}_{\theta,t}$ (left) and $Re_{\theta,c}$ (right) for the flat-plate test case when using the $\gamma - Re_{\theta}$ model combined with the $k - \omega$ SST and SSG-LRR turbulence models.

Appendix C

Equations for the Decay of Freestream Turbulence

C.1 $k - \omega$ SST Model

The two transport equations of the $k - \omega$ SST model can be written for the steady flow of an incompressible fluid as:

$$U_j \frac{\partial k}{\partial x_j} = \nu_t S^2 - \beta^* \omega k + \frac{\partial}{\partial x_i} \left((\nu + \sigma_k \nu_t) \frac{\partial k}{\partial x_i} \right) \quad (\text{C.1})$$

$$U_j \frac{\partial \omega}{\partial x_j} = P_\omega - \beta \omega^2 + \frac{\partial}{\partial x_i} \left((\nu + \sigma_\omega \nu_t) \frac{\partial \omega}{\partial x_i} \right) + CD_{k\omega} \quad (\text{C.2})$$

Considering steady, uniform flow aligned with the x axis and neglecting the diffusion and cross-diffusion terms, the equations simplify to:

$$U \frac{dk}{dx} = -\beta^* \omega k \quad (\text{C.3})$$

$$U \frac{d\omega}{dx} = -\beta (\omega)^2 \quad (\text{C.4})$$

Under these conditions the eddy-viscosity is obtained from:

$$\nu_t = \frac{k}{\omega} \quad (\text{C.5})$$

Writing these equations using dimensionless variables $k^* = k/V_\infty^2$, $\omega^* = \omega * L_{ref}/V_\infty$, $U^* = U/V_\infty$, $x^* = x/L_{ref}$ with $U^* = 1$ results in:

$$\frac{dk^*}{dx^*} = -\beta^* \omega^* k^* \quad (\text{C.6})$$

$$\frac{d\omega^*}{dx^*} = -\beta (\omega^*)^2 \quad (\text{C.7})$$

Additionally:

$$\frac{k^*}{\omega^*} = \frac{\nu_t}{V_\infty L} = \frac{\nu_t}{\nu} \frac{1}{Re} \quad (C.8)$$

Equations C.6 and C.7 possess an analytical solution. Starting with the ω^* equation:

$$\begin{aligned} \frac{d\omega^*}{dx^*} &= -\beta(\omega^*)^2 \\ \frac{1}{(\omega^*)^2} d\omega^* &= -\beta dx^* \\ \int_{\omega_{in}}^{\omega} \frac{1}{(\omega^*)^2} d\omega^* &= \int_{x_{in}^*}^{x^*} -\beta dx^* \\ -\left[\frac{1}{\omega^*}\right]_{\omega_{in}}^{\omega} &= -\beta(x^* - x_{in}^*) \\ \frac{1}{\omega^*} - \frac{1}{\omega_{in}^*} &= \beta(x^* - x_{in}^*) \\ \frac{1}{\omega^*} &= \frac{1 + \beta(x^* - x_{in}^*)\omega_{in}^*}{\omega_{in}^*} \\ \omega^* &= \frac{\omega_{in}^*}{1 + \beta(x^* - x_{in}^*)\omega_{in}^*}. \end{aligned}$$

The k equation can now be solved as well:

$$\begin{aligned} \frac{dk^*}{dx^*} &= -\beta^* \omega^* k^* \\ \frac{dk^*}{dx^*} &= -\beta^* k^* \frac{\omega_{in}^*}{1 + \beta(x^* - x_{in}^*)\omega_{in}^*} \\ \frac{1}{k^*} dk^* &= -\beta^* \frac{\omega_{in}^*}{1 + \beta(x^* - x_{in}^*)\omega_{in}^*} dx \\ \int_{k_{in}^*}^{k^*} \frac{1}{k^*} dk^* &= -\int_{x_{in}^*}^{x^*} \beta^* \frac{\omega_{in}^*}{1 + \beta(x^* - x_{in}^*)\omega_{in}^*} dx \\ [\ln k^*]_{k_{in}^*}^{k^*} &= -\frac{\beta^* \omega_{in}^*}{\beta \omega_{in}^*} [\ln(1 + \beta(x^* - x_{in}^*)\omega_{in}^*)]_{x_{in}^*}^{x^*} \\ \ln k^* - \ln k_{in}^* &= -\frac{\beta^*}{\beta} \ln(1 + \beta(x^* - x_{in}^*)\omega_{in}^*) \\ \ln \frac{k^*}{k_{in}^*} &= -\frac{\beta^*}{\beta} \ln(1 + \beta(x^* - x_{in}^*)\omega_{in}^*) \\ \frac{k^*}{k_{in}^*} &= (1 + \beta(x^* - x_{in}^*)\omega_{in}^*)^{-\frac{\beta^*}{\beta}} \\ k^* &= \frac{k_{in}^*}{(1 + \beta(x^* - x_{in}^*)\omega_{in}^*)^{\frac{\beta^*}{\beta}}} \end{aligned}$$

Making use of $\omega^* = k^* \frac{\nu}{\nu_t} Re$, the equations for the decay of k and ω can be written as:

$$k^* = \frac{k_{in}^*}{\left(1 + \beta(x^* - x_{in}^*)k_{in}^* \left(\frac{\nu}{\nu_t}\right)_{in} Re\right)^{\frac{\beta^*}{\beta}}} \quad (C.9)$$

$$\omega^* = \frac{\omega_{in}^*}{1 + \beta(x^* - x_{in}^*)k_{in}^* \left(\frac{\nu}{\nu_t}\right)_{in} Re} \quad (C.10)$$

C.2 KSKL Model

Again considering the steady flow of an incompressible fluid, the transport equations of the KSKL model can be written as:

$$U_j \frac{\partial k}{\partial x_j} = \nu_t S^2 - c_\mu^{3/4} \frac{k^{3/2}}{L} - 2\nu \frac{k}{d^2} + \frac{\partial}{\partial x_j} \left[\left(\nu + \frac{\nu_t}{\sigma_k} \right) \frac{\partial k}{\partial x_j} \right], \quad (C.11)$$

$$U_j \frac{\partial \Phi}{\partial x_j} = \frac{\Phi}{k} \nu_t S^2 \left[\zeta_1 - \zeta_2 \left(\frac{L}{L_{v\kappa}} \right)^2 \right] - \zeta_3 k - 6\nu \frac{\Phi}{d^2} f_\Phi + \frac{\partial}{\partial x_j} \left[\left(\nu + \frac{\nu_t}{\sigma_\Phi} \right) \frac{\partial \Phi}{\partial x_j} \right]. \quad (C.12)$$

Under the assumption of steady, uniform flow aligned with the x axis, sufficiently far away from walls and neglecting the diffusion terms, the equations simplify to:

$$U \frac{dk}{dx} = -c_\mu^{3/4} \frac{k^{3/2}}{L} = -c_\mu^{3/4} \frac{k^2}{\Phi}, \quad (C.13)$$

$$U \frac{d\Phi}{dx} = -\zeta_3 k. \quad (C.14)$$

Unlike for the $k-\omega$ SST model, these equations do not appear to have a simple solution, as the equation involving the derivative of k depends on Φ , and the equation with the derivative of Φ depends on k . To avoid this problem, a transport equation for the eddy-viscosity is considered. In the KSKL model, and under the assumption on uniform flow, the eddy-viscosity is computed as

$$\nu_t = c_\mu^{1/4} \Phi. \quad (C.15)$$

Hence, it follows that

$$U \frac{dk}{dx} = -c_\mu \frac{k^2}{\nu_t}, \quad (C.16)$$

and

$$U \frac{d\nu_t}{dx} = -c_\mu^{1/4} \zeta_3 k \quad (C.17)$$

Doing a similar process for the equations of the $k-\omega$ SST model, but converting the equation for ω into one for ν_t results in:

$$U \frac{dk}{dx} = -\beta^* \frac{k^2}{\nu_t}, \quad (C.18)$$

and

$$U \frac{d\nu_t}{dx} = U \frac{d\frac{k}{\omega}}{dx} = U \left(\frac{\frac{dk}{dx} \omega - \frac{d\omega}{dx} k}{\omega^2} \right) = \frac{-\beta^* \omega^2 k + \beta \omega^2 k}{\omega^2} = -(\beta^* - \beta) k. \quad (C.19)$$

Comparing Equations C.16 and C.17 to Equations C.18 and C.19 shows that they have the same form, only the constants of the second equation are different. This means that the form of the decay

equations is the same. Equation C.17 can be written as

$$U \frac{d\nu_t}{dx} = -(\beta^* - \beta_{KSKL}) k \quad (\text{C.20})$$

with β_{KSKL} such that the relation

$$c_\mu^{1/4} \zeta_3 = \beta^* - \beta_{KSKL} \quad (\text{C.21})$$

is verified.

Thus, the equation for the decay of k and ν_t in dimensionless form in the KSKL model are given by

$$k^* = \frac{k_{in}^*}{\left(1 + \beta_{KSKL}(x^* - x_{in}^*) k_{in}^* \left(\frac{\nu_t}{\nu_t}\right)_{in} Re\right)^{\frac{\beta^*}{\beta_{KSKL}}}} \quad (\text{C.22})$$

and

$$\frac{\nu_t}{\nu} = \frac{\left(\frac{\nu_t}{\nu}\right)_{in}}{\left(1 + \beta_{KSKL}(x^* - x_{in}^*) k_{in}^* \left(\frac{\nu_t}{\nu_t}\right)_{in} Re\right)^{\frac{\beta^*}{\beta_{KSKL}} - 1}}. \quad (\text{C.23})$$

C.3 SSG-LRR Model

The transport equations for the Reynolds stresses and specific turbulence dissipation rate in the SSG-LRR model are given by

$$\frac{\partial(\rho R_{ij})}{\partial t} + \frac{\partial(\rho U_k R_{ij})}{\partial x_k} = \rho P_{ij} + \rho \Pi_{ij} - \rho \varepsilon_{ij} + \frac{\partial}{\partial x_k} \left[\left(\mu + \frac{D}{C_\mu} \mu_t \right) \frac{\partial R_{ij}}{\partial x_k} \right],$$

and

$$\begin{aligned} \frac{\partial(\rho \omega)}{\partial t} + \frac{\partial(\rho U_k \omega)}{\partial x_k} &= \frac{\alpha_\omega \omega}{k} \frac{\rho P_{kk}}{2} - \beta_\omega \rho \omega^2 + \frac{\partial}{\partial x_k} \left[\left(\mu + \sigma_\omega \frac{\rho k}{\omega} \right) \frac{\partial \omega}{\partial x_k} \right] \\ &+ \sigma_d \frac{\rho}{\omega} \max \left(\frac{\partial k}{\partial x_j} \frac{\partial \omega}{\partial x_j}, 0 \right). \end{aligned}$$

Making the base assumption of steady, uniform flow aligned with the x axis, the equation for the Reynolds stresses can be written as

$$\frac{\partial R_{ij}}{\partial x} = P_{ij} + \Pi_{ij} - \varepsilon_{ij} + \frac{\partial}{\partial x_k} \left[\left(\nu + \frac{D}{C_\mu} \nu_t \right) \frac{\partial R_{ij}}{\partial x_k} \right].$$

The production term, P_{ij} has the form

$$P_{ij} = -R_{ik} \frac{\partial U_j}{\partial x_k} - R_{jk} \frac{\partial U_i}{\partial x_k}. \quad (\text{C.24})$$

Under a uniform flow field, the production term vanishes as there are no velocity derivatives. Therefore

$$P_{ij} = 0. \quad (\text{C.25})$$

The pressure-strain correlation term Π_{ij} is

$$\begin{aligned}\Pi_{ij} = & - \left(C_1 \varepsilon + \frac{1}{2} C_1^* P_{kk} \right) a_{ij} + C_2 \varepsilon \left(a_{ik} a_{kj} - \frac{1}{3} a_{kl} a_{kl} \delta_{ij} \right) \\ & + (C_3 - C_3^* \sqrt{a_{kl} a_{kl}}) k S_{ij}^* \\ & + C_4 k \left(a_{ik} S_{jk} + a_{jk} S_{ik} - \frac{2}{3} a_{kl} S_{kl} \delta_{ij} \right) \\ & + C_5 k (a_{ik} W_{jk} + a_{jk} W_{ik}).\end{aligned}$$

Due to the uniform flow field assumption, the last three terms vanish, leaving

$$\Pi_{ij} = -C_1 \varepsilon a_{ij} + C_2 \varepsilon \left(a_{ik} a_{kj} - \frac{1}{3} a_{kl} a_{kl} \delta_{ij} \right),$$

with

$$a_{ij} = \frac{R_{ij}}{k} - \frac{2}{3} \delta_{ij}.$$

First, we consider the shear Reynolds stresses, for which $i \neq j$. The pressure-strain correlation can be written as

$$\Pi_{ij} = -C_1 \varepsilon \frac{R_{ij}}{k} + C_2 \varepsilon \frac{R_{ik}}{k} \frac{R_{kj}}{k}.$$

Furthermore, for the shear Reynolds stresses,

$$\varepsilon_{ij} = \frac{2}{3} \varepsilon \delta_{ij} = 0.$$

it follows then that in the equation for R_{ij} with $i \neq j$, all terms are directly dependent on the shear Reynolds stresses and independent of the normal stresses. Adding the fact that the boundary condition at the inlet for these components of the Reynolds stress tensor is $R_{ij} = 0$, it follows that $R_{ij} = 0$ is the solution in the freestream for all shear Reynolds stresses, as it satisfies both the transport equations and the boundary conditions. We now consider the normal Reynolds stresses, for which $i = j$.

The pressure-strain correlation term takes the form

$$\Pi_{ii} = -C_1 \varepsilon a_{ii} + C_2 \varepsilon \left(a_{ik} a_{ki} - \frac{1}{3} a_{kl} a_{kl} \right),$$

while the dissipation term is the same for all normal stresses and given by

$$\varepsilon_{ij} = \frac{2}{3} \varepsilon. \tag{C.26}$$

We consider the particular case of $i = j = 1$ for which the pressure-strain correlation term is written

as

$$\begin{aligned}\Pi_{11} = & -C_1\varepsilon \left(\frac{R_{11}}{k} - \frac{2}{3} \right) \\ & + C_2\varepsilon \left(\left(\frac{R_{11}}{k} - \frac{2}{3} \right)^2 + \left(\frac{R_{12}}{k} \right)^2 + \left(\frac{R_{13}}{k} \right)^2 \right. \\ & \left. - \frac{1}{3} (a_{11}^2 + a_{22}^2 + a_{33}^2 + a_{12}^2 + a_{13}^2 + a_{23}^2) \right),\end{aligned}$$

which simplifies to

$$\begin{aligned}\Pi_{11} = & -C_1\varepsilon \left(\frac{R_{11}}{k} - \frac{2}{3} \right) \\ & + C_2\varepsilon \left(\left(\frac{R_{11}}{k} - \frac{2}{3} \right)^2 - \frac{1}{3} (a_{11}^2 + a_{22}^2 + a_{33}^2) \right).\end{aligned}$$

A similar procedure for $i = j = 2$ and $i = j = 3$ yields

$$\begin{aligned}\Pi_{22} = & -C_1\varepsilon \left(\frac{R_{22}}{k} - \frac{2}{3} \right) \\ & + C_2\varepsilon \left(\left(\frac{R_{22}}{k} - \frac{2}{3} \right)^2 - \frac{1}{3} (a_{11}^2 + a_{22}^2 + a_{33}^2) \right).\end{aligned}$$

and

$$\begin{aligned}\Pi_{33} = & -C_1\varepsilon \left(\frac{R_{33}}{k} - \frac{2}{3} \right) \\ & + C_2\varepsilon \left(\left(\frac{R_{33}}{k} - \frac{2}{3} \right)^2 - \frac{1}{3} (a_{11}^2 + a_{22}^2 + a_{33}^2) \right).\end{aligned}$$

A comparison of the pressure strain term for all three normal components of the Reynolds stress tensor shows that in the absence of the shear stresses, the transport equations for each normal Reynolds stress are the same. Recalling that the inlet boundary condition is $R_{ii} = 2k/3$, it follows that $R_{11} = R_{22} = R_{33}$ and $k = 3R_{ii}/2$ throughout the freestream. These results simply state that for the *SSG-LRR* model in an uniform flow field, isotropic turbulence will remain isotropic. With these results, it is trivial to build the transport equation for k .

$$U \frac{dk}{dx} = U \frac{3}{2} \frac{dR_{11}}{dx} = \frac{3}{2} \Pi_{11} - \frac{3}{2} \varepsilon_{11} + \frac{3}{2} \frac{\partial}{\partial x_k} \left[\left(\nu + \frac{D}{C_\mu} \nu_t \right) \frac{\partial R_{11}}{\partial x_k} \right].$$

Using the relation $k = 3R_{ii}/2$, it follows that $a_{11} = 0$ leading to

$$\Pi_{11} = -C_1\varepsilon \left(\frac{R_{11}}{k} - \frac{2}{3} \right) + C_2\varepsilon \left(\left(\frac{R_{11}}{k} - \frac{2}{3} \right)^2 \right) = 0 \quad (\text{C.27})$$

The dissipation term is

$$\varepsilon_{11} = \frac{2}{3} \varepsilon = \frac{2}{3} C_\mu k \omega.$$

Combining results, and including the assumption that the diffusion term is negligible, the equation for k

can be written as

$$U \frac{dk}{dx} = -C_\mu k \omega.$$

Recalling that $C_\mu = \beta^*$, the equation for k has the same form than the one of the $k - \omega$ SST model.

Returning now to the transport equation for ω , and applying the assumption of uniform flow and negligible diffusion and cross-diffusion terms results in

$$U \frac{d\omega}{dx} = \beta_\omega \omega^2. \quad (\text{C.28})$$

These two equations are exactly the same as the ones obtained for the $k - \omega$ SST model. Therefore, the decay of freestream turbulence obeys the same equation, meaning that the decay predicted by the two models is identical if the same inlet boundary conditions for k and ω are used.

Appendix D

Quantification of Modelling Differences

This chapter contains the tabulated data for the force coefficients and locations of transition for some of the test cases addressed in Chapter 7. Discussion of the results has been performed in that section and is not repeated here. Available experimental data and the estimated value for the numerical (discretization) uncertainty are given as well.

Table D.1: Lift and drag coefficients for the NACA 0015 airfoil at different angles of attack.

Angle of Attack	Quantity	$k - \omega$ SST	
		$\gamma - Re_{\theta}$	γ
$\alpha = 5^\circ$	$C_d \times 10^3$	16.6 ± 0.3	15.6 ± 0.08
	C_l	0.65 ± 0.000	0.65 ± 0.002
$\alpha = 10^\circ$	$C_d \times 10^3$	30.1 ± 0.86	28.5 ± 0.29
	C_l	0.88 ± 0.007	0.89 ± 0.003

Table D.2: Lift and drag coefficients for the S809 airfoil at different angles of attack. Experimental data from [152].

Angle of Attack	Quantity	$k - \omega$ SST		KSKL		Exp.
		$\gamma - Re_\theta$	γ	$\gamma - Re_\theta$	γ	
$\alpha = 0^\circ$	$C_d \times 10^3$	6.53 ± 0.18	6.44 ± 0.17	6.67 ± 0.08	6.67 ± 0.24	7.08
	C_l	0.149 ± 0.001	0.149 ± 0.001	0.149 ± 0.001	0.149 ± 0.001	0.14
$\alpha = 1^\circ$	$C_d \times 10^3$	6.59 ± 0.12	6.50 ± 0.08	6.73 ± 0.07	6.73 ± 0.09	7.27
	C_l	0.27 ± 0.001	0.27 ± 0.001	0.27 ± 0.000	0.27 ± 0.000	0.26
$\alpha = 3^\circ$	$C_d \times 10^3$	6.85 ± 0.21	6.77 ± 0.05	6.99 ± 0.10	7.00 ± 0.18	7.17
	C_l	0.52 ± 0.002	0.52 ± 0.003	0.52 ± 0.000	0.51 ± 0.002	0.51
$\alpha = 5^\circ$	$C_d \times 10^3$	7.23 ± 0.08	7.26 ± 0.05	9.13 ± 0.06	7.49 ± 0.14	6.99
	C_l	0.76 ± 0.003	0.76 ± 0.001	0.73 ± 0.000	0.76 ± 0.000	0.72
$\alpha = 6^\circ$	$C_d \times 10^3$	8.35 ± 0.26	7.59 ± 0.11	10.8 ± 0.06	7.84 ± 0.20	7.79
	C_l	0.87 ± 0.004	0.88 ± 0.001	0.84 ± 0.003	0.88 ± 0.001	0.79
$\alpha = 7^\circ$	$C_d \times 10^3$	10.20 ± 0.16	7.98 ± 0.08	12.3 ± 0.05	9.17 ± 0.05	12.9
	C_l	0.96 ± 0.002	0.99 ± 0.005	0.94 ± 0.003	0.98 ± 0.001	0.89

Table D.3: Start and end positions of transition on the upper and lower surfaces of the S809 airfoil for several angles of attack. Experimental data taken from [152].

Angle of Attack	Quantity	Surface	$k - \omega$ SST		KSKL		Exp.
			$\gamma - Re_\theta$	γ	$\gamma - Re_\theta$	γ	
$\alpha = 0^\circ$	x_{start}/c	Upper	0.55 ± 0.004	0.54 ± 0.002	0.54 ± 0.002	0.53 ± 0.014	0.55
	x_{end}/c	Upper	0.59 ± 0.004	0.60 ± 0.001	0.56 ± 0.011	0.56 ± 0.008	0.55
	x_{start}/c	Lower	0.50 ± 0.003	0.49 ± 0.006	0.49 ± 0.008	0.48 ± 0.017	0.50
	x_{end}/c	Lower	0.53 ± 0.009	0.53 ± 0.001	0.51 ± 0.017	0.51 ± 0.011	0.50
$\alpha = 1^\circ$	x_{start}/c	Upper	0.54 ± 0.004	0.53 ± 0.002	0.54 ± 0.006	0.53 ± 0.020	0.55
	x_{end}/c	Upper	0.59 ± 0.006	0.59 ± 0.002	0.56 ± 0.014	0.55 ± 0.008	0.55
	x_{start}/c	Lower	0.50 ± 0.003	0.49 ± 0.004	0.50 ± 0.003	0.49 ± 0.011	0.50
	x_{end}/c	Lower	0.54 ± 0.004	0.54 ± 0.001	0.52 ± 0.003	0.51 ± 0.008	0.50
$\alpha = 3^\circ$	x_{start}/c	Upper	0.54 ± 0.003	0.53 ± 0.003	0.53 ± 0.011	0.52 ± 0.007	0.54
	x_{end}/c	Upper	0.58 ± 0.003	0.58 ± 0.002	0.55 ± 0.013	0.54 ± 0.022	0.54
	x_{start}/c	Lower	0.51 ± 0.004	0.50 ± 0.003	0.51 ± 0.004	0.50 ± 0.014	0.51
	x_{end}/c	Lower	0.54 ± 0.003	0.54 ± 0.006	0.52 ± 0.012	0.52 ± 0.011	0.51
$\alpha = 5^\circ$	x_{start}/c	Upper	0.52 ± 0.003	0.052 ± 0.003	0.25 ± 0.006	0.51 ± 0.051	0.51
	x_{end}/c	Upper	0.57 ± 0.190	0.57 ± 0.006	0.35 ± 0.001	0.53 ± 0.012	0.51
	x_{start}/c	Lower	0.52 ± 0.006	0.51 ± 0.006	0.51 ± 0.004	0.51 ± 0.010	0.51
	x_{end}/c	Lower	0.55 ± 0.003	0.55 ± 0.001	0.53 ± 0.005	0.53 ± 0.008	0.51
$\alpha = 6^\circ$	x_{start}/c	Upper	0.25 ± 0.096	0.51 ± 0.003	0.15 ± 0.007	0.50 ± 0.012	0.27
	x_{end}/c	Upper	0.47 ± 0.015	0.57 ± 0.013	0.23 ± 0.008	0.52 ± 0.006	0.29
	x_{start}/c	Lower	0.52 ± 0.002	0.51 ± 0.002	0.52 ± 0.006	0.51 ± 0.035	0.52
	x_{end}/c	Lower	0.56 ± 0.006	0.56 ± 0.002	0.54 ± 0.024	0.54 ± 0.030	0.52
$\alpha = 7^\circ$	x_{start}/c	Upper	0.13 ± 0.009	0.50 ± 0.011	0.09 ± 0.014	0.35 ± 0.004	0.13
	x_{end}/c	Upper	0.36 ± 0.026	0.55 ± 0.009	0.16 ± 0.008	0.43 ± 0.017	0.13
	x_{start}/c	Lower	0.53 ± 0.006	0.52 ± 0.003	0.52 ± 0.002	0.51 ± 0.008	0.52
	x_{end}/c	Lower	0.56 ± 0.002	0.57 ± 0.001	0.54 ± 0.042	0.54 ± 0.003	0.52

Table D.4: Lift and drag coefficients for the NLF₁-0416 airfoil at different angles of attack. Experimental data from [147].

Angle of Attack	Quantity	$k - \omega$ SST		KSKL		Exp.
		$\gamma - Re_\theta$	γ	$\gamma - Re_\theta$	γ	
$\alpha = -2^\circ$	$C_d \times 10^3$	5.20 ± 0.03	5.78 ± 0.05	6.25 ± 0.04	6.02 ± 0.49	6.2
	C_l	0.237 ± 0.000	0.233 ± 0.001	0.233 ± 0.000	0.232 ± 0.006	0.21
$\alpha = 0^\circ$	$C_d \times 10^3$	5.37 ± 0.11	5.61 ± 0.08	5.91 ± 0.20	5.84 ± 0.33	5.9
	C_l	0.48 ± 0.003	0.47 ± 0.002	0.47 ± 0.003	0.47 ± 0.004	0.45
$\alpha = 2^\circ$	$C_d \times 10^3$	6.00 ± 0.23	6.26 ± 0.09	6.42 ± 0.05	6.51 ± 0.55	6.1
	C_l	0.71 ± 0.003	0.71 ± 0.002	0.71 ± 0.001	0.71 ± 0.006	0.68
$\alpha = 4^\circ$	$C_d \times 10^3$	6.91 ± 0.09	7.48 ± 0.17	7.82 ± 0.06	7.76 ± 0.62	6.7
	C_l	0.95 ± 0.002	0.94 ± 0.003	0.94 ± 0.001	0.94 ± 0.006	0.89
$\alpha = 6^\circ$	$C_d \times 10^3$	8.61 ± 0.08	9.22 ± 0.11	9.72 ± 0.07	9.51 ± 0.76	8.7
	C_l	1.17 ± 0.003	1.16 ± 0.004	1.16 ± 0.000	1.16 ± 0.01	1.11

Table D.5: Start and end positions of transition on the upper and lower surfaces of the NLF₁-0416 airfoil for several angles of attack. Experimental data taken from [147].

Angle of Attack	Quantity	Surface	$k - \omega$ SST		KSKL		Exp.
			$\gamma - Re_\theta$	γ	$\gamma - Re_\theta$	γ	
$\alpha = -2^\circ$	x_{start}/c	Upper	0.48 ± 0.01	0.42 ± 0.00	0.43 ± 0.01	0.40 ± 0.22	0.35
	x_{end}/c	Upper	0.53 ± 0.01	0.48 ± 0.01	0.45 ± 0.00	0.44 ± 0.04	0.4
	x_{start}/c	Lower	0.46 ± 0.01	0.41 ± 0.01	0.30 ± 0.01	0.38 ± 0.04	-
	x_{end}/c	Lower	0.56 ± 0.01	0.51 ± 0.01	0.36 ± 0.01	0.45 ± 0.01	-
$\alpha = 0^\circ$	x_{start}/c	Upper	0.44 ± 0.01	0.40 ± 0.01	0.40 ± 0.01	0.37 ± 0.05	0.35
	x_{end}/c	Upper	0.49 ± 0.01	0.45 ± 0.01	0.42 ± 0.00	0.41 ± 0.01	0.4
	x_{start}/c	Lower	0.62 ± 0.00	0.60 ± 0.01	0.47 ± 0.02	0.58 ± 0.01	0.5
	x_{end}/c	Lower	0.65 ± 0.00	0.64 ± 0.00	0.55 ± 0.05	0.61 ± 0.00	0.55
$\alpha = 2^\circ$	x_{start}/c	Upper	0.41 ± 0.00	0.37 ± 0.00	0.36 ± 0.12	0.34 ± 0.10	0.325
	x_{end}/c	Upper	0.45 ± 0.00	0.41 ± 0.00	0.38 ± 0.01	0.38 ± 0.01	0.375
	x_{start}/c	Lower	0.63 ± 0.00	0.62 ± 0.00	0.62 ± 0.01	0.60 ± 0.02	0.55
	x_{end}/c	Lower	0.67 ± 0.01	0.66 ± 0.00	0.64 ± 0.00	0.63 ± 0.01	0.6
$\alpha = 4^\circ$	x_{start}/c	Upper	0.37 ± 0.01	0.28 ± 0.01	0.26 ± 0.01	0.27 ± 0.05	-
	x_{end}/c	Upper	0.41 ± 0.01	0.35 ± 0.00	0.30 ± 0.00	0.31 ± 0.05	-
	x_{start}/c	Lower	0.64 ± 0.01	0.63 ± 0.01	0.63 ± 0.00	0.61 ± 0.19	0.6
	x_{end}/c	Lower	0.68 ± 0.01	0.67 ± 0.00	0.65 ± 0.00	0.64 ± 0.00	0.65
$\alpha = 6^\circ$	x_{start}/c	Upper	0.26 ± 0.02	0.21 ± 0.00	0.18 ± 0.00	0.20 ± 0.04	-
	x_{end}/c	Upper	0.32 ± 0.00	0.27 ± 0.01	0.21 ± 0.00	0.24 ± 0.02	-
	x_{start}/c	Lower	0.65 ± 0.01	0.63 ± 0.01	0.64 ± 0.01	0.63 ± 0.05	0.6
	x_{end}/c	Lower	0.68 ± 0.03	0.68 ± 0.00	0.66 ± 0.00	0.65 ± 0.02	0.65

Table D.6: Lift and drag coefficients for the Eppler 387 airfoil at different angles of attack. Experimental data from [151].

Angle of Attack	Quantity	$k - \omega$ SST			Exp.
		$\gamma - Re_\theta$	γ	AFT	
$\alpha = 1^\circ$	$C_d \times 10^3$	9.62 ± 0.02	8.71 ± 0.02	8.84 ± 0.04	8.9
	C_l	0.49 ± 0.000	0.48 ± 0.000	0.49 ± 0.000	0.48
$\alpha = 7^\circ$	$C_d \times 10^3$	14.13 ± 0.03	13.65 ± 0.05	14.43 ± 0.03	12.8
	C_l	1.12 ± 0.000	1.12 ± 0.000	1.11 ± 0.000	1.08

Table D.7: Start and end positions of transition on the upper surfaces of the Eppler 387 airfoil for several angles of attack. Experimental data from [149].

Angle of Attack	Quantity	$k - \omega$ SST			Exp.
		$\gamma - Re_\theta$	γ	AFT	
$\alpha = 1^\circ$	x_{sep}/c	0.46 ± 0.00	0.48 ± 0.00	0.48 ± 0.00	0.46
	x_{ret}/c	0.73 ± 0.00	0.68 ± 0.00	0.69 ± 0.00	0.7
	x_{start}/c	0.69 ± 0.00	0.65 ± 0.00	0.65 ± 0.00	0.64
	x_{end}/c	0.81 ± 0.00	0.78 ± 0.00	0.80 ± 0.00	0.64
$\alpha = 7^\circ$	x_{sep}/c	0.31 ± 0.00	0.32 ± 0.00	-	-
	x_{ret}/c	0.52 ± 0.00	0.50 ± 0.00	-	-
	x_{start}/c	0.50 ± 0.00	0.48 ± 0.00	0.18 ± 0.00	0.4
	x_{end}/c	0.58 ± 0.00	0.59 ± 0.00	0.37 ± 0.00	0.4

Table D.8: Lift and drag coefficients for the 6:1 prolate spheroid at different angles of attack. Simulations without crossflow extension.

Angle of Attack	Quantity	$k - \omega$ SST			KSKL	
		$\gamma - Re_\theta$	γ	AFT	$\gamma - Re_\theta$	γ
$\alpha = 5^\circ$	$C_D \times 10^3$	4.93 ± 0.03	5.16 ± 0.03	4.94 ± 0.14	7.83 ± 0.06	6.19 ± 0.05
	$C_L \times 10^3$	2.74 ± 0.02	2.73 ± 0.03	3.06 ± 0.54	4.88 ± 0.09	3.17 ± 0.04
$\alpha = 10^\circ$	$C_D \times 10^3$	6.58 ± 0.15	6.9 ± 0.2	-	-	-
	$C_L \times 10^3$	9.48 ± 0.17	9.95 ± 0.17	-	-	-

Table D.9: Lift and drag coefficients for the 6:1 prolate spheroid at different angles of attack. Simulations with crossflow extension.

Angle of Attack	Quantity	$k - \omega$ SST		KSKL	
		$\gamma - Re_\theta$	γ	$\gamma - Re_\theta$	γ
$\alpha = 5^\circ$	$C_D \times 10^3$	6.11 ± 0.12	6.77 ± 0.39	8.42 ± 0.19	7.26 ± 0.44
	$C_L \times 10^3$	3.54 ± 0.32	3.82 ± 1.04	5.18 ± 0.07	4.04 ± 1.7
$\alpha = 10^\circ$	$C_D \times 10^3$	10.72 ± 0.35	11.36 ± 1.04	-	-
	$C_L \times 10^3$	14.5 ± 0.49	15.42 ± 4.77	-	-
$\alpha = 15^\circ$	$C_D \times 10^3$	17.62 ± 0.14	18.45 ± 0.18	-	-
	$C_L \times 10^3$	35.32 ± 0.22	36.47 ± 0.71	-	-

Table D.10: Lift and drag coefficients for the sickle wing. Simulations on the Hexpress grid set.

Crossflow Extension	Quantity	$k - \omega$ SST		
		-	$\gamma - Re_\theta$	γ
No	$C_D \times 10^3$	9.43 ± 2.42	4.78 ± 1.05	8.48 ± 24.66
	C_L	-0.08 ± 0.002	-0.06 ± 0.007	-0.07 ± 0.132
Yes	$C_D \times 10^3$	-	7.87 ± 1.97	-
	C_L	-	-0.08 ± 0.007	-

Table D.11: Lift and drag coefficients for the sickle wing. Simulations on the GridPro grid set.

Crossflow Extension	Quantity	-	$k - \omega$ SST	
			$\gamma - Re_\theta$	γ
No	$C_D \times 10^3$	9.46 ± 0.32	4.85 ± 0.51	5.64 ± 0.27
	C_L	-0.08 ± 0.001	-0.06 ± 0.003	-0.06 ± 0.004
Yes	$C_D \times 10^3$	-	7.92 ± 0.75	8.63 ± 0.52
	C_L	-	-0.08 ± 0.002	-0.08 ± 0.002

